Investigation of the Electrode/Electrolyte Interface using ultra fast Electrochemical Ellipsometry

Julia Catherine Abel

UNIVERSITY OF NEWCASTLE UPON TYNE
Department of Chemistry

A thesis submitted to the University of Newcastle
for the degree of Doctor of Philosophy

August 2001

Abstract

Electrochemical ellipsometry is employed to determine the real and imaginary parts of the refractive index and the thickness of thin films as functions of the potential applied to the electrode upon which the film is grown. The relatively recent advent of an analyser with no moving parts, the Stokesmeter, has removed previous time restraints and allows microsecond resolution. The Newcastle system is extremely novel, using a Stokesmeter, and thus being capable of 325 μs resolution, and also being electrochemically interfaced.

The ellipsometric studies have concentrated on the growth and behaviour of a series of electroactive polymers derived from salicylaldehydes (Salens). [Ni(SaltMe)] and [Ni(SaldMe)] were found to yield stable homogeneous films upon polymerisation, however while the behaviour during film growth was similar, marked differences were observed during potential cycling, poly[Ni(SaldMe)] showing a marked decrease in thickness near the anodic limit not observed for poly[Ni(SaltMe)], indicating that even minor changes to ligand structure well away from the site of polymerisation may have significant effects on the resulting film. The behaviour of poly[Ni(OMeSaltMe)] during polymerisation is more complicated; initially a homogeneous film is produced, however about half way through the growth process the film becomes inhomogeneous, and remains so during subsequent potential cycling. This behaviour was also observed for poly[Pd(OMeSalen)], indicating electron donating groups around the phenyl rings of the ligand have a profound effect on the nature of the polymer films, possibly far more so than the identity of the central metal.

Table of Contents

Declaration

All of the work presented in this dissertation was carried out in the department of chemistry, University of Newcastle upon Tyne, between October 1997 and August 2001. Except where stated the work was carried out by the author and is believed to be original.

Acknowledgments

I would like to take this opportunity to thank several people without whom this thesis would never have been possible. Firstly my supervisors, Prof. Andrew Hamnett and Dr. Paul Christensen, for their advice and support throughout the project. Thanks are also due to the mechanical, electrical, and glassblowing workshops of the chemistry department, especially to Bruce Atkinson and John Marshall.

I am grateful to all past and present members of the AH/PAC research group for their help and friendship, particularly Dr. Rob Reeve, Dr. Gordon Walker, Dr. Andy Doherty, Dr. Miguel Vilas-Boas, Sarah Hill, Ian Tooley and David Earley, and especially Dr. Angus Dickinson

I would also like to thank my family for their support throughout my education, and Fiona Dickinson and George Gibson for being the only other people to understand the importance of ice hockey.

1.1 General Introduction

1.1.1 Historical Background.

Although the term ellipsometry was introduced in 1945 by Alexandre Rothen [1], the first determination of a thin film thickness using the technique now known by this phrase was reported by P. Drude in 1889 [2]. While the term ellipsometry was often used in the past to mean any analysis of elliptically polarised light, it is now generally restricted to the determination of the refractive index and thickness of a film from the analysis of the change in polarisation state of a reflected beam.

As early as 1775 it had been reported that the polarisation state of light was altered by reflection from a surface. Fresnel quantified this effect, relating reflection coefficients to angles of incidence and refraction and to refractive index; however these formulae failed to account for the frequently observed elliptical polarisation of the reflected beam. Rayleigh later concluded that surface films were responsible for the ellipticity observed, and Drude [3] quantified the production of elliptically polarised light by a film covered surface, giving a general expression valid for films of any thickness on any surface. The so called Drude Equation is the basis of ellipsometry.

1.1.2 Overview of Ellipsometry.

In this section a brief introduction to the basis of an ellipsometric experiment and the parameters measured is given, for more detailed reviews of the application and theory of the technique see, for example, [4] to [8].

Ellipsometry is used to determine the thickness and complex refractive index [9] of thin films. The complex index of refraction, $\tilde{N}$, describes the interaction of light with its medium, and is a complex quantity because absorption (usually) occurs as well as refraction, and so may be defined by the equation

$$\tilde{N} = n - ik \qquad \text{(eqn. 1.1)}$$

where $i = \sqrt{-1}$. n is the index of refraction, defined as the ratio of the speed of light in a vacuum to its speed in the medium concerned, and k is the extinction coefficient, which is related to the absorption coefficient α by:

$$k = (\lambda/4\pi)\alpha \qquad \text{(eqn. 1.2)}$$

where λ is the wavelength. It is worth noting that though α has units of length^{-1}, both n and k are unitless.

During an experiment, a monochromatic beam of light of known polarisation is reflected by a film-covered substrate at a known angle of incidence, and the polarisation state of the reflected beam is determined. By analysis of this polarisation state it is possible to determine the film thickness and refractive index.

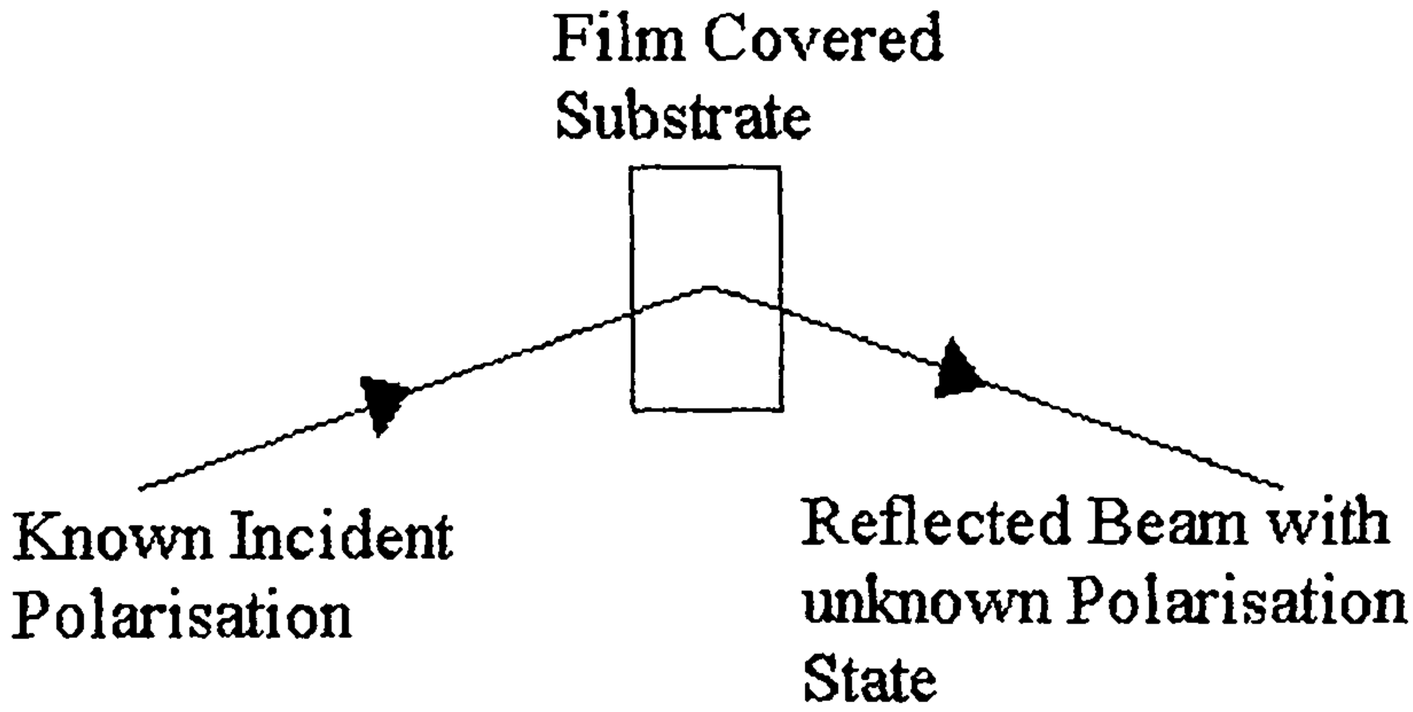

Fig. 1.1. The basis of an ellipsometric experiment. A light beam of known polarisation is incident on a film covered substrate, and the polarisation state of the reflected beam must be determined.

Electrochemical ellipsometry is performed in exactly the same manner, with the substrate upon which the film is deposited being the working electrode. The behaviour of the film as a function of potential is probed by monitoring changes in the polarisation state of the reflected beam as the potential of the electrode is altered.

The polarisation state of a light ray will alter upon reflection, whether a film is present upon the reflecting surface or not. A light wave can be considered to be the resultant of two orthogonal vector components, normally denoted as E_s and E_p, where E_s is amplitude of the beam along the s axis, and E_p that along the p axis. These axes are defined with respect to the plane of incidence, as shown in Fig. 1.2 , p being the component lying parallel to the plane, and s perpendicular to it (coming from the German for perpendicular, *senkrecht*). The s and p components undergo different phase changes when reflected, which results in the polarisation change of the beam.

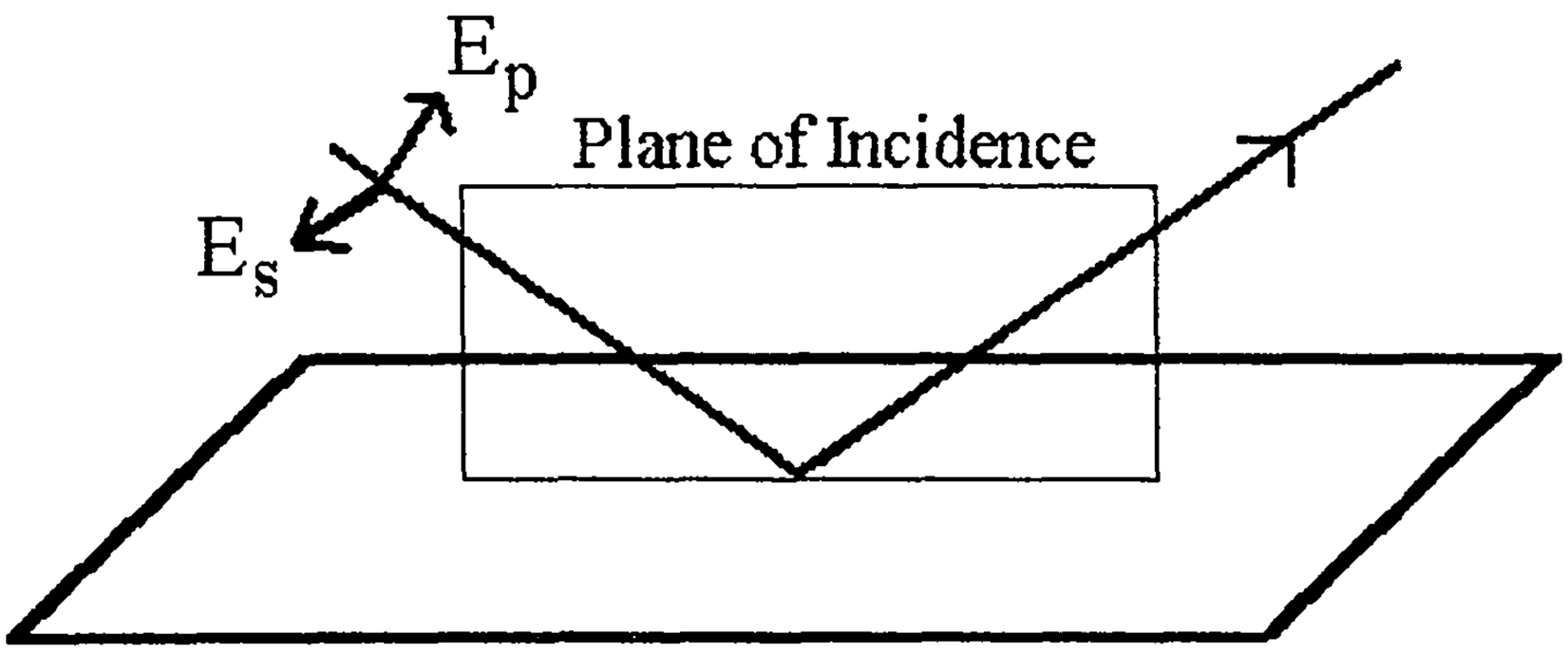

Fig. 1.2. A light wave can be considered to the resultant of two orthogonal vectors, E_s and E_p, Defined as the amplitude of the wave perpendicular and parallel, respectively, to the plane of incidence

The polarisation data consists of two angles, Δ and Ψ. These can be described by the equations

$$\Delta = \delta_p - \delta_s \qquad \text{(eqn. 1.3)}$$

$$\tan\Psi = \frac{|r_p|}{|r_s|} \qquad \text{(eqn. 1.4)}$$

Where δ_p and δ_s are the phase changes upon reflection of the p and s components, respectively, and r_p and r_s are the reflectivity coefficients of the p and s components, respectively. The reason these parameters contain information about the film thickness and refractive index can be seen from Fig. 1.3. When a light ray is incident upon a film-covered substrate, part of the beam is reflected by the upper surface of the film, and part refracted through the film and reflected by the substrate underneath, resulting in two reflected beams. These will interfere with one another to yield a resultant beam. The polarisation of this beam will depend on the phase difference

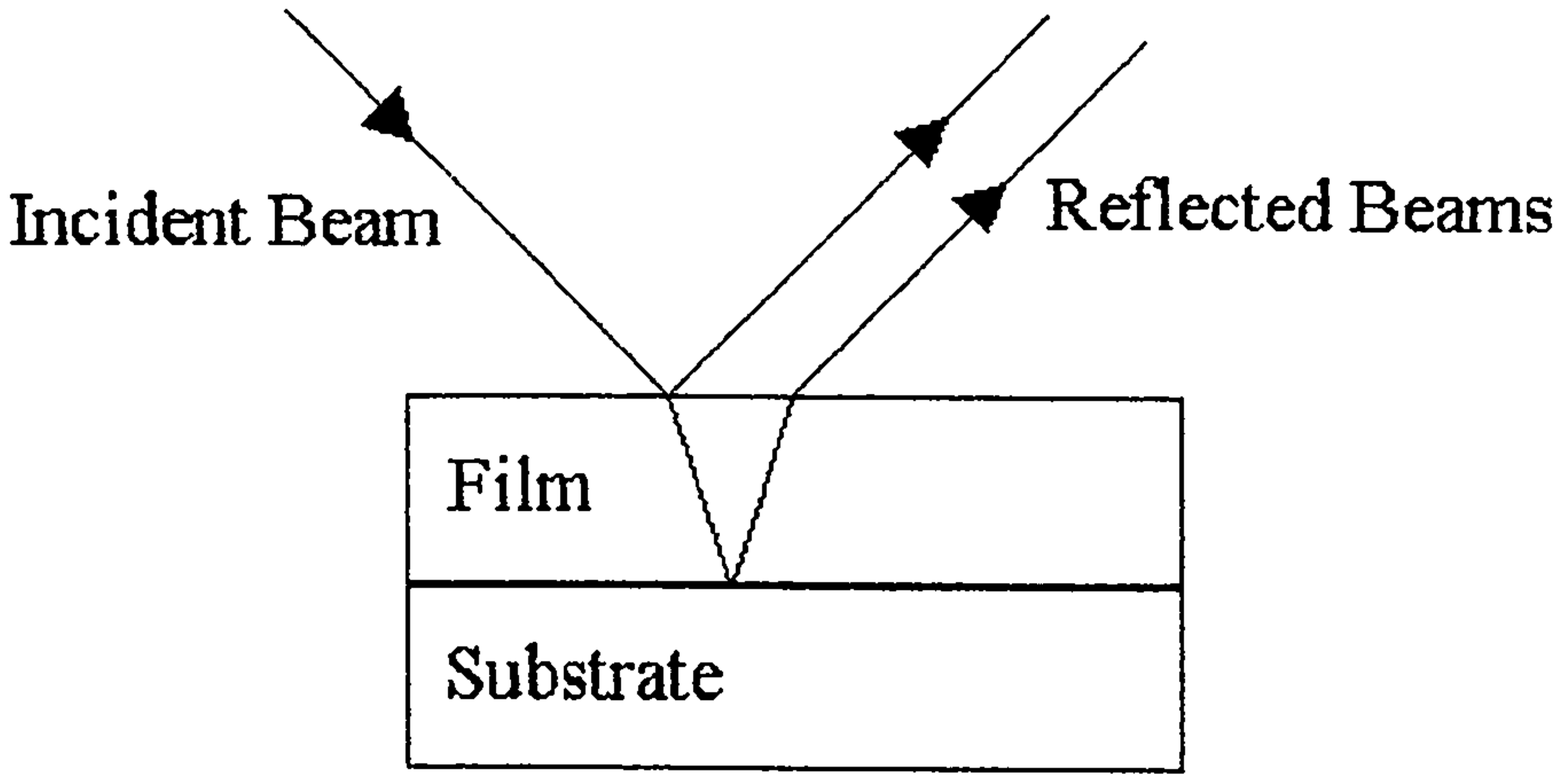

Fig. 1.3. A beam incident on a film covered surface will be partially reflected by the upper surface of the film, and part refracted through the film. The two reflected beams will interfere to give a resultant polarisation.

two reflected beams, which will be determined by the thickness of the film through which the refracted beam had to travel and the angle through which it was refracted, hence why ellipsometry yields information about these properties.

Intensity measurements can also be made, and the ratio of the reflected beam to the incident beam can be recorded. It should be noted that reflectance measurements are different from ellipsometric measurements, as Δ and Ψ are surface sensitive parameters, while this is not necessarily the case for the relative intensity as the formation of absorbing products in solution will affect this parameter, and great care has to be taken to verify that the changes observed are due to surface processes and are suitable for analysis.

The equations describing the behaviour of light at the solution/film and film/electrode interface are complex (see Section 1.3), and cannot be solved analytically, so using the relative intensity, Δ and Ψ, the system under investigation is

modelled. Educated guesses are made for the values of the complex refractive index (n and k) and the thickness, and then the values of Δ, Ψ and intensity such a system would exhibit are calculated and compared to the observed data. In light of this comparison the initial estimates for the calculations are adjusted until the calculated and experimental systems yield the same values of Δ, Ψ and intensity

Ellipsometry has many attractive features, including:

1. Ellipsometric measurements are performed *in-situ*. This is particularly useful for electrochemical experiments, where changes in the optical properties of the electrochemical interface can be followed with the incident and reflected beams passing through the electrolyte and the electrode can be probed while immersed.
2. Extremely high sensitivity to changes in surface coverage. Films much thinner than the probe wavelength can be investigated, since it is changes in the phase of the beam which are monitored and Δ and Ψ can be measured very precisely. Sub-monolayer detection is possible with many systems.
3. The parameters Δ and Ψ are highly surface selective. The formation of an absorbing product in solution would not affect their values (though would affect any reflectance measurements made)
4. It is non-destructive: samples may be used repeatedly.
5. Speed. Polarisation detectors are now available that instantaneously determine the polarisation state, and the time resolution of such systems is limited by the rate at which the interfaced computer can record the data.

1.2 Polarised light

1.2.1 Plane, Circularly and Elliptically Polarised Light

Huygens was the first to suggest light was not a scalar quantity, based on his work on the prorogation of light through crystals; it appeared that light had "sides" in the words of Newton. While it is quite common for polarised light to be represented as a transverse wave, this is in fact an oversimplification in most cases and only one extreme of behaviour [9, 10].

The electromagnetic disturbance can be considered as two vector components orthogonal to one another, E_x and E_y In the case of Fig 1.4 E_y is shown in blue and

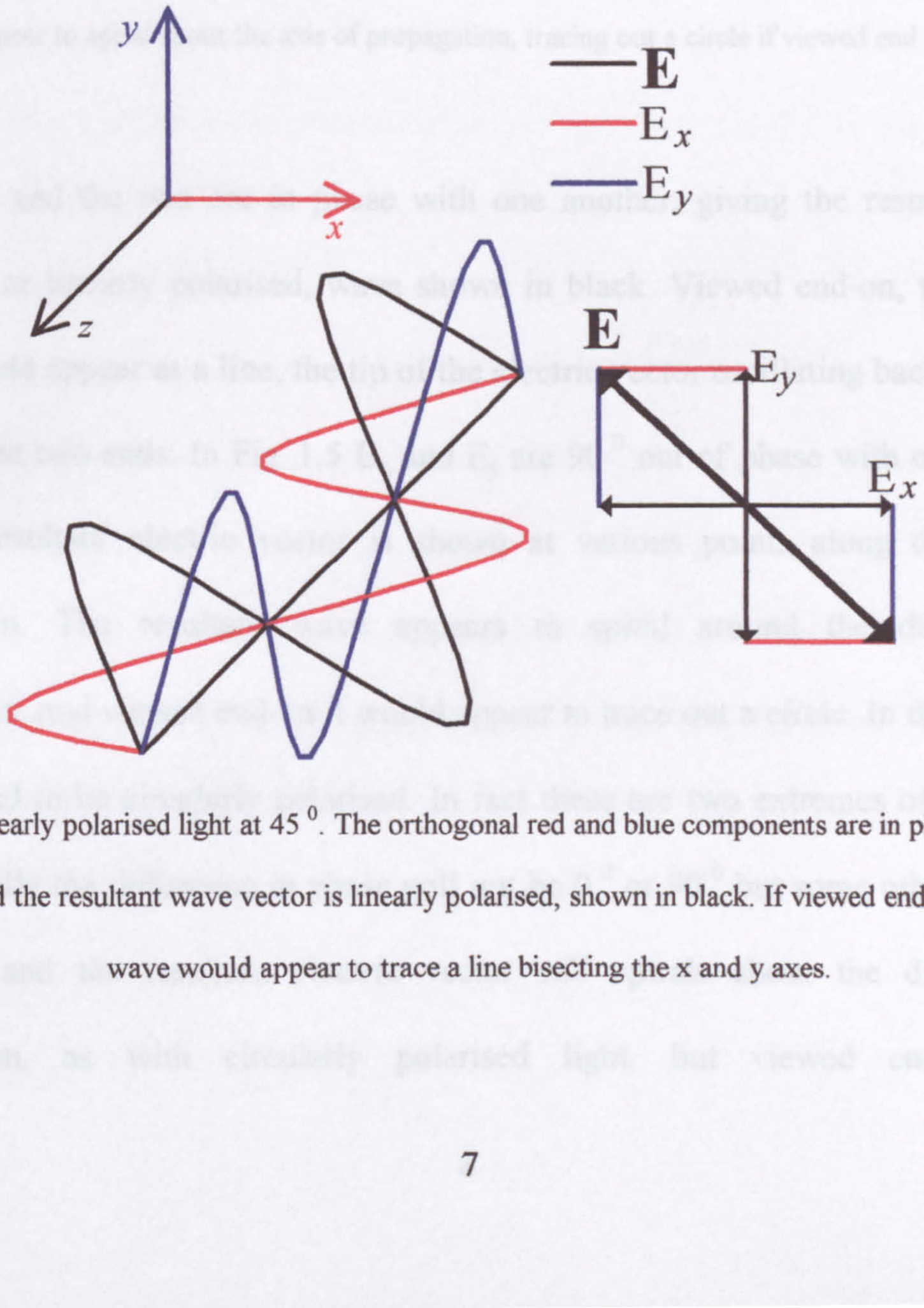

Fig. 1.4. Linearly polarised light at 45 ^{0}. The orthogonal red and blue components are in phase with one another, and the resultant wave vector is linearly polarised, shown in black. If viewed end on the black wave would appear to trace a line bisecting the x and y axes.

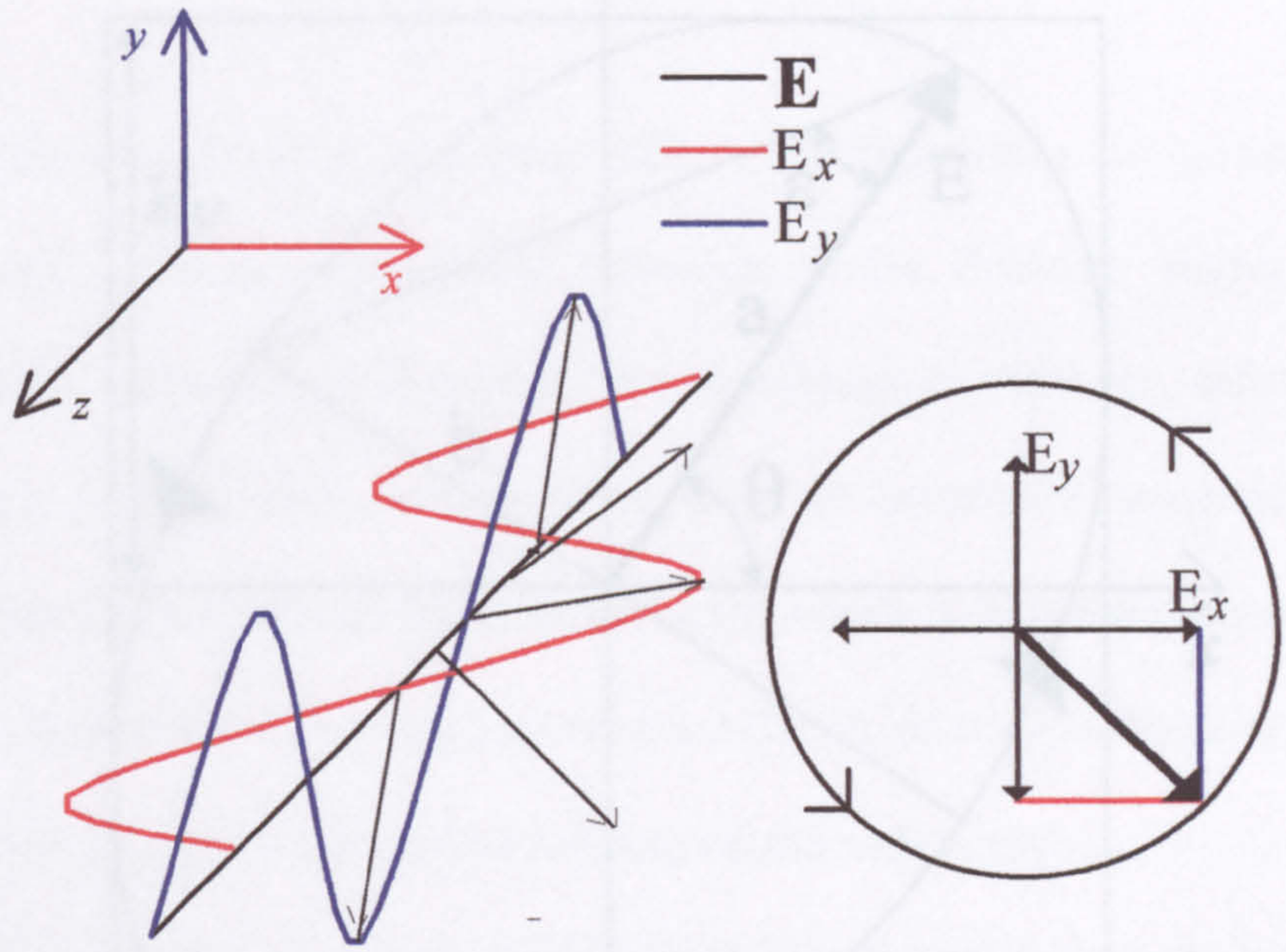

Fig. 1.5 Circularly polarised light. The orthogonal components shown in red and blue are 90 ^{0} out of phase with one another. The resultant vector is shown at various stages by the black arrows, which appear to spiral about the axis of propagation, tracing out a circle if viewed end on.

E_x in red, and the two are in phase with one another, giving the resultant plane polarised, or linearly polarised, wave shown in black. Viewed end-on, the electric vector would appear as a line, the tip of the electric vector oscillating back and forth between the two ends. In Fig. 1.5 E_x and E_y are 90 ^{0} out of phase with one another and the resultant electric vector is shown at various points along the axis of propagation. The resultant wave appears to spiral around the direction of propagation, and viewed end-on it would appear to trace out a circle. In this case the light is said to be circularly polarised. In fact these are two extremes of behaviour and normally the difference in phase will not be 0 ^{0} or 90 ^{0} but some other value in between, and the resultant electric vector still spirals about the direction of propagation, as with circularly polarised light, but viewed end on the

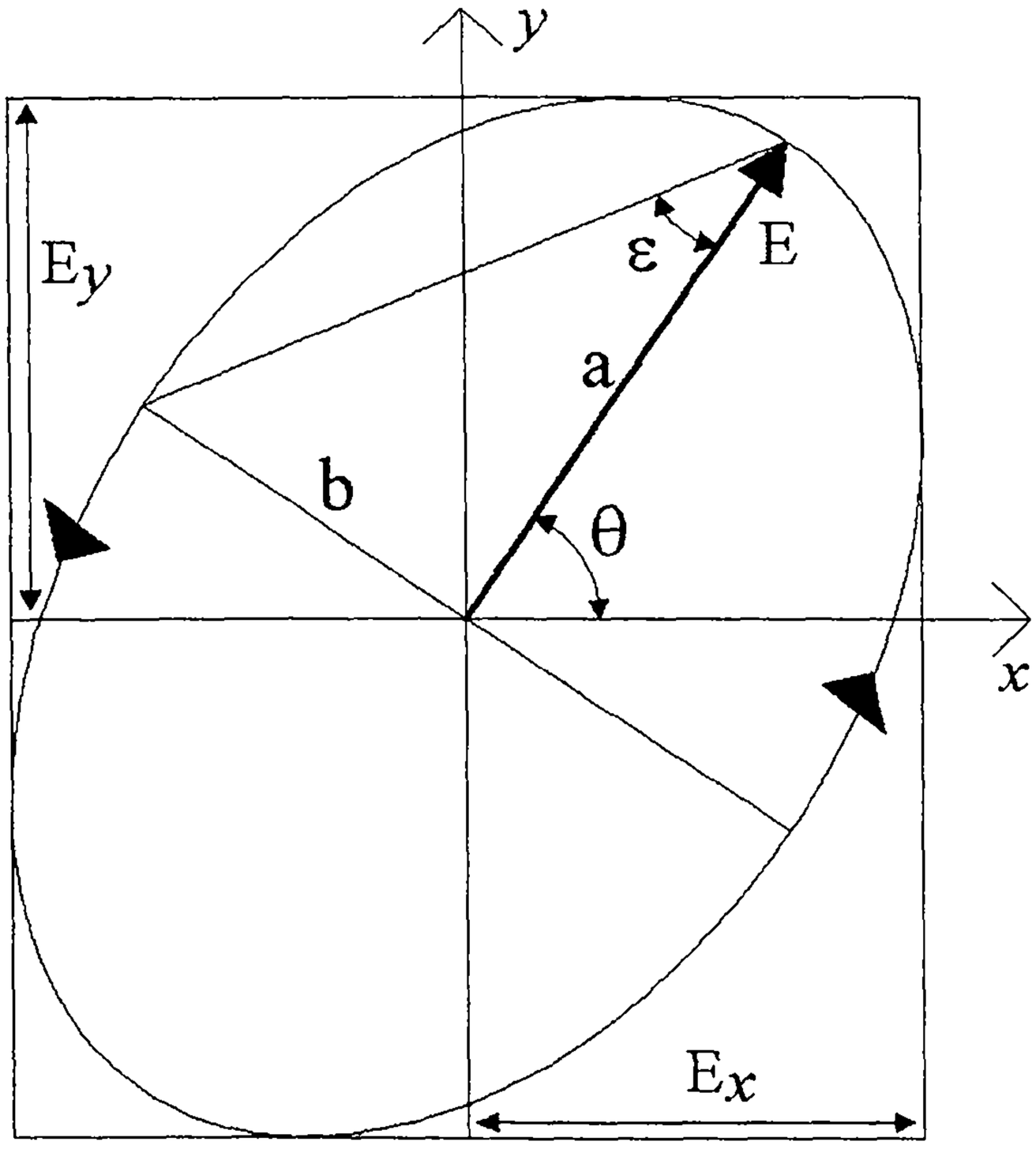

Fig. 1.6. The polarisation ellipse. Elliptically polarised light can be described by two angles, θ, the azimuthal angle, and ε, the degree of ellipticity.

electric vector appears to trace out an ellipse, hence "elliptically polarised" light. This polarisation ellipse can be characterised by two angles, shown as θ and ε on Fig 1.6. θ is the azimuthal angle and ε, defined as $\tan^{-1}(b/a)$, describes the degree of ellipticity, and it is these two angles which are measured during an ellipsometric experiment and converted to two related angles, Δ and Ψ by the relations:

$$\tan 2\theta = -\tan 2\Psi \cos\Delta \qquad \text{(eqn. 1.5)}$$

$$\cos 2\Psi = -\cos 2\varepsilon \cos 2\theta \qquad \text{(eqn. 1.6)}$$

1.2.2 Creation of Polarised light

Polarisers [9-11] come in many different configurations, but are based on four fundamental physical mechanisms; reflection at the Brewster angle, scattering, dichromism (selective absorption), and birefringence (double refraction), the underlying property they share is some form of asymmetry associated with the propagation of light through them. Any material which is completely absorbing along one axis while transmitting along an orthogonal axis can act as a linear polariser, two of the most commonly used materials being calcite and quartz .

If a material is anisotropic but light is transmitted through both axes the material acts as a retarder [9-11]. The anisotropy results in the refractive index, *n*, being different along the two axes so when light passes through the component in the plane of the optical axis of the crystal is transmitted faster than the component normal to it, and the resultant wave emerges with a phase shift between (arbitrarily) E_x and E_y, e.g. linearly polarised light can be changed to elliptically or circularly polarised. A combination of a linear polariser and retarder can be used to generate any polarisation state.

One very important class of retarders is known as a quarter wave plate (QWP), which induces a phase difference of 45^0 between the x and y components; thus if the x and y components are of equal magnitude the emerging beam is circularly polarised. The simplest way for E_x and E_y to be of equal magnitude is to polarise

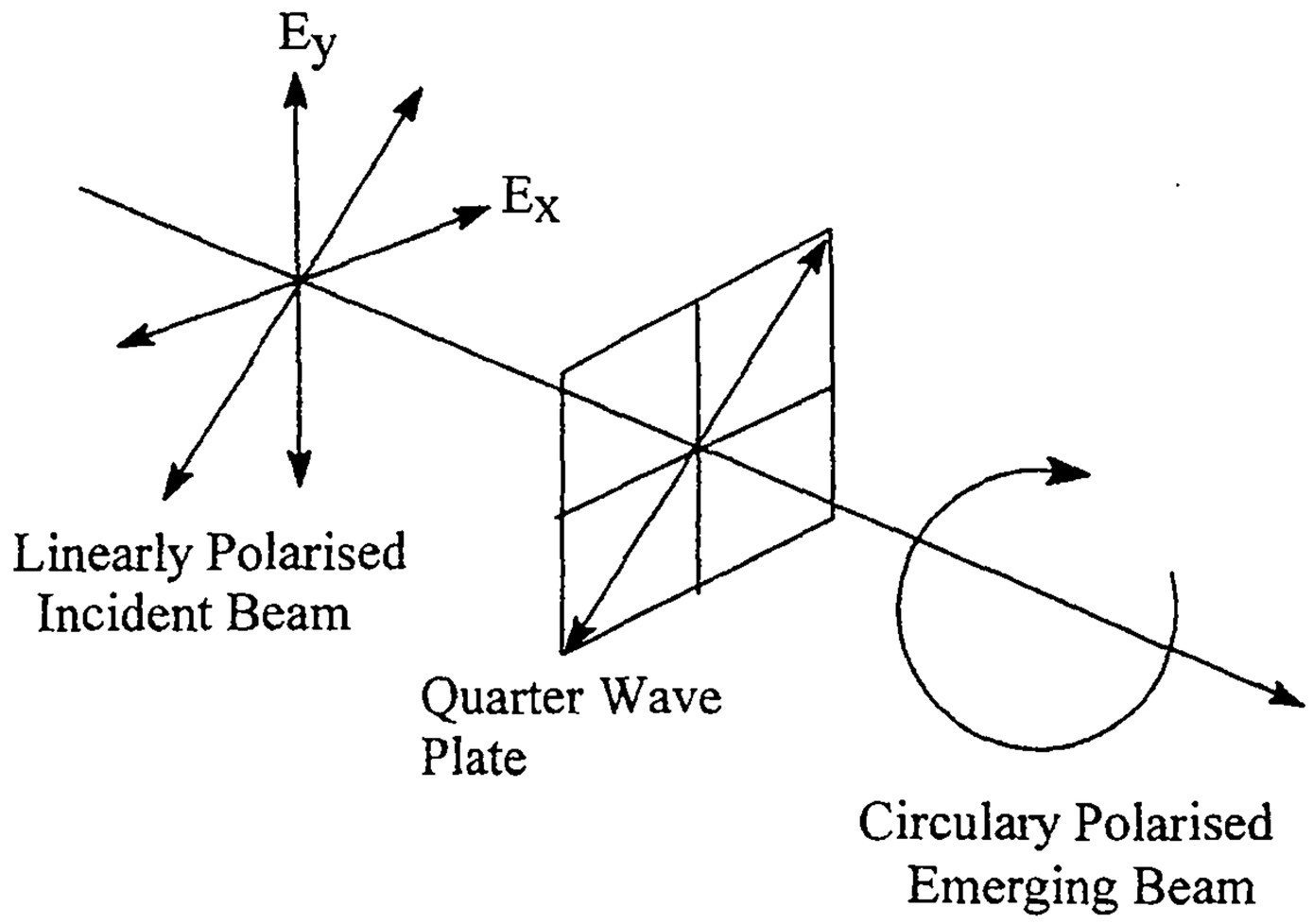

Fig. 1.7. When 45 ^{0} linearly polarised light is incident on a Quarter Wave Plate, the emerging beam is circularly polarised.

the incident beam to be linearly polarised at 45 ^{0} to the fast (or slow) axis, as shown in Fig. 1.7. The ability to generate circularly polarised light is important in optical experiments, as when incident on a polarising element, regardless of the angle of the element, the emerging beam will be of a constant intensity.

1.2.3 Representation of Polarised Light and Polarising Components.

1.2.3.1 Stokes Vectors

Polarised light is commonly described in terms of the electric field component of the wave, the most general representation of that being elliptically polarised light where the endpoint of the vector **E** continuously sweeps out the path of an ellipse. The period over which the ellipse is traversed is equal to the period of the light wave, roughly 10^{-15} s, far too short to be detected, as no technique is capable of recording measurements over such a short timescale, thus alternative descriptions of polarisation in terms of observable parameters, i.e. irradiances, or intensities, are required.

In 1852 Sir George Gabriel Stokes [12] introduced four quantities that are functions only of observables of the electromagnetic wave, which have now become known as the Stokes parameters [10,11]. These parameters were introduced by Stokes as a way of describing partially polarised light, a problem that had long troubled physicists, and although they described how the polarisation of light can be determined simply by measuring its intensity at four different angles, Stokes did not realise this at the time, due mainly to the most sensitive intensity detector of the day being the eye, and it was not until the advent of photovoltaics that the full potential of the parameters was realised. Consider a pair of plane waves, orthogonal to each other propagating along the z axis and represented by the equations

$$E_x = E_{0x}\cos(\tau + \delta_x) \qquad \text{(eqn. 1.7a)}$$

$$E_y = E_{0y}\cos(\tau + \delta_y) \qquad \text{(eqn. 1.7b)}$$

Where $\tau = \omega t - \kappa z$ is the propagator (ω is the angular frequency and $\kappa = 2\pi/\lambda$), the subscripts x and y refer to the components in the x and y directions, E_{0x} and E_{0y} are the maximum amplitudes and δ_x and δ_y are the phases. As the field propagates, E_x and E_y give rise to a resultant vector, which describes a locus of points in space; the curve generated by these points can be derived. Equations 1.7a and b can be rewritten as:

$$\frac{E_x}{E_{0x}} = \cos\tau \cos\delta_x - \sin\tau \sin\delta_x \qquad \text{(eqn. 1.8a)}$$

$$\frac{E_y}{E_{0y}} = \cos\tau \cos\delta_y - \sin\tau \sin\delta_y \qquad \text{(eqn. 1.8b)}$$

and using simple trigonometric identities and rearranging gives:

$$\frac{E_x}{E_{0x}} \sin\delta_y - \frac{E_y}{E_{0y}} \sin\delta_x = \cos\tau \sin(\delta_y - \delta_x) \qquad \text{(eqn. 1.9a)}$$

$$\frac{E_x}{E_{0x}} \cos\delta_y - \frac{E_y}{E_{0y}} \cos\delta_x = \sin\tau \sin(\delta_y - \delta_x) \qquad \text{(eqn. 1.9b)}$$

Squaring each of the above equations and adding them together gives:

$$\frac{E_x^2}{E_{0x}^2} + \frac{E_y^2}{E_{0y}^2} - 2\frac{E_x}{E_{0x}}\frac{E_y}{E_{0y}}\cos\delta = \sin^2\delta \qquad \text{(eqn. 1.10)}$$

where $\delta = \delta_y - \delta_x$, which is recognisable as the equation of an ellipse (the cross product showing that it is rotated about the z axis), showing the locus of points

described by the electric vector of any light beam is indeed an ellipse, linear and circular polarised light being specialised forms of the polarisation ellipse.

E_{0x}, E_{0y}, and δ are constants, however E_x and E_y are dependent on time. During an experiment we must therefore take an average of these parameters over the time of observation. The time average is represented by the symbol $\langle \ldots \rangle$, and equation 1.10 can be rewritten

$$\frac{\langle E_x^2 \rangle}{E_{0x}^2} + \frac{\langle E_y^2 \rangle}{E_{0y}^2} - \frac{2\langle E_x E_y \rangle}{E_{0x} E_{0y}} \cos\delta = \sin^2 \delta \qquad \text{(eqn. 1.11)}$$

Where

$$\langle E_x E_y \rangle = \lim_{T \to \infty} \frac{1}{T} \int_0^T E_x E_y dt \qquad \text{(eqn. 1.12)}$$

Using equations 1.7 in 1.12, and averaging over one period of oscillation (i.e. $T = 1/f = 2\pi/\omega$), the average values of eqn. 1.11 can be determined to be [10,13]

$$\langle E_x^2 \rangle = \frac{1}{2} E_{0x}^2 \qquad \text{(eqn. 1.13a)}$$

$$\langle E_y^2 \rangle = \frac{1}{2} E_{0y}^2 \qquad \text{(eqn. 1.13b}$$

$$\langle E_x E_y \rangle = \frac{1}{2} E_{0x} E_{0y} \cos\delta \qquad \text{(eqn. 1.13c)}$$

Multiplying equation 1.11 by $4E_{0x}^2 E_{0y}^2$ and inserting the averaged values from equation 1.13 yields

$$4E_{0x}^2E_{0y}^2-(2E_{0x}E_{0y}\cos\delta)^2=(2E_{0x}E_{0y}\sin\delta)^2 \qquad \text{(eqn. 1.14)}$$

which may be written

$$(E_{0x}^2+E_{0y}^2)^2-(E_{0x}^2-E_{0y}^2)^2-(2E_{0x}E_{0y}\cos\delta)^2=(2E_{0x}E_{0y}\sin\delta)^2 \qquad \text{(eqn. 1.15)}$$

We can now write the quantities in parentheses as

$$S_0=E_{0x}^2+E_{0y}^2 \qquad \text{(eqn. 1.16a)}$$

$$S_1=E_{0x}^2-E_{0y}^2 \qquad \text{(eqn. 1.16b)}$$

$$S_2=2E_{0x}E_{0y}\cos\delta \qquad \text{(eqn. 1.16c)}$$

$$S_3=2E_{0x}E_{0y}\sin\delta \qquad \text{(eqn 1.16d)}$$

and then express equation 1.15 as

$$S_0^2=S_1^2+S_2^2+S_3^2 \qquad \text{(eqn. 1.17)}$$

The four equations given by 1.16 are the Stokes polarisation parameters [12]. S_0 is the total intensity of the light, S_1 the amount of linear horizontal or vertical polarisation, S_2 the amount of linear $+45^0$ or -45^0 polarisation, and S_3 the amount of right or left circular polarisation within the beam. Using the complex representation of a wave [9,10], for convenience taken at $z = 0$

$$E_x = E_{0x}\exp[i(\tau + \delta_x)] \quad \text{(eqn. 1.18a)}$$

$$E_y = E_{0y}\exp[i(\tau + \delta_y)] \quad \text{(eqn. 1.18b)}$$

it is straight forward to show the Stokes parameters can also be represented as

$$S_0 = E_x E_x^* + E_y E_y^* \quad \text{(eqn. 1.19a)}$$

$$S_1 = E_x E_x^* - E_y E_y^* \quad \text{(eqn 1.19b)}$$

$$S_2 = E_x E_y^* + E_y E_x^* \quad \text{(eqn. 1.19c)}$$

$$S_3 = i(E_x E_y^* - E_y E_x^*) \quad \text{(eqn. 1.19d)}$$

and with a little more work [see for example 10] it is also possible to show that the Stokes parameters can be described by the angles of the polarisation ellipse:

$$S_0 = S_0 \quad \text{(eqn. 1.20a)}$$

$$S_1 = S_0 \cos 2\theta \cos 2\varepsilon \quad \text{(eqn. 1.20b)}$$

$$S_2 = S_0 \sin 2\theta \cos 2\varepsilon \quad \text{(eqn. 1.20c)}$$

$$S_3 = S_0 \sin 2\varepsilon \quad \text{(eqn. 1.20d)}$$

As examples of the representation of polarised light using the Stokes parameters, if we consider again the parameters in the form of equation 1.16, it is easy to see how horizontal, vertical, $+45^0$, -45^0 linear polarised light and left and right circularly polarised light can be described as shown in table 1.1, where E_0 applies in cases where $E_{0x} = E_{0y} = E_0$

Linear Horizontal Polarised Light	$S_0 = E_{0x}^2$ $S_1 = E_{0x}^2$ $S_2 = 0$ $S_3 = 0$	Linear Vertical Polarised Light	$S_0 = E_{0y}^2$ $S_1 = -E_{0y}^2$ $S_2 = 0$ $S_3 = 0$
Linear $+45^0$ Light	$S_0 = 2E_0^2$ $S_1 = 0$ $S_2 = 2E_0^2$ $S_3 = 0$	Linear -45^0 Light	$S_0 = 2E_0^2$ $S_1 = 0$ $S_2 = -2E_0^2$ $S_3 = 0$
Right Circularly Polarised light	$S_0 = 2E_0^2$ $S_1 = 0$ $S_2 = 0$ $S_3 = 2E_0^2$	Left Circularly Polarised Light	$S_0 = 2E_0^2$ $S_1 = 0$ $S_2 = 0$ $S_3 = -2E_0^2$

Table 1.1. Examples of polarisations represented by Stokes parameters.

The four Stokes parameters are often arranged in the form of a column matrix and referred to as the Stokes vector, written as

$$S = \begin{pmatrix} S_0 \\ S_1 \\ S_2 \\ S_3 \end{pmatrix} \qquad \text{(eqn. 1.21)}$$

Frequently, the total intensity is removed outside the bracket on the right hand side of the equation, for example the Stokes vector for horizontal linear polarised light may be written as

$$S = I_0 \begin{pmatrix} 1 \\ 1 \\ 0 \\ 0 \end{pmatrix} \qquad \text{(eqn. 1.22)}$$

and by normalising the intensity, can be written simply as

$$S = \begin{pmatrix} 1 \\ 1 \\ 0 \\ 0 \end{pmatrix} \qquad \text{(eqn. 1.23)}$$

Table 1.2 shows the Stokes vectors written in this form for the examples in table 1.

State of Polarisation	Stokes Vectors	State of Polarisation	Stokes Vectors
Horizontal Linear Polarisation	$\begin{pmatrix} 1 \\ 1 \\ 0 \\ 0 \end{pmatrix}$	Linearly Polarised at -45^0	$\begin{pmatrix} 1 \\ 0 \\ -1 \\ 0 \end{pmatrix}$
Vertical Linear Polarisation	$\begin{pmatrix} 1 \\ -1 \\ 0 \\ 0 \end{pmatrix}$	Circularly Polarised Clockwise (R)	$\begin{pmatrix} 1 \\ 0 \\ 0 \\ 1 \end{pmatrix}$
Linearly Polarised at $+45^0$	$\begin{pmatrix} 1 \\ 0 \\ 1 \\ 0 \end{pmatrix}$	Circularly Polarised Anti-clockwise (L)	$\begin{pmatrix} 1 \\ 0 \\ 0 \\ -1 \end{pmatrix}$

Table 1.2. Representations of polarisations using Stokes vectors.

1.2.3.2. The Poincaré sphere

One very useful method of describing the various states of polarised light is the Poincaré Sphere. In this representation the radius of the sphere is equal to the total intensity of the light (S_0), with 2θ plotted around the horizontal plane of the sphere, and 2ε plotted vertically around the sphere, θ and ε being the azimuthal angle and degrees of ellipticity respectively (see section 1.2.1). The resultant sphere is shown in Fig. 1.8, and every point on the surface of the sphere represents a different polarisation state. For example, any polarisation state with $\varepsilon = 0^0$ will be linearly polarised and will lie at some point on the circumference of the sphere. Horizontally (X) and vertically (Y) linearly polarised states are shown on the right and left hand

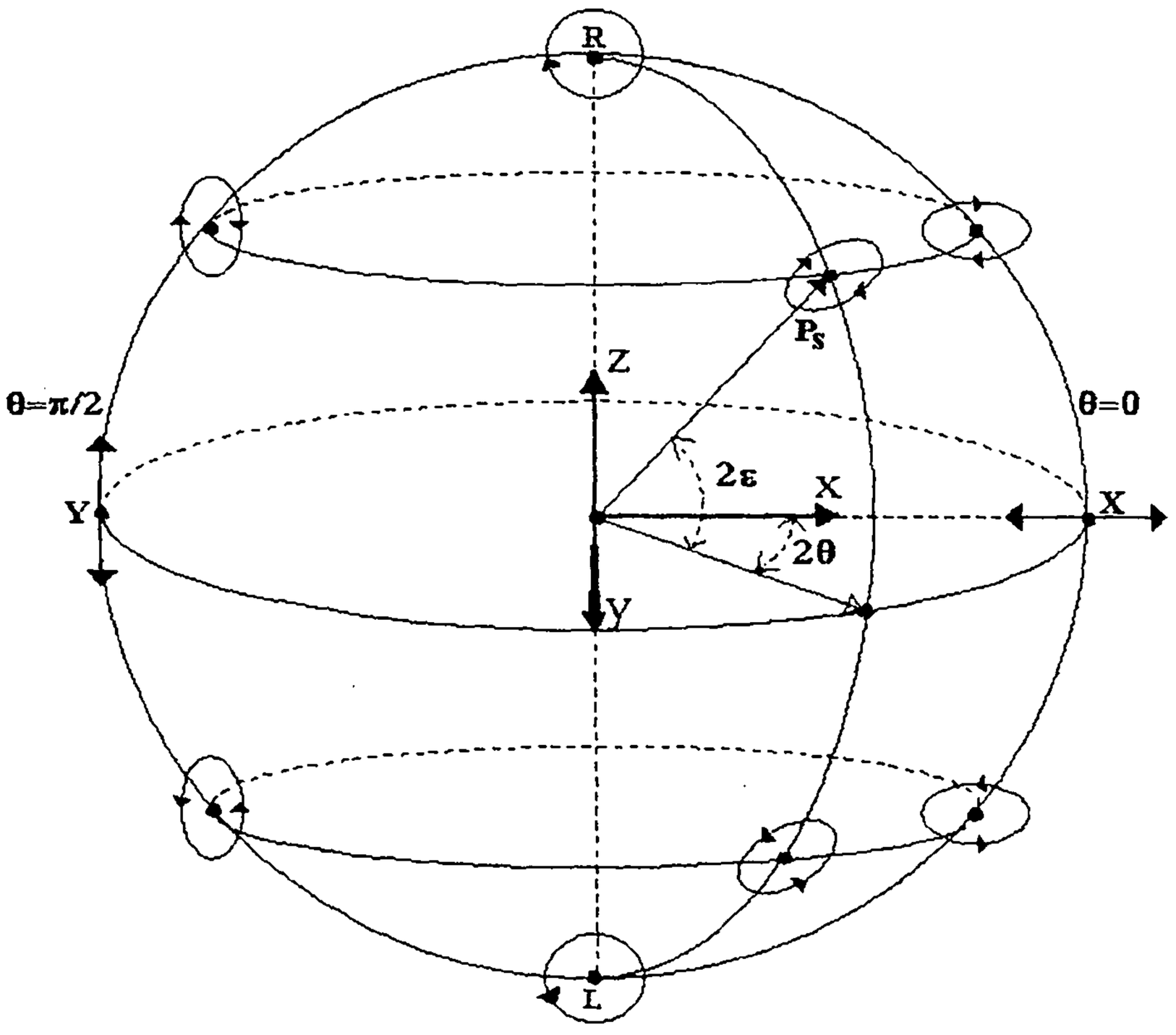

Fig. 1.8 The Poincaré Sphere. 2θ is plotted around the horizontal plane, and 2ε around the vertical plane. Any state of polarisation can be represented by a point on the surface of the sphere.

sides of Fig. 1.8, linearly polarised light at other angles is represented by a point between them on the circumference. A polarisation state with $\varepsilon = 45^0$ will be circularly polarised, and is represented on the Sphere by one of the two poles ($2\varepsilon = \pm 90^0$), right handed circularly polarised light at the top pole and left at the bottom. Between the circumference and the poles the various states of elliptically polarised light are represented, increasing in ellipticity as the poles are approached.

Recall equations 1.20:

$$S_0 = S_0 \qquad \text{(eqn. 1.20a)}$$

$$S_1 = S_0 \cos 2\theta \cos 2\varepsilon \qquad \text{(eqn. 1.20b)}$$

$$S_2 = S_0 \sin 2\theta \cos 2\varepsilon \qquad \text{(eqn. 1.20c)}$$

$$S_3 = S_0 \sin 2\varepsilon \qquad \text{(eqn. 1.20d)}$$

It is straightforward to verify that with S_0 as the radius of the sphere, S_1, S_2, and S_3 are the three dimensional polar coordinates of the surface position relating to the polarisation state: if a point on the surface is translated onto the three axis shown in the centre of the sphere, S_1 is the distance along the x axis, S_2 the distance along the y axis, and S_3 the distance along the z axis. If we recall the description of each of the parameters given in section 1.2.3.1, S_1 describes the amount of horizontal or vertical linear polarisation, and in the Poincaré sphere represents the coordinate along the x axis, the two extremes of this axis being 0^0 and 90^0 linear polarisation. The y axis intercepts the sphere surface at $+45^0$ at the front and -45^0 if extended to the rear of the plane of the page, clearly representing the amount of polarisation along these axes, as described in the previous section. $S_3 = S_0 \sin 2\varepsilon$, which from Fig. 1.4

describes the elevation of the point from the circumference, describing the degree of ellipticity or the amount of circular polarisation. It is also clear from this representation that, S_0 being the hypotenuse, by Pythagoras' theorem $S_0^2 = S_1^2 + S_2^2 + S_3^2$.

Henri Poincaré first discussed the sphere around 1890 as a tool for performing polarisation calculations; though it simplified the mathematics involved, considerable mathematical effort was still required. The advent of matrix methods and computers has simplified the mathematical processes involved considerably, and Mueller matrices are discussed in the next section. Ironically, understanding of the full extent of the Poincaré spheres usefulness came only after the advent of Jones and Mueller matrix. For further information about the sphere's properties and applications see [9,10]

1.2.3.3. Mueller matrices

H. Mueller was the first person to describe polarising components in terms of matrices. Although his 4x4 matrix appears to be based on the work of F. Perrin [14], and a still earlier paper by P. Soleillet [15], and Mueller himself never published his work on matrices, his name is still firmly attached to them.

Imagine a beam of light is incident on a polarising element, as shown in Fig. 1.9.

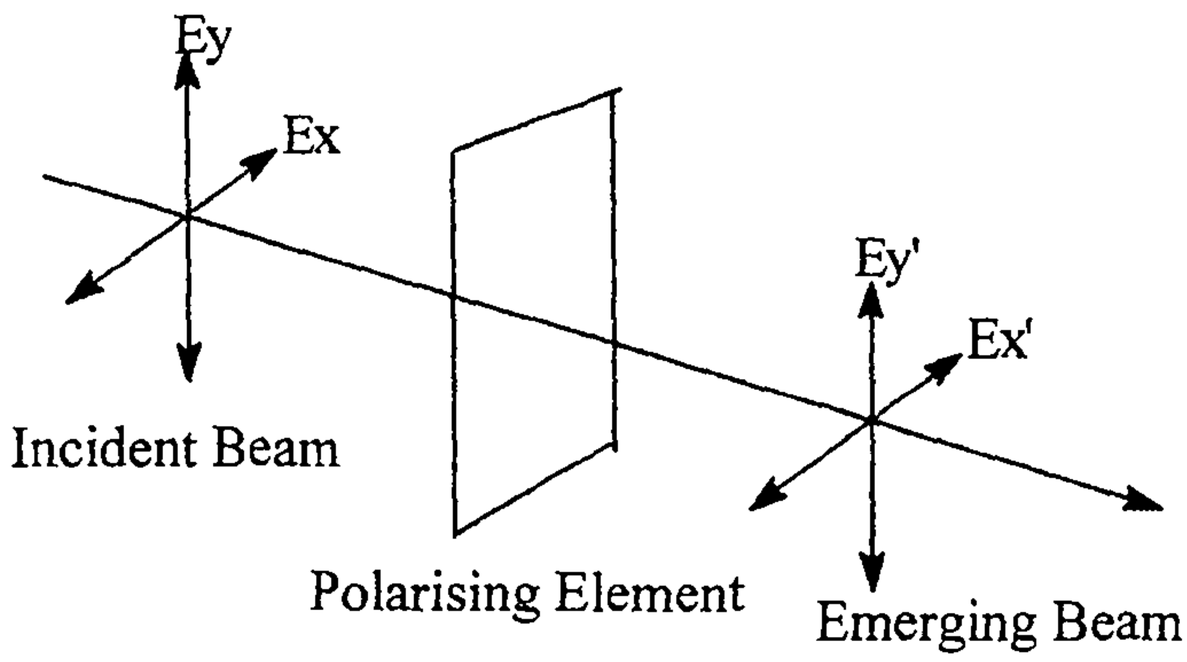

Fig. 1.9. The interaction of a polarised beam with a polarising element.

The incident beam can be characterised by its Stokes parameters, $[S_0,S_1,S_2,S_3]$, and the emergent beam can be described by $[S_0^1,S_1^1,S_2^1,S_3^1]$. We now assume that the Stokes vector of the emergent beam can be expressed as a linear combination of the four Stokes parameters of the incident beam by the relations:

$$S_0^1 = m_{00}S_0 + m_{01}S_1 + m_{02}S_2 + m_{03}S_3 \quad \text{(eqn. 1.24a)}$$

$$S_1^1 = m_{10}S_1 + m_{11}S_1 + m_{12}S_2 + m_{13}S_3 \quad \text{(eqn. 1.24b)}$$

$$S_2^1 = m_{20}S_2 + m_{21}S_1 + m_{22}S_2 + m_{23}S_3 \quad \text{(eqn. 1.24c)}$$

$$S_3^1 = m_{30}S_3 + m_{31}S_1 + m_{32}S_2 + m_{33}S_3 \quad \text{(eqn. 1.24d)}$$

Which can be written in matrix form as

$$\begin{pmatrix} S_0^1 \\ S_1^1 \\ S_2^1 \\ S_3^1 \end{pmatrix} = \begin{pmatrix} m_{00} & m_{01} & m_{02} & m_{03} \\ m_{10} & m_{11} & m_{12} & m_{13} \\ m_{20} & m_{21} & m_{22} & m_{23} \\ m_{30} & m_{31} & m_{32} & m_{03} \end{pmatrix} \begin{pmatrix} S_0 \\ S_1 \\ S_2 \\ S_3 \end{pmatrix} \quad \text{(eqn. 1.25)}$$

or simply $\mathbf{S}^1 = \mathbf{M}\,\mathbf{S}$. The 4x4 matrix $\mathbf{M}$ is known as the Mueller matrix, and this representation can be used to describe changes in polarisation state introduced by any polarising element (see [9] or [10] for derivations). Table 1.3 Shows the Mueller matrices for some common polarisers.

We can show the effect a polariser has on the polarisation of a beam by multiplying the Stokes vector of the incident beam by the Mueller matrix of a polariser. Multiplying the Mueller matrix for a horizontal linear polariser with an arbitrary Stokes vector gives

$$\frac{1}{2}\begin{pmatrix} 1 & 1 & 0 & 0 \\ 1 & 1 & 0 & 0 \\ 0 & 0 & 0 & 0 \\ 0 & 0 & 0 & 0 \end{pmatrix} \begin{pmatrix} S_0 \\ S_1 \\ S_2 \\ S_3 \end{pmatrix} = \frac{1}{2}(S_0 + S_1) \begin{pmatrix} 1 \\ 1 \\ 0 \\ 0 \end{pmatrix} \quad \text{(eqn. 1.26)}$$

Which is the Stokes vector of horizontal linear polarised light.

State of Polarisation	Mueller Matrix	State of Polarisation	Mueller Matrix
Horizontal Linear Polariser	$\frac{1}{2}\begin{bmatrix}1&1&0&0\\1&1&0&0\\0&0&0&0\\0&0&0&0\end{bmatrix}$	Vertical Linear Polariser	$\frac{1}{2}\begin{bmatrix}1&-1&0&0\\-1&1&0&0\\0&0&0&0\\0&0&0&0\end{bmatrix}$
Linear Polariser at $+45^0$	$\frac{1}{2}\begin{bmatrix}1&0&1&0\\0&0&0&0\\1&0&1&0\\0&0&0&0\end{bmatrix}$	Linear Polariser at -45^0	$\frac{1}{2}\begin{bmatrix}1&0&-1&0\\0&0&0&0\\-1&0&1&0\\0&0&0&0\end{bmatrix}$
Quarter-wave plate, fast axis vertical	$\begin{bmatrix}1&0&0&0\\0&1&0&0\\0&0&0&-1\\0&0&1&0\end{bmatrix}$	Quarter-wave plate, fast axis horizontal	$\begin{bmatrix}1&0&0&0\\0&1&0&0\\0&0&0&1\\0&0&-1&0\end{bmatrix}$
Circular Polariser right	$\frac{1}{2}\begin{bmatrix}1&0&0&1\\0&0&0&0\\0&0&0&0\\1&0&0&1\end{bmatrix}$	Circular Polariser left	$\frac{1}{2}\begin{bmatrix}1&0&0&-1\\0&0&0&0\\0&0&0&0\\-1&0&0&1\end{bmatrix}$

Table 1.3. The Mueller Matrices for some common polarising elements.

1.2.4 Determination of the Polarisation State

Over the years many methods of determining the polarisation state of the reflected beam during an ellipsometric experiment have been developed. Five of the most common methods [7, 10] are described below, followed by the method used in this thesis.

1. Stokes Method.

Recalling that the Stokes parameters S_0, S_1, S_2, and S_3, refer to the total intensity, the amount of horizontal linearly polarised light, the amount of 45^0 linearly polarised light, and the amount of circularly polarised light, respectively, the Stokes relation can be written as:

$$S_0 = I(0^0,0^0) + I(90^0, 0^0) \qquad \text{(eqn. 1.27a)}$$

$$S_1 = I(0^0, 0^0) - I(90^0, 0^0) \qquad \text{(eqn. 1.27b)}$$

$$S_2 = 2I(45^0, 0^0) - S_0 \qquad \text{(eqn. 1.27c)}$$

$$S_3 = 2I(45^0, 90^0) - S_0 \qquad \text{(eqn. 1.27d)}$$

where the first figure in brackets refers to the polarisation setting and the second to the retardation angle, and I to the intensity measured with the polarising elements at those settings. Thus simply by measuring the intensity at $(P, R) = (0^0,0^0)$, $(45^0, 0^0)$, $(90^0, 0^0)$, and $(45^0, 90^0)$ it is possible to determine all four Stokes parameters.

2. The Null Intensity Method.

In this method a continuously adjustable compensator is used, and altered until the incoming light is linearly polarised. The beam is then incident on a rotatable polariser, which is adjusted until a null intensity is observed, i.e. the transmission axis is at 90^0 to the polarisation angle of the incident linearly polarised light. The retardation and polariser settings used to obtain the null intensity are then used to calculate the polarisation of the incident beam.

3. Fourier Transform Analysis

In this method the beam is incident on a continuously rotating retarder, and then a fixed linear polariser. The oscillating intensity emerging from the two elements can be represented as a truncated Fourier series which contains the Stokes parameters, all four of which can be determined by Fourier analysis.

4. The Method of Kent and Lawson

With the advent of photovoltaics, Kent and Lawson noted that a photomultiplier tube (PMT) could obviously replace the human eye as an intensity detector. They also observed that the PMT operated best under conditions of maximum illumination rather than null intensity, and the way to achieve this was to convert the incident beam to circularly rather than linearly polarised. The beam passed through an adjustable retarder, a rotating polariser, and was then incident on the PMT. By adjusting the retarder until the PMT reported a constant intensity, i.e. the angle of the polariser has no effect on the emerging intensity, circularly polarised

light was generated, and the retarder settings could be used to determine the polarisation of the incident beam.

In 1985, R. M. A. Azzam first described a new solid state polarisation detector [16], which had no moving parts and determined all four Stokes polarisation parameters simultaneously. The detector has become known as a Stokesmeter, and consists of four non-coplanar photodiodes, from which incident light is reflected serially from one to the next. Each photodiode will produce an output current proportional to the intensity it absorbs, and by analysis of the Mueller matrices of the photodiodes, or by a simple calibration of the detector, these output currents can be

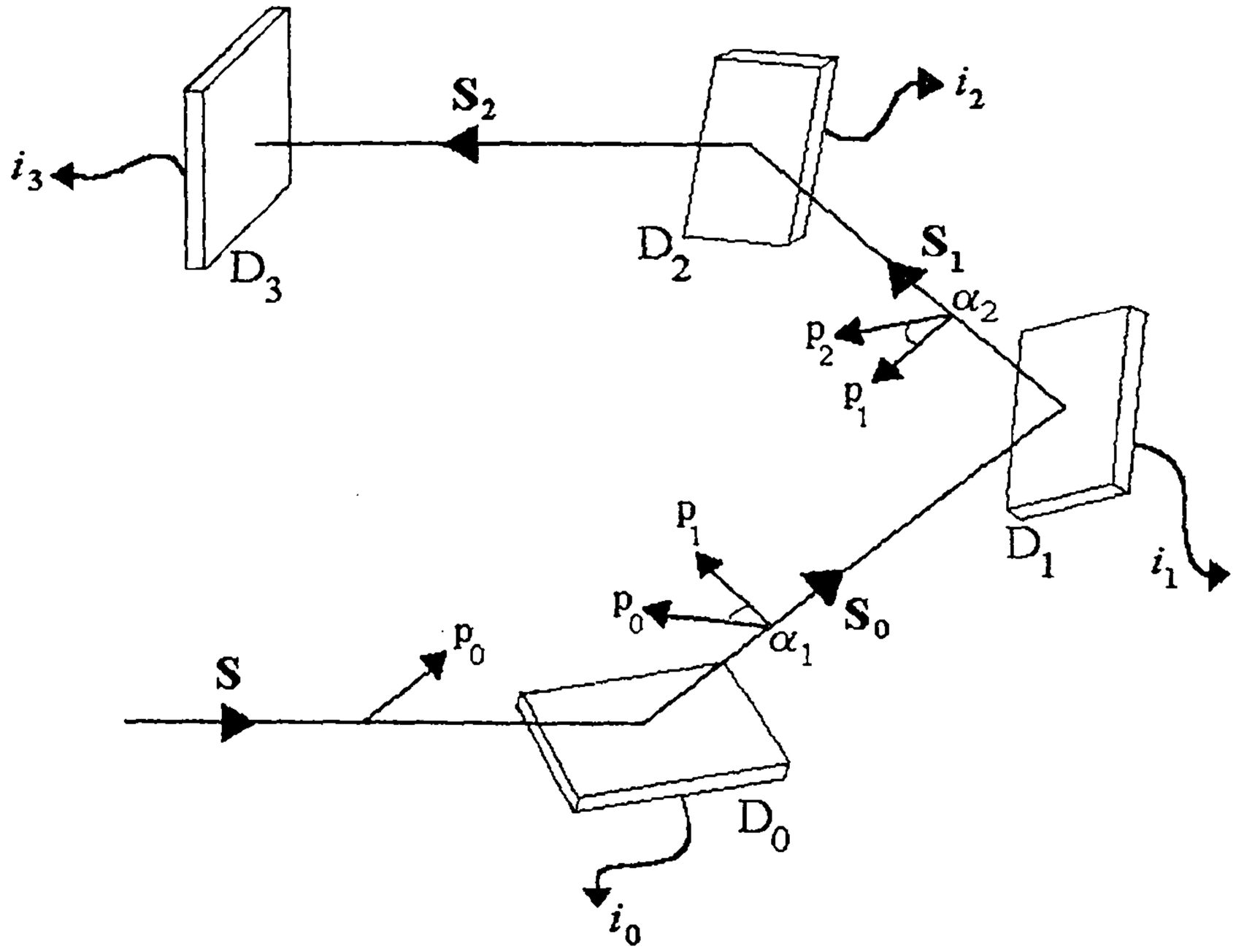

Fig. 1.10. The photodiode arrangement in the Stokesmeter. The surfaces of photodetectors D_0, D_1, and D_2 are specularly reflecting, while that of D_3 is totally absorbing. The four output currents i_0 - i_3 determine the input Stokes vector S

converted to give the Stokes parameters of the incident light [16-18]. Having no moving parts, this detector is capable of a much higher time resolution than any of the methods described above.

At the heart of the instrument are four planar diffused silicon diodes, labeled D_0 to D_3 in Fig. 1.10. Each diode has a 1 inch diameter, and the first three are coated with a half-wavelength thickness oxide layer for maximum reflectance, while the fourth is coated with a quarter-wave thickness for minimum reflectance. Each photodetector D_m generates an output current i_m (m = 0, 1, 2, 3) that is proportional to the light flux that it absorbs. The output signal current of each detector is then converted to a voltage by an operational amplifier.

S is the Stokes vector of the incident light, and $\mathbf{S_0}$, $\mathbf{S_1}$, and $\mathbf{S_2}$ the Stokes vectors of the light reflected from the surfaces D_0, D_1 and D_2 respectively, and can be defined by

$$\mathbf{S_0} = \mathbf{M_0 S} \qquad \text{(eqn. 1.28a)}$$

$$\mathbf{S_1} = \mathbf{M_1 R_1}(\alpha_1)\, \mathbf{M_0 S} \qquad \text{(eqn. 1.28b)}$$

$$\mathbf{S_2} = \mathbf{M_2 R_2}(\alpha_2)\, \mathbf{M_1 R_1}(\alpha_1)\, \mathbf{M_0 S} \qquad \text{(eqn. 1.28c)}$$

$\mathbf{S_n}$ is defined with respect to p_n parallel to the plane of incidence, shown in Fig. 1.10, and the orthogonal component s_n perpendicular to it. The effect of reflection on the state of polarisation is described by the Mueller matrices $\mathbf{M_n}$, and the Mueller rotation matrices $\mathbf{R_1}$ and $\mathbf{R_2}$ account for rotations of the plane of incidence from one reflection to the next.

If we assume we have imperfection-free polarising optics, the Stokes parameters incident on the Stokesmeter are given by

$$\mathbf{S} = \begin{pmatrix} S_0 \\ S_1 \\ S_2 \\ S_3 \end{pmatrix} = \begin{pmatrix} S_0 \\ S_0 \cos 2\theta \cos 2\varepsilon \\ S_0 \sin 2\theta \cos 2\varepsilon \\ S_0 \sin 2\varepsilon \end{pmatrix} \qquad \text{(eqn. 1.29)}$$

The response of the Stokesmeter to the input light with Stokes vector $\mathbf{S} = [S_0, S_1, S_2, S_3]^t$ is given by the output current vector

$$\begin{pmatrix} i_0 \\ i_1 \\ i_2 \\ i_3 \end{pmatrix} = \begin{pmatrix} a_{00} & a_{01} & a_{02} & a_{03} \\ a_{10} & a_{11} & a_{12} & a_{13} \\ a_{20} & a_{21} & a_{22} & a_{23} \\ a_{30} & a_{31} & a_{32} & a_{33} \end{pmatrix} \begin{pmatrix} S_0 \\ S_1 \\ S_2 \\ S_3 \end{pmatrix} \qquad \text{(eqn. 1.30)}$$

or more simply

$$\mathbf{I} = \mathbf{A}\,\mathbf{S} \qquad \text{(eqn. 1.31)}$$

where **A** is a real 4x4 matrix characteristic of the Stokesmeter, determined during the calibration procedure which measures the four photodiode outputs at four different polarisations, the four different polarisation states being chosen to be as different from one another as possible, as described in section 2.2.2. From equation 1.31 it follows that

$$\mathbf{A} = I S^{-1} \qquad \text{(eqn. 1.32)}$$

Where S is the 4x4 matrix whose four columns are the four Stokes vectors of the calibration states, and I is the 4x4 matrix of the corresponding output current vectors. From equation 1.31 it also follows that $\mathbf{S} = \mathbf{A}^{-1}\mathbf{I}$, which means that after the measurement of **A**, the inverse of the 4x4 matrix must be determined.

It is possible to calculate the instrument matrix **A** from the arrangement and characteristics of the four photodiodes, however it is more practical to perform a calibration for a given arrangement. Using four different known polarisation states and monitoring the output for each photodiode is sufficient to specify **A** through eqn. 1.31. It should be noted that **A** is a function of wavelength, and must be determined for each wavelength used.

The Stokesmeter has several advantages over the more traditional methods of determining the polarisation state of a beam, as all four Stokes parameters are determined, and no separate polarising elements are needed. The instrument has no moving parts, in contrast to methods which require the rotation of optical elements, a process which generally limits the time resolution to seconds, and at best hundreds of milliseconds per point [19, 4]. The time resolution possible with the Stokesmeter is determined by the rate at which the computer to which it is interfaced can collect and process the optical data, which with the current experimental set-up has a limit of *ca.* 300 μs.

1.3 The Key Equations of Ellipsometry

1.3.1 The Fresnel and Drude Equations

The determination of the polarisation state is perhaps the most straightforward part of ellipsometry, as the mathematics necessary to relate the change in polarisation state undergone upon reflection to the refractive index and thickness of a film is quite complex. In this section a brief overview of how the parameters are related is given, for a more detailed description see [4, 10]

In Fig. 1.11 a beam is incident on a boundary at angle ϕ_0, and is partially transmitted through the boundary at angle ϕ_1, and partially reflected.

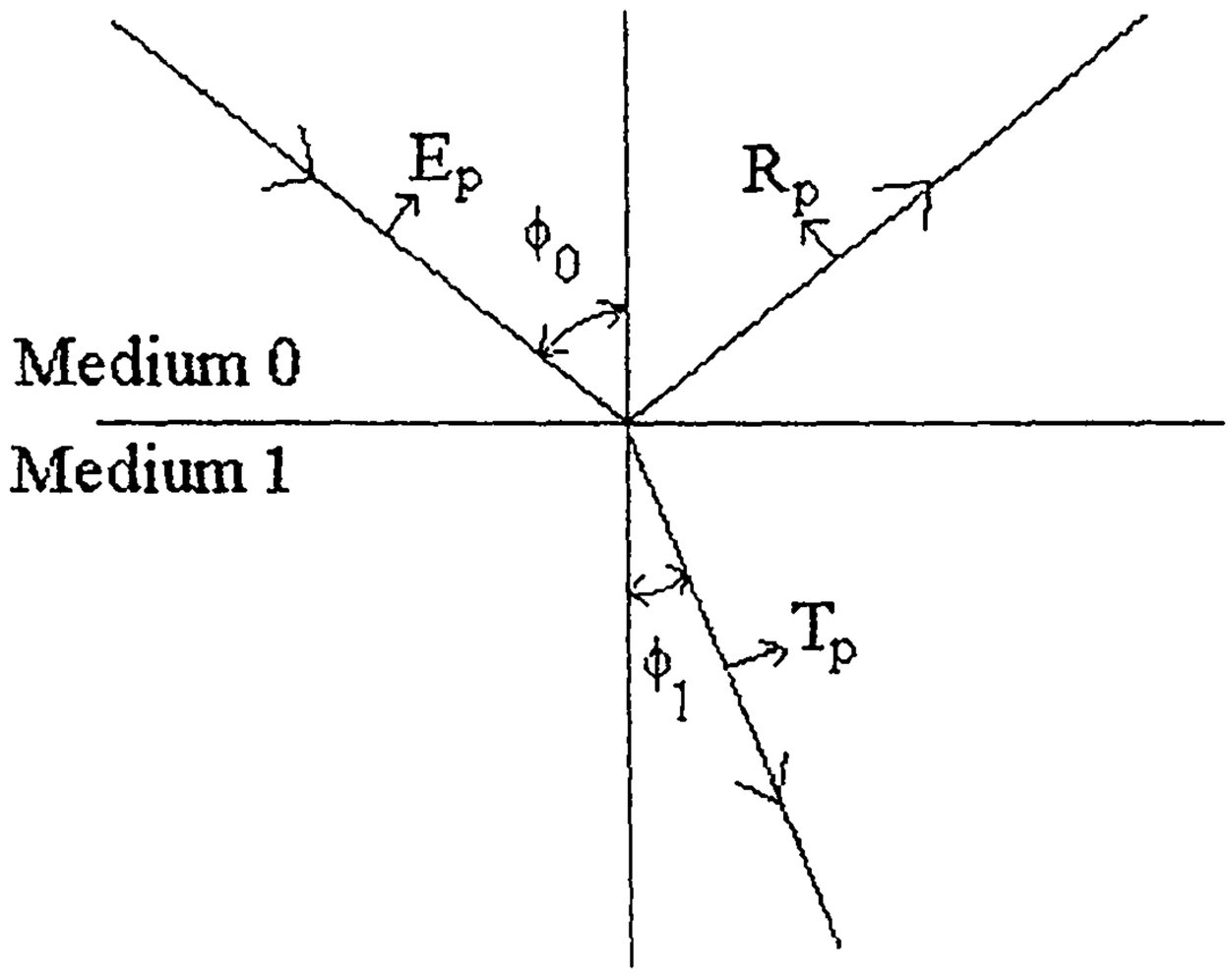

Fig. 1.11. Reflection and transmission of a wave incident on a boundary. The wave is incident at angle ϕ_0 and refracted at angle ϕ_1. The direction of p polarisation for the incident, reflected and transmitted waves are indicated.

Fresnel's Equations describe the reflection coefficients r_s and r_p in terms of angles ϕ_0 and ϕ_1, and the refractive indices n_0 and n_1, and may be written as [9]

$$r_p = \frac{n_1 \cos\phi_0 - n_0 \cos\phi_1}{n_1 \cos\phi_0 + n_0 \cos\phi_1} \qquad \text{(eqn. 1.33a)}$$

$$r_s = \frac{n_0 \cos\phi_0 - n_1 \cos\phi_1}{n_0 \cos\phi_0 + n_1 \cos\phi_1} \qquad \text{(eqn. 1.33b)}$$

and for the transmitted beam

$$t_p = \frac{2n_0 \cos\phi_0}{n_1 \cos\phi_0 + n_0 \cos\phi_1} \qquad \text{(eqn. 1.34a)}$$

$$t_s = \frac{2n_0 \cos\phi_0}{n_0 \cos\phi_0 + n_1 \cos\phi_1} \qquad \text{(eqn. 1.34b)}$$

These equations are valid for a film-free substrate, i.e. when the beam is incident at a single interface. When a beam is incident on a film-covered substrate, as shown in Fig. 1.12, transmission and reflection at both the ambient/film interface and

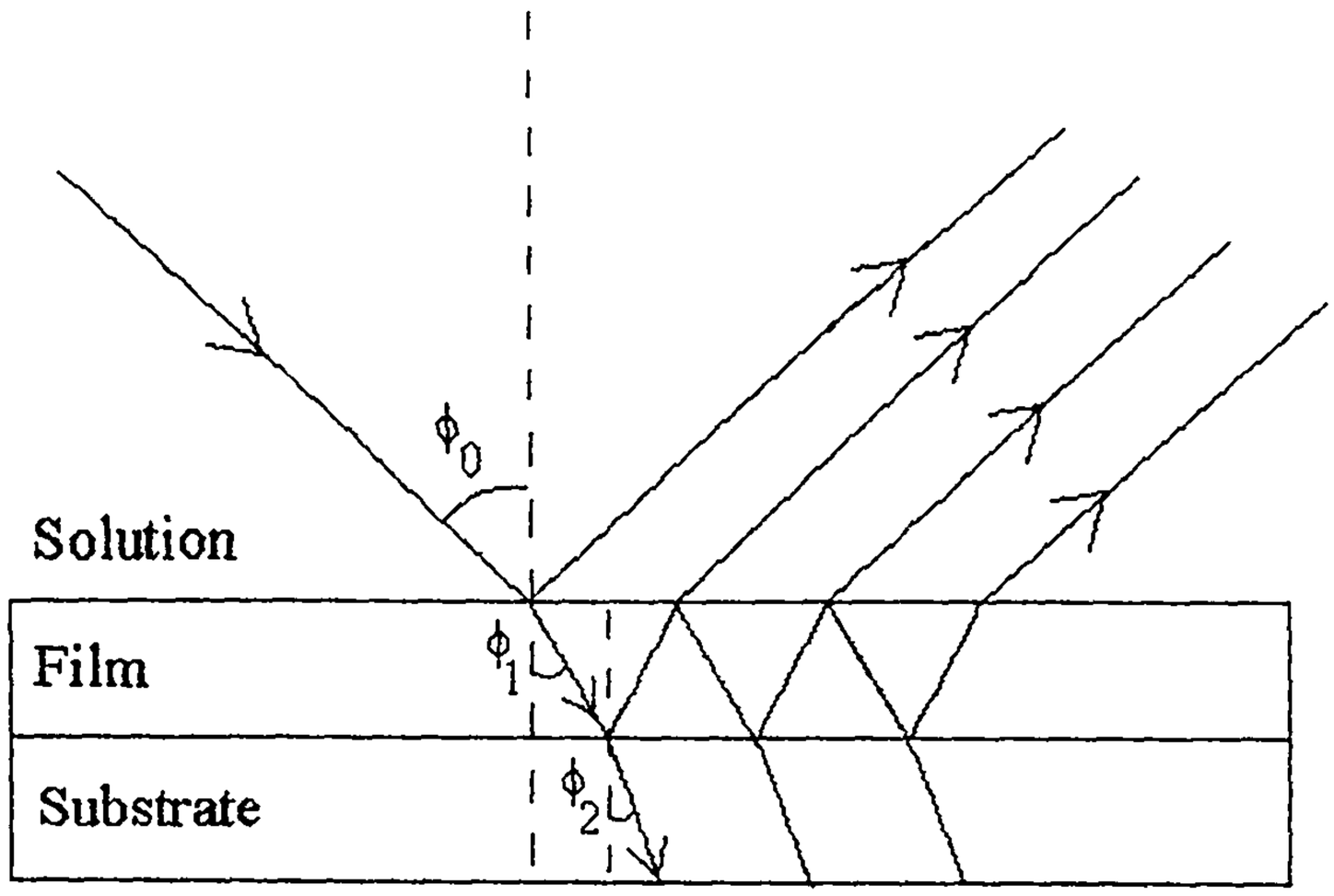

Fig. 1.12 Refraction of a beam at a film-covered interface. After refraction through the film the beam is reflected by the substrate. Multiple reflections may occur within the film.

film/substrate interfaces must be considered, and multiple reflections within the film must also be accounted for. The result is the Drude equation [5, 9, 10]:

$$R_p = \frac{r_{01p} + r_{12p}e^{-i\Delta\phi}}{1 + r_{01p}r_{12p}e^{-i\Delta\phi}} \qquad \text{(eqn. 1.35a)}$$

$$R_s = \frac{r_{01s} + r_{12s}e^{-i\Delta\phi}}{1 + r_{01s}r_{12s}e^{-i\Delta\phi}} \qquad \text{(eqn. 1.35b)}$$

R_p and R_s are the reflection coefficients over both interfaces, and could also be written $r_{012p/s}$, and the subscripts 0, 1, and 2 refer to the ambient(solution) phase, the film, and the substrate (electrode) respectively. ϕ_3 is the angle of propagation within the metal phase, defined according to Snell's laws, $n_1\sin\phi_1 = \tilde{N}_3\sin\phi_3$, where $\tilde{N}_3$ is the complex refractive index of the metal, and $\tilde{N}_3 = n_3\text{-}ik_3$. $\Delta\phi$ is the phase difference due to the thickness of the film through which the beam has to travel, and is equal to $2\pi\Delta l/\lambda$ where Δl is the difference in pathlength between the beams reflected from the upper surface of the film and the substrate beneath. $\Delta\phi$ is therefore the same for the s and p components of the beam. From Drude's equation the fundamental equation of ellipsometry can be derived, and may be written

$$\rho = \frac{R_p}{R_s} = \tan\psi e^{i\Delta} = \frac{r_{01p} + r_{12p}e^{-i\Delta\phi}}{1 + r_{01p}r_{12p}e^{-i\Delta\phi}} \frac{1 + r_{01s}r_{12s}e^{-i\Delta\phi}}{r_{01s} + r_{12s}e^{-i\Delta\phi}} \qquad \text{(eqn. 1.36)}$$

Since $\Delta\phi$ is related to the pathlength of the beam through the film, it is clearly related to the film thickness, and r_{01} and r_{12} are related by Fresnels equation to n_0 and n_1, and n_1 and n_2 respectively, so although equation 1.36 is far from simple to derive, or

indeed solve, it clearly does relate the polarisation angles Δ and Ψ to the refractive index of the film, n (and k if the film is absorbing) and the film thickness.

One reason for a resurgence in the use of ellipsometry over the past few decades is the advent of computers and relatively simple routines which makes solving equation 1.36 a great deal easier and quicker. Given the far greater number of variables on the right hand side of equation 1.36 it is hardly surprising that the system needs to be modeled. Values of n, k for the solvent are generally known, and for the substrate readily calculated from data for a film free surface. n, k and the thickness of the film are estimated, and the values of Δ and Ψ that would be observed for this system calculated. A computer program then essentially minimises the function

$$(\Delta_{calc} - \Delta_{expt})^2 + (\Psi_{calc} - \Psi_{expt})^2 \qquad \text{(eqn. 1.37)}$$

returning the values of n, k and thickness for the film which gave the best fit. The fitting procedure used for the data presented in this thesis is described in Section 2.3.

1.3.2 Reflectance Measurements.

One way to provide more experimental data during an ellipsometric experiment is to take reflectance measurements at the same wavelength and angle of incidence [5, 20]. While in theory it is possible to measure the absolute intensity of the reflected beam, in practice this is extremely difficult to determine accurately. Relative changes in the intensity are far more easily determined, and reflectance measurements are commonly used to compliment ellipsometric data. The reflectance

R is defined as the ratio between the intensities of the incident and reflected beams, and the relationships may be written

$$R_p = |r_p|^2 \qquad R_s = |r_s|^2 \qquad \text{(eqn. 1.38)}$$

$$I_{(ref)_{p,s}} = I_{[inc]_{p,s}} R_{p,s} \qquad \text{(eqn. 1.39)}$$

The relative intensity is therefore clearly related to the Fresnel equations through the reflection coefficients, and is therefore dependent on the same parameters as Δ and Ψ and can be of great use during the data fitting procedures.

The Stokesmeter (section 1.2.4) determines the polarisation state of the reflected beam by measuring the intensity incident on a series of four photodiodes. The total intensity of the beam is therefore proportional to the sum of the four output currents, and changes in the intensity (output currents) are easily related to changes in reflectance as the intensity of the beam incident on the electrode is constant. Thus reflectance and ellipsometric measurements are recorded simultaneously, and with no change in the experimental setup necessary to record the extra data.

Reflectance measurements are more sensitive to fluctuations in the intensity of the incident beam than Δ and Ψ, which (in principle) are unaffected by intensity changes; it is also important to note that, unlike Δ and Ψ, intensity changes are not necessarily surface sensitive, but may arise from the formation of an absorbing species or precipitation in the solution phase. Some care must therefore be taken to ensure that reflectance measurements are suitable for analysis along with the ellipsometric data.

1.4 Conducting polymers

The first report of an electronically conducting polymer was made in 1973 by Walatka [21], who found that polymeric (SN)x displayed metallic properties. It was not long thereafter before the first organic conducting polymer was discovered, [22] with the demonstration of the conducting properties of polyacetylene. Since the conducting properties of polyacetylenes were discovered, many organic polymers, including materials such as polythiophene [23], polypyrrole [23, 24, 25] etc. have been prepared as stable, electronically conducting films on electrodes via electropolymerisation from solution or chemical oxidation.

While materials are normally classed as insulators, semiconductors or conductors, and under all conditions display only the properties of the class to which they were assigned, conducting polymers can be switched between an insulating and a conducting (or semiconducting) state, and several show electrochromism.

Generally organic polymers are only conducting in the oxidised state, the removal of one or more electrons resulting in a charge carrier being formed on the polymer chain. Diaz *et al* [25] considered the residence time of such charge carriers, i.e. the time spent at a particular site in the polymer lattice. If this residence time were much shorter than the time taken for vibrations within the polymer, the carriers would in effect be free to move along a rigid backbone, which is essentially the form of conduction found in metals. If, however, the residence time is significantly longer than the time taken for lattice vibrations, the atoms around the charge carrier can relax, and the carrier is effectively stuck until the vibrations provide a favourable route for it to escape to the next site, resulting in a much lower conductivity. The

latter case is now widely accepted as being the more accurate description of the conduction mechanism in a majority of polymer systems, and most can be considered in terms of semiconductor behaviour, and thought of as having a valence and a conduction band [25], as shown in Fig. 1.13. The removal of one electron leads to the formation of a charge carrier with a single positive charge, known as a polaron, while the removal of a second electron results in a doubly charged charge carrier known as a bipolaron. The effect the removal of two successive electrons from the valence band, i.e. the formation of a polaron or bipolaron, has on the band energies is shown in Fig. 1.13, along with representations of the structure of a heterocyclic polymer chain in the various states of oxidation.

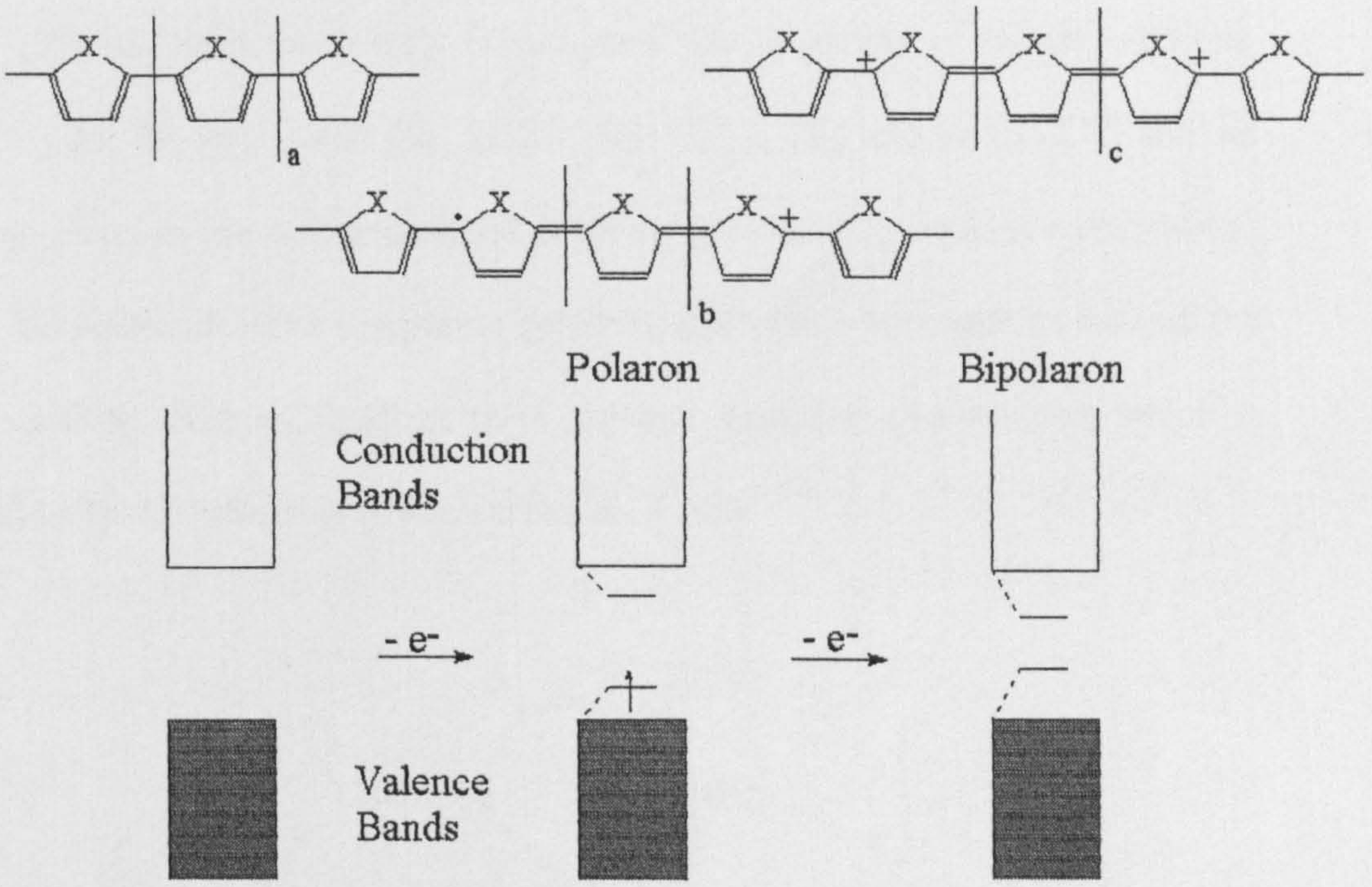

Fig. 1.13 Schematic representations of, from left to right, the structure and band gap energy of a heterocyclic polymer, a polaron and a bipolaron. a, b and c, represent the number of monomer units within the brackets.

Once the polaron or bipolaron has been formed, the extent to which the charge carrier is then able to move along the polymer chain determines the electronic conduction properties of the material. In an attempt to improve the charge transfer characteristics, conducting polymers formed from metal-containing organic monomers have been studied, and one particular polymer of interest is based around salicylaldehyde (Salen) monomers with a central transition metal ion. These metal salens are of interest due to their potential application as electrocatalysts in a variety of important redox reactions, and are discussed in more detail in the next section.

1.5 Salens

Metal bis(salicylidene)ethylenediamine (Salen) complexes (see Fig. 1.14) have been known for over 150 years [26]. Metal salen and salen derivatives have long been of interest as homogeneous catalysts for a variety of redox reactions such as the carbonylation of methanol to dimethylcarbonate [27], dehalogenation of alkyl and aryl halides [28, 29, 30], and the epoxidation of simple olefins [31, 32, 33, 34], and recently attention has focused on the possibility of enantioselective syntheses using chiral salen derivatives, and epoxidation of olefins with up to 92 % enantiomeric excess has been reported using chiral Mn Salen catalysts [31, 32, 33].

The electrochemistry of metal salen complexes in solvents with a large donor number [35] has been extensively investigated with a variety of metals including Co(II) [27, 28, 29, 36], Cu(II) [36], Ni(II) [30, 36, 37, 38], and Mn(II) [27] and the oxidative processes are well understood as all metal salens display a reversible M/M^{+} couple. The reduced metal complexes prefer square planar coordination around the metal, however when oxidised the metal prefers octahedral coordination, which is achieved by the coordination of two solvent molecules

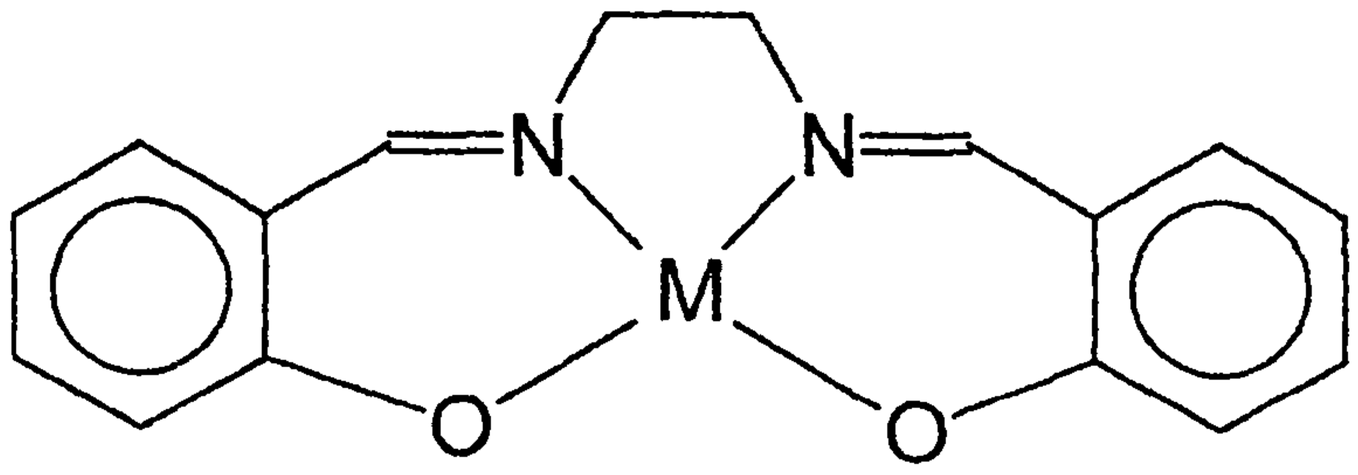

Fig. 1.14 A metal bis(salicylidene)ethylenediamine (Salen) complex. M is a transition metal.

in the axial positions. The similarity of the cyclic voltammograms of the complex to those of the corresponding free metal [39, 40, 41] and EPR studies of the oxidised species [42, 43, 44, 45, 46] indicate the central metal to be the site of oxidation.

The electrochemistry of these complexes in weak donor solvents is much more complicated and less well understood. In 1988 Goldsby first reported that Ni Salens could be oxidatively polymerised at the electrode surface simply by cycling a disk electrode in a 1 mmol dm^{-3} solution of the metal Salen in acetonitrile [40]. Three Ni(Salen) derivatives were studied in a variety of solvents, and reversible voltammograms were obtained for all three Salens in strong donor solvents [35] such as pyridine (DN = 33.1), dimethylsulphoxide (DN = 29.8) and N,N-dimethylformaldehyde (DN = 26.6). In acetonitrile (DN = 14.1), in all three cases two distinct oxidations were observed in the potential range 0.8 - 1.2 V vs SSCE followed by a single reduction of lesser current intensity. An insoluble orange film formed on the electrode surface and an increase in current was observed with each scan, indicative of polymer formation. Goldsby explained this behaviour in terms of the solvent dependence of the site of oxidation; thus, as described above, in strong donor solvents the oxidation of the square planar Ni complexes results in an increase in coordination number as the higher oxidation state is stabilised by axial ligation of two solvent molecules, but the degree of stabilisation offered by this process will depend on the donating ability of the solvent and will not be as effective in the case of a weak donor solvent such as acetonitrile. Using a variety of Schiff complexes it has been shown that if ligand oxidations are also accessible the ultimate site of oxidation is determined largely by the ability of the solvent to stabilise Ni(III) through ligation [47]. The salen ligands used by Goldsby [40] were irreversibly oxidised at potentials *ca.* 200 mV higher than the oxidation potentials of the

corresponding Ni complexes, leading to the proposal that in weakly donating solvents the stabilisation of the Ni(III) state is not sufficient, resulting in ligand oxidation and oxidative polymerisation *via* a ligand radical coupling mechanism, resulting in the polymer structure shown in Fig. 1.15.

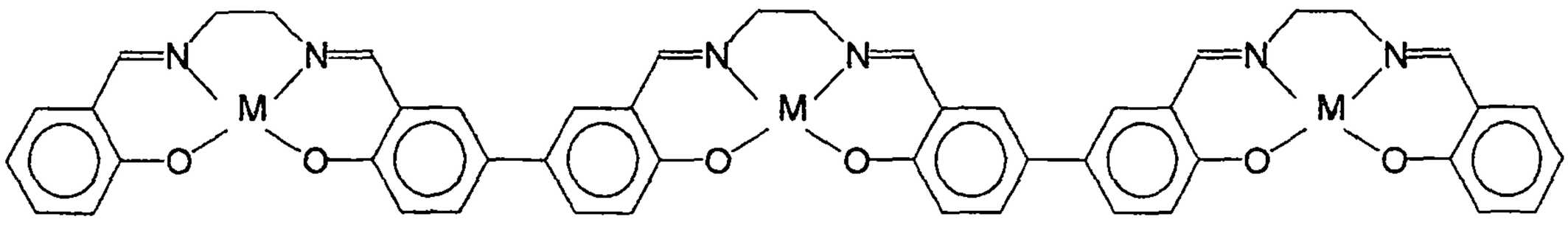

Fig. 1.15. The proposed structure of a salen polymer formed by oxidative polymerisation.

Investigation of the polymerisation mechanism has been intense but it remains a matter of debate, though there is much evidence to support Goldsby's assertion that linkages are formed between the carbons of the phenyl moieties in the position para to the oxygen. Dahm and co-workers estimated the number of electrons passed per monomer during polymerisation [48] and found three electrons were lost per monomer, this was suggested to be due to the reversible loss of one from the metal and the irreversible loss of one from each of the phenyl rings during coupling. Cleavage of salen polymers by removing the metal by reduction with sodium hydrosulphite in H_2SO_3 solution, followed by cleavage of the amino linkages by 25 % H_2SO_4, yields the corresponding bis-salicylaldehydes, as shown in Fig 1.16, which have been shown to be linked by the para carbon, indicating polymerisation must indeed have occurred at these sites.

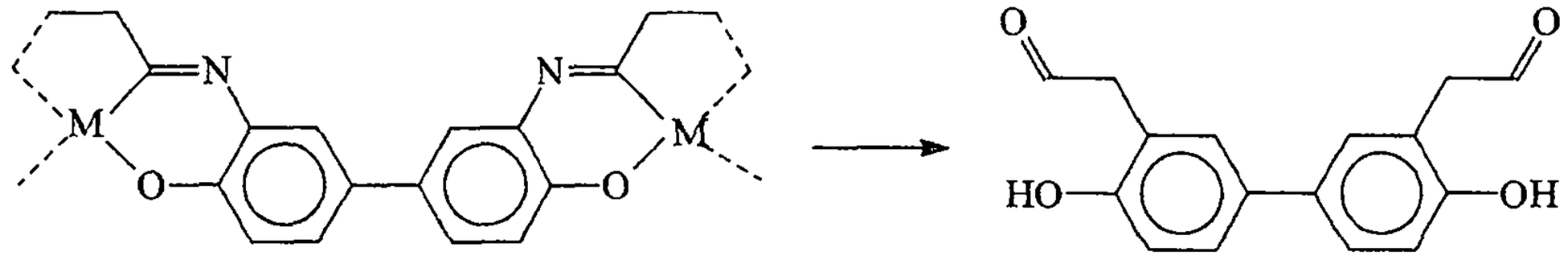

Fig 1.16. Cleavage of the polymer results in the corresponding bis-salicylaldehyde, which has been shown to contain a para linkage.

Goldsby [40] and others [49] have shown that adding a substituent to the para carbon yields a voltammogram displaying two distinct oxidations, but no evidence of polymerisation, though substituting other carbons on the phenyl rings still allows polymerisation to occur. However, Timonov has reported polymerising salens with the para positions of the phenyl groups blocked with either chlorine or bromine [50] and believes polymerisation of the films proceeds by charge transfer stacking, as shown in Fig. 1.17, resulting in a dense deposit with interstitial anions from the electrolyte countering the charge.

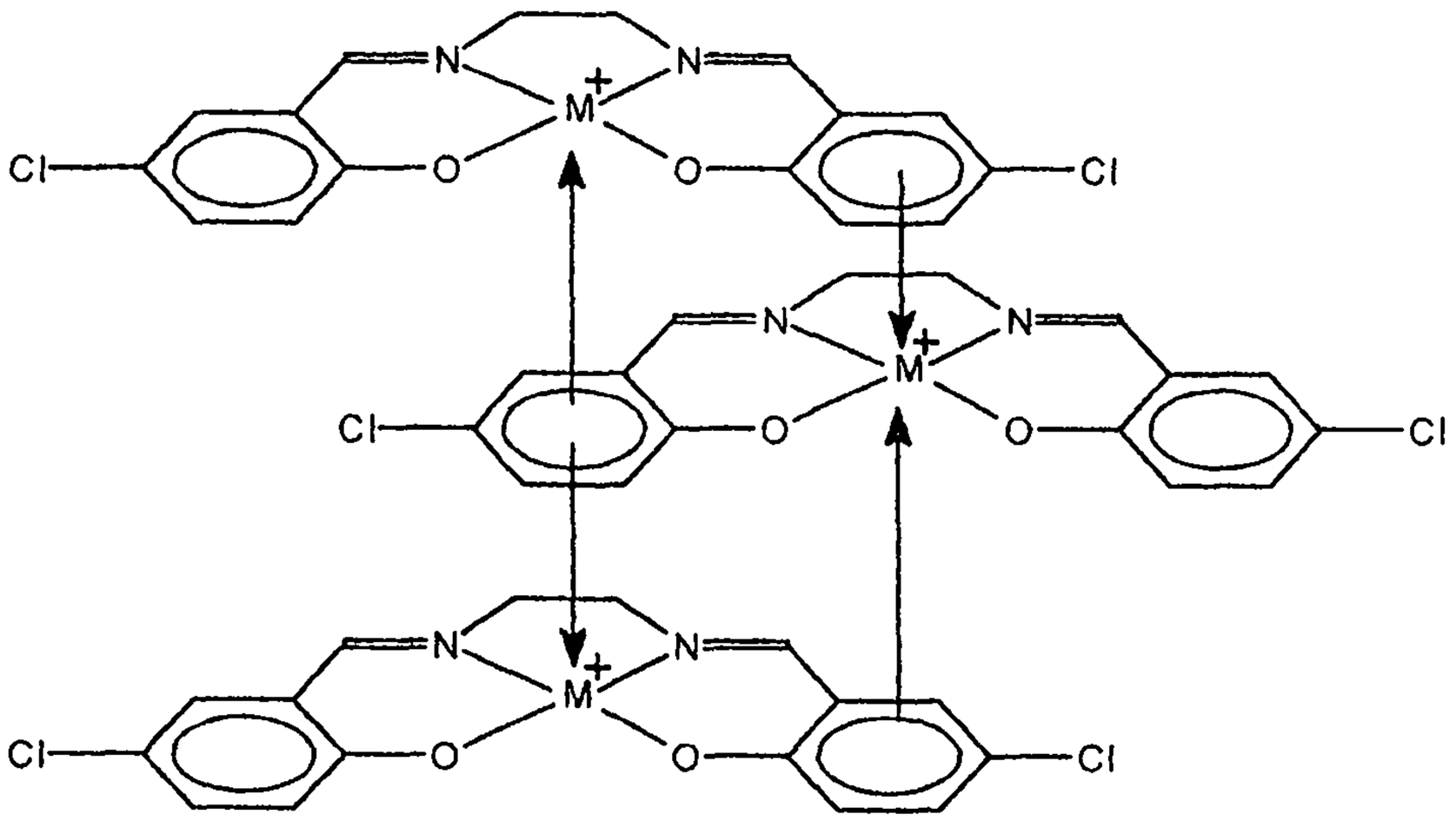

Fig 1.17. Charge transfer stacking of salen monomer units. Interstitial anions from the electrolyte would be present to counter the charge.

Though most investigations support the formation of carbon linkages as the method of polymerisation, it has been proposed that charge transfer stacking may still play a role within these processes; Dahm and co-workers [48] have postulated that, prior to polymerisation, a charge transfer deposit forms on the electrode. Voltammograms display two oxidative waves during polymerisation, the second of which is normally attributed to oxidative coupling. Dahm held the working electrode at a potential at the edge of the first oxidative wave and observed the formation of a stable deposit, formed by the loss of less than three electrons per monomer, which gave similar voltammetric responses as the salen film during cycling. This was suggested to be a charge transfer stack and the first step of the polymerisation process, the subsequent step being the oxidative coupling of adjacent monomer units in the stack once a high enough potential was reached.

The identity of the metal appears to have little effect on the polymerisation, however a central metal ion is clearly necessary for polymerisation to occur, as there are several papers in the literature which report that metal-free Salen ligands do not form an electroactive film, but instead result in an insulating deposit at the electrode, inhibiting further electrochemical response during subsequent cycles [51-56]. It also appears necessary that the metal be able to be oxidised, as attempts to polymerise [Zn(Salen)] and [Cd(Salen)], or indeed any Salen complex of a metal with only one oxidation state, have failed to produce a conducting polymer [55, 57]. This has led to suggestions that the initial site of oxidation is the metal, and Goldsby suggested rapid intra-molecular electron exchange then resulted in the oxidation of the ligand and polymerisation [58]. A comparison of Ni(salen), a Ni(bis(β-ketoimine)) (which does not polymerise), and a Ni mixed complex with one side a salen ligand and the other a

β-ketoimine was made. For each complex a sharp irreversible oxidation was followed by a broad oxidation of greatly reduced current intensity, and the potential of the first peak for the mixed complex lay almost exactly halfway between the potentials of the other two complexes. This is consistent with metal-localised rather than ligand-localised oxidation; were oxidation ligand-based the mixed complex would be expected to be oxidised at a potential closer to that of the bis(β-ketoimine), which displayed the lowest oxidation potential, and for the voltammogram to display features of both ligand systems rather than behaviour midway between the two.

The electronic conduction mechanism of these polymers is also less than well understood. While the presence of the central metal atom in the film after polymerisation has been confirmed by elemental analysis [40, 56], investigation by FTIR showed the bands arising from the coordination sphere around the metal displayed little difference between the monomer and polymeric systems, or indeed the polymer in the oxidised state [49, 59]. This suggested the conduction mechanism does not include the metal, though as the organic chains are not conjugated, due to the saturated bridge in each monomer unit, it is difficult to see what form this mechanism takes. The only clear changes in the FTIR spectra can be assigned to stretches of the phenyl rings, again indicating polymerisation occurs by coupling of the phenyl moieties, and also their importance in the conduction mechanism.

The addition of substituents at various points around the ligand have varied effects on the behaviour of the monomers and polymeric film, having little effect when around the carbon - carbon bridge [40, 55, 56, 60], but being quite pronounced when on the phenyl rings [50, 53, 60]. The addition of a methoxy group to each phenyl ring has a drastic effect on the properties of the film [50, 53, 60]. Whereas all

the polymer films derived from salens with unsubstituted phenyl rings display one broad oxidation process, all those with methoxy groups exhibited a twofold system, which Audebert suggested may be due to the electron donating methoxy groups lowering the ligand redox potential so ligand and metal oxidations become distinct from one another [60], which may also explain the potential at which polymerisation commences being lowered by *ca.* 200 mV when a methoxy substituent is added compared to the corresponding unsubstituted salen. It had also been demonstrated that methoxy substituted salens display conductivity even in the dry state [53, 60] of around 10^{-3} S cm^{-1}, which no other salens exhibited, including those which had fully conjugated ligands [40, 55, 56, 60].

As far as can be ascertained from the literature, the polymerisation of salen complexes has never been studied by ellipsometry before, even though the technique is unparalleled in the investigation and characterisation of thin films. In this thesis the ellipsometric investigations of five related Salens (Fig. 1.18) are presented in an attempt to further elucidate the effects that the following:

i) Substituents on the carbon-carbon bridge

ii) Electron donating substituents on the phenyl rings

iii) The identity of the central metal ion

have on the polymerisation processes and characteristics of the completed polymers.

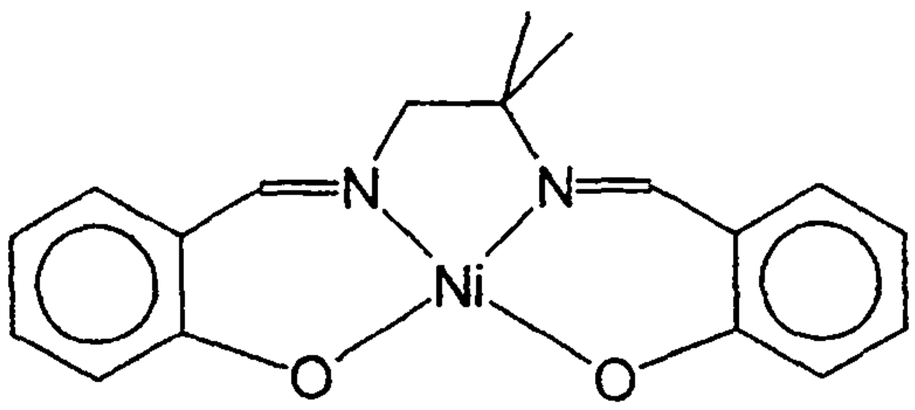

Ni(SaldMe)

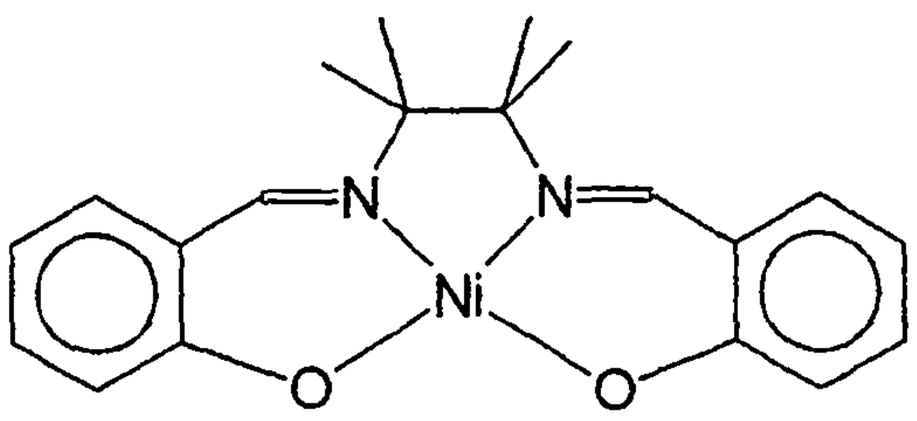

Ni(SaltMe)

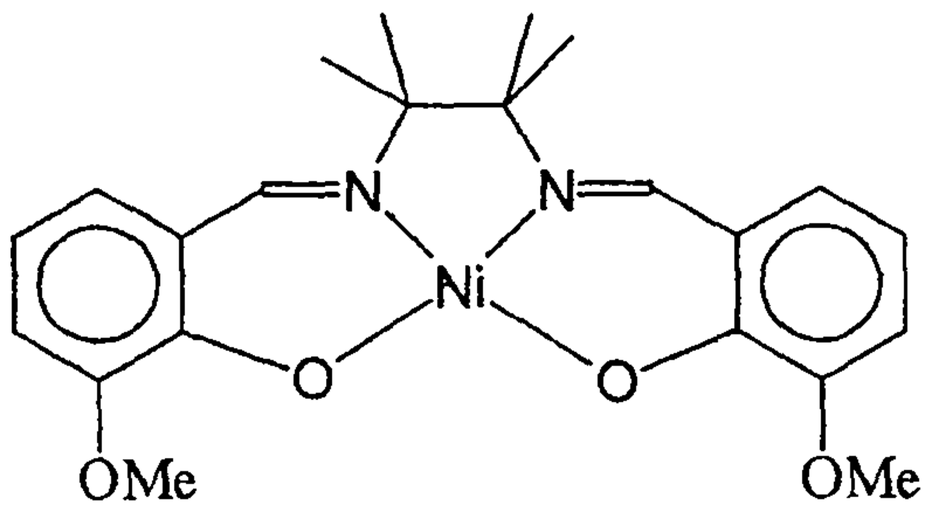

Ni(OMeSaltMe)

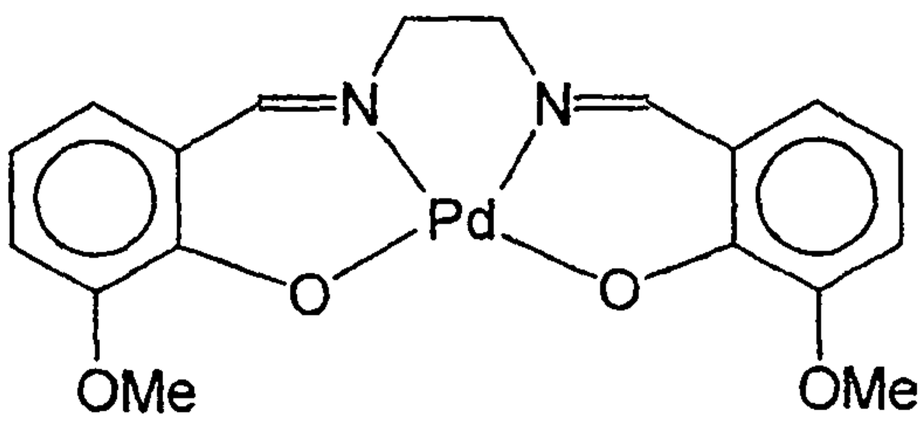

Pd(OMeSalen)

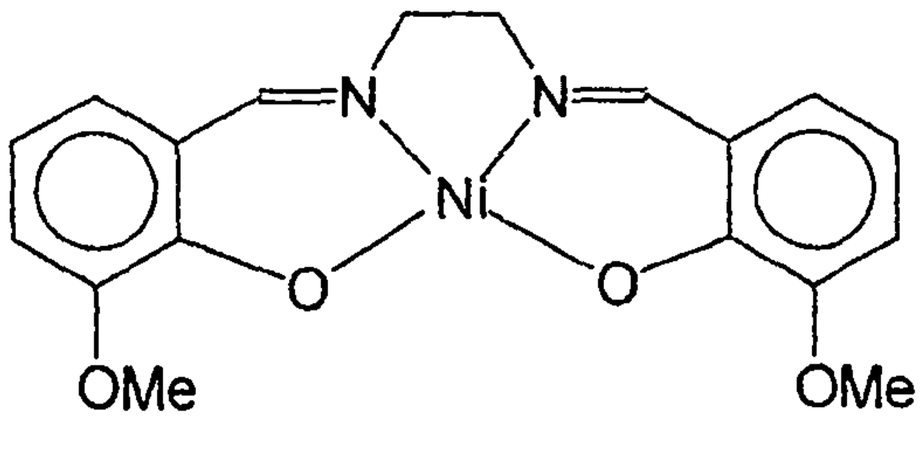

Ni(OMeSalen)

Fig. 1.18. The structure of the five Salens studied in this thesis with their abbreviated names.

The Stokesmeter is still a relatively new instrument, and to our knowledge the ellipsometer at Newcastle is the only system to use a Stokesmeter *and* be electrochemically interfaced, therefore the primary aim of this thesis was to exploit this new and unique ellipsometer. The electro-polymerisation of the five Salens shown in Fig. 1.18 provided suitable systems to investigate ellipsometrically, particularly with the unsurpassed time resolution permitted by the use of the Stokesmeter, allowing investigation of the initial polymerisation processes, and highly detailed measurements of potential-dependent changes within the films during potential cycling.

1.6 References

1. A. Rothen, *Rev. Sci. Instrum.*, 1945, **16**, 26.

2. P. Drude, *Annalen der Physik und Chemie*, a) 1889, **36**, 532, b) 1889, **36**, 865.

3. P. Drude, *Ann. Physik*, a) 1888, **272**, 532, b) 1889, **272**, 865, c) 1890,**275**, 481.

4. R. M. A. Azzam, N. M. Bahshara, *Ellipsometry and Polarised Light*, North-Holland, Amsterdam, 1977.

5. S. Gottesfeld, *Electroanalytical Chemistry, - A Series of Advances*, 1989, **15**, 143.

6. D. E. Aspnes, *Surf. Sci.*, 1980, **101**, 84.

7. P. S. Hauge, *Surf. Sci.*, 1980, **96**, 108.

8. H. G. Tompkins, W. A. McGahan, *Spectroscopic Ellipsometry and Reflectometry: A User's Guide*, 1999, J. Wiley and Sons, Canada.

9. M. Born and E. Wolf, *Principles of Optics*, 6th ed., Pergamon Press, New York, 1993.

10. E. Collett, *Polarized Light: Fundamentals and Applications* 1993, Marcel Dekker, New York .

11. E. Hecht, *Optics*, 2nd Ed., 1987, Addison-Wesley Publishing Company, Inc., Canada.

12. G. G. Stokes, *Trans. Camb. Phil. Soc.*, 1852, **9**, 399. Reprinted in *Mathematical and Physical Papers*, 1901, **3**, 233.

13. E. Hecht, *Am. J. Phys*, 1970, **38**, 1156.

14. F. Perrin, *J. Chem. Phys*, 1942, **10**, 415.

15. P. Soleillet, *Ann. Phys.,* 1929, **12**, 23.

16. R. M. A. Azzam, *Optics Letters*, 1985, **10**, 309.

17. R. M. A. Azzam, I. M. Eliminyawi, A. M. El-Saba, *J. Opt. Soc. Am. A*, 1988, **5**, 681.

18. R. M. A. Azzam, E. Masetti, I. M. Eliminyawi, F. G. Grosz, *Rev. Sci. Instrum.*, 1988, **59**, 84.

19. R. Greef, *Thin Solid Films*, 1993, **233**, 32.

20. W. Paik, J. O'M Bockris, *Surf. Sci.*, 1971, **28**, 61.

21. V. V. Walatka, M. M. Labes, J. H. Perlstein, *Phys. Rev. Lett.*, 1973, **31**, 1139.

22. H.Shirakawa, E. J. Louis, A. G. MacDiarmid, C. K. Chiang, *J. Chem. Soc. Chem. Comm.*, 1978, 578.

23. Handbook of Conducting Polymers, 1986, Ed. T. A.. Skotheim, Vols. I and II. Marcel Dekker, New York.

24. K. K. Kazanawa, A. F. Diaz, R. H. Geiss, W. D. Gill, J. F. Kwak, J. a. Logan, J. F. Rabolt, G. B. Street, *J. Chem. Soc., Chem. Commun.*, 1979, 854.

25. A. F. Diaz, J. I. Castillo, J. A. Logan, W.-Y. Lee, *J. Electroanal. Chem.* 1981, **129**, 115.

26. R. H. Holm, G. W. Everett, A. Chakravorty, *Prog. Inorg. Chem.*, 1966, 7, 83, and references therein.

27. G. Filardo, A. Galia, F. Rivetti, O. Scialdone, G. Silvestri, *Electrochim. Acta*, 1997, **42**, 1961.

28. A. Puxeddu, G. Costa, N. Marsich, *J. Chem. Soc., Dalton Trans.*, 1980, 1489.

29. K. S. Alleman, D. G. Peters, *J. Electroanal. Chem.*, 1998, **451**, 121.

30. A. D. Butler, D. G. Peters, *J. Electrochem. Soc.*, 1997, **144**, 4212.

31. K. Imagawa, T. Nagata, T. Yamada, T. Mukaiyama, *Chem. Lett.*, 1994, 527.

32. T. Yamada, K. Imagawa, T. Nagata, T. Mukaiyama, *Chem. Lett.*, 1992, 2231.

33. J. C. Moutet, A. Ourari, *Electrochim. Acta*, 1997, **42**, 2525.

34. L. Canali, D. Sherrington, *Chem. Soc. Rev.*, 1999, **28**, 85, and references therein.

35. J. R. Chipperfield, *Non-Aqueous Solvents*, 1999, Oxford University Press.

36. K. Ueno, A. E. Martell, *J. Phys. Chem.*, 1956, **60**, 1270.

37. C. Gosden, J. B. Kerr, D. Pletcher, R. Roas, *J. Electroanal. Chem.*, 1981, **117** 101.

38. C. Gosden, K. P. Healy, D. Pletcher, *J. Chem. Soc, Dalton Trans*. 1978, 972.

39. M. J. Samide, D. G. Peters, *J. Electroanal. Chem.*, 1998, **443**, 95.

40. K. A. Goldsby, J. K. Blaho, L. A. Hofferkamp, *Polyhedron*, 1989, **8**,113.

41. A. Kapturkiewicz, B. Behr, *Inorganica Chm. Acta*, 1983, **69**, 247.

42. M. de C. T. Corrondo, B. de Castro, A. M. Coelho, D. Domingues, C. Freire, J. Morais, *Inorganica Chim.*, Acta, 1993, **205**, 157.

43. F. Azevedo, M. de C. T. Carrondo, B. de Castro, M. Convery, D. Domingues, C. Freire, M. Teresa-Duarte, K. Nielsen, I. C. Santos, *Inorg. Chim. Acta*, 1994, **219**, 43.

44. B. de Castro, C. Freire, *Inorg. Chem.* 1990, **29**, 5113.

45. C. Freire, B. de Castro, *J. Chem. Soc., Dalton Trans.*, 1998, 1491.

46. I. C. Santon, M. Vilas-Boas, M. F. M. Piedade, C. Freire, M. T. Duarte, B. de Castro, *Polyhedron*, 2000, **19**, 655.

47. M. Y. Chavan, T. J. Meade, D. H. Busch, T. Kuwana, *Inorg. Chem.* 1986, **25**, 314.

48. C. E. Dahm, D. G. Peters, J. Simonet, *J. Electroanal. Chem.*,1996, **410**, 163.

49. M. Vilas-Boas, C. Freire, B. de Castro, P. A. Christensen, A. R. Hillman, *Chem. Eur. J.*, 2001, **7**, 139.

50. S. V. Vasil'eva, K. P. Balashev, A. M. Timonov, *Russ. J. Electrochem.*, 1998, **34**, 978.

51. C. P. Horwitz, R. W. Murray, *Mol. Cryst. Liq. Cryst.*, 1988, **160**, 389.

52. R. P. Kingsborough, T. M. Swager, *Adv. Mater.*, 1998, **10**, 1100.

53. P. Audbert, P. Hapiot, P. Capdevielle, M. Maumy, *J. Electroanal. Chem.*, 1992, **338**, 269.

54. F. Bedioui, E. L. Abbe, S. Gutierrez-Granados, J. Devynck, *J. Electroanal. Chem.*, 1991, **301**, 267.

55. P. Audbert, P. Capdevielle, M. Maumy, *New J., Chem.*, 1992, **16**, 697.

56. P.Audbert, P. Capdevielle, M. Maumy, *New J., Chem.*, 1991, **15**, 235.

57. I. E. Popeko, V. V. Vasiliev, A. M. Timonov, G. A. Sahgisultanova, *Russ. J. Coord. Chem.*, 1990, **35**, 933.

58. K. A. Goldsby, *J. Coord. Chem*. 1988, **19**, 83.

59. M. Vilas-Boas, C. Freire, B. de Castro, P. A. Christensen, A. R. Hillman, *Inorg. Chem.*, **36**, 4919.

60. P. Audebert, P. Capdevielle, M. Maumy, *Synth. Met.*, 1991, **41**, 3049.

2.1 Introduction

In this chapter the experimental aspects of the work presented in this thesis are discussed. The ellipsometric set-up, calibration, and data fitting procedures are described, and the design of the ellipsometric electrochemical cell presented. The synthesis of the Salen monomers is described, and details of the experimental parameters for their electro-polymerisation and the subsequent experiments performed on the polymer films given. A brief introduction to FTIR is also included.

2.2 Experimental Setup

2.2.1 Overview

A schematic overview of the ellipsometric system is shown in Fig. 2.1. The light source was a continuous wave laser, which was passed through a Glan-Taylor prism, which acts as a linear polariser, and a continuously adjustable retarder, enabling the generation of any polarisation state desired. This beam of known polarisation was then incident on the working electrode, which was polished to a mirror finish, and reflected to the Stokesmeter, which determined the polarisation state of the reflected beam.

Four lasers were available for use as the light source, three HeNe lasers (Melles Griot) with wavelengths of 632.8 nm, 594.1 nm, and 543.5 nm, and also a diode laser (RS Components) with a wavelength of 670 nm. The 543.5 nm and

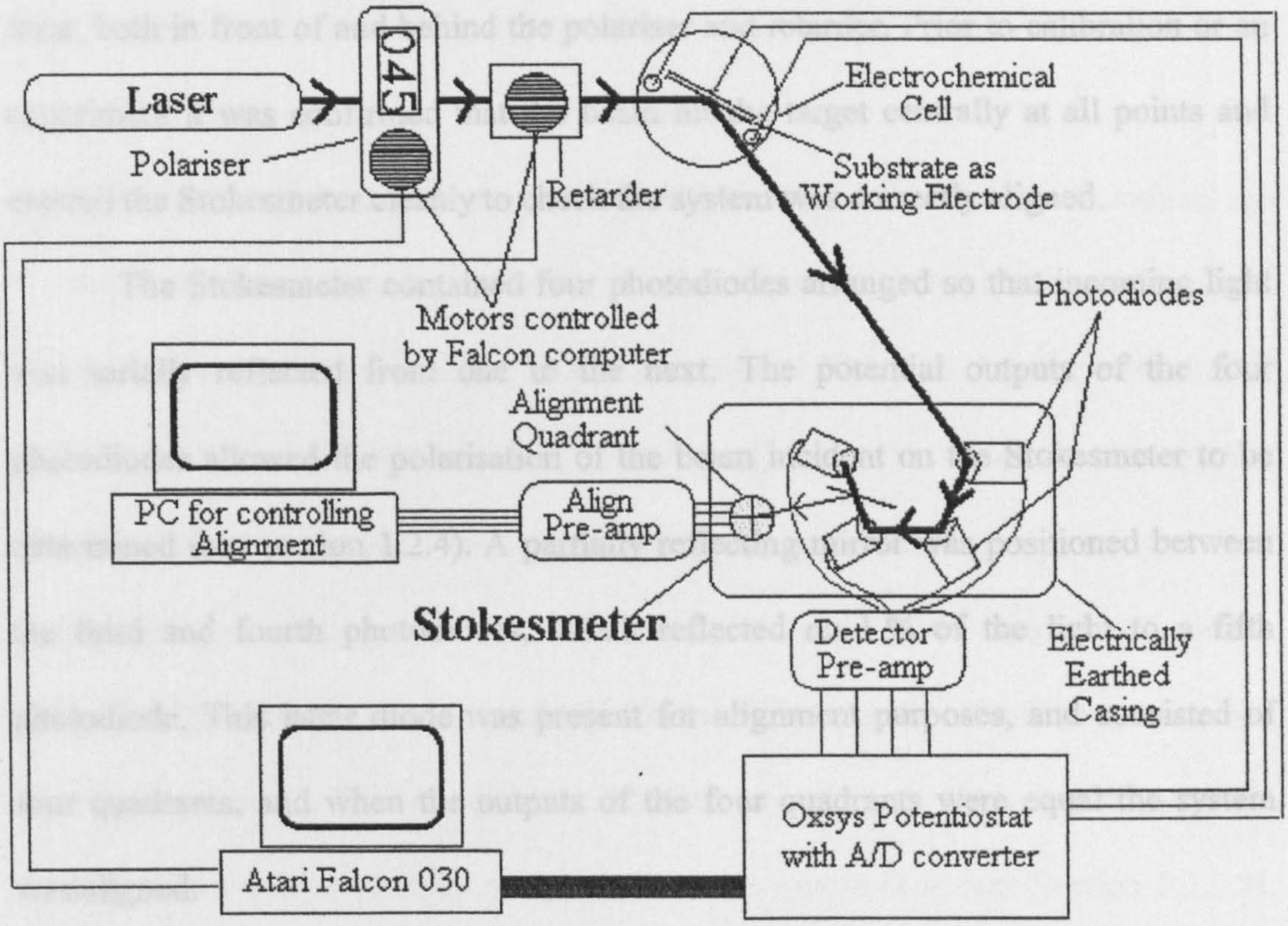

Fig. 2.1 Overview of the ellipsometric system.

670 nm lasers were acquired during the course of the work described in this thesis, consequently not all the electrochemical systems studied have been investigated at all of the wavelengths now available. The ellipsometer consisted of two arms, along which two metal bars ran, parallel to the beam path. These supported the laser, polariser, retarder and Stokesmeter, and are used for alignment purposes. The laser, polariser, and retarder were positioned on the first arm, which was stationary, the cell was placed at the pivot, and the second arm, upon which the Stokesmeter was positioned at the end furthest from the cell, was adjustable and could accommodate a wide range of incidence angles, though it was usually set at 60^0, which proved adequate for most experiments. A metal target displaying concentric circles and designed to sit square on the rails was positioned at various points along the two

arms, both in front of and behind the polariser and retarder. Prior to calibration or an experiment it was confirmed that the beam hit the target centrally at all points and entered the Stokesmeter cleanly to check the system was correctly aligned.

The Stokesmeter contained four photodiodes arranged so that incoming light was serially reflected from one to the next. The potential outputs of the four photodiodes allowed the polarisation of the beam incident on the Stokesmeter to be determined (see section 1.2.4). A partially reflecting mirror was positioned between the third and fourth photodiodes, which reflected *ca.* 1 % of the light to a fifth photodiode. This latter diode was present for alignment purposes, and consisted of four quadrants, and when the outputs of the four quadrants were equal the system was aligned.

The outputs of the four current-to-voltage followers connected to the quadrant diode were monitored by a PC which was used exclusively to display the alignment of the system. An Oxsys electrochemical interface, utilising an Atari Falcon computer, was employed to record the electrochemical data, and measure the outputs of the four current-to-voltage followers connected to the Stokesmeter, which relate to the principle diodes. This computer also controlled the motors attached to the polariser and retarder. The data from the four principle photodiodes was stored in the same buffer as the measurements collected from the electrochemical cell, giving real time ellipsometric information, with a resolution in the sub-millisecond region, which was limited by the rate at which the data could be gathered by the computer, rather than the rate of detection.

2.2.2 Calibration

During calibration, the arms of the ellipsometer were set to 180^0 without the electrochemical cell present, such that the beam passed through the polariser and retarder and was directly incident on the Stokesmeter (this was also the setup for all of the noise measurements described in Chapter 3). In order to calibrate the system, four known polarisation states were generated and the response of the four photodiodes recorded, generating a 4x4 matrix, **A**. Clearly, the best choice for the calibration polarisation states would be to have four states as different from one another as possible. These were calculated as according to the original paper by Azzam and co-workers [1], by using the Poincaré sphere [2,3] (see Section 1.2.3.2). In this representation, each point on the surface of the sphere represents a different polarisation. The sphere was created by plotting 2θ around ellipticity respectively, and the radius is S_0, the intensity. This powerful representation of polarisation can be used in a fairly straightforward manner to choose four suitable polarisation states for the calibration of the Stokesmeter, as four polarisations which differ to the greatest degree possible will describe a tetrahedron. As shown in Fig. 2.2, one of the simplest ways to choose points is to take one of the poles of the sphere, and three points lying at equal values of ε (or 2ε), with $\theta = 60^0$ ($2\theta = 120^0$) between them. The chosen values are shown in Table 2.1, where θ and ε are the principle angle and degree of ellipticity, respectively, and δ and P are the corresponding angles of retardation and polarisation. During calibration, the polariser and retarder were altered by the computer to sequentially generate the four desired states. The output of the four photodiodes was recorded at each of the polarisation states to generate a 4x4 matrix,

A, which essentially acts as a calibration factor for the photodiode outputs recorded during an experiment.

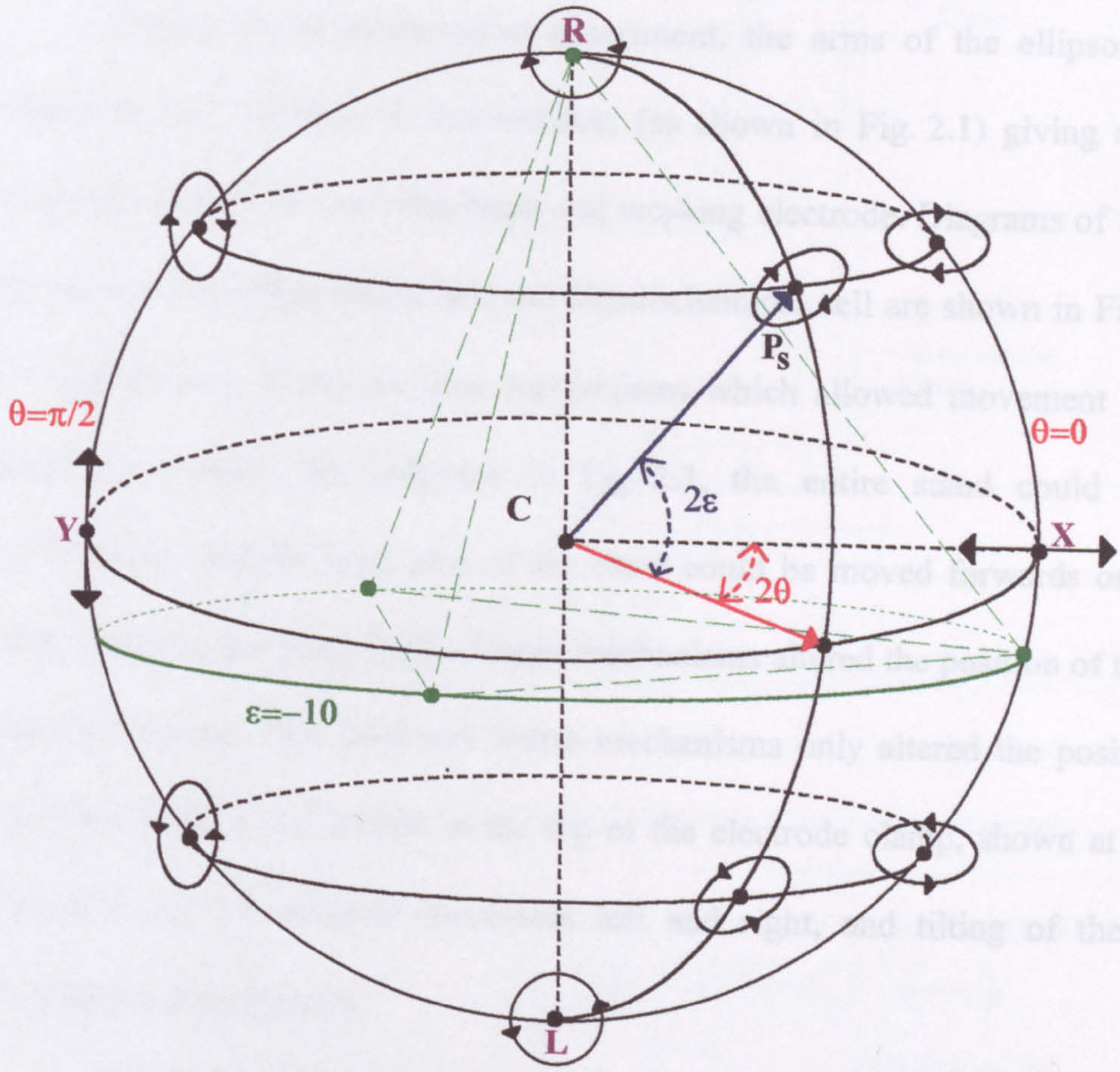

Fig. 2.2. The Poincaré Sphere. The four polarisation states used to calibrate the Stokesmeter form a tetrahedron on the spheres surface, indicating they are as different from one another as possible.

ε/°	θ/°	δ/°	P/°
45	0	90	-45
-10	0	90	10
-10	60	22.79	59.01
-10	-60	-22.79	59.01

Table 2.1. The four polarisation states chosen for the calibration of the Stokesmeter. δ and P are the retardation and polarisation angles, respectively.

2.2.3 Experimental Procedure and the Electrochemical Cell.

During an electrochemical experiment, the arms of the ellipsometer were moved to 120^0 relative to one another, (as shown in Fig. 2.1) giving an angle of incidence of 60^0 between the beam and working electrode. Diagrams of the stand at the pivot of the ellipsometer and the electrochemical cell are shown in Figs. 2.3 and 2.4 respectively. There are four mechanisms which allowed movement in order to align the system. As indicated in Fig. 2.3, the entire stand could be rotated horizontally, and the main part of the stand could be moved forwards or backward with respect to the base. Both of these mechanisms altered the position of the cell and electrode holder. The third and fourth mechanisms only altered the position of the electrode holder; two screws at the top of the electrode clamp, shown at the top of Figs. 2.3 and 2.4 allowed movement left and right, and tilting of the electrode forwards and backwards

Figs. 2.5 and 2.6 show the electrode holder and the construction of the cell windows. The 0.64 cm^2 disk working electrode was placed in the holder from behind, the front polished surface lying on an O-ring to form a seal. Level with the back of the electrode was a second O-ring which formed a seal when the back-piece of the holder was screwed on and exerting pressure on it. A final O-ring surrounded the wire as it entered the electrode holder. The wire was insulated with a plastic coating, except for *ca.* 1 mm which was exposed to form a contact on the back surface of the electrode. Considerable thought was given to the design of the cell windows, shown in Fig. 2.6, as a system was required that would allow compensation for the small deviations from perpendicular associated with normal

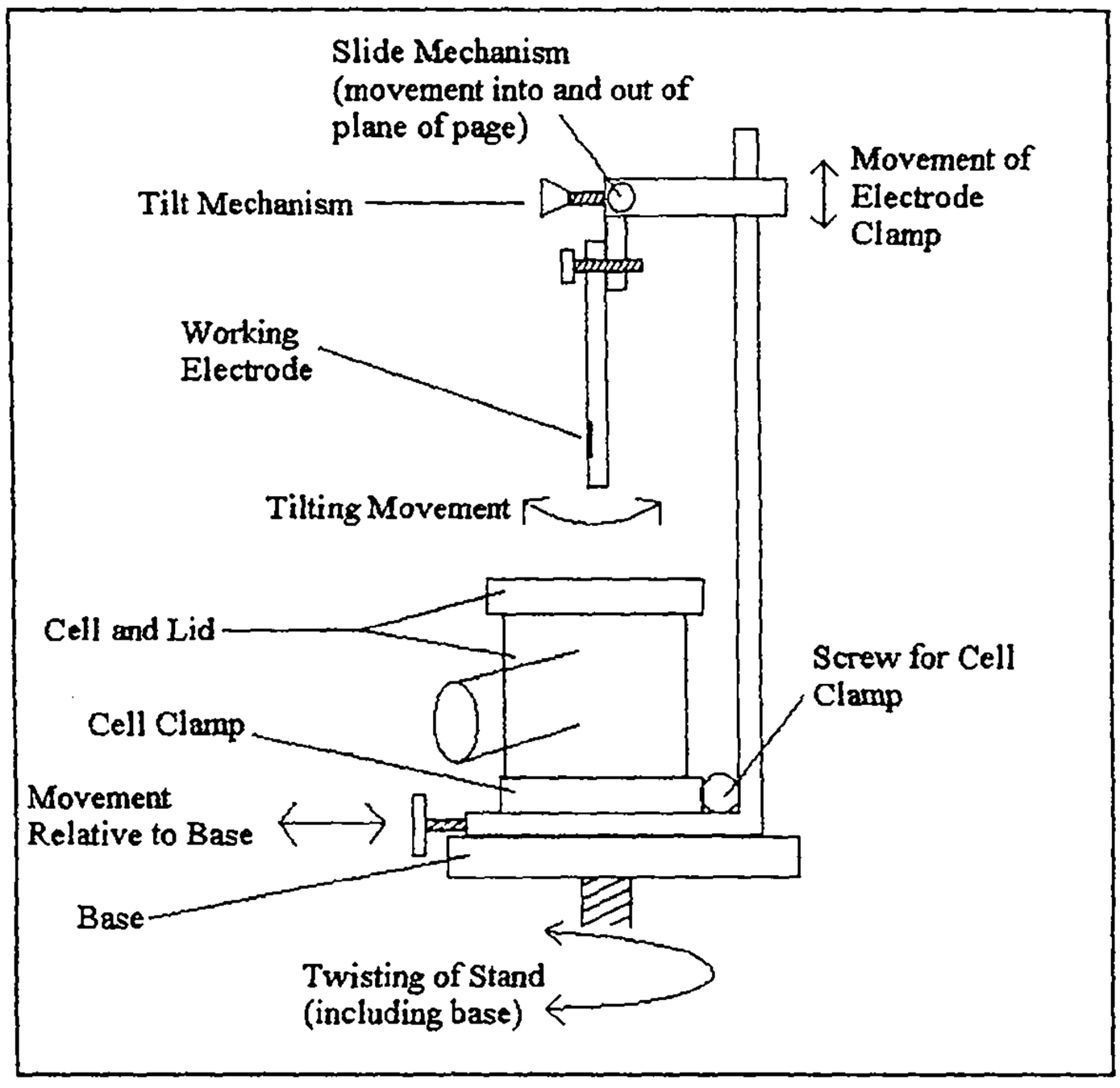

Fig. 2.3 The electrochemical stand at the pivot of the ellipsometer. The cell and electrode holder can be adjusted as indicated by the four arrows in order to align the system.

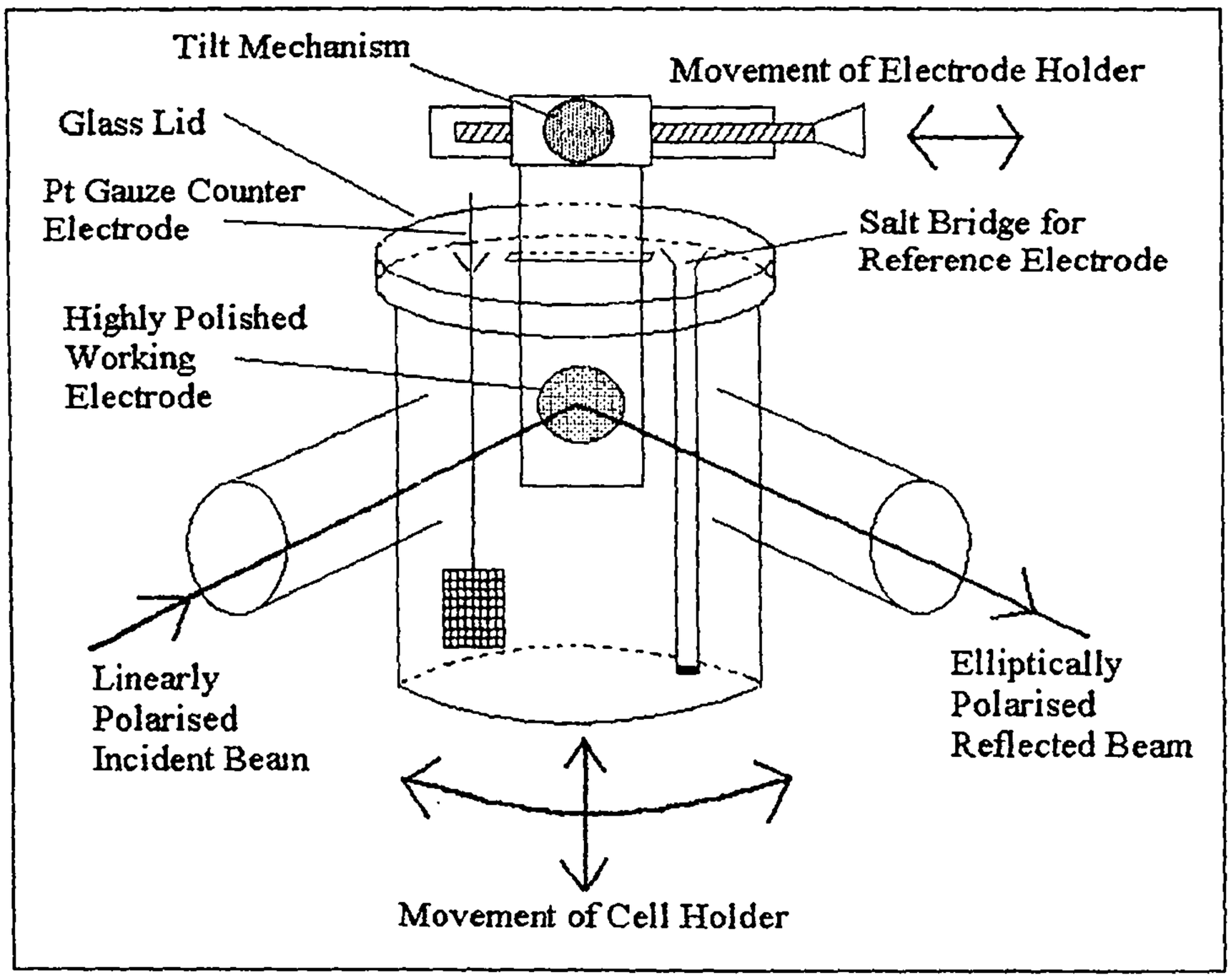

Fig. 2.4 The electrochemical cell. Two arms protrude form the cell with 120 ^{0} between them Two glass joints in the lid allow entry of the counter and reference electrodes, and the working electrode holder passes through a rectangular hole.

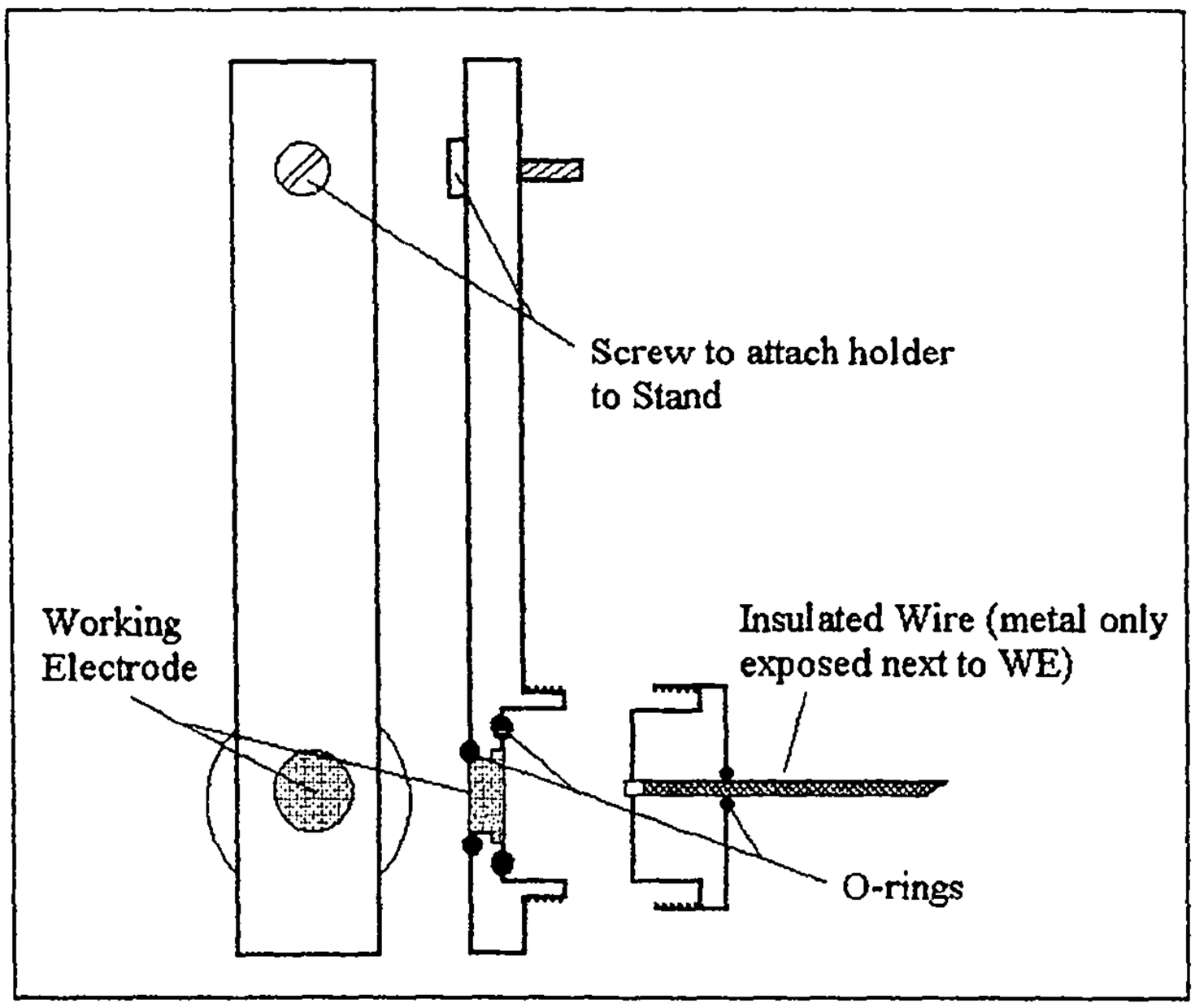

Fig. 2.5 A schematic diagram of the working electrode holder. The disk electrode is placed into the holder from the rear side and a back piece securely screwed into place, the pressure exerted ensures the O-rings to form watertight seals and a good electrical contact between the wire and electrode.

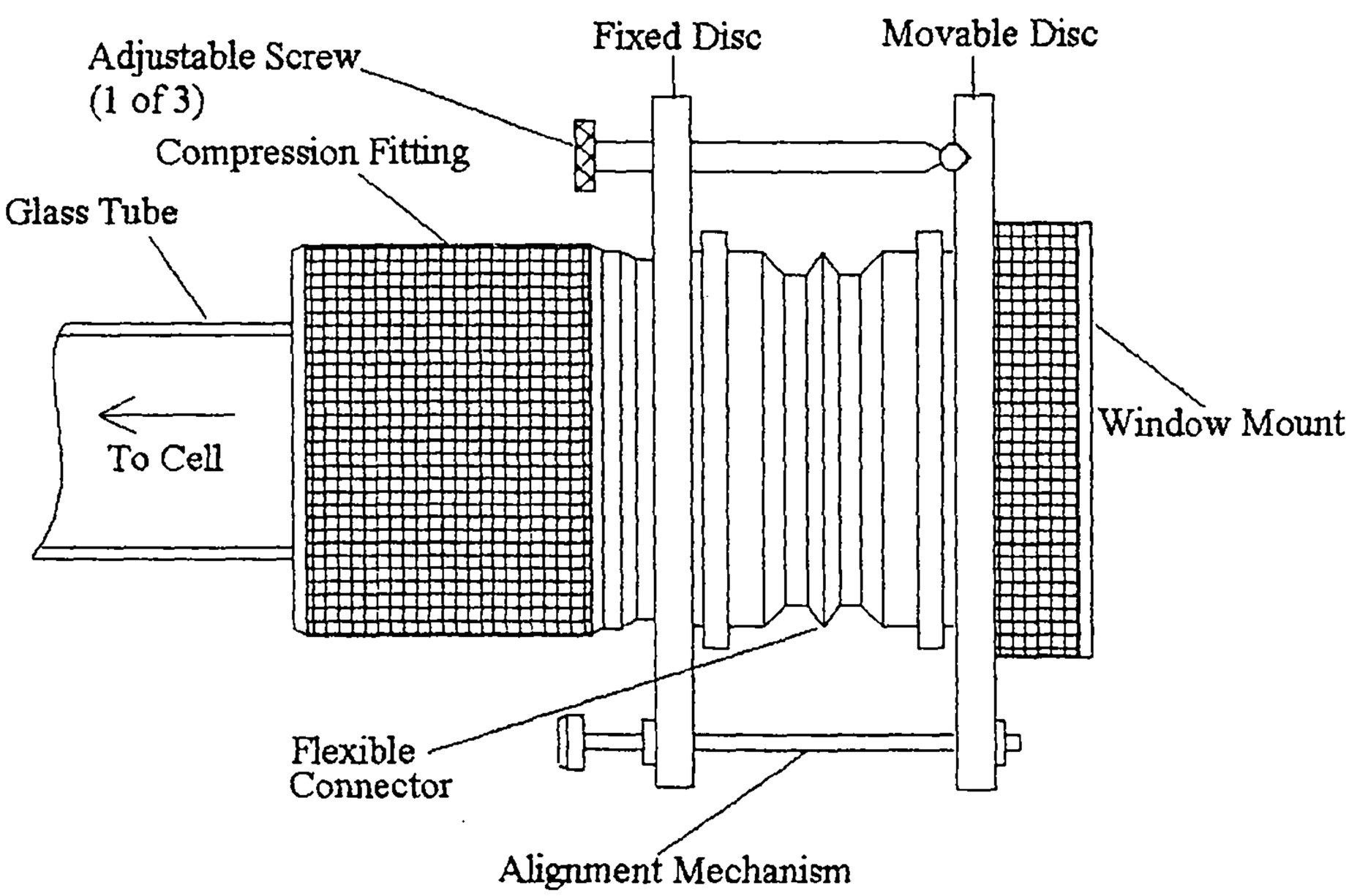

Fig. 2.6. Schematic diagram of the cell window. PTFE bellows allow the compensation of angles up to 10^{0}. The plane of the window is altered to be perpendicular to the beam path by adjustment of the screws pressing on the moveable disc.

glass-blowing precision. The design incorporated PTFE bellows, with the cell and windows both sealed with O-rings. By means of adjustable screws and springs, a range of up to 10^0 could be accommodated, more than sufficient to compensate for any problems in the glass-blowing.

When aligning the system for an experiment, during the first step only the working electrode holder was in place. Using the four mechanisms of movement available for the electrode holder, the reflected beam was aligned so that it hit the centre of the alignment target along the length of the second arm, i.e. from the electrode to the Stokesmeter. Once this has been achieved, the cell was placed about the electrode, and the window facing the arm of the ellipsometer with the retarder and polariser was adjusted until the reflection of the beam from the cell window overlay the incoming beam on a neutral density filter placed perpendicular to the beam path. This was achieved by firstly rotating the whole cell by hand, then clamping it firmly to prevent further movement, and further adjustment achieved using the screws indicated in Fig. 2.6 to adjust the plane of the window until it was perpendicular to the beam. The electrolyte was now introduced to the cell, and the window facing the Stokesmeter adjusted until the beam reflected from the electrode hit the centre of the metal target along the length of the arm and so entered the Stokemeter cleanly.

2.3 Fitting Procedures

A Pascal program, was written in-house to solve the complex equations involved in determining *n*, *k* and the thickness of a film from the polarisation data. (see section 1.3). Data could be input in the form of a complete file, or manually, a point at a time, the latter case normally used to fit the first few points of a file prior to the entire file being entered.

When entering data manually, a section at the start of the program required the input of various experimental variables, including the angle of incidence, the wavelength, the experimental values of Δ, Ψ, and relative intensity, and the complex refractive indices of the solvent, film, and electrode. Generally data was collected using the bare electrode prior to the electropolymerisation of a film onto it. This considerably simplifies the fitting procedure as there is only one interface (electrolyte/electrode), and these values of Δ and Ψ were readily used to calculate the complex refractive index and the reflectance coefficient of the electrode. The reflectance coefficient gave a predicted relative intensity, and the ratio of the predicted intensity to the arbitrary experimental value generated by the output currents of the Stokesmeter was then used to scale every intensity reading in the file.

When fitting data with a film present, the modified intensity, and *n* and *k* for the electrode returned by this initial procedure were entered, along with all the other parameters mentioned above. The program then required an input of how many films were present, whether each was homogeneous or inhomogeneous, and if inhomogeneous, how many layers the film is considered to consist of. In each case presented in this thesis only one film is present on the electrode, however both

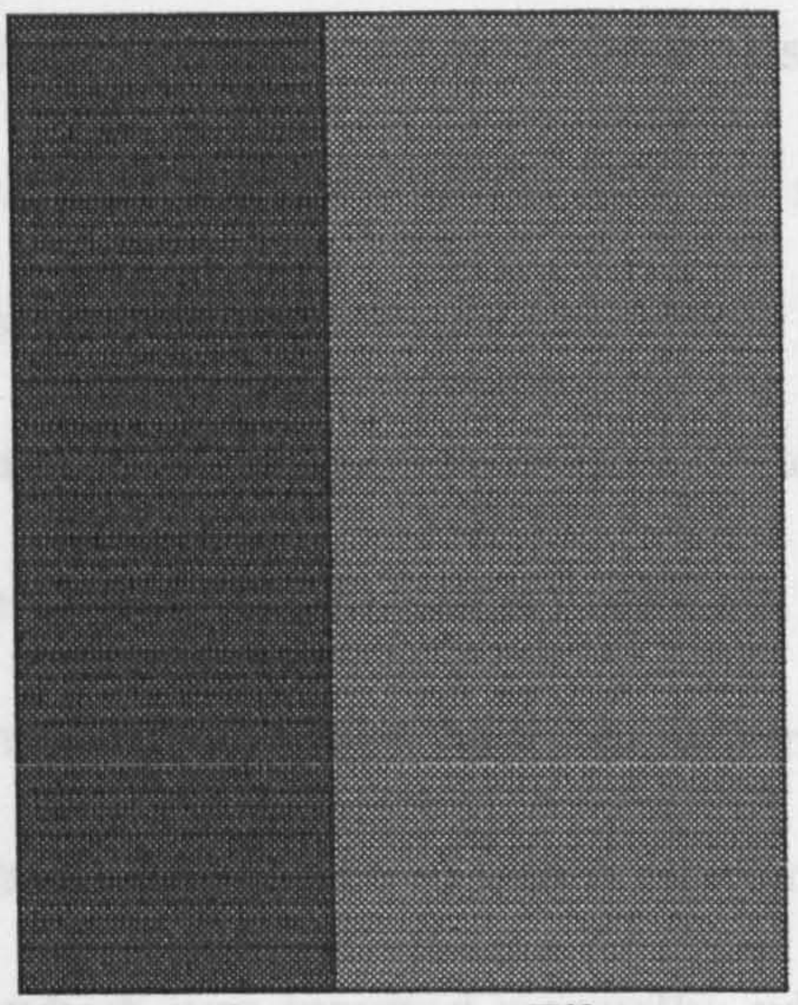

Fig. 2.7. The structure of an electrode covered with a homogeneous polymer. *n* and *k* are constant throughout the polymer.

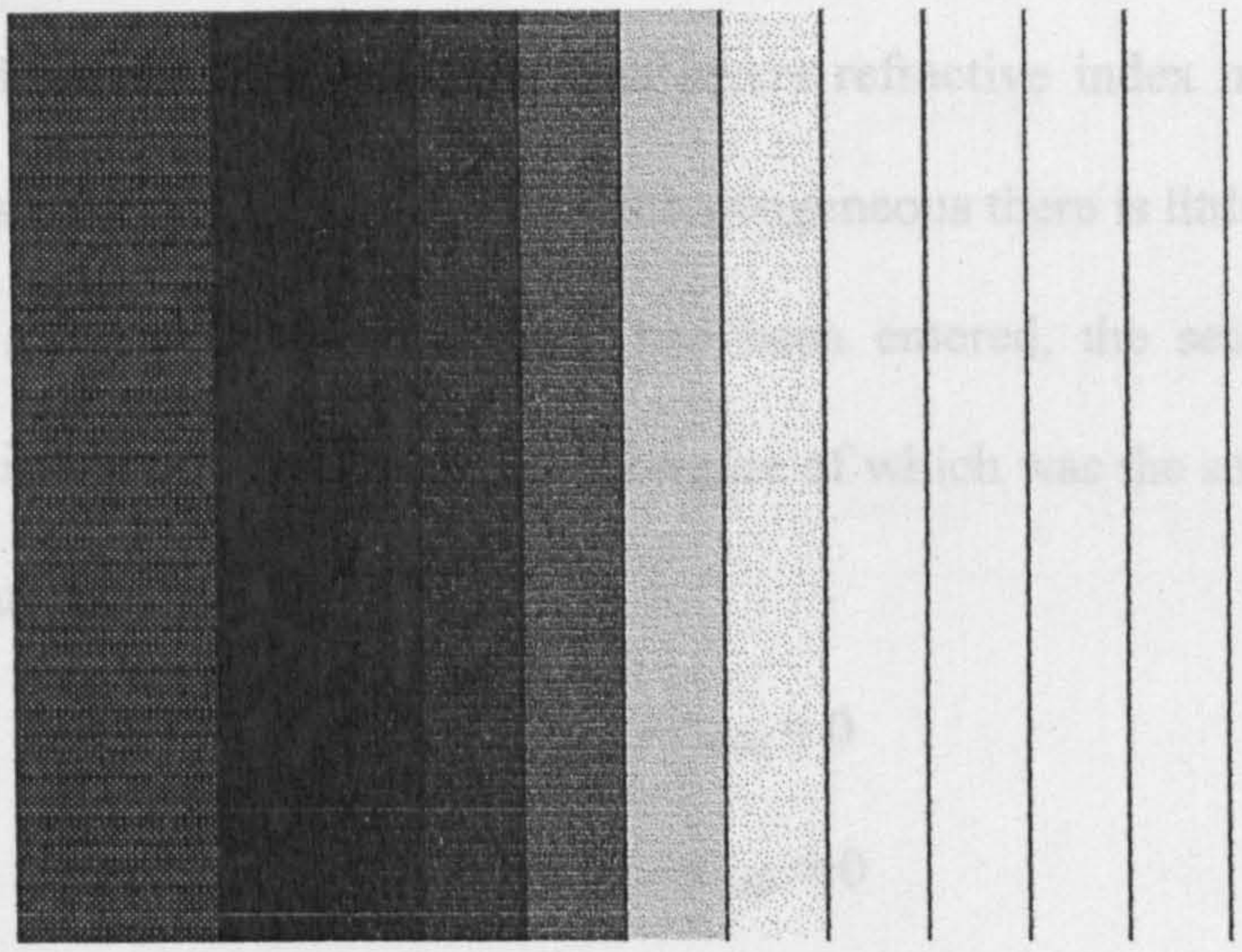

Fig. 2.8. Structure of an inhomogenous film. The model used has 10 layers of equal thickness and varying refractive index. The refractive index of the inner layers vary linearly between the values for the innermost and outermost layers.

homogeneous and inhomogenous Salen films were grown. In the case of a homogeneous film the fitting procedure was a great deal simpler as n and k of the film are constant throughout the thickness of the film, as shown in Fig. 2.7. In the case of an inhomogeneous film the values of n and k vary throughout the film. The simplest method of fitting an inhomogeneous film is to consider it as several homogeneous layers, each layer being the same thickness, with the refractive index varying linearly between the values of the inner and outermost layers, as shown in Fig. 2.8. When fitting a film in this manner the refractive index of the outermost layer was fixed to some value which was inputted manually, while the overall thickness and the refractive index of the innermost layer are allowed to float. As the refractive indices of the inner layers are determined by the values of the inner and outermost layers, this resulted in there still only being three variables being fitted. The necessary assumption of the value of the outermost layers refractive index makes the fitting procedure less rigorous, but if the film is inhomogeneous there is little other choice.

Once all the known parameters had been entered, the second part of the program consisted of a fitting routine, at the core of which was the solution to a set of non-linear equations:

$$\Delta_{exp} - \Delta_{calc} = 0 \qquad \text{(eqn. 2.1a)}$$

$$\Psi_{exp} - \Psi_{calc} = 0 \qquad \text{(eqn. 2.1b)}$$

$$R_{exp} - R_{calc} = 0 \qquad \text{(eqn. 2.1c)}$$

In order to solve these equations an approximate starting point must be found.

The Newton-Raphson method [4,5] is one of the most common methods of solution, and can be described in one dimension for the solution of $f(x) = 0$ by

$$x_2 = x_1 - \frac{f(x_1)}{f'(x_1)} \quad \text{where} \quad f'(x_1) = \left(\frac{df}{dx}\right)_{x=x_1} \qquad \text{(eqn. 2.2)}$$

where x_1 is the initial guess at a solution, and x_2 the better guess returned by the method. The formula is used iteratively and the i^{th} iteration has the form

$$x_{i+1} = x_i - \frac{f(x_i)}{f'(x_i)} \qquad \text{(eqn. 2.3)}$$

For a one dimensional problem the method can be easily visualised, as shown in Fig. 2.9. If **x** is the root for $f(x) = 0$, and x_0 the initial estimate of this root, the

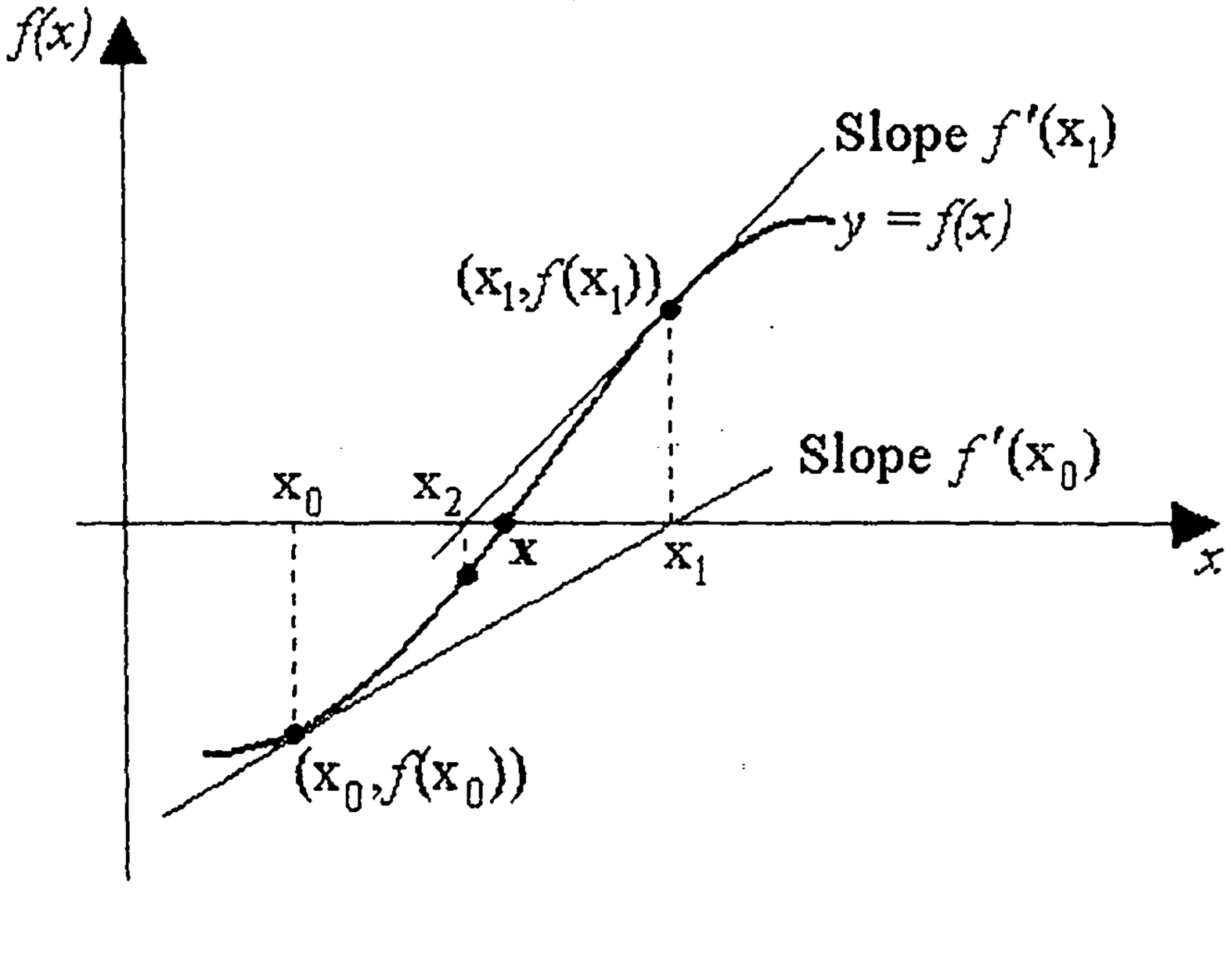

Fig. 2.9. An illustration of how the Newton-Raphson method is used to refine estimates of $f(x) = 0$.

tangent at point $(x_0, f(x_0))$ has a gradient of $f'(x_0)$. Where this tangent intercepts the x-axis is then taken as the new estimate, x_1, and as the process is repeated x_i approaches **x**.

The method may equally applied to a set of non-linear equations, and in this case the notation may be simplified by using vector symbols. If $\mathbf{x_i}$ is a column vector of solutions at iteration i, and $\mathbf{f_i}$ is a column vector containing the values of the functions $f^{(1)}...f^{(n)}$ at the values of the n variables in $\mathbf{x_i}$, it can be shown [4] that an iteration formula will now take the form

$$\mathbf{x_{i+1}} = \mathbf{x_i} - t_i\mathbf{H_i f_i} \qquad \text{(eqn. 2.4)}$$

where t_i is a scaling factor, normally set to unity, and $\mathbf{H_i}$ is an nxn matrix, the form of which is determined by the method used. For the Newton Raphson method it is just the inverse Jacobian, $\mathbf{J_i^{-1}}$, where the $(j,k)^{th}$ element of $\mathbf{J_i}$ is

$$\mathbf{J_i^{(j,k)}} = \left(\frac{df^{(j)}}{dx^{(k)}}\right) \qquad \text{(eqn. 2.5)}$$

and

$$\mathbf{x_{i+1}} = \mathbf{x_i} - \mathbf{J_i^{-1}}\,\mathbf{f_i} \qquad \text{(eqn. 2.6)}$$

If the initial approximation is fairly close to the solution, the Newton-Raphson method will converge very rapidly, however the main difficulty with this method is that if the initial approximation is not accurate then often convergence is not achieved.

The method of steepest descent [4,5] operates by starting from a particular point P_0, and moving a certain step distance in the direction of steepest descent to point P_1, and repeating the process until a minimum is reached. For example, solving

$$f(x, y) = 0 \qquad g(x, y) = 0 \qquad \text{(eqn. 2.7)}$$

is clearly equivalent to minimising

$$S(x, y) = [f(x, y)]^2 + [g(x, y)]^2 \qquad \text{(eqn. 2.8)}$$

Beginning at an initial approximation (x_0, y_0), the next approximation is selected by

$$x_1 = x_0 - tS_{x0} \qquad y_1 = y_0 - tS_{y0} \qquad \text{(eqn. 2.9)}$$

where S_{x0} and S_{y0} are the components of the gradient vector at (x_0, y_0), and the selection of t determines the step size.

In the case of a set of non-linear equations, the steepest descent method may be represented by Eqn. 2.10

$$\mathbf{x}_{i+1} = \mathbf{x}_i + t_i \nabla \mathbf{f}_i^T \qquad \text{(eqn. 2.10)}$$

This does not usually lead to the optimal way of reaching the minimum, however it does guarantee a minimum will be reached eventually. Although the steepest descent method is very slow at the final stages of convergence, it is very robust should the initial approximation be quite a way from a solution, thus a combination of the Newton-Raphson and Steepest Descent methods proves very useful. The Levenberg-Marquardt algorithm [4,5] is a cross between the two methods, and may be written as

$$\mathbf{H}_i = \left(\mathbf{J}_i^T \mathbf{J}_i + \lambda_i\right)^{-1} \mathbf{J}_i^T = \left(\frac{1}{\lambda_i}\right)\left(1 + \lambda_i^{-1} \mathbf{J}_i^T \mathbf{J}_i\right)^{-1} \mathbf{J}_i^T \qquad \text{(eqn. 2.11)}$$

where $\mathbf{J}_i^T$ is the transpose of $\mathbf{J}_i$ and λ_i is a numerical parameter that can be adjusted manually at every iteration to increase the speed of convergence. When $\lambda_i = 0$ the Newton-Raphson method is recovered; however as $\lambda_i \to \infty$, $\mathbf{H}_i \to \lambda_i^{-1} \mathbf{J}_i^T$ which is a form of the steepest descent method. Thus when fitting data, initially a very high value of λ is chosen (e.g. 100 - 1000), and as the approximation improves, as measured by the sum of squares

$$S = (\Delta_{exp} - \Delta_{calc})^2 + (\Psi_{exp} - \Psi_{calc})^2 + (R_{exp} - R_{calc})^2 \qquad \text{(eqn. 2.12)}$$

then λ is decreased, normally being reduced to unity or below as a solution is approached.

2.4 Salen Monomer Synthesis

2.4.1 [Pd(OMeSalen)] and [Ni(OMeSalen)]

Performed by A. Timonov and S. Vasil'eva, Pedagogical Institute, Univesity A. I. Herzen. St. Petersburg, Russia.

The Salen was obtained commercially from Aldrich and the methoxy derivative was synthesised [6-9] by combining stoichiometric amounts of hot ethanolic solutions of *o*-vanillin (Aldrich, 97 %) and ethylenediamine (Vecton, 98 %). The product was filtered, washed with water and cold ethanol, and dried in air. [Pd(OMeSalen)] was synthesised by combining stoichiometric amounts of a hot ethanolic solution of the ligand and an aqueous solution of $K_2[PdCl_4]$ (Aldrich). The pH of the mixture was adjusted to 7 by the addition of triethylamine (Vecton, 98 %) and the mixture refluxed for 30 min. The product was filtered, washed with water and cold ethanol and twice re-crystallised from ethanol; its identity was confirmed by elemental analysis. [Ni(OMeSalen)] was prepared in a similar manner, and the identity of both monomers was confirmed by elemental analysis.

2.4.2 [Ni(SaltMe)], [Ni(OMeSaltMe)] and [Ni(SaldMe)]

Performed by C. Freire and M. Vilas-Boas, University of Porto, Portugal.

The syntheses of [Ni(SaltMe)] and [Ni(SaldMe)] were as described in literature [10,11]. All solvents, 2-methylpropane-2,3-diamine (for the (SaldMe)) and the salicylaldehyde were obtained commercially and used as received and 2-3-

Dimethylbutane-2-,3-diamine (for (SaltMe) and (OMeSaltMe)) was prepared by a modification of the method of Sayre [12]. The Schiff base was prepared by standard methods [13], in which an ethanolic solution of the diamine was added to a rapidly stirred ethanolic solution of salicylaldehyde ((Saldme) and (SaltMe)) or 3-Methoxysalicyladehyde (OMeSaltMe) and the resulting mixture was then refluxed. On cooling to room temperature, the yellow solid formed was filtered off, washed with cold ethanol and cold diethyl ether, and dried under vacuum for several hours. The Nickel(II) complex was also synthesised by standard procedures [13]: an ethanolic solution of the Schiff base was added to ethanolic nickel(II) acetate solutions and the resulting mixture was then refluxed. After cooling the red-brown microcrystalline solid was filtered off, washed with ethanol and diethyl ether, and dried under vacuum. The N,N'-2,3-dimethylbutane-2,3-diyl-bis(salicylideneiminate)nickel(II) or [Ni(SaltMe)], N,N'-2-methylpropane-2,3-diyl-bis(salicylideneiminate)nickel(II) or [Ni(SaldMe)] and the N,N'-2,3-dimethylbutane-2,3-diyl-bis(3-methoxysalicylideneiminate)nickel(II) were recrystallised from acetonitrile before use, and the identity of all three salens confirmed by NMR and elemental analysis.

2.5 Polymerisation and Potential Cycling and Stepping of Salens.

2.5.1 [Pd(OMeSalen)] and [Ni(OMeSalen)]

Poly[Pd(OMeSalen)] films were deposited on a highly polished Pt electrode having an area of 0.64 cm^2. Prior to use, the working electrode was polished with an aqueous suspension of 0.05 μm alumina (Beuhler) on a master Tex (Beuhler) polishing pad. A Pt gauze was used as a counter electrode and all potentials are referred to a Ag/AgCl reference electrode.

The films were deposited by cycling the potential of the working electrode between 0 and 1.2 V at 100 mV s^{-1} in a solution containing 1 mmol dm^{-3} [Pd(OMeSalen)] in 0.1 mol dm^{-3} tetrabutylammonium tetrafluotoborate (TBAT, Aldrich) in acetonitrile (MeCN, HPLC grade, Aldrich). After fifteen cycles, the electrode was removed from solution and washed with a small amount of acetonitrile to remove any residual monomer. The modified electrode was immersed in 0.1 mol dm^{-3} TBAT - MeCN and cycled between -0.2 V and 1.1 V at 100 mV s^{-1}, and stepped from 0 V to 1.1 V and back to 0 V in 100 mV steps with 35 s at each potential.

The growth of poly[Ni(OMeSalen)] was performed in a similar manner, but due to the small amount of [Ni(OMeSalen)] synthesised, polymerisation had to be performed in a cell smaller than that used for the ellipsometer in order for a concentration of 1mmol dm^{-3} to be obtainable, so film growth could not be observed using the ellipsometer. Once growth was complete and the electrode rinsed it was transferred to a solution of the monomer free electrolyte in the ellipsometric cell and

the behaviour of the modified electrode under cycling and stepping conditions analogous to those employed in the poly[Pd(OMeSalen)] experiments was studied.

The ellipsometric measurements were performed with an angle of incidence of 60^0 and using probe wavelengths of 633 nm and 594.1 nm. The cell and ellipsometric setup have been described in section 2.2.

2.5.2 [Ni(SaldMe)], [Ni(SaltMe)], and [Ni(OMeSaltMe)]

All three films were grown in the same manner to allow direct comparison between them. As with the Pd(OMeSalen), deposition was onto a highly polished Pt disk electrode of area 0.64 cm^2, which had been polished to a mirror finish using an aqueous suspension of 0.05 μm alumina on a Master Tex polishing pad (Beuhler).

Deposition was performed by cycling the Pt working electrode between 0.0 V and 1.3 V at 100 mV s^{-1} in a solution containing 1.0 mmol dm^{-3} of the appropriate monomer and 0.1 mol dm^{-3} tetraethylammonium perchlorate (TEAP, Fluka, Puriss) in acetonitrile (HPLC Grade, Aldrich). After five cycles the electrode was removed and rinsed with acetonitrile before being immersed in 0.1 mol dm^{-3} TEAP in acetonitrile. The modified electrodes were cycled between 0.0 V and 1.3 V at 100 mV s^{-1}, and stepped from 0 V to 1.3 V and back to 0 V in 100 mV steps with 35 s at each potential.

The ellipsometric measurements were performed with an angle of incidence of 60^0 and using probe wavelengths of 670 nm, 633 nm, 594.1 nm, and 543.5 nm, though as some lasers were bought during the period of the study all four wavelengths could not be used on each of the three polymers.

2.6 FTIR *In-Situ* Spectroscopy

This section is intended to be a brief introduction to the technique of Fourier Transform Infra-Red Spectroscopy, which has been used alongside ellipsometry in the investigation of [Pd(OMeSalen)] and [Ni(SaltMe)]. For a more detailed description of the technique see [14, 15]

Although it was long recognised that IR spectroscopy would be a useful *in-situ* tool, problems with sensitivity and solvent absorption limited systems to which it could be applied. The advent of FTIR instruments greatly increased the signal to noise ratio, as the enhanced speed at which spectra could be collected allowed a number of scans to be collected and averaged, taking as little as 15 ms each, and is also used as a difference technique; several spectra are gathered and averaged at a baseline potential, before the potential is then stepped to some region of interest where a second spectrum is collected and ratioed to the first. The signal to noise ratio increases as $\sqrt{N}$, where N is the number of individual scans. In practice the spectra are plotted as normalised difference spectra, that is

$$\left(\frac{\Delta R}{R}\right) = \frac{\left(S_n - S_r\right)}{S_n} \qquad \text{(eqn. 2.9)}$$

where S_r is the reference spectrum and S_n the spectrum of interest, is plotted against wavenumber. As a result of this data manipulation, any peaks pointing up, to ($+\Delta R/R$), correspond to a loss of absorbing species in S_n with respect to S_r , while any peaks pointing down, to ($-\Delta R/R$), correspond to a gain of absorbing species in S_n.

The problem of solvent absorption is overcome simply by minimising the solvent pathlength. A reflective working electrode is pressed against the IR transparent window of the electrochemical cell, trapping a thin layer of electrolyte between the electrode and window. The electrochemical cell is shown in Fig. 2.10.

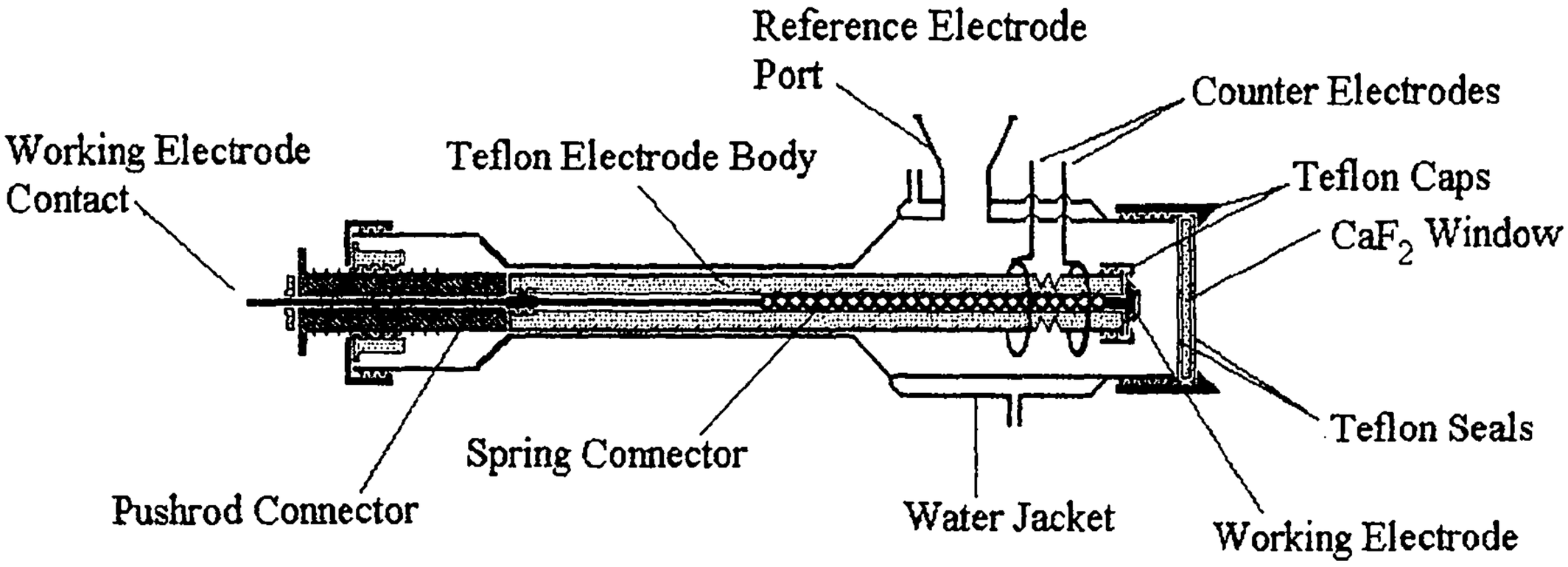

Fig. 2.10. The *in-situ* FTIR Electrochemical Cell

The FTIR spectrometer used for the data presented in this thesis was a Bio-Rad FTS-40 controlled by an Oxsys Micros Electrochemical Interface, which also controlled the electrochemistry of the cell. The thin film mode adopted to minimise solvent absorptions precludes the use of this technique to study growth processes. Instead the working electrode was pulled back from the cell window while polymerisation was performed in an identical manner to those described in sections 2.5.1 and 2.5.2 for Pd(OMeSalen) and Ni(SaltMe), respectively. As used in the ellipsometric experiments, the working electrode was a polished Pt 0.64 cm^2 disk, and all potentials were referenced to Ag/AgCl. In order to allow time to gather the spectra the potential was stepped rather than cycled, with 35 s at each potential, allowing the accumulation of 100 interferograms at 8 cm^{-1} resolution. In the case of

poly[Ni(SaltMe)] the potential was altered in 100 mV steps from 0 to 1.3 V, and back to 0 V, while poly[Pd(OMeSalen)] was stepped by the same increments but between 0 V and 1.2 V

2.7 References

1. R. M. A. Azzam, E. Masetti, L. Eliminyawi, F. G. Grosz, *Rev. Sci. Instrum.*, 1988, **59**, 84.
2. R. M. A. Azzam, N. M. Bashara, *Ellipsometry and Polarised Light*, 1987, North-Holland, Amsterdam.
3. E. Collett, *Polarised Light, Fundamentals and Applications*, 1993, Marcel Dekker, New York.
4. A, Ralston, P. Rabinowitz, *A First Course in Numerical Analysis*, 2nd Ed., 1978, McGraw-Hill, Inc.
5. R. L. Burden, J. D. Faires, *Numerical Analysis*, 6th Ed., 1997, Brockes/Cole Publishing Co., California.
6. V. N. Aleynikova, V. V. Vasiliev, A. M. Timonov, G. A. Shagisultanova, *Russ. J. Phys. Chem.*, 1987, **61**, 1117.
7. I. E. Popeko, V. V. Vasiliev, A. M. Timonov, A. G. Shagisultanova, *Abstr. 14th Chernyev Conference on the Chemistry of Platinum Group Metals*, Siberian Branch of the Academy of Science, Novosibirsk, Russia, 1989, vol. **1**, p. 38.
8. I. E. Popeko, V. V. Vasiliev, A. M. Timonov, A. G. Shagisultanova, *Russ. J. Inorg. Chem.*, 1990, **35**, 933.
9. I. E. Popeko, V. V. Vasiliev, A. M. Timonov, A. G. Shagisultanova, *Russ. J. Coord. Chem.*, 1990, **16**, 1107.
10. C. Freire, B. de Castro, *J. Chem. Soc., Dalton Trans.*, 1998, 1491.
11. I. C. Santos, M. Vilas-Boas, M. F. M. Piedade, C. Freire, M. T. Duarte, B. de Castro, *Polyhedron*, 2000, **19**, 655.

12. R. Sayre, *J. Am. Chem.Soc.*,1955, 77, 6689

13. R. H. Holm, G. W. Everett, Jr, A. Chakravorty, *Inorg. Chem.*, 1966, **7**, 183.

14. P. A. Christensen, A. Hamnett, *Techniques and Mechanisms in Electrochemistry*, 1994, Chapman and Hall, Glasgow.

15. P. R. Griffiths, J. A. deHaseth, *Fourier Transform Infrared Spectrometry*, 1986, Wiley-Interscience, New York.

3.1 Introduction

During the course of the work described in this thesis, the ellipsometer was moved to take advantage of a vacant air table; the relocation occurred after the investigations of [Pd(OMeSalen)], [Ni(OMeSalen)] and [Ni(SaltMe)] had been performed, and prior to the studies of [Ni(OMeSaltMe)] and [Ni(SaldMe)]. The noise levels present in the system were insufficient to impinge on any of the Salen studies, both prior to and after the move, as the changes in the ellipsometric parameters during film growth and switching were large enough for the signal to noise ratio to be well within acceptable limits. However, when an attempt was made to study iron passivation, a process previous studies [1,2] have shown to result in only a few degrees change in Δ and less than a 1^{0} change in Ψ, the noise levels were clearly unacceptable, in many cases the signal being completely unobservable, and an investigation of the sources of noise intrinsic and extrinsic to the system was undertaken, the results of which are described in this chapter.

3.2 Results and Discussion

All the data presented in this chapter were obtained with no electrode or cell present in the beam path, instead the ellipsometer arms were set at 180^{0} and the beam passed from the laser source through the polariser and retarder, and this known incident polarisation state was directly incident on the (already calibrated) Stokesmeter. Typical examples of the data observed with the ellipsometer in this

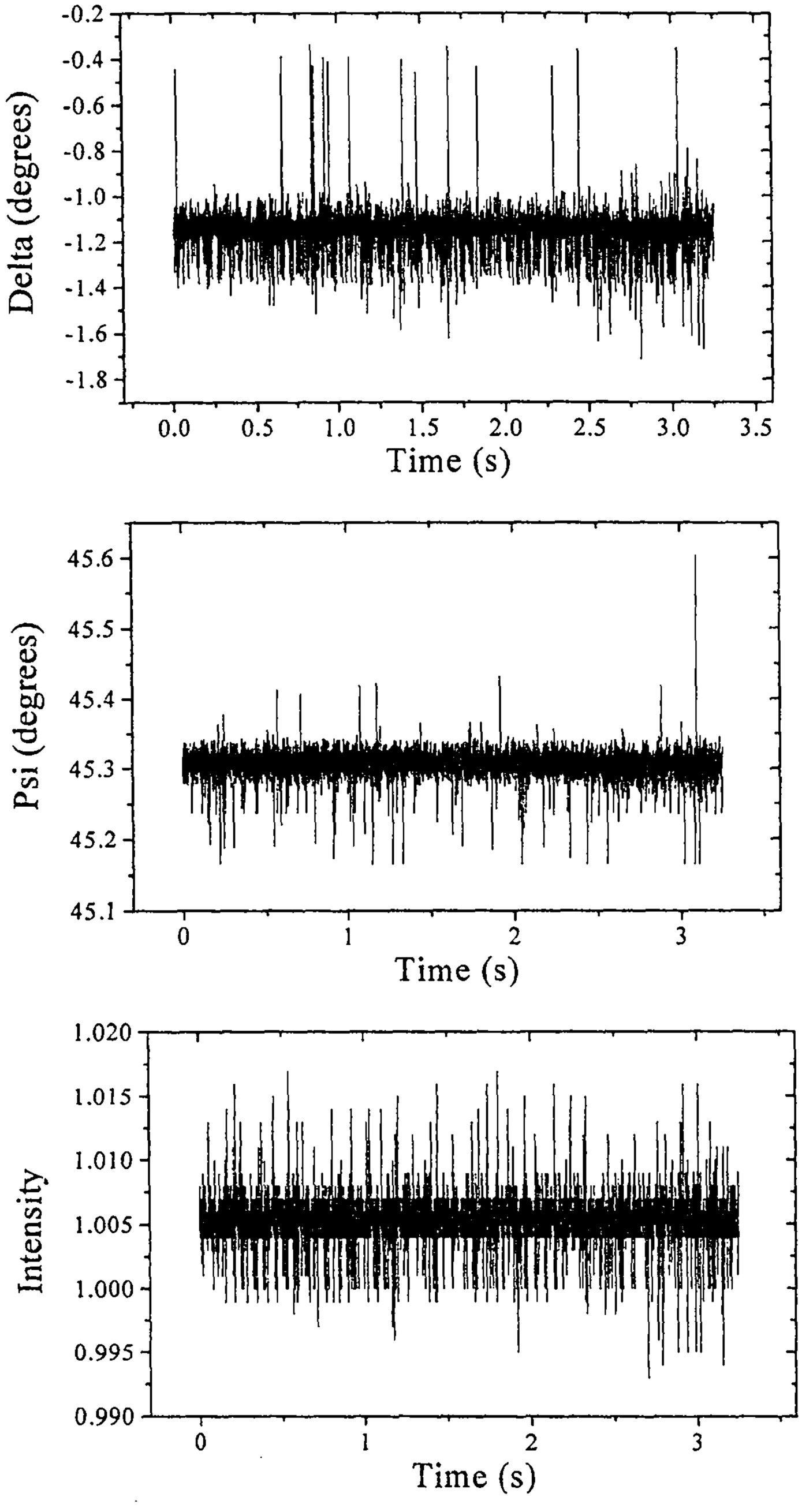

Fig. 3.1. The variation of Δ, Ψ and intensity over a 3.25 s time period; the data were collected with a 45^{0} linearly polarised laser beam, 632.8 nm, directly incident upon the Stokesmeter. Readings were taken every 325 μs, with no data averaging.

arrangement are shown in Fig. 3.1, and a great deal of noise is clearly present: up to *ca.* 1^{0} on Δ, 0.3^{0} on Ψ, and 1 % on the intensity, peak to peak (standard deviations of 0.08 on Δ, 0.02 on Ψ and 0.002 on the Intensity). The first step in the analysis of this noise was to determine if it was random or non-random, as the latter would clearly indicate a particular source(s) of the noise.

If a population is random, then if N readings are repeatedly taken from it and their mean taken to create a new population of means, the variance of the new population will be a factor of N smaller than that of the parent population, i.e. the standard deviation will be $1/(N)^{1/2}$th that of the parent population [3]. To establish whether a linear relationship existed between the standard deviation and $1/(N)^{1/2}$ for the noise observed in the ellipsometric system, the data shown in Fig. 3.1 were used as the parent population and various values of N employed. Using the programming language Pascal [4,5], a computer program was written to read in a file and request a manual input of how many rows are to be averaged (N), e.g. an input of N = 10 for a file of 10000 data points will return a file of 1000 points, each the average of ten consecutive points of the original file. Using this method with various values of N, the data shown in Fig. 3.2 were generated, which exhibit an almost linear relationship between $1/(N)^{1/2}$ and the standard deviation, except for the values arising from the parent population itself (N = 1). To see if non-random shot noise was overlying a source of random noise, resulting in the non-linear plots, a second program was written to remove the spikes clearly present in Δ, Ψ and in the intensity to a lesser extent in Fig 3.1. This program operates by taking the mean of the input file, then asking for acceptable upper and lower limits; any points falling outside the

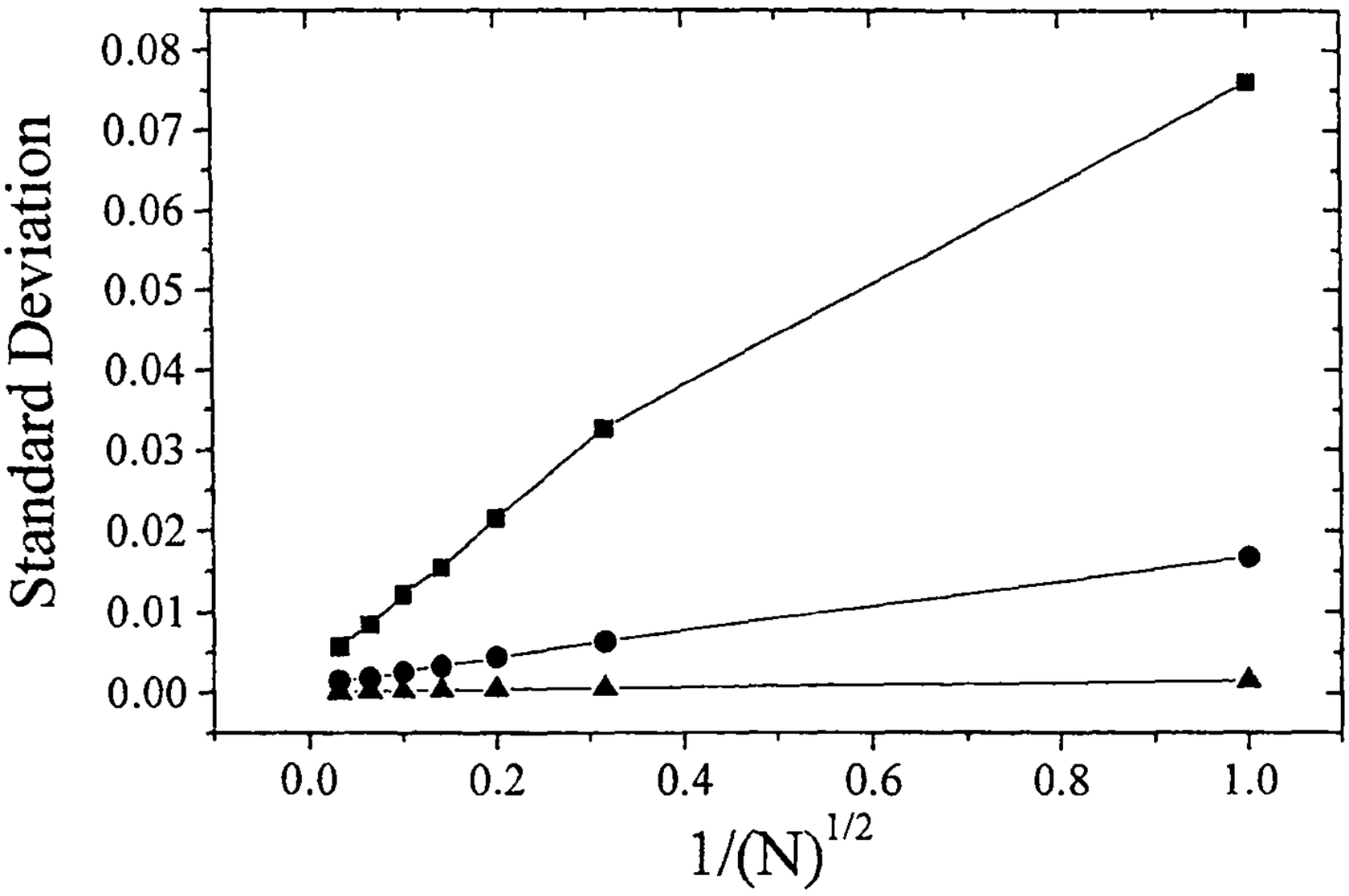

Fig. 3.2. The relationship between the standard deviation of the data shown in Fig. 1 and the square root of the number of readings averaged for each data point (N). Squares - Δ, Circles - Ψ, and triangles - intensity

specified range are replaced with the mean value taken at the start of the program (though this will of course be different from the mean of the output file if any points are replaced). Using this program the data in Fig. 3.1 were modified by replacing any point that fell outside one standard deviation either side of the mean with the mean value itself. In this manner the data in Fig. 3.3 were generated, and analysed as described above for the original data. Fig. 3.4 shows the relationship between the standard deviation and $1/(N)^{1/2}$ for the modified data, for all three parameters. Removing the spikes from the data still does not yield a perfect linear relationship between $1/(N)^{1/2}$ and the standard deviation, the points arising from the parent populations with N = 1 still deviating slightly, but the data is still closer to linearity than that in Fig. 3.2. This indicates the source(s) of noise are very nearly random,

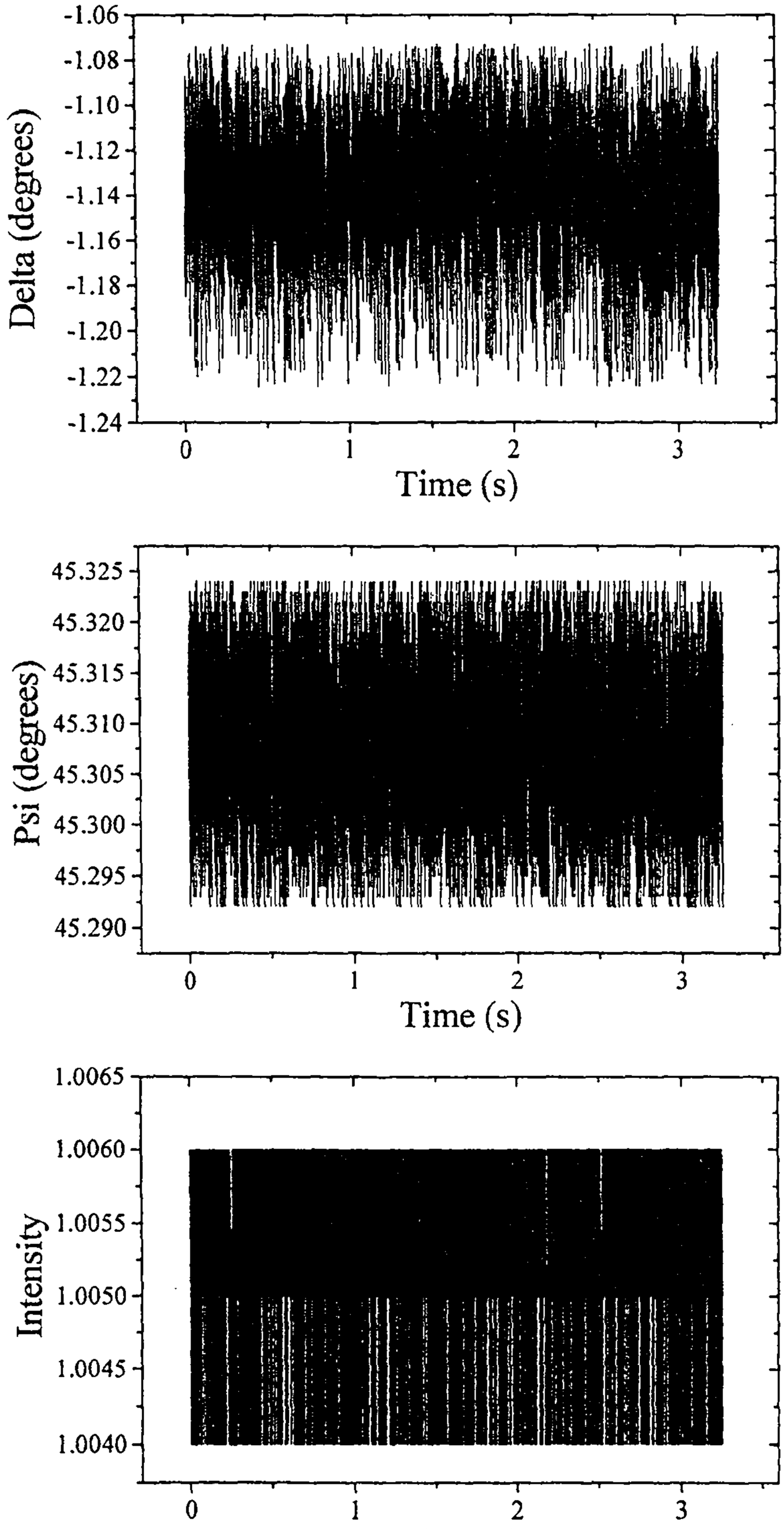

Fig. 3.3. The data in Fig. 1 with the shot noise removed. Any point lying further than one standard deviation from the mean was replaced with the mean value itself.

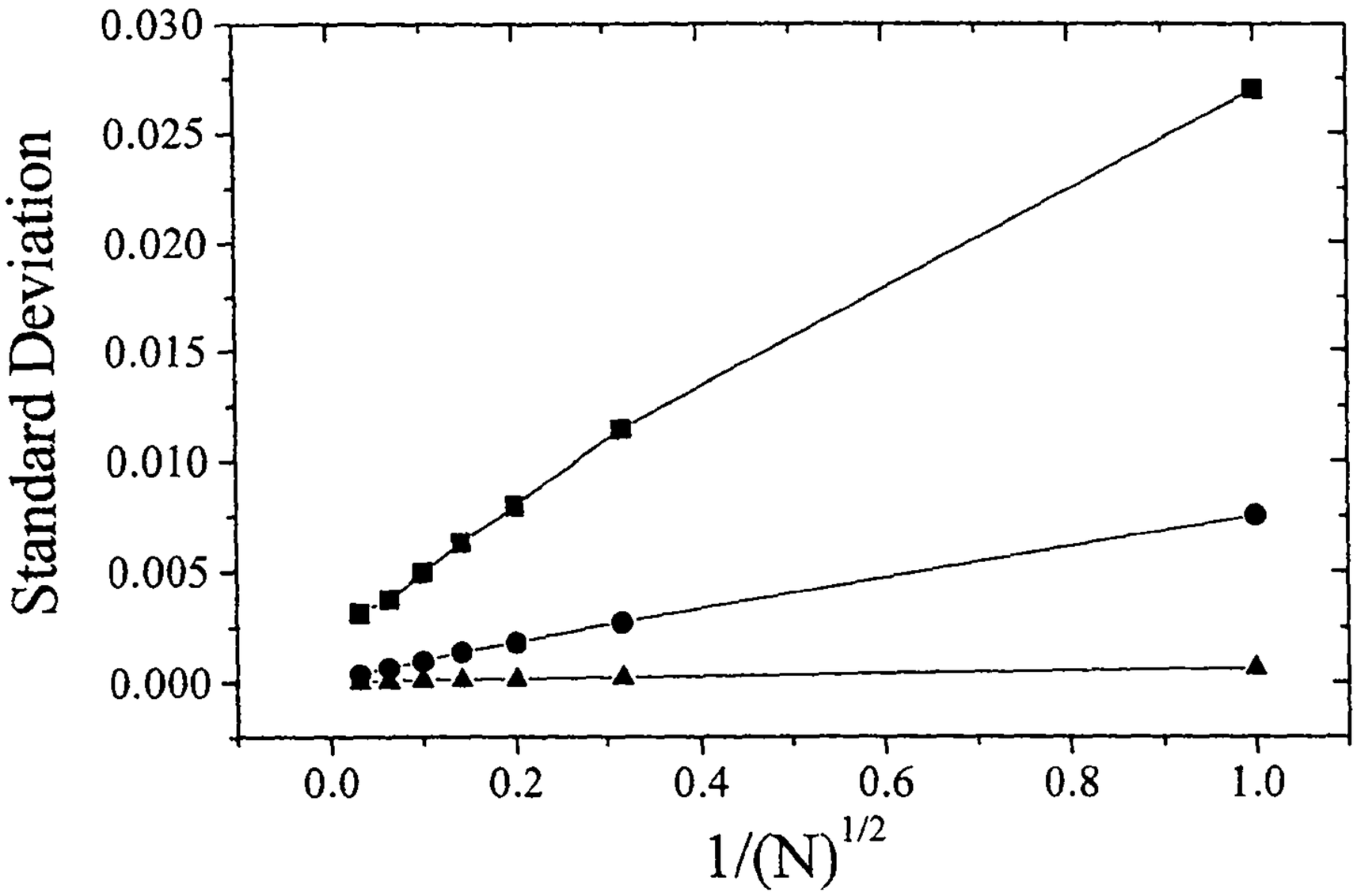

Fig. 3.4. The relationship between the standard deviation and the square root of the number of readings averaged for each point for the data in Fig. 3.3. Squares - Delta, circles - psi, and triangles - intensity

possibly with some degree of underlying patterned noise resulting in the slightly off linear nature of the plots in Figs. 3.2 and 3.4.

It is interesting to note that the intensity is highly digitised even before the removal of any noise outside one standard deviation. This digitisation indicates the computer is already at maximum resolution for the intensity measurements and no further improvement is possible, however, this is not the case for Δ and Ψ, and it should be possible to improve the noise levels of these two parameters.

The extent to which vibrational noise from the surroundings was affecting the ellispometric system and the degree to which it could be minimised was assessed from the effect the air table had on the noise levels. To prevent the transmission of vibrational noise to the air table no equipment was in contact with the table at any point around it, and all leads to equipment on the table (laser, Stokesmeter, polariser,

retarder) were encased in foam, and a metal plate placed over them and screwed down to the air table to secure them and keep any movement to a minimum. Figs. 3.4, 3.5 and 3.6 compare the typical noise observed with the air supply to the air table switched off, with the air table on at *ca*. 3 bar, and with the air table on at the same pressure and a half inflated tyre under the ellipsometer. These measurements were taken using a HeNe laser with a wavelength of 632.8 nm, the beam linearly polarised at 45 ^{0}, and the ellipsometer set at 180 ^{0} with no sample present. With no air supply to the air table, the noise (peak to peak) on Δ is about 0.6 ^{0}, on $\Psi \approx 0.1$ ^{0}, and is 1.8 % for the intensity. With the air table functioning at 3 bar the variation in the intensity decreases to approximately 1.3 %, and although the overall variation in the values of Δ and Ψ is hardly altered, the main body of the noise is reduced but a wave with a period of *ca*. 3 s becomes clear, particularly on Ψ. Upon inserting the tyre between the air table and ellipsometer, the high frequency noise decreases to 0.1 ^{0} for Δ, 0.03 ^{0} for Ψ, 0.4 % for intensity, and the low frequency oscillation becomes a good deal more pronounced for Δ and Ψ. The change in the intensity is so small the data has become digitised so no wave is visible. This clearly indicates that a great deal of the noise present in Fig. 3.4 is vibrational. The wave is present even in Fig. 3.6, the most vibrationally isolated of the three experiments. Its origin remains uncertain: it was present in some experiments but not others, and when present it was *not* seen to diminish during late evenings etc., suggesting it is not necessarily vibrational in nature.

Raising the operating pressure of the air table had no further effect on the noise, indicating the vibrational noise had been minimised as far as was readily possible. Further to vibrational noise, the signal itself may be noisy, or electronic

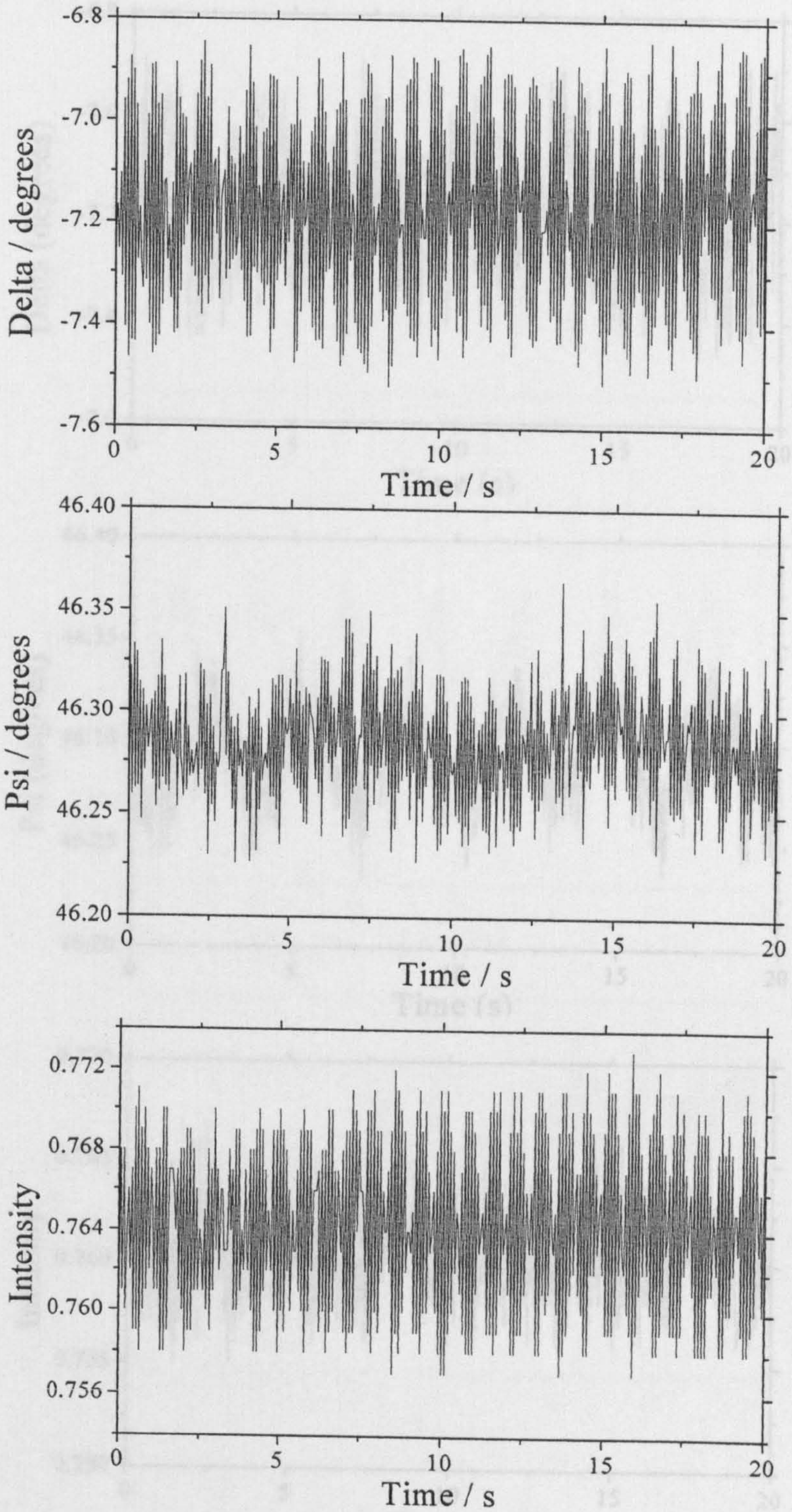

Fig. 3.4 The typical noise observed on Δ, Ψ and intensity with the air supply to the air table switched off and no tyre under the equipment. 24 readings were averaged to give one point every 50 ms.

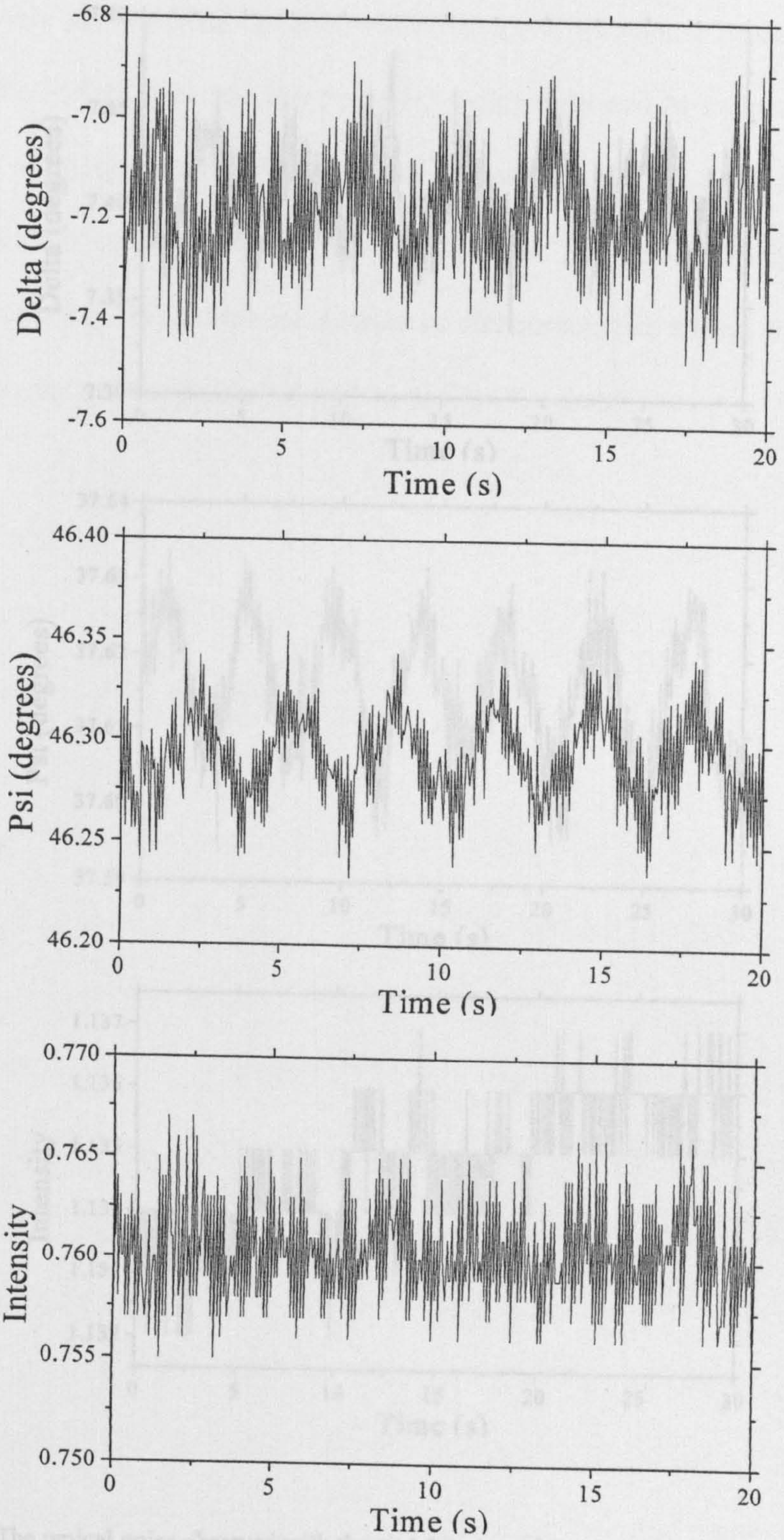

Fig.3.5. The typical noise observed on Δ, Ψ and intensity with air table operating at a pressure of *ca.* 3 bar, and no tyre under the equipment. 24 readings were averaged to give one point every 50 ms

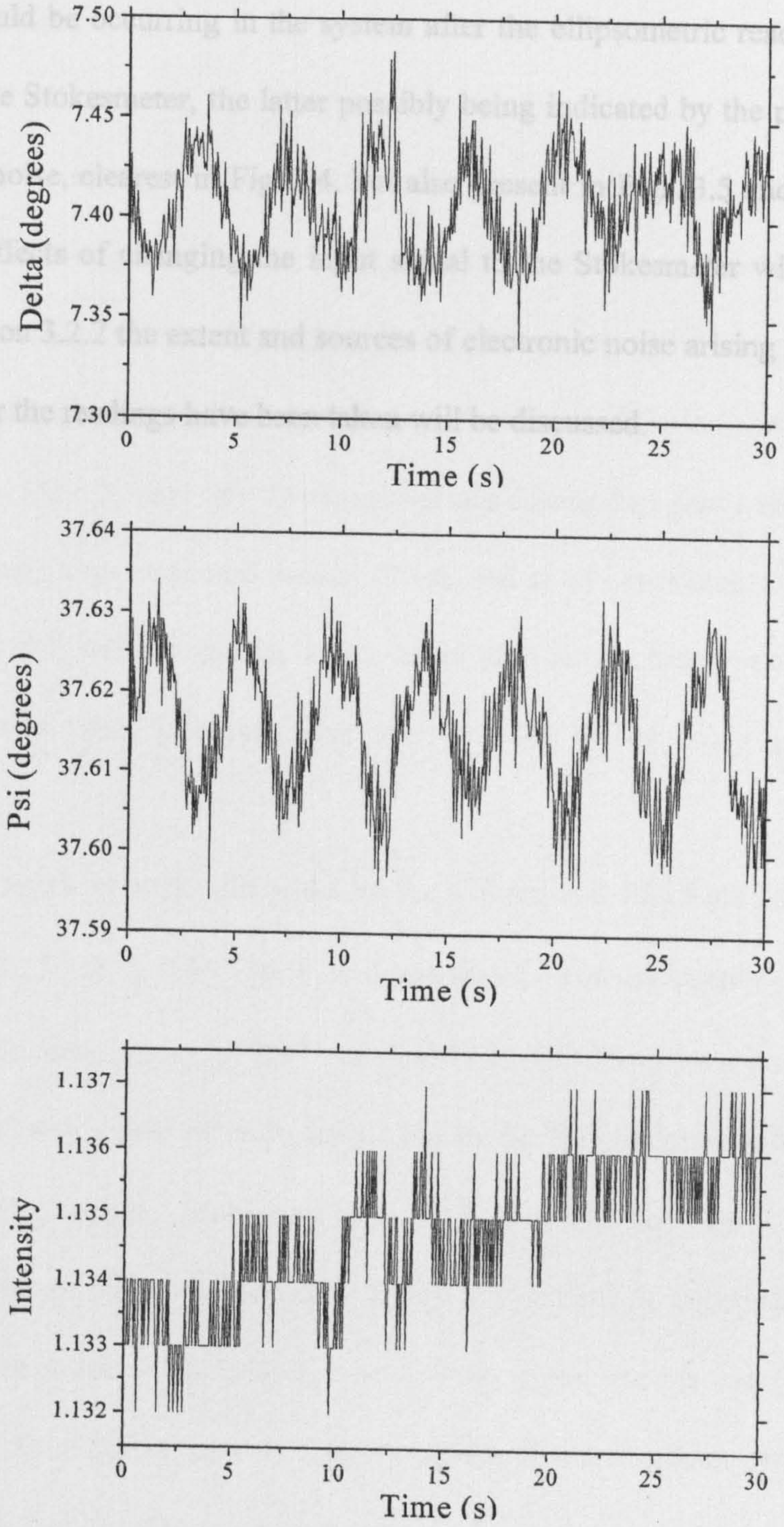

Fig.3.6. The typical noise observed with the air table operating at *ca.* 3 bar and a half inflated motorcycle inner tube underneath the ellipsometer. 24 readings were averaged to give one point every 50 ms

pick up could be occurring in the system after the ellipsometric readings have been taken by the Stokesmeter, the latter possibly being indicated by the presence of high frequency noise, clearest in Fig. 3.4, but also present in Figs. 3.5 and 3.6. In section 3.2.1 the effects of changing the input signal to the Stokesmeter will be described, and in section 3.2.2 the extent and sources of electronic noise arising in the computer system after the readings have been taken will be discussed.

3.2.1 Signal Noise

Four lasers could be employed with the ellipsometric system, three HeNe lasers with wavelengths of 543.5, 594.1, and 632.8 nm, and a diode laser operating at 670 nm. To study whether changing the laser had any effect on the noise level present, data were recorded using each laser in turn, and typical data for each laser are shown in Figs. 3.7(a) - (d). The intensity was adjusted to give a similar reading in each case using a set of neutral density filters, and in all experiments the ellipsometer was set at 180^0, with no sample in the beam path so the beam passed through the neutral density filter, polariser, and then retarder before being incident on the Stokesmeter.

The levels of noise displayed by the 670 nm and 632.8 nm lasers are clearly the lowest: 0.15^0 on Δ, 0.06^0 on Ψ, and less than 1 % on the intensity. The 594.1 nm laser is a little more noisy, *ca.* 0.3^0 variation in Δ, 0.08^0 in Ψ, and just over 0.5 % in intensity, but with a drift of up to 1.6 %; but by far the noisiest data is that from the 543.5 nm laser, with a 1^0 variation in Δ, 0.1^0 in Ψ and just over 1 % in intensity. However, this variation in the noise levels is not entirely unexpected, given the different polarisation of each laser. The 670 nm diode laser is circularly polarised, and the 632.8 nm HeNe laser is linearly polarised but a quarter wavelength plate (QWP) calibrated for 633 nm may be attached to the front of the laser. When the optical axis of the QWP was positioned so that the linearly polarised light from the laser was incident at the correct angle, the emerging beam was circularly polarised. The importance of circular polarisation is that when passed through a polariser the

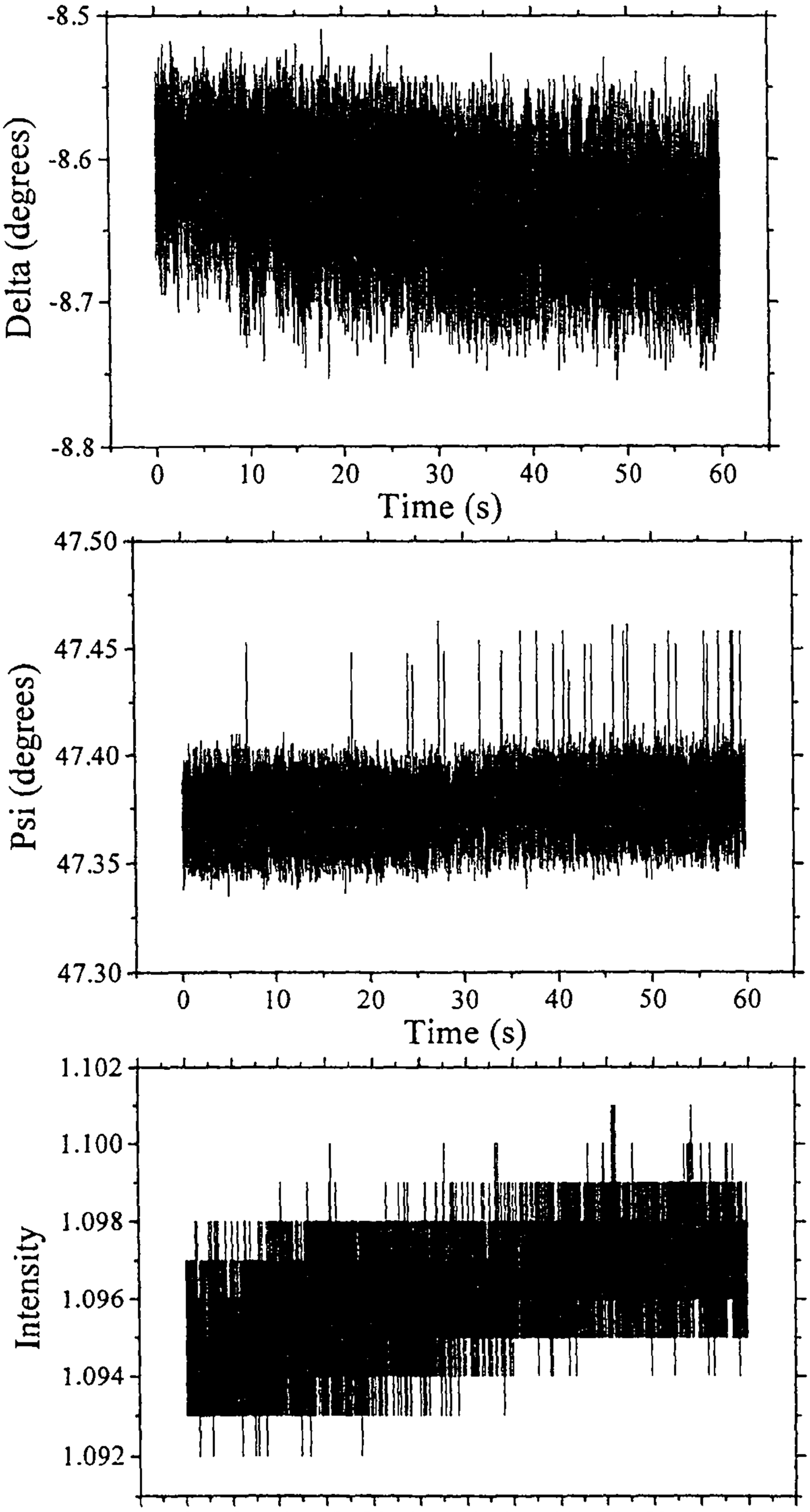

Fig. 3.7(a) Typical data gathered using the 670 nm diode laser, with the ellipsometer set at 180 ^{0} and no sample present: 45 ^{0} linearly polarised light is directly incident on the Stokesmeter, one reading was taken every 5 ms with no averaging of the data.

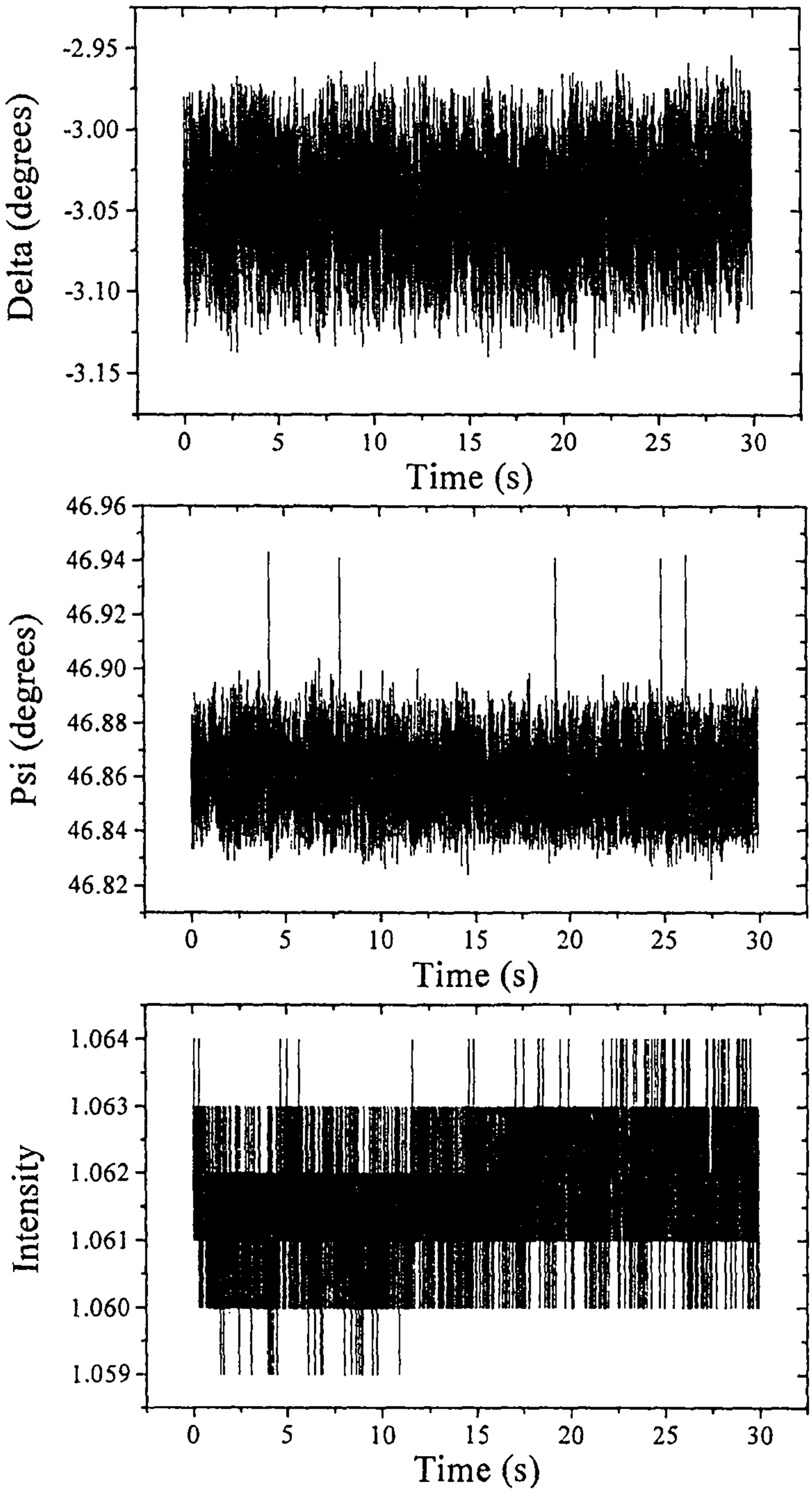

Fig. 3.7(b). Typical data gathered using the 632.8 nm HeNe laser with the 633 nm quarter wave plate. The ellipsometer was set at 180 ^{0} with no sample present: 45 ^{0} linearly polsrised light is directly incident on the Stokesmeter, one reading was taken every 5 ms with no averaging of the data

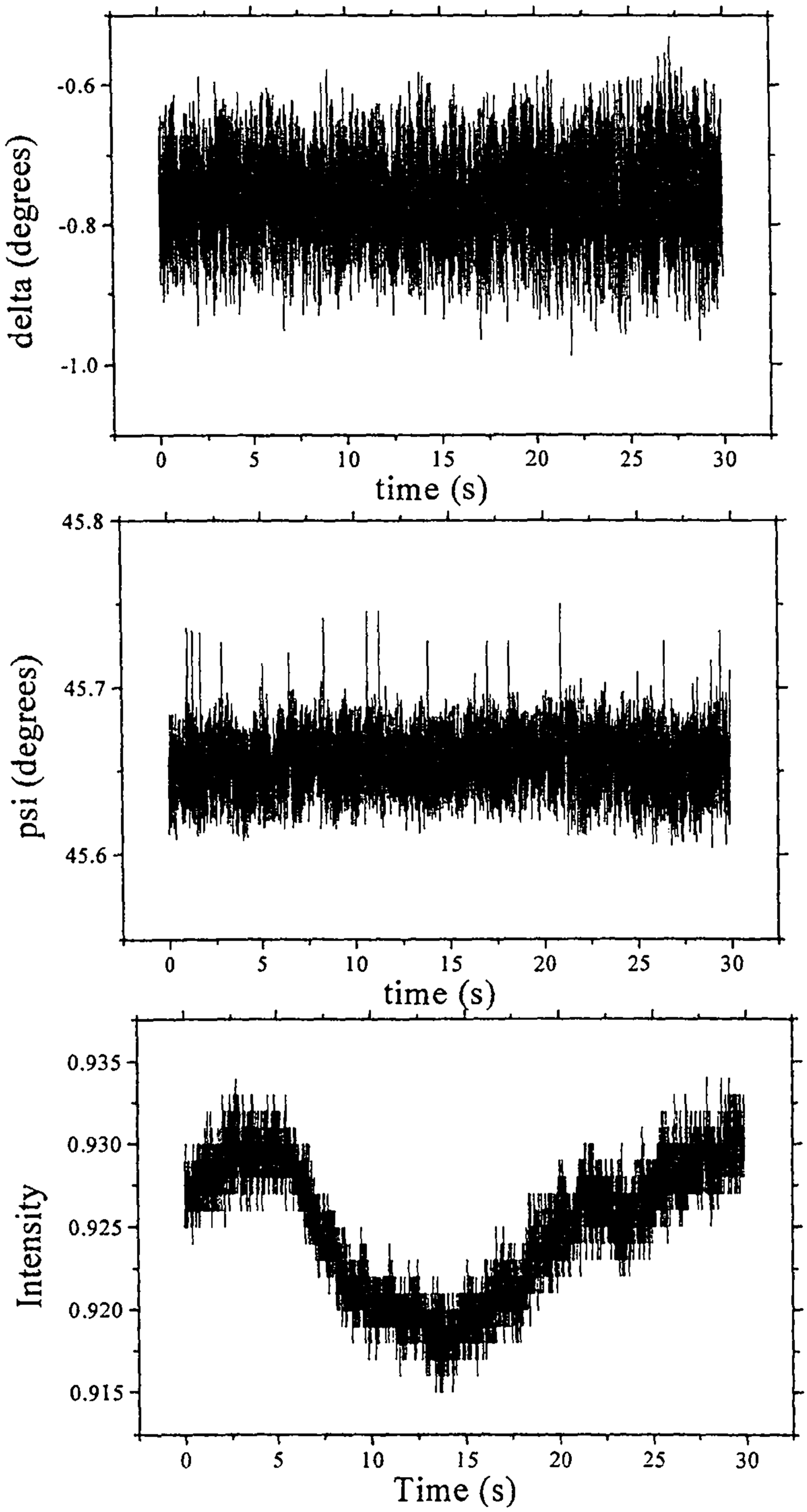

Fig. 3.7(c). Typical data gathered using the 594.1 nm HeNe laser with the 633 nm quarter wave plate. The ellipsometer was set at 180 ^{0} with no sample present: 45 ^{0} linearly polsrised light is directly incident on the Stokesmeter, one reading was taken every 5 ms with no averaging of the data.

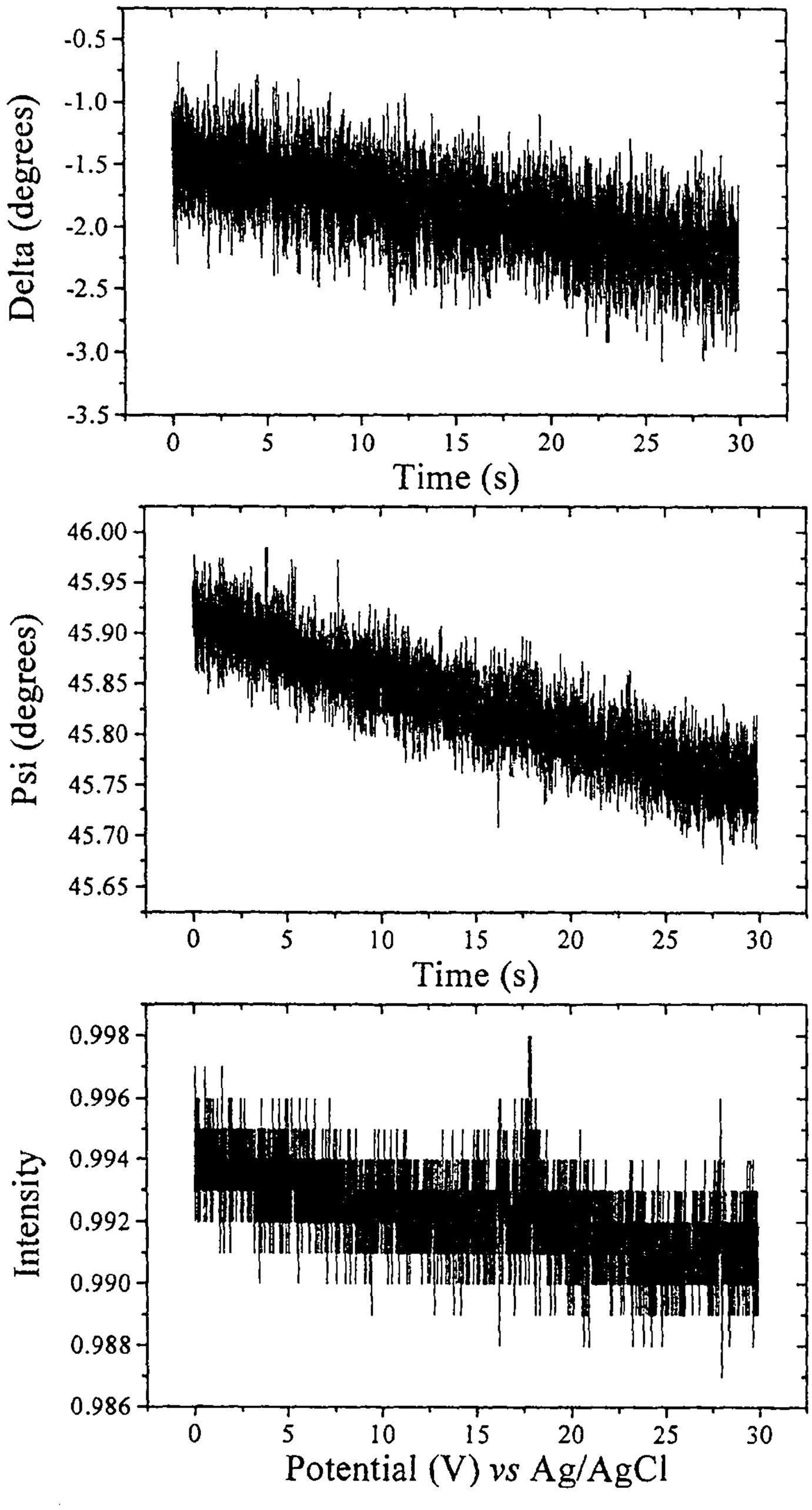

Fig. 3.7(d) Typical data gathered using the 543.5 nm HeNe laser with the 546 nm QWP attached. The ellipsometer was set at 180^0 with no sample present: 45^0 linearly polarised light is directly incident on the Stokesmeter, one reading was taken every 5 ms with no averaging of the data.

emergent beam will be of constant intensity regardless of the orientation of the polariser. The 594.1 and 543.5 nm lasers are randomly polarised, they emit linearly polarised photons but at random angles. If directly incident on the polariser this will lead to a large fluctuation in the intensity of the transmitted beam. Using a QWP, even one calibrated to the correct wavelength will not yield circularly polarised light as the photons have to pass through at a particular angle to the optical axis of the plate; the randomly orientated photons from the 594.1 and 543.5 nm lasers will pass through at random angles, emerging in various states of elliptically polarised light. While the addition of a QWP to produce various elliptical polarisations will reduce the fluctuation in intensity compared to having random linear polarisations incident on the polariser, a significant amount of noise in the intensity recorded is still to be expected (See more detailed discussion of QWP in section 1.2.2) In the case of Fig. 3.7(c) the QWP calibrated to 633 nm was used, and in (d) a QWP calibrated to 546 nm, to reduce the variation in intensity to some extent.

Fig. 3.8 shows data for the 594.1 nm laser without the 633 nm QWP attached, and Figs. 3.9(a) and (b) show data for the 543.5 nm laser with and without the 633 nm QWP respectively. In Fig. 3.8 the noise on the intensity is over 2 %, compared to 0.5 % with the 633 nm QWP, and in the case of the 543.5 nm laser the difference is even more obvious, a 4 % variation in the intensity in Fig. (b), *ca.* 2 % in Fig. 9(a) with the 633 nm QWP, compared to *ca.* 1 % with the 546 QWP in fig. 3.7(d). The Melles Griot catalogue quotes a variation in intensity of *ca.* 0.1 % for all three of the HeNe lasers, which is considerably less than the variation observed even with the 632.8 nm laser and QWP. To act as a check on the intensity

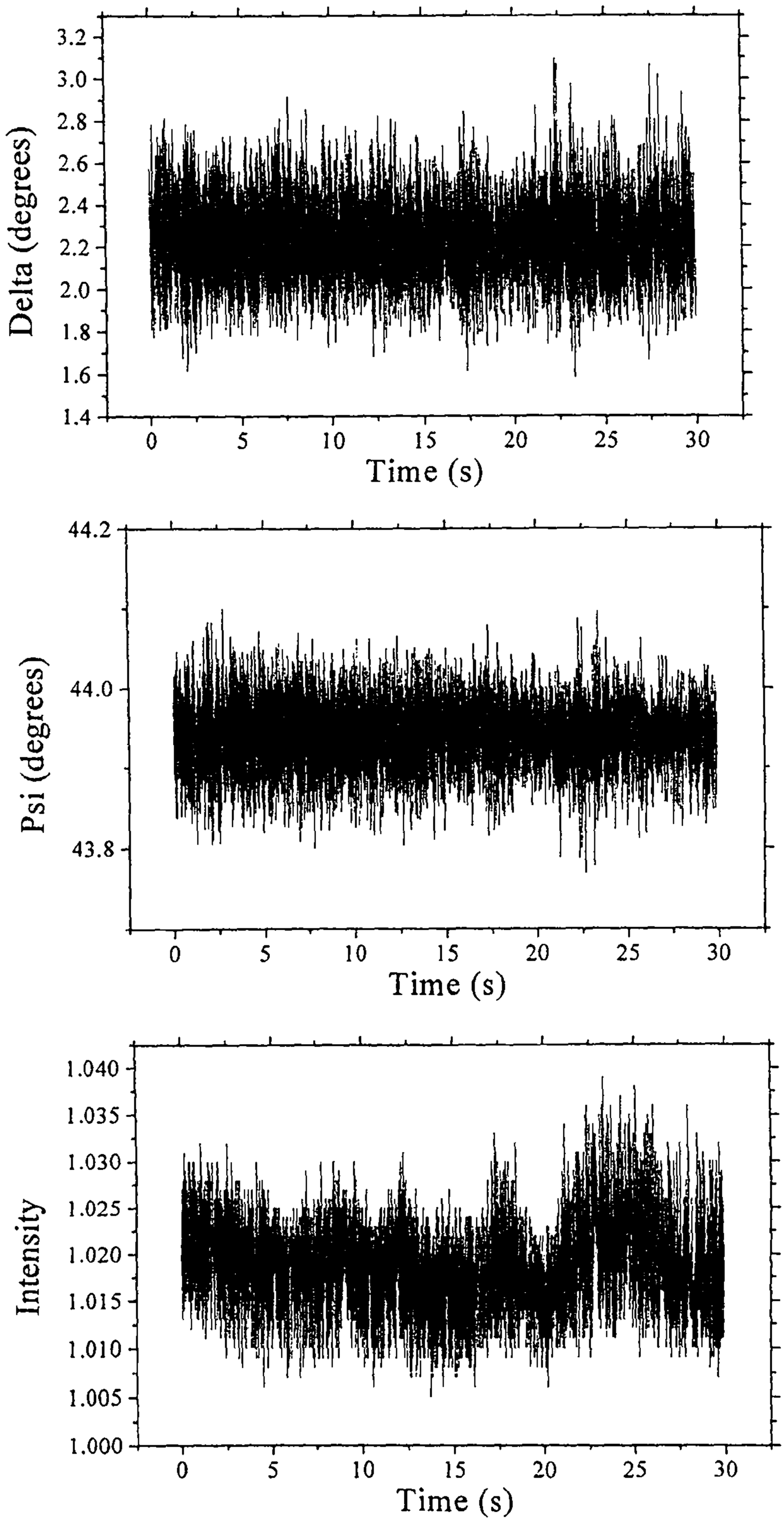

Fig. 3.8. Data gathered with the randomly polarised 594.1 nm HeNe laser *without* the 633 nm QWP. I reading taken every 5 ms, no data averaging.

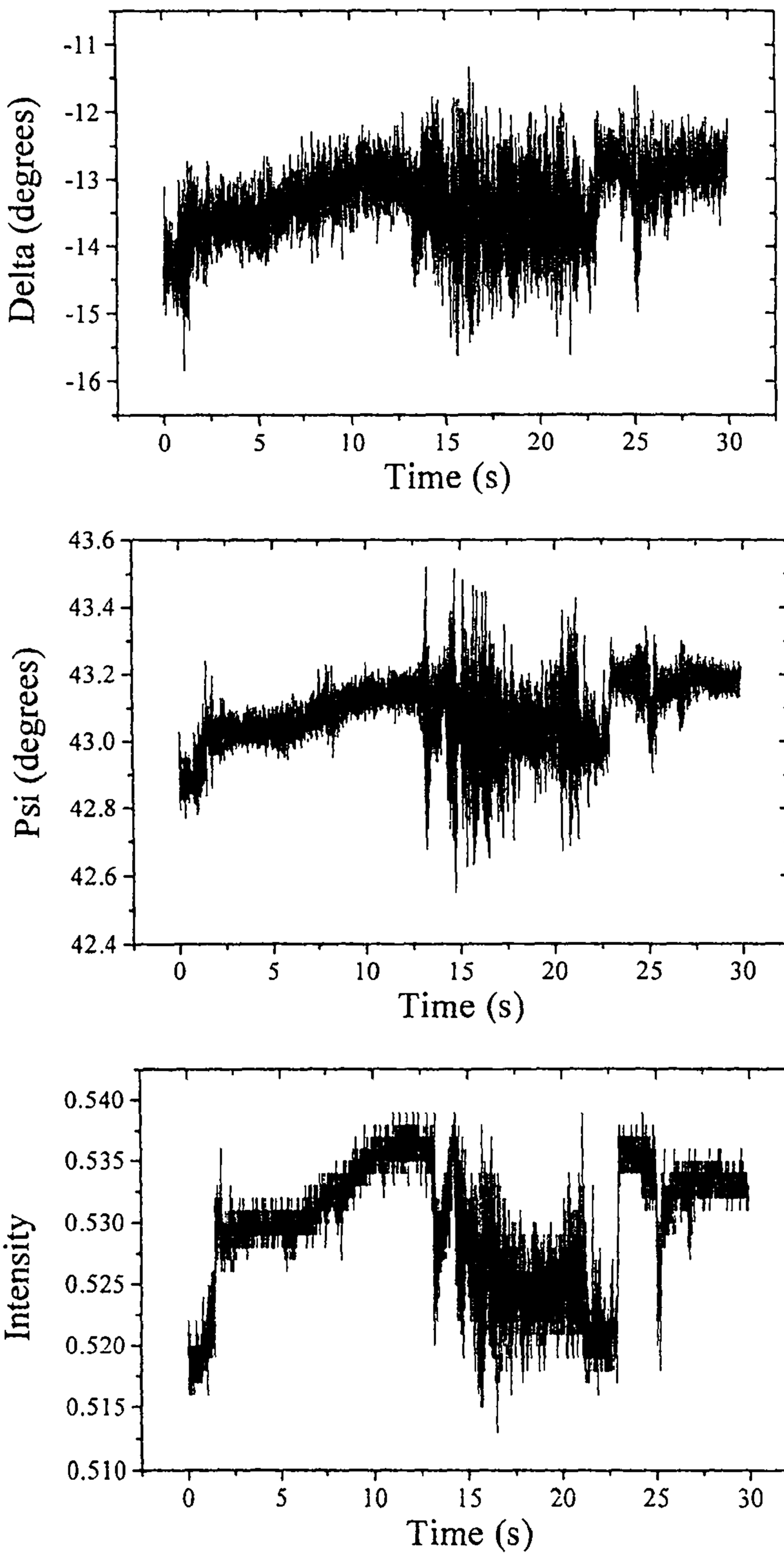

Fig. 3.9(a). Data gathered at 543.5 nm using a QWP calibrated to 633 nm. One reading collected every 5 ms, no signal averaging.

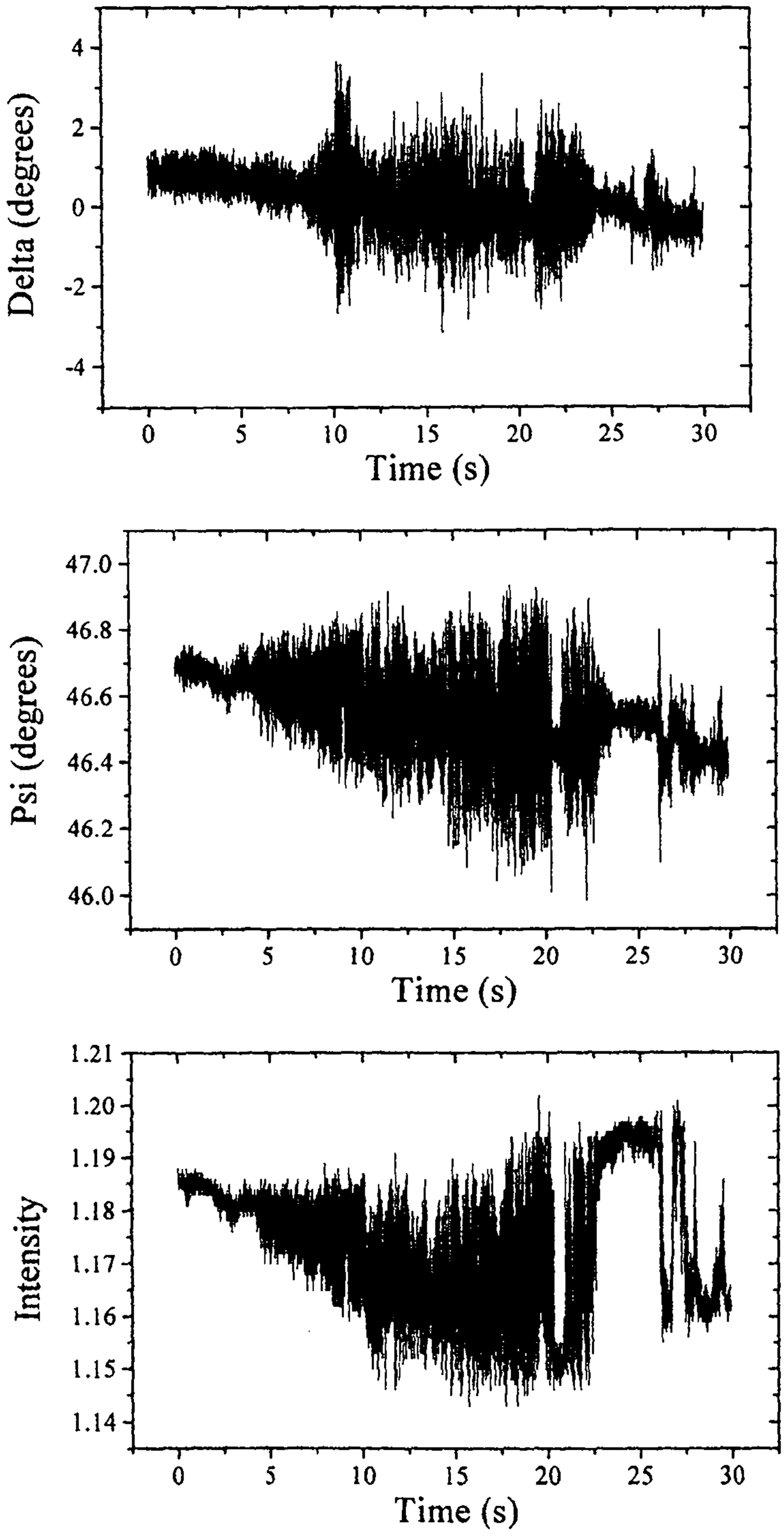

Fig. 3.9(b) Data gathered at 543.5 nm with no QWP used, 1 reading taken every 5 ms, no signal averaging.

fluctuations observed with the Stokesmeter, a photodiode tube was used as a secondary method of measuring the intensity. In the case of all experiments using the photodiode tube the intensity of the laser beam was reduced sufficiently to register on the scale of the photodiode meter using various neutral density filters, the beam then passed through the polariser and retarder to emerge linearly polarised at 45^0, and then passed through a beam expander to produce a beam roughly 1 - 1.5 cm in diameter, as the diode was not designed to measure the beams of a few millimeters diameter as produced by the lasers. The photodiode was connected to a plotter, and the traces recorded on 1 mm^2 graph paper. Fig. 3.10 shows the output from the photodiode with no light incident on it, and Figs.3.11 and 3.12 show traces recorded for the 670 nm and 632.8 nm lasers respectively; the latter with the 633 nm QWP attached. There is up to 1 mV drift during the blank run, and less then 0.1 mV variation on the trace itself, which can be regarded as insignificant compared to the experimental traces, all recorded at 0.1 or 0.2 Vcm^{-1}. In Fig. 3.12, very little change in intensity is observed, the 632.8 nm laser displayed no visible fluctuation in intensity, while the 670 nm laser displayed *ca.* 1 % variation in the main noise (i.e. the short time scale variation on the trace), but up to a 3 % drift over the course of the experiment (*ca.* 9 min). These prolonged drifts in intensity have been observed sporadically with all four lasers, and with both the photodiode and the Stokesmeter. The origin is unknown, but as both detectors display them, it does seem likely that they are a real effect generated by the lasers. One concern was that the age of the lasers could be responsible for a decrease in the consistency in performance. The 632.8 nm laser being the oldest of the four, a new linearly polarised 632.8 nm laser

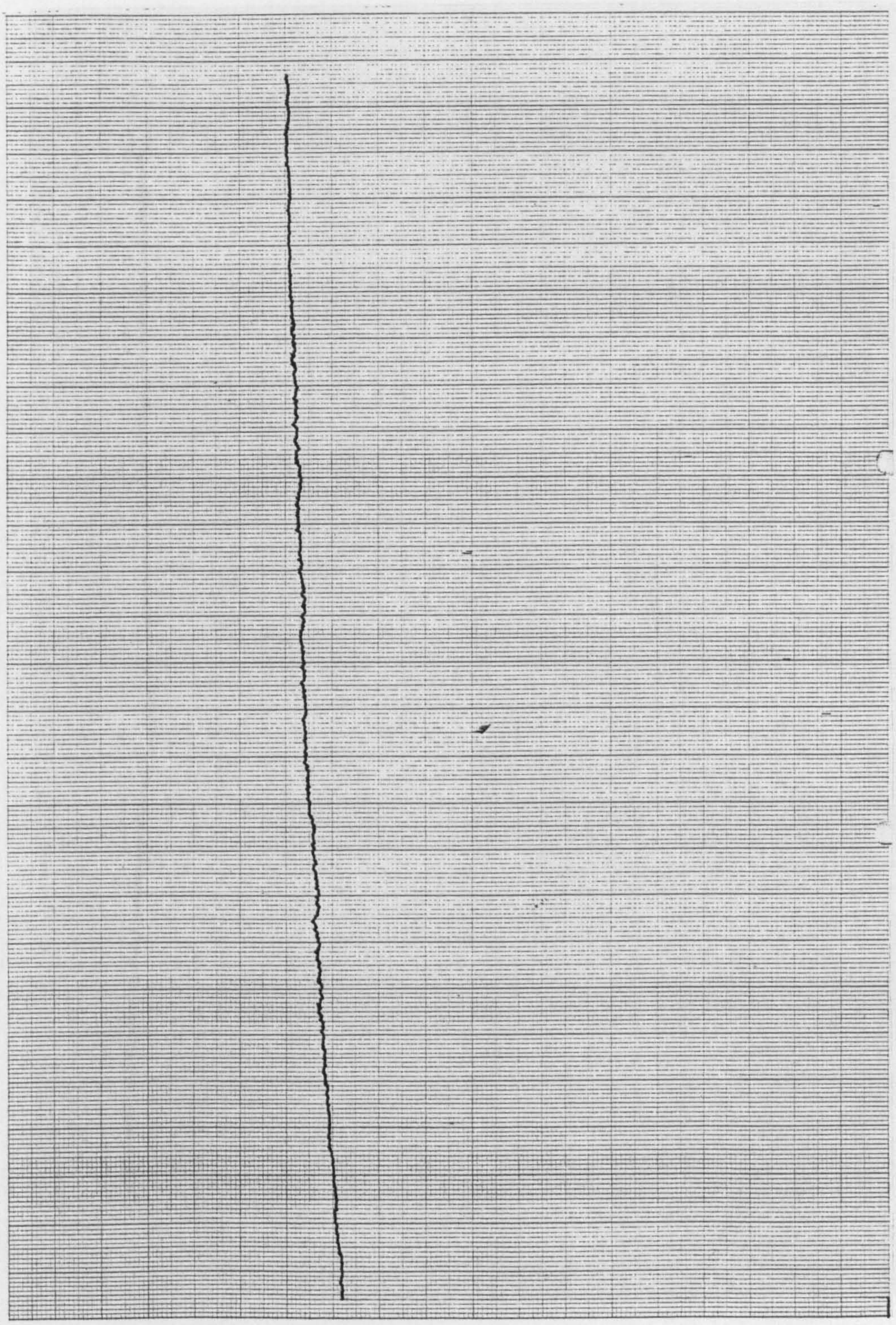

Fig. 3.10 The potential output from the photodiode tube over *ca.* 9 min with no light incident. Each of the smallest squares is 1 mm^2 on the original trace. Scale: X: 20 s cm^{-1}, Y: 1 mV cm^{-1} Zero for the potential axis shown over 4 mm in bottom right hand corner.

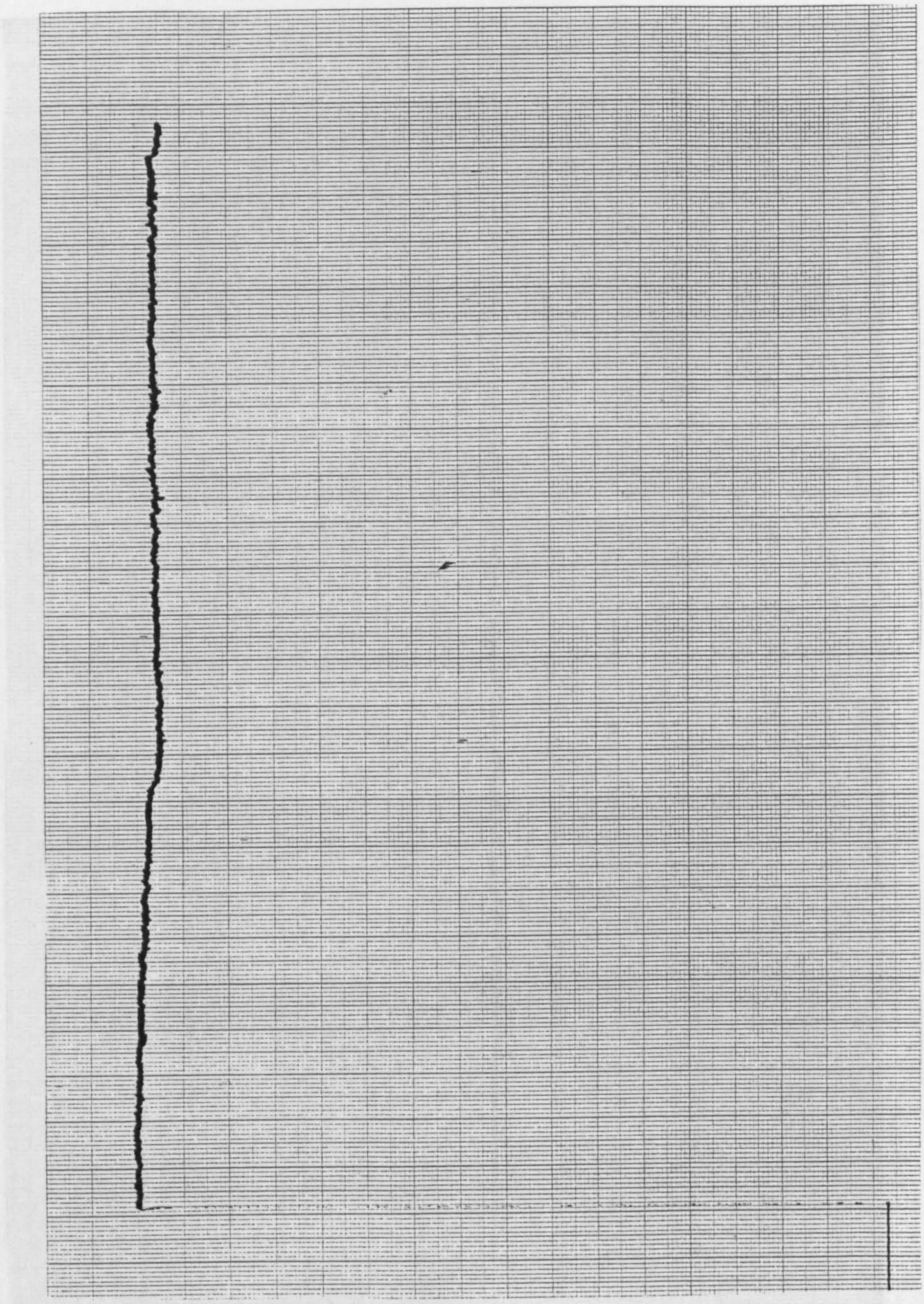

Fig. 3.11. The potential output from the photodiode tube with linearly polarised light generated by the 670 nm laser. Each of the smallest squares is 1 mm^2 on the original trace. Scale: X: 50 s cm^{-1}, Y: 0.2 V cm^{-1}. Zero for the potential axis shown over 20 mm in bottom right hand corner.

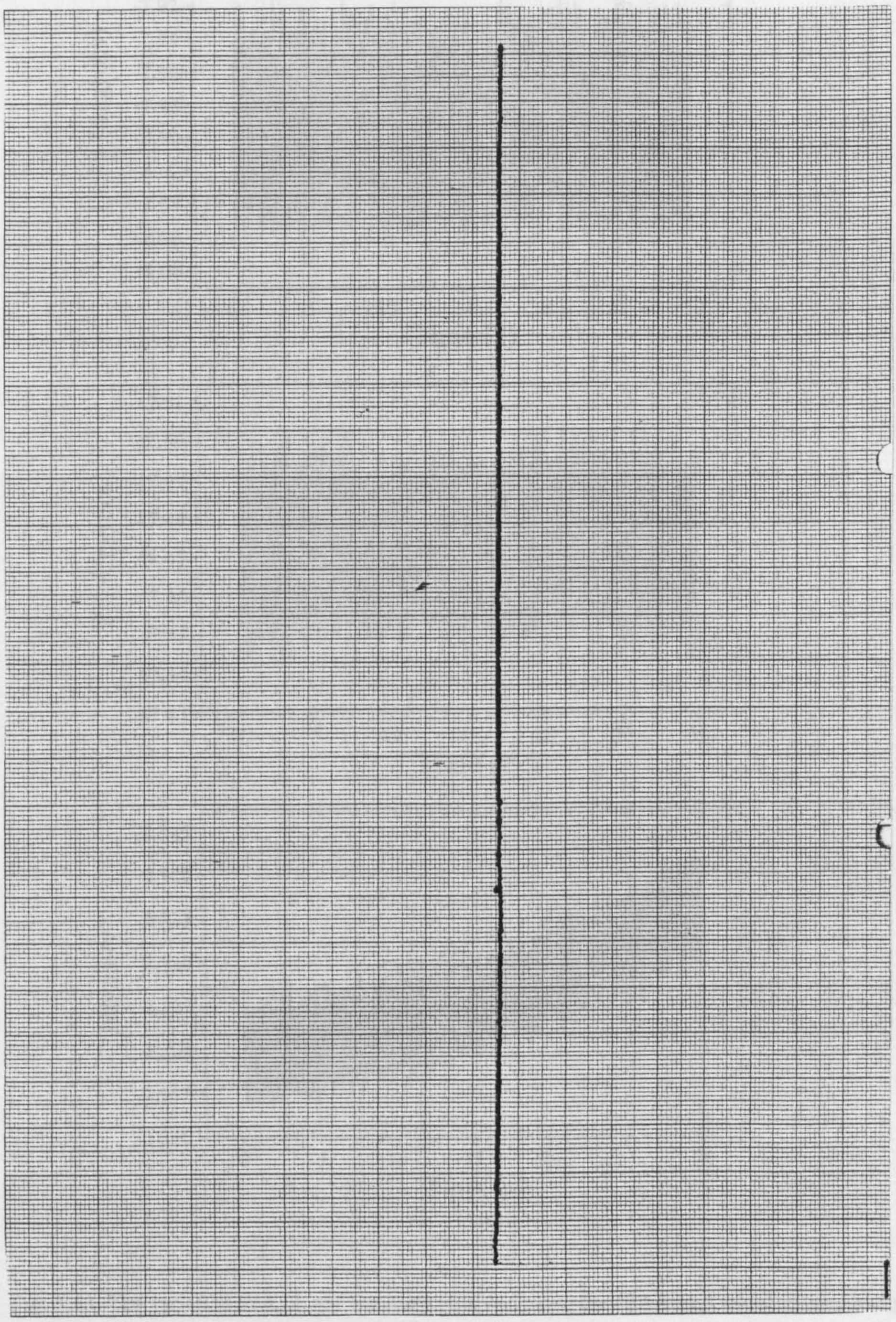

Fig. 3.12. The potential output from the photodiode tube with linearly polarised light generated by the 632.8 nm laser. Each of the smallest squares is 1 mm^2 on the original trace. Scale: X: 50 s cm^{-1}, Y: 0.1 V cm^{-1}. Zero for the potential axis shown over 7 mm in bottom right hand corner

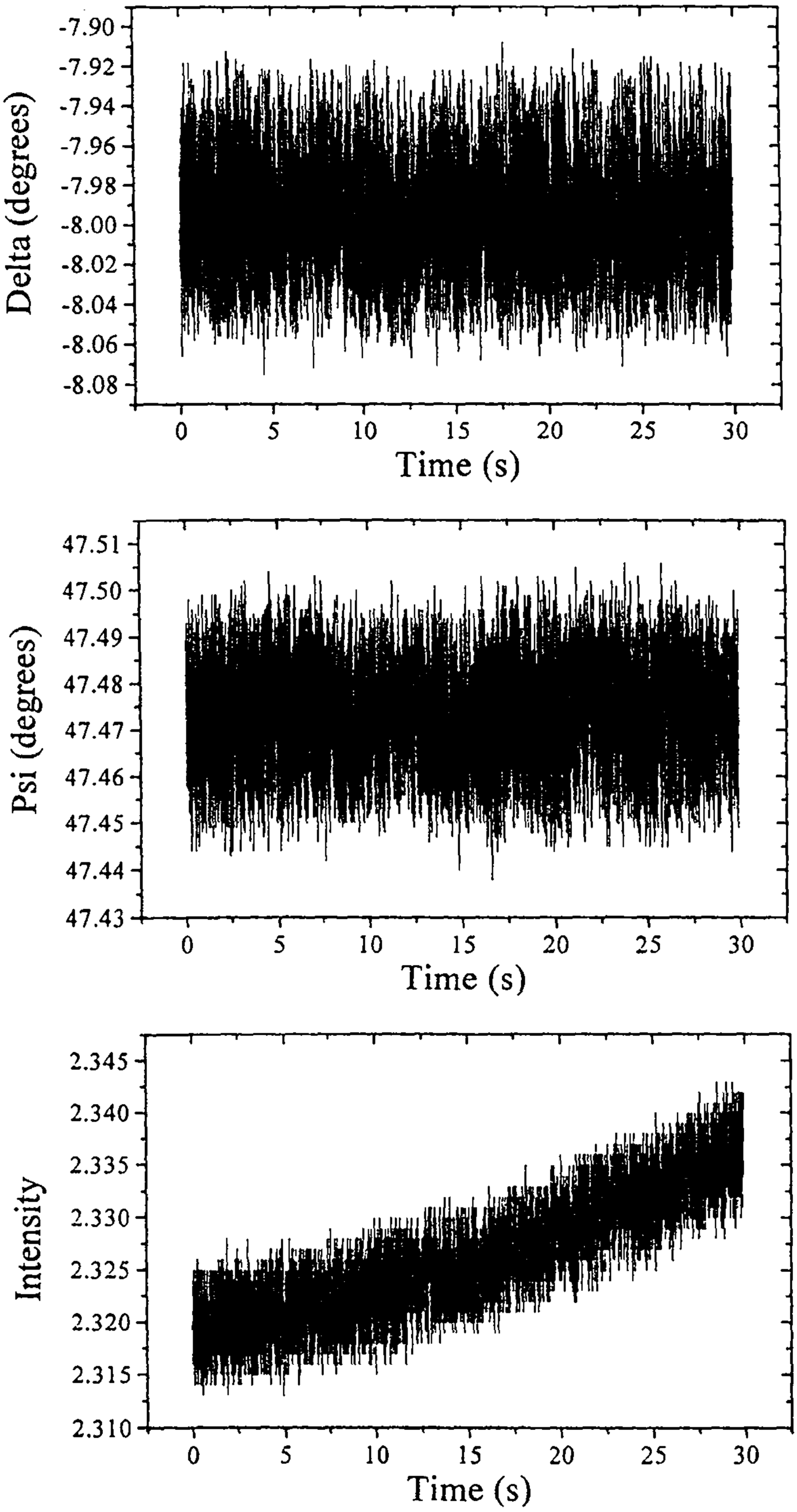

Fig. 3.13. The variation in Δ, Ψ and intensity obtained using the 632.8 nm Uniphase laser and power supply. The beam passed through the 633 nm QWP, polariser and retarder to yield linearly polarised light at 45 ^{0}, which was then directly incident on the Stokesmeter.

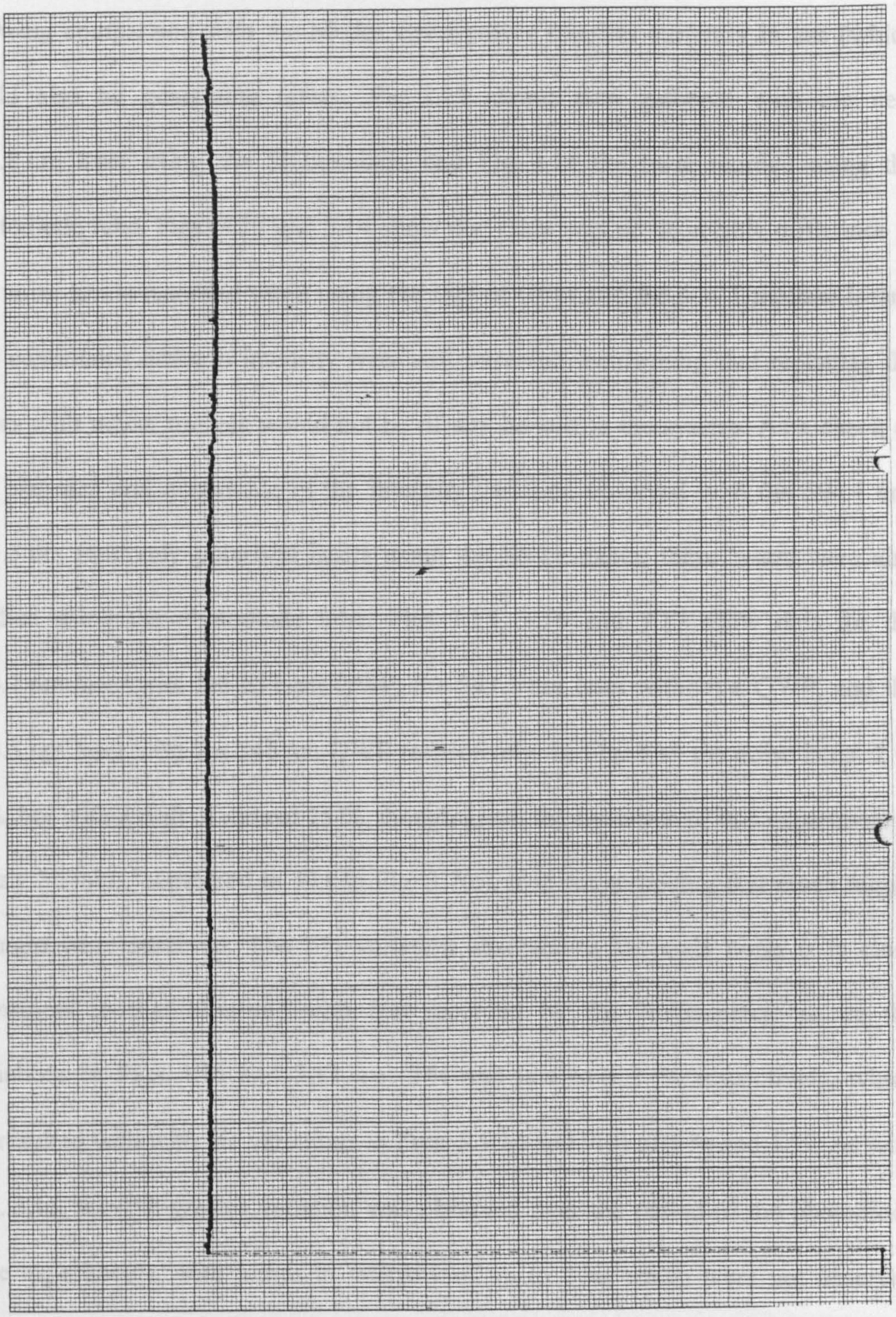

Fig. 3.14. The potential output from the photodiode with the Uniphase 633 nm laser and power supply. Each of the smallest squares is 1 mm^2 on the original trace. Scale: X: 50 s cm^{-1}, Y: 0.1 V cm^{-1}. Zero for the potential axis shown over 5 mm in bottom right hand corner

was obtained on loan from Uniphase, which also came with a new power supply, allowing comparison with the Melles Griot power supplies currently in use (which could also be generating noise). Fig. 3.13 shows data gathered with the new 632.8 nm laser using the Stokesmeter, and Fig. 3.14 the trace reorded using the photodiode tube. Figs. 3.13 and 3.14 show that there was no detectable difference in the noise levels recorded when using the Melles Griot and the new Uniphase lasers, and continuous drifts in intensity were still observed, confirming that replacing the lasers with newer models would not be of any benefit to the system. As a check of the presence and magnitude of the intensity variation observed with the 594.1 and 543.5 nm randomly polarised lasers using the Stokesmeter, these lasers were also studied using the photodiode tube. Figs. 3.15, 3.16 and 3.17 show data for the 594.1 nm laser with the 633 nm QWP, the 543.5 nm laser without a QWP, and the 543.5 nm laser with the 546 nm QWP respectively. In Fig. 3.15 the noise is *ca.* 2 to 3 %, but with a drift of almost 25 %, though given the timescale of this experiment is nearly 30 mins, compared to 30 s in Fig. 3.7(c), it is not surprising that much bigger changes were observed. The 2 % variation observed as the main noise is in close agreement to that observed with that recorded by the Stokesmeter, as are the variations in Figs. 3.16 and 3.17, *ca.* 5 % and just over 1 % respectively, which correspond well with the variations in Figs. 3.9(b) and 7(d) of 4 % and 1 %. As with Fig. 3.15, a much greater variation was observed over the period of the photodiode tube experiments, with jumps in intensity of up to 7 %, which were not observed during the much shorter timescale Stokesmeter experiments. Figs. 3.16 and 3.17 also show the introduction of the QWP between the laser and polariser yields a

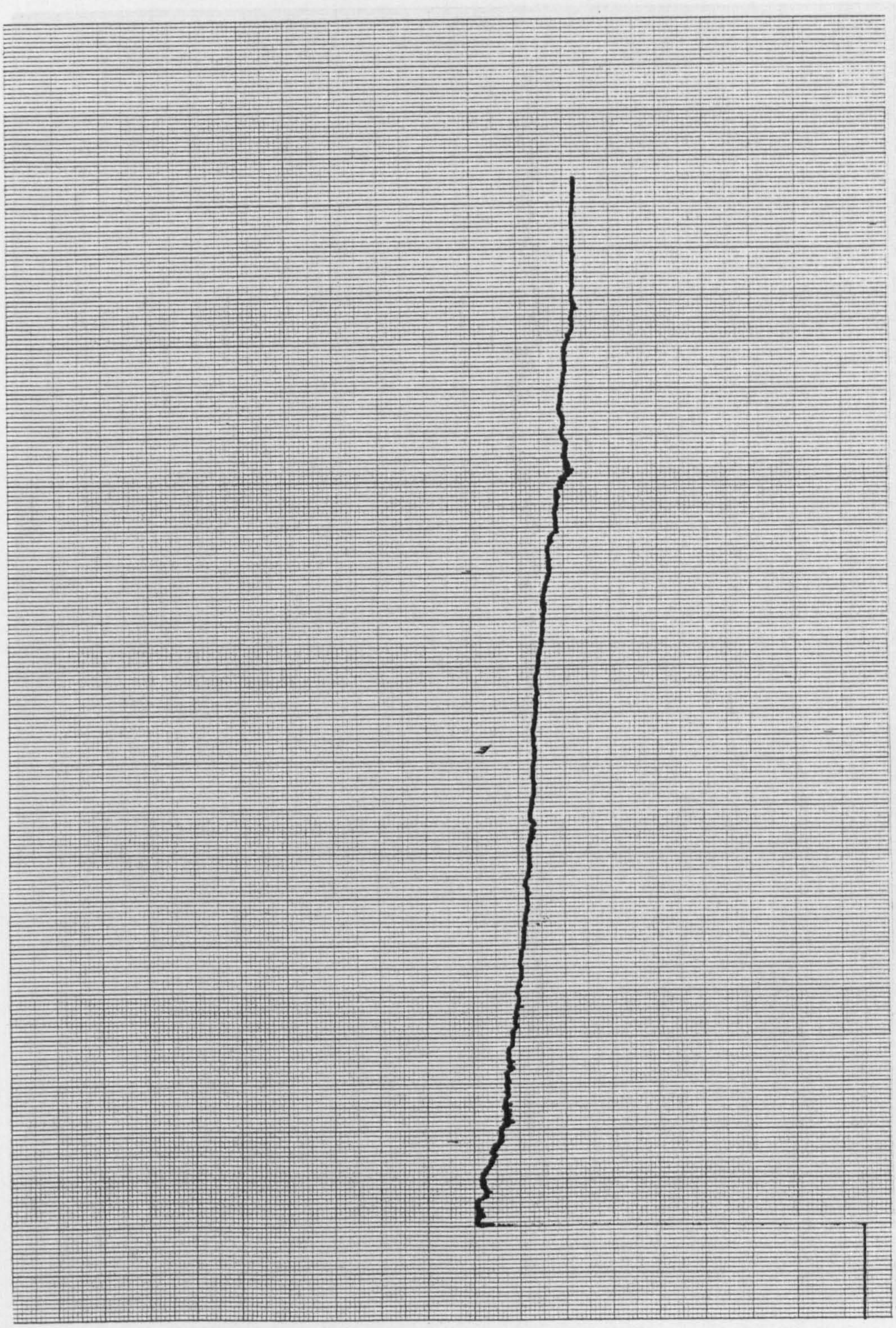

Fig. 3.15. The potential output from the photodiode with the 594.1 nm laser with the 633 nm QWP. Each of the smallest squares is 1 mm^2 on the original trace. Scale: X: 50 s cm^{-1}, Y: 0.2 V cm^{-1}. Zero for the potential axis shown over 20 mm in bottom right hand corner

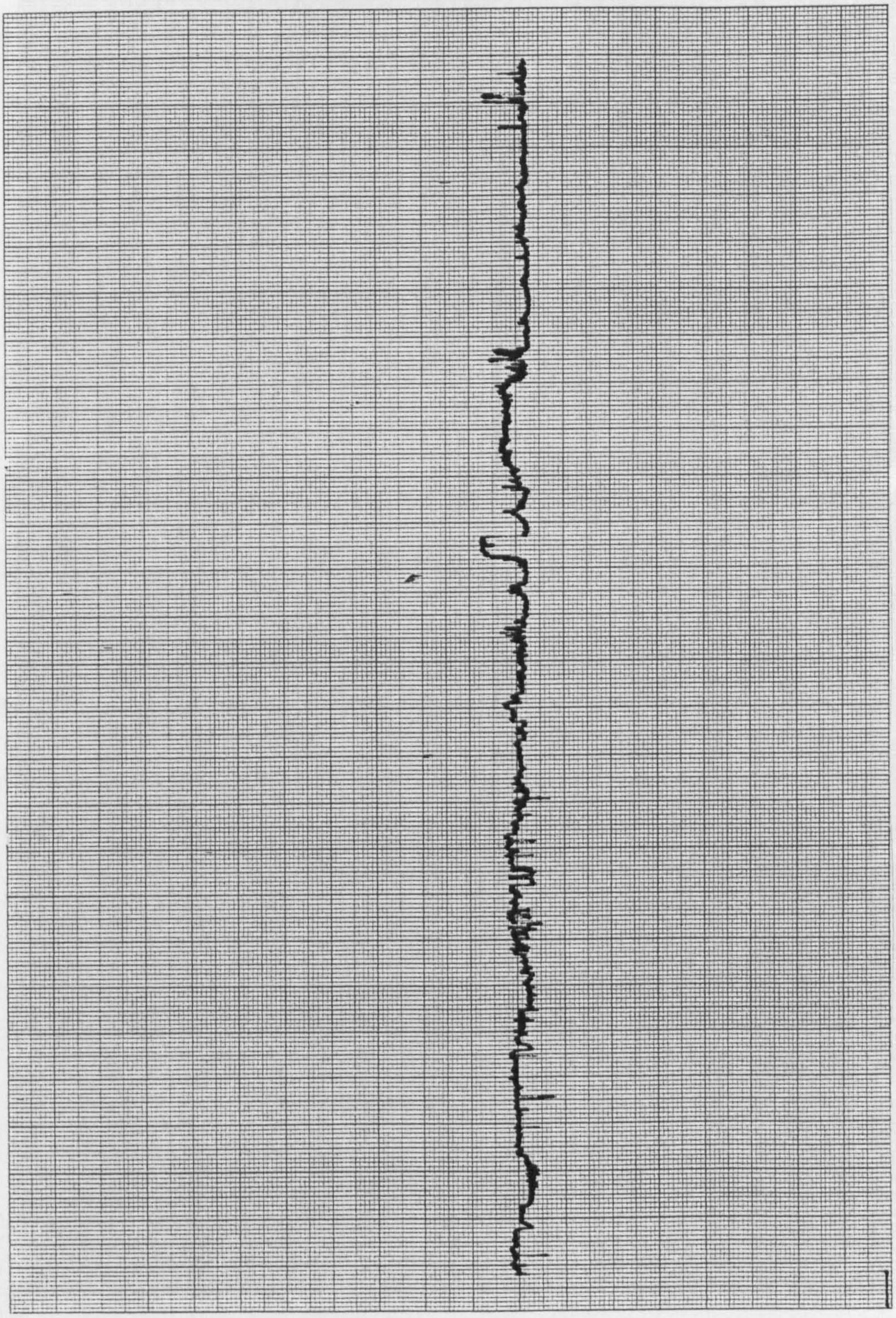

Fig. 3.16. The potential output from the photodiode with the 543.5 nm laser with no QWP. Each of the smallest squares is 1 mm^2 on the original trace. Scale: X: 50 s cm^{-1}, Y: 0.05 V cm^{-1}. Zero for the potential axis shown over 8 mm in bottom right hand corner.

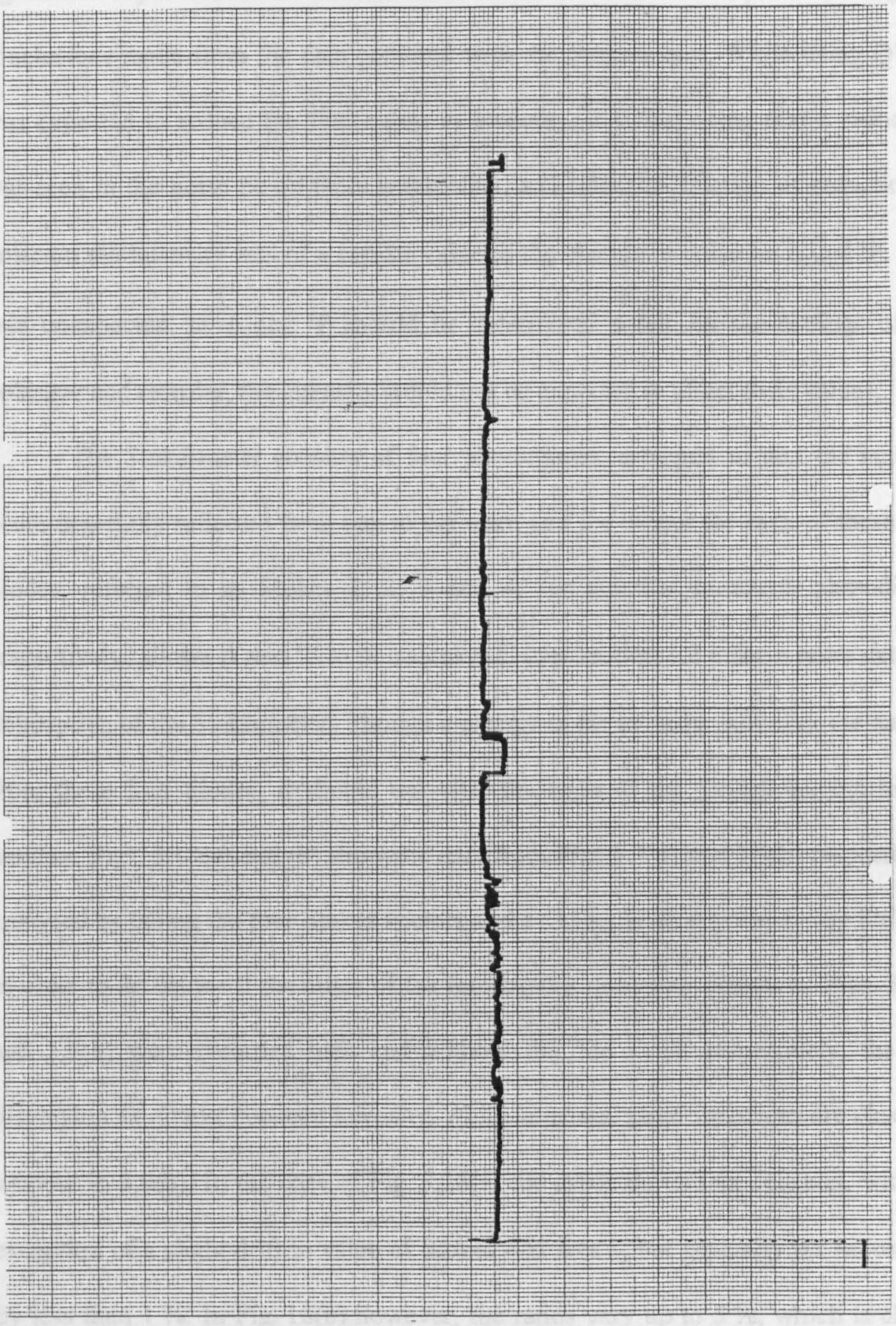

Fig. 3.17. The potential output from the photodiode with the 543.5 nm laser with the 546 nm QWP. Each of the smallest squares is 1 mm^2 on the original trace. Scale: X: 50 s cm^{-1}, Y: 0.2 V cm^{-1}. Zero for the potential axis shown over 6 mm in bottom right hand corner.

significant improvement in the short term variation of the intensity, confirming the conclusions made from the data gathered with the Stokesmeter. While using QWPs was expected to reduce the fluctuation in intensity, it is surprising that a reduction was seen in the noise on all three parameters, and often the fraction of reduction in noise on the intensity was of a similar value to the change in noise on Δ and Ψ. This was unexpected, as Δ and Ψ should be determined solely by the settings of the polariser and retarder, the intensity would not be expected to affect their values.

The Stokesmeter consists of four photodiodes, arranged so that the incident beam is serially reflected from one to the next, and the output for each of these four diodes, referred to as Stokes 1, 2, 3 and 4, for the first to fourth photodiodes respectively, allows Δ and Ψ to be calculated. (see section 1.2.4 for a more detailed description of the Stokesmeter) Though a change in the intensity will alter the outputs from these four diodes, it should not alter the *ratio* of the Stokes vectors to one another. Figs. 3.18(a) and (b) show the data from Figs.3.7(d) and 3.9(b) respectively, analysed by taking the four Stokes vectors and dividing Stokes 2, 3 and 4 by Stokes 1 in order to determine if the ratios of the four signals do remain constant. Figs. 3.7(d) and 3.9(b) were recorded with and without the 546 QWP respectively, the first displaying an almost constant intensity, while large and rapid variations are observed without in 3.9(b). In the case of Fig. 3.18(a) the ratios do remain constant, with the exception of a slight drift in value of Stokes 4/Stokes 1, but generally the ratios vary by less than 1 %. In Fig. 18(b) however, the ratios vary up to 5 %, which is clearly resulting in the noise observed on Δ and Ψ. It would seem the fluctuation of the incident intensity is directly causing this effect given the clear

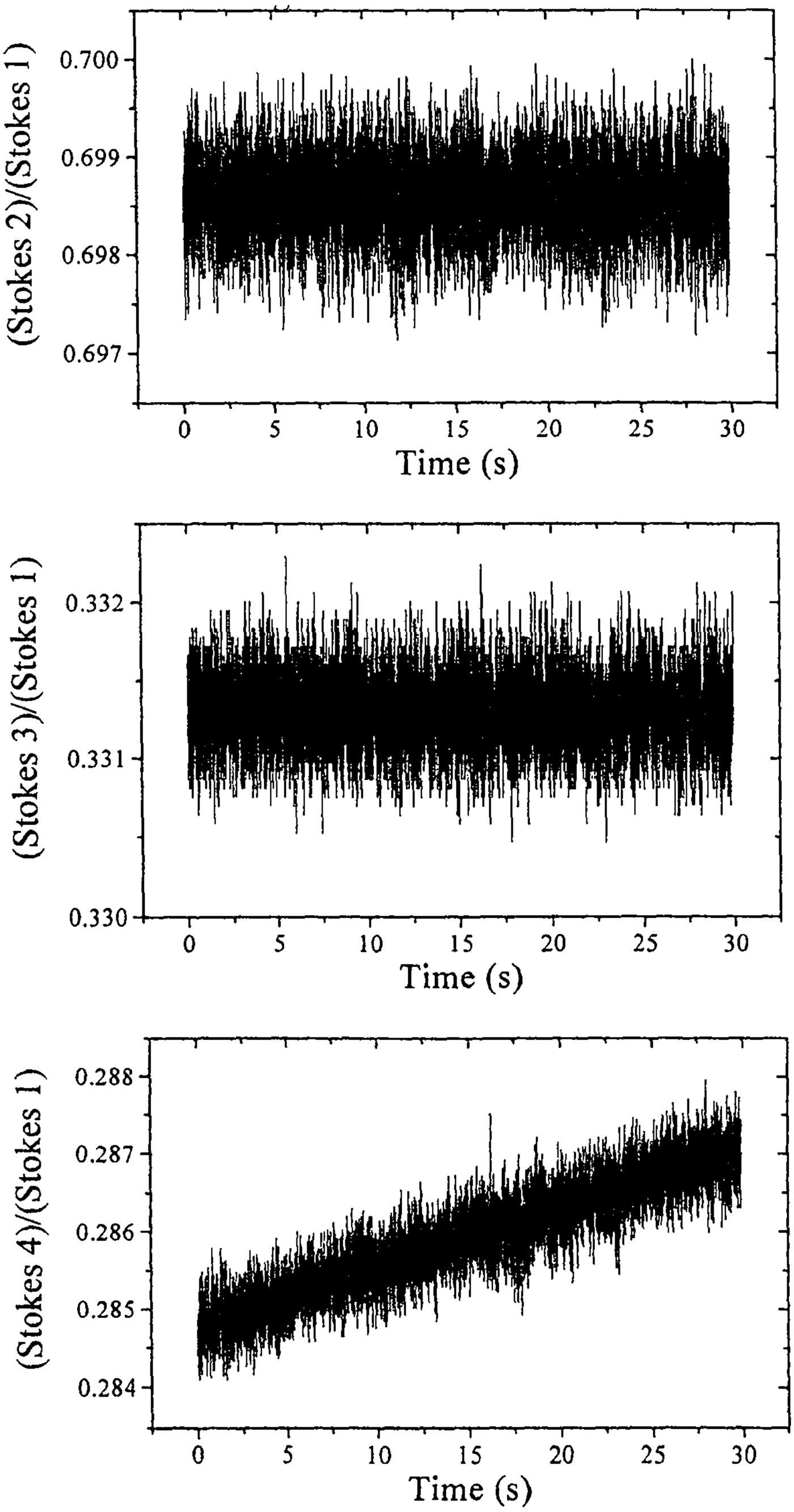

Fig. 3.18(a). The ratios of Stokes 2, 3, and 4 to Stokes1 for the data in Fig. 3.7(d), collected at 543.5 nm using a QWP calibrated for 546 nm

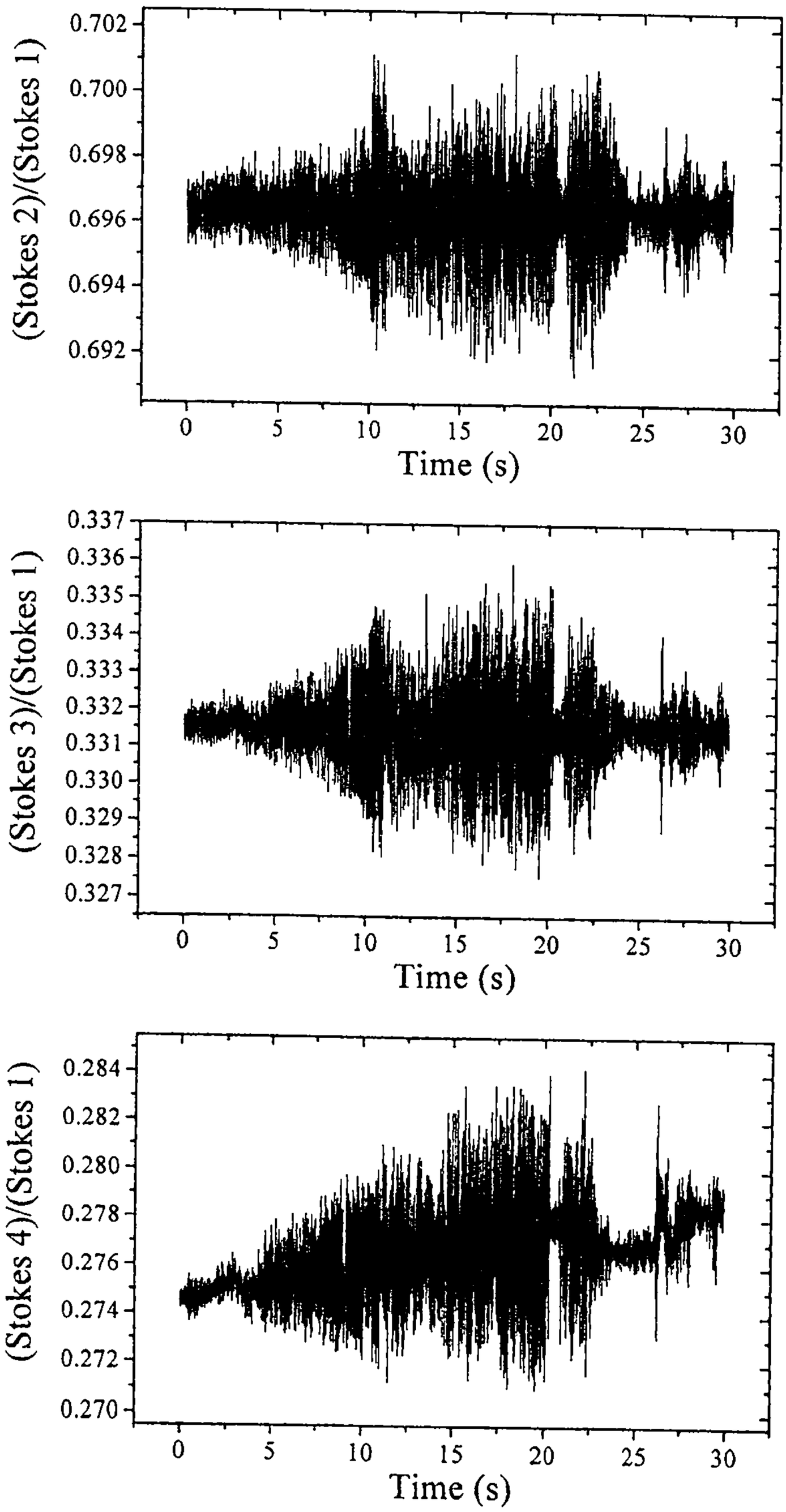

Fig. 3.18(b). The ratios of Stokes 2, 3, and 4 to Stokes 1 for the data presented in Fig. 3.9(b), gathered at 543.5 nm without a QWP.

difference between Figs. 3.18(a) and (b), as this is the only difference between the two experiments.

The effect of intensity fluctuations on the values of Δ and Ψ recorded can be understood by considering the experimental setup and the manner in which the Stokes outputs are read. While it would be preferable to have all four inputs read simultaneously, this would require more hardware and expense, so not envisioning any problems with a very short time delay between each Stokes output being read, the system was instead designed to read the outputs sequentially. In the normal data collection mode the time elapsed between each Stokes reading is just under 1 ms, all four Stokes readings being read within a 2.9 ms period. The CW lasers used which are randomly polarised will generate a beam incident on the Stokesmeter of constantly varying intensity, so by the time Stokes 2 is read the intensity incident on it is different from the incident intensity *ca.* 1 ms before when Stokes 1 was recorded, and so on for each of the Stokes readings, resulting in the fluctuating ratios in Fig 18(b), and clearly the degree of fluctuation over a *ca.* 3 ms period is sufficient to introduce the levels of noise displayed in Fig. 9(b).The obvious and easy solution, though expensive, would be to replace the randomly polarised lasers with ones either circularly polarised, or linearly polarised with a suitably calibrated QWP. Also, it is planned to replace the Oxsys system which collects the electrochemical and ellipsometric data with a customised PC, in which, if at all possible, the ability for the simultaneous reading of all four Stokes inputs will be included.

3.2.2 Electronic Noise

Examination of the shielding around the Stokesmeter revealed some of the connections exhibited little or no conductivity. Leads are exposed outside the Stokesmeter casing between each of the four diodes, and from the fifth quadrant diode to the alignment computer. The earthed foil shielding around each of these sections was replaced, and the separate sections connected with copper wire, giving a resistance from the most remote shielded section to the earth of the main plug of less than 2 Ω. This had no detectable effect on the noise levels recorded, and short of placing the entire ellipsometer in a Faraday cage it is difficult to see how the system could be better shielded, and other possible sources of noise were considered.

One very noticeable effect which could not be in any way due to the light sources is the difference in noise between measurements taken with the normal data collection program, which has a maximum sampling rate of 1 reading every 5 ms, and those taken with the program written for transient measurements (one reading every 325 μs). Frequently data collected by the two programs have the same basic level of noise, but repeated spiking is seen using the transient program, which is not present using the normal data collection procedure, even at the maximum sampling rate with no signal averaging. Figs. 3.19 and 3.20 below show data collected at 594.1 nm using the normal and transient data collection programs respectively. Using the normal program for data collection, the noise on Δ, Ψ and the intensity was 0.4^{0}, 0.15^{0}, and 1.1 % respectively, compared to the main noise recorded using the transient program of 0.5^{0}, 0.2^{0} and 1.1 %. However, spikes of up to 2^{0}, 0.6^{0} and

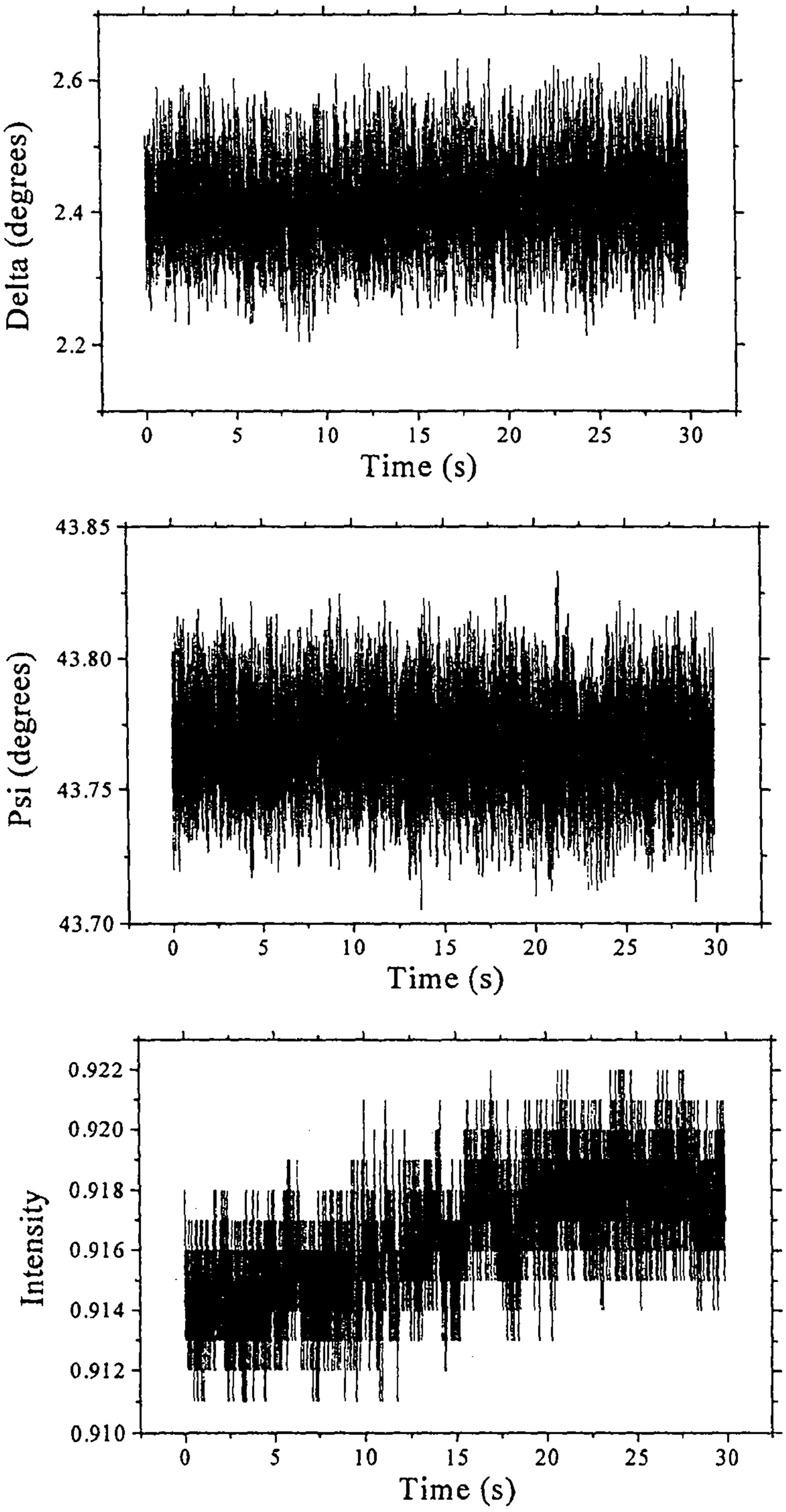

Fig. 3.19 The variation in Δ, Ψ and intensity, recorded at 594.1 nm with the 633 nm QWP, and using the normal data collection program. One reading was taken every 5 ms, with no averaging of data points.

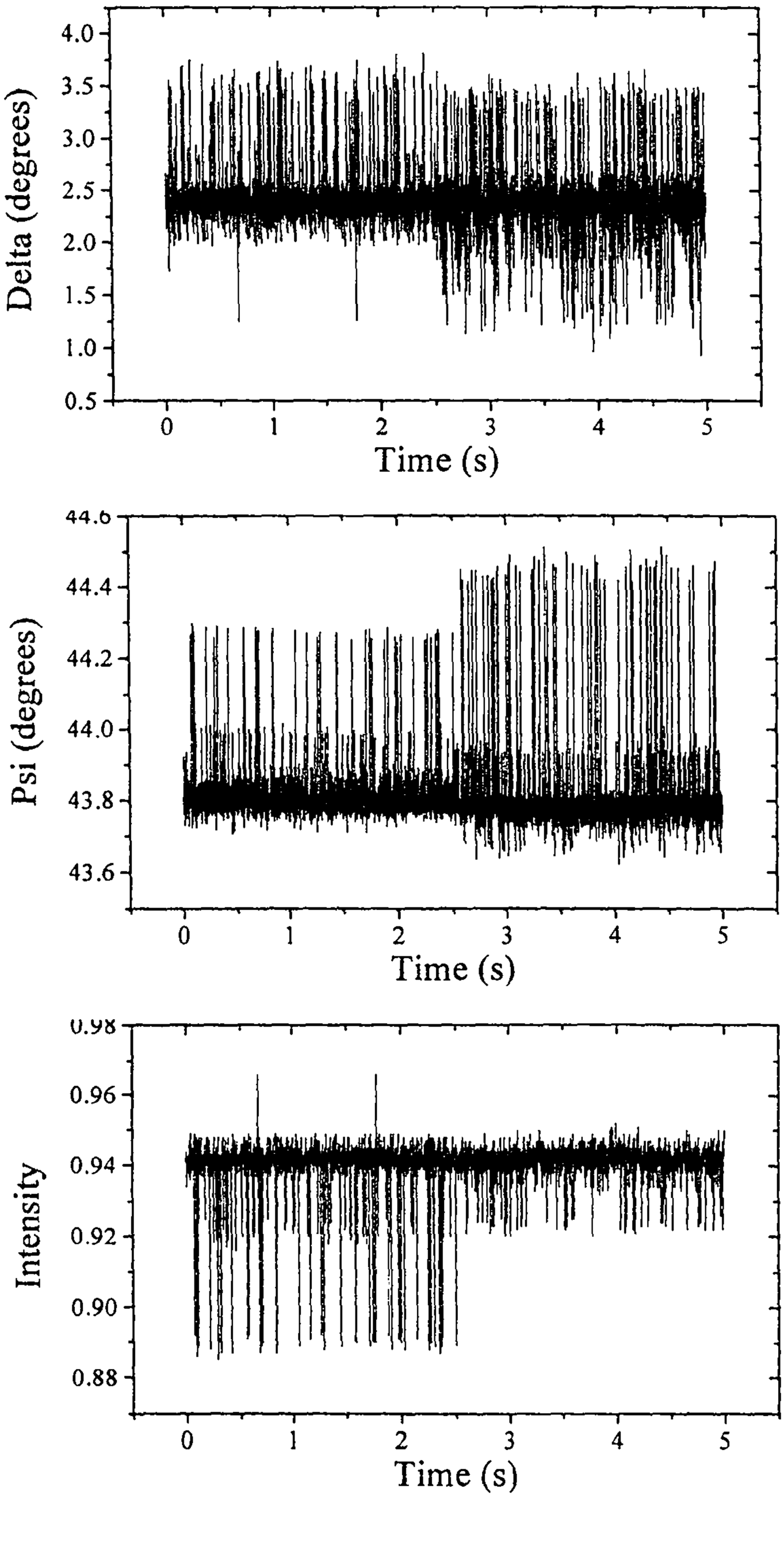

Fig. 3.20 The variation in Δ, Ψ and intensity, measured at 594.1 nm with the 633 nm QWP, using the transient data collection program. One reading was taken every 325 μs, with no averaging of data points.

over 6 % are observed for Δ, Ψ and the intensity respectively, during the transient measurements. It is noticeable that there is a clear change in the magnitude of the spikes half way through the program, this was frequently, though not always, observed with the transient program, suggesting there may be a problem with the program itself and/or the manner in which the data is collected and stored. Another surprising result arose from the investigation of the shielding of the four coax cables which carry the four Stokesmeter readings to the computer. When connecting up the outer shielding of the coax cable and the central signal carrying wire to an oscilloscope to investigate any electronic pick up it was found quite clearly and reproducibly that the extent of the noise observed on the oscilloscope was dependent on the screen displayed on the computer monitor, in particular a large pattern of some 15 mV, which appeared to beat with a period of 1 to 2 s, was observed when the screen displayed the latest outputs from the Stokes meter in real time. This noise was not observed when the Atari computer displayed any other screen, and given the transient measurements were gathered with this screen displayed suggests that the spikes may be due to pickup, present only when the components necessary to display the Stokesmeter outputs in real time are being used. This supports the suggestion that the difference in the noise observed using the two data collection programs originates from the computer itself.

To investigate whether noise is being injected by the system after detection by the Stokesmeter, a dummy connector was used as an input into the computer. The electrochemical leads were connected to a dummy cell, consisting of two 1 kΩ resistors connected in series, while a connector with the outer shield and inner wire shorted to give a 0 V input replaced each stokes input in turn with the other three

connected as usual, to see how cleanly the computer could read it. In Fig. 3.21(a) - (d) below the results for Stokes 1 to 4 are shown as each was connected to the 0 V input and data collected using the normal program. The inputs vary by up to 8 mV. There is clearly a great deal of digitisation in the data, indicating the computer is working at the limit of its resolution. Fig. 3.22 shows the Stokes outputs for the data shown in Fig 3.7(b) above, which can be seen to vary by a similar amount to the data collected with the shorted input. Fig. 3.7(b) shows noise on Δ, Ψ and intensity of *ca.*0.15 ^{0}, 0.04 ^{0}, and 0.5 % respectively, and these clearly represent the resolution limits possible with the current experimental setup. Each of the Stokes inputs was also monitored with the shorted input while collecting data with the transient program, the data for which is shown if Fig. 3.23. All four inputs when connected to the 0 V input, displayed roughly twice the variation when data is collected with the transient program rather than with the normal one, and again display a number of spikes in the data, indicating conclusively that the spikes are generated by the computer. Given the current experimental setup it is difficult to see how the transient program can be made to operate adequately given unacceptable noise levels are being generated by the computer itself. It is planned to replace the computer and electrochemical systems in the near future, as the Atari and Oxsys systems are of considerable age and increasing unreliability. It should be possible to create a computer designed solely to execute the ellipsometric and electrochemical programs, and thus each component can be tested for the noise levels it creates as the computer is constructed.

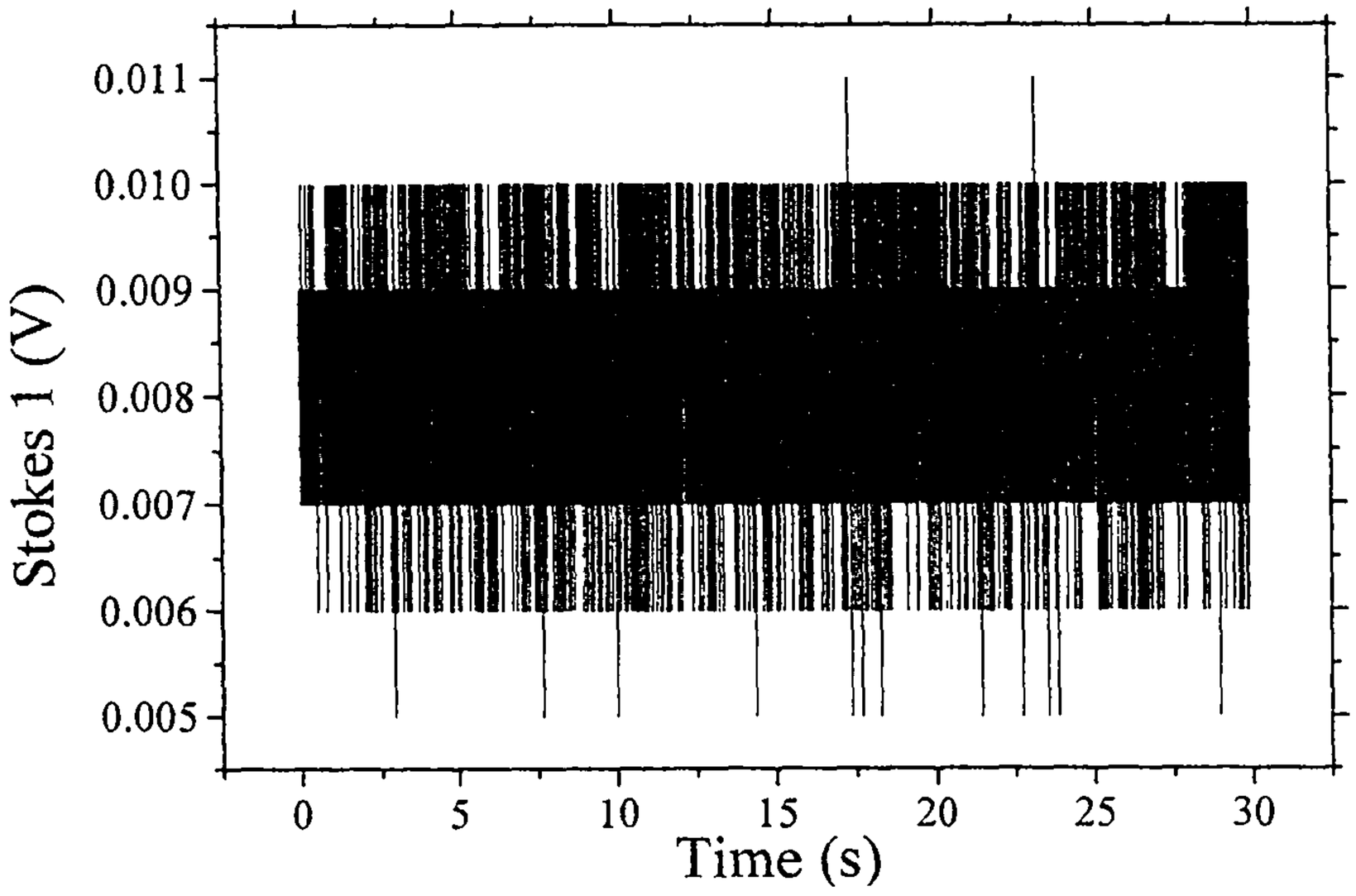

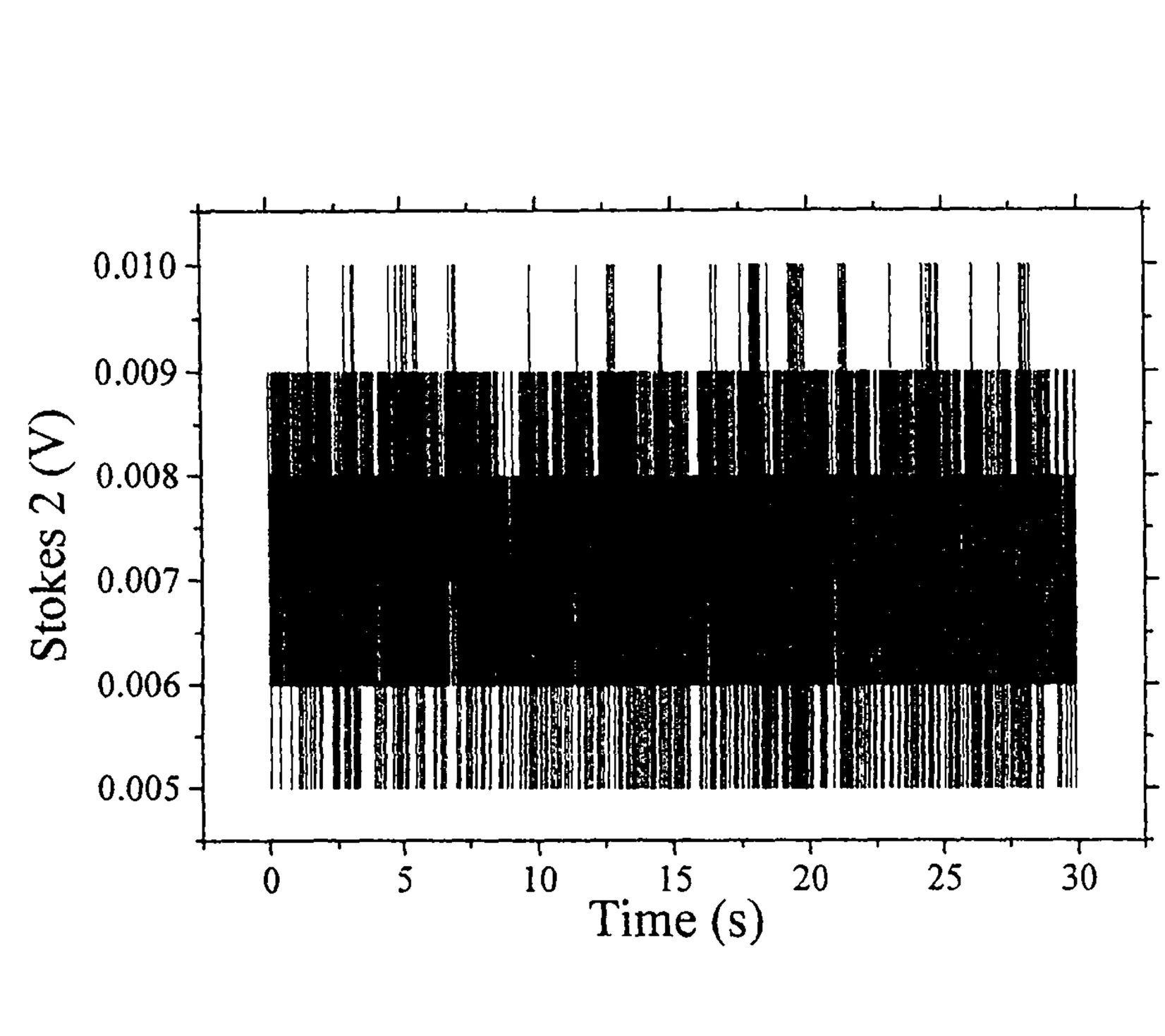

Fig. 3.21 (a) and (b). The variation in the Stokes readings as each Stokes input is replaced with a shorted 0 V input, all three other leads connected as normal for each experiment. Data collected with the normal program, one reading taken every 5 ms, no data averaging

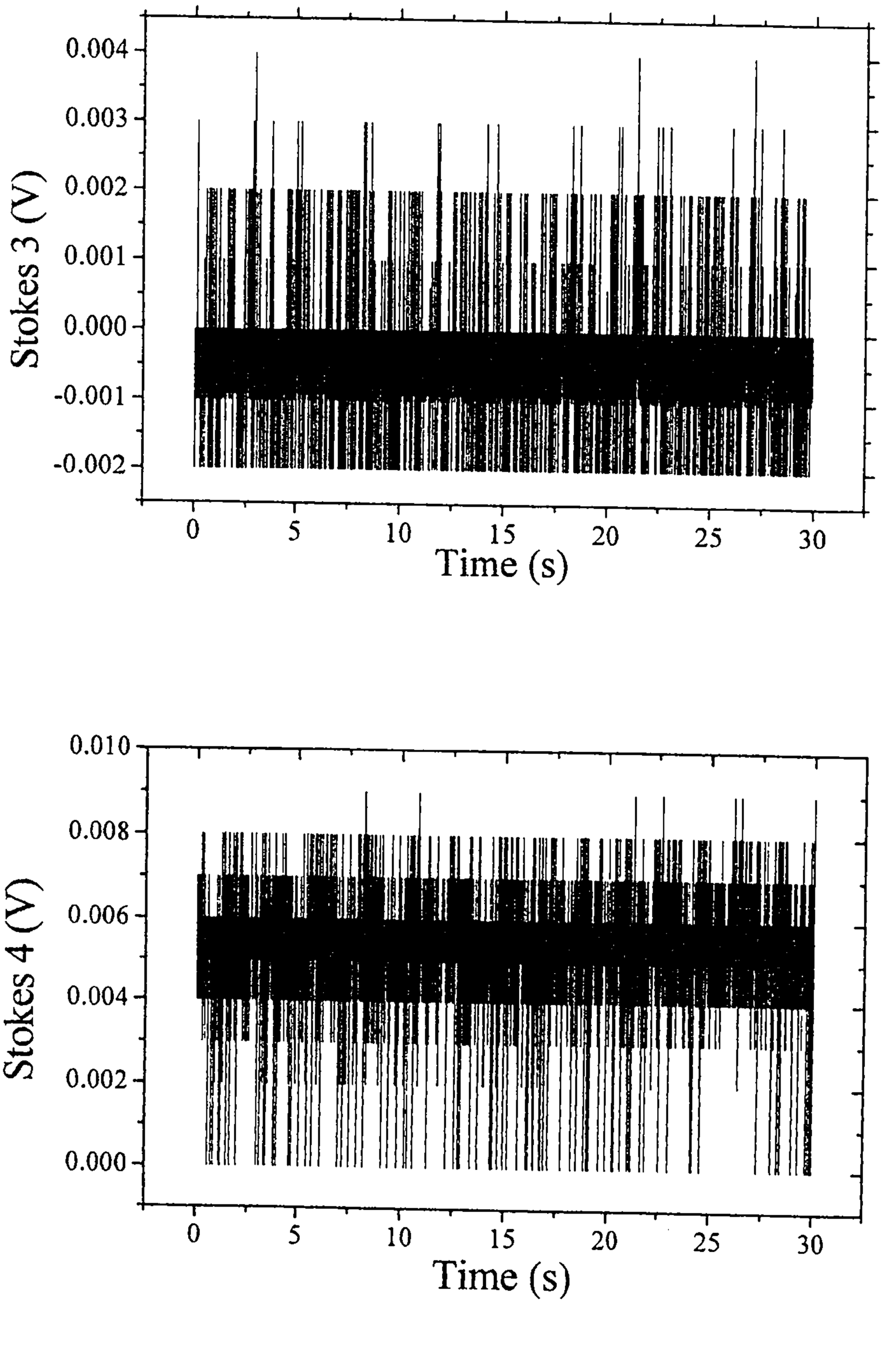

Fig. 3.21 (c) and (d). The variation in the Stokes readngs as each Stokes input is replaced with a shorted 0 V input, all three other leads connected as normal for each experiment. Data collected with the normal program, one reading taken every 5 ms, no data averaging

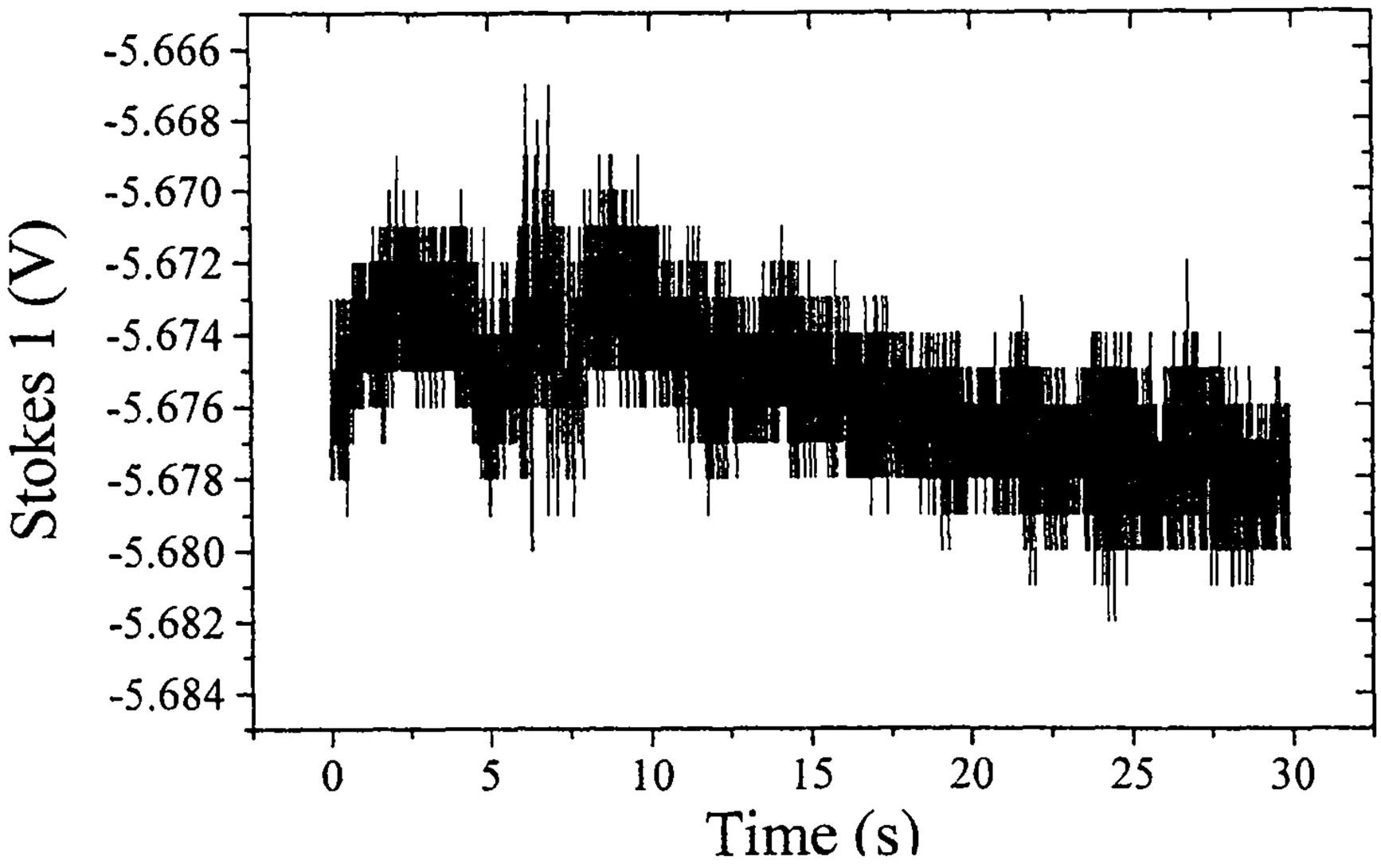

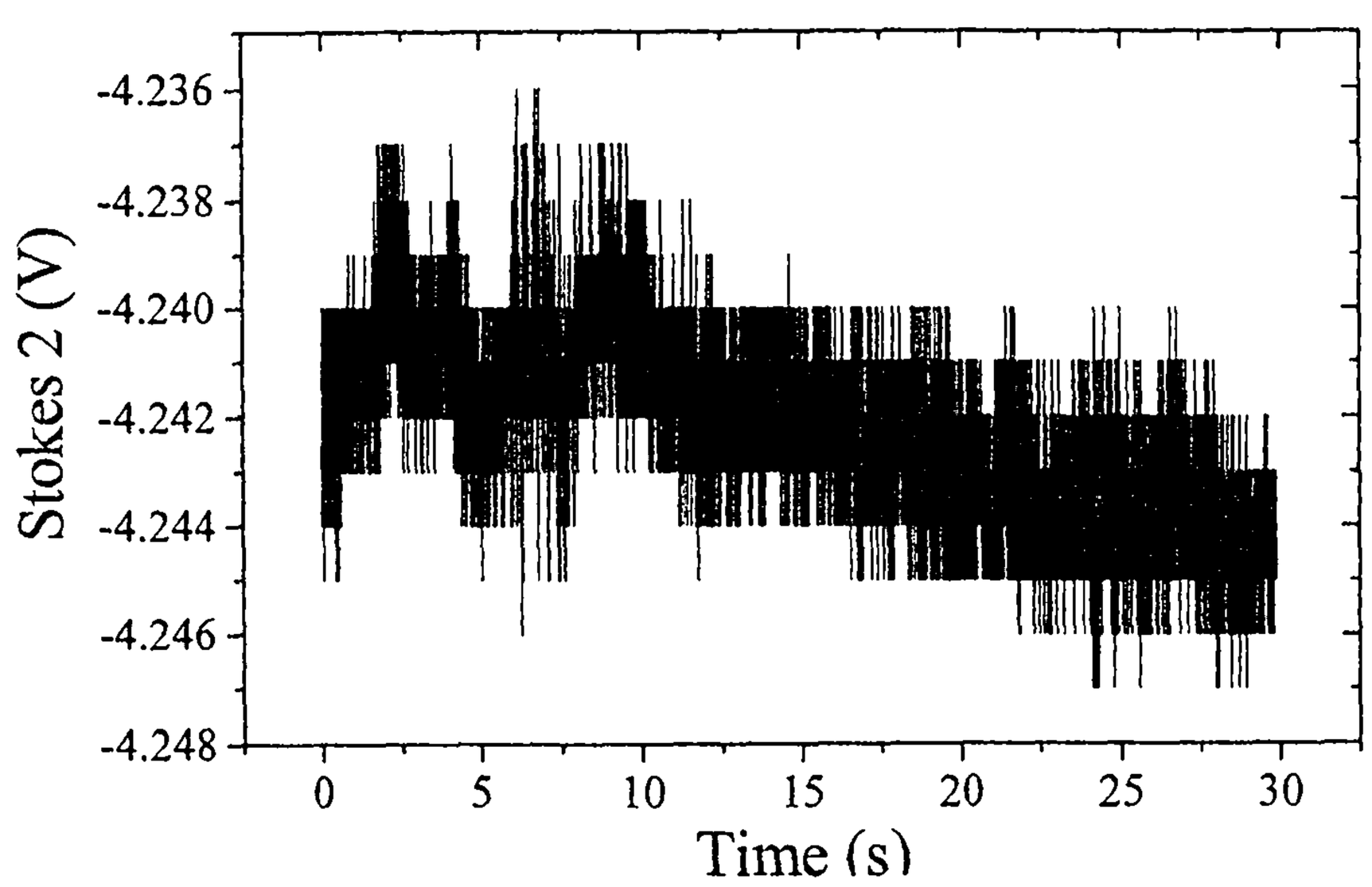

Fig. 3.22(a) and (b). The variation in the Stokes readings for the data in Fig. 3.7(b). Data collected at 632.8 nm using the normal program, one reading taken every 5 ms with no data averaging.

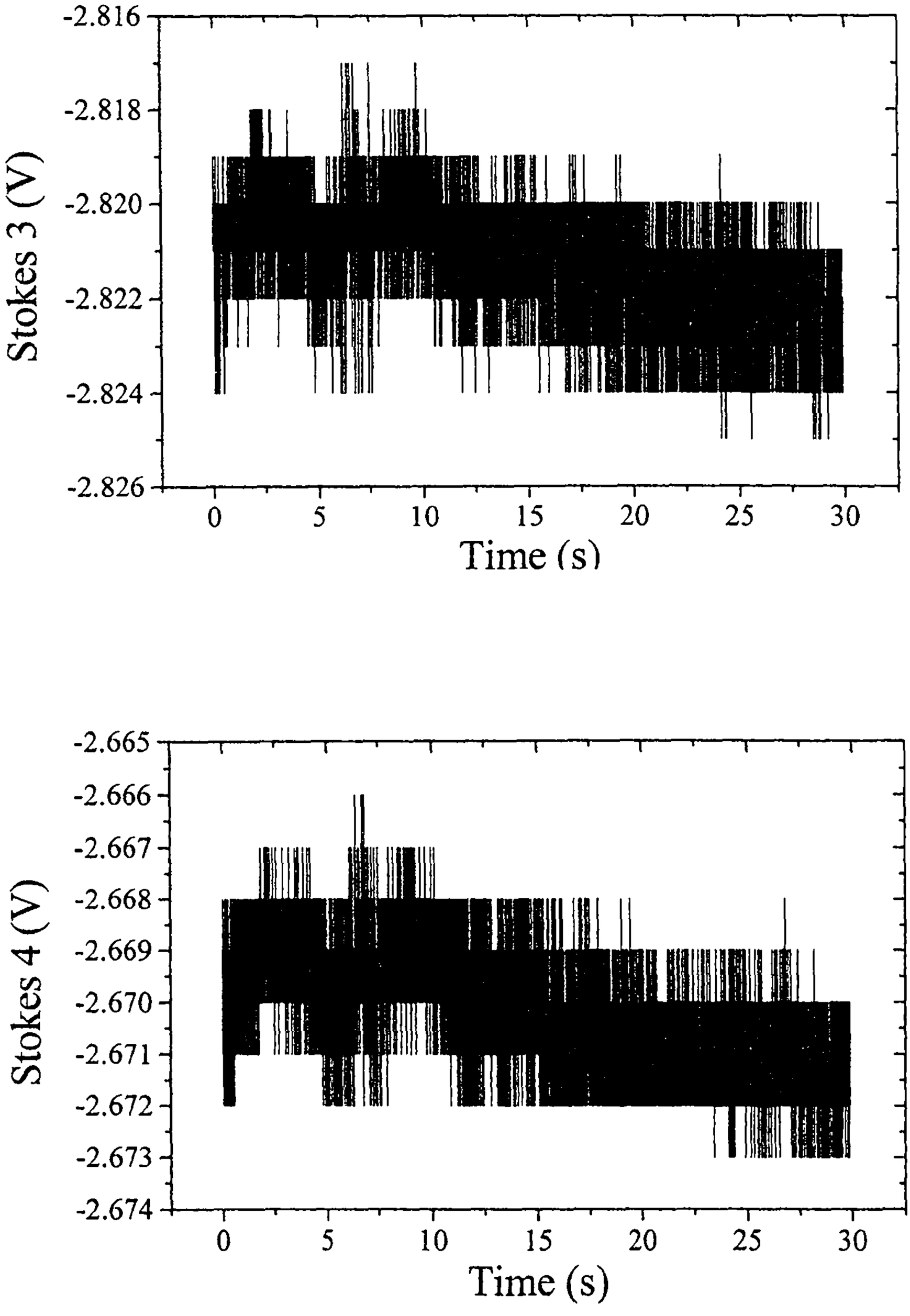

Fig. 3.22(c) and (d). The variation in the Stokes readings for the data in Fig. 3.7(b). Data collected at 632.8 nm using the normal program, one reading taken every 5 ms with no data averaging.

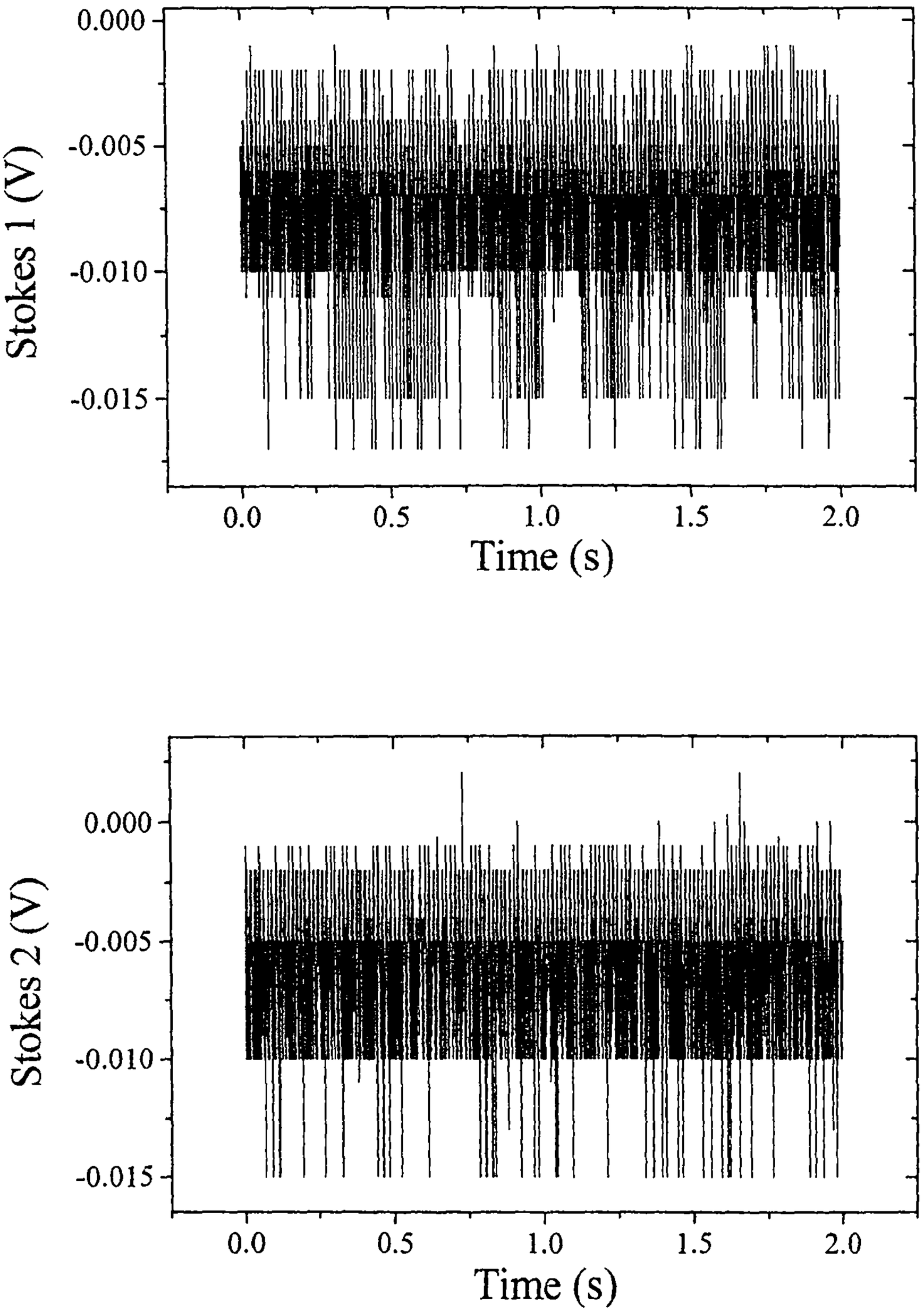

Fig. 3.23. The variation in the Stokes readings as each Stokes input is replaced with a shorted 0 V input, all three other leads connected as normal for each experiment. Data collected with the transient program, one reading taken every 325 μs, no data averaging

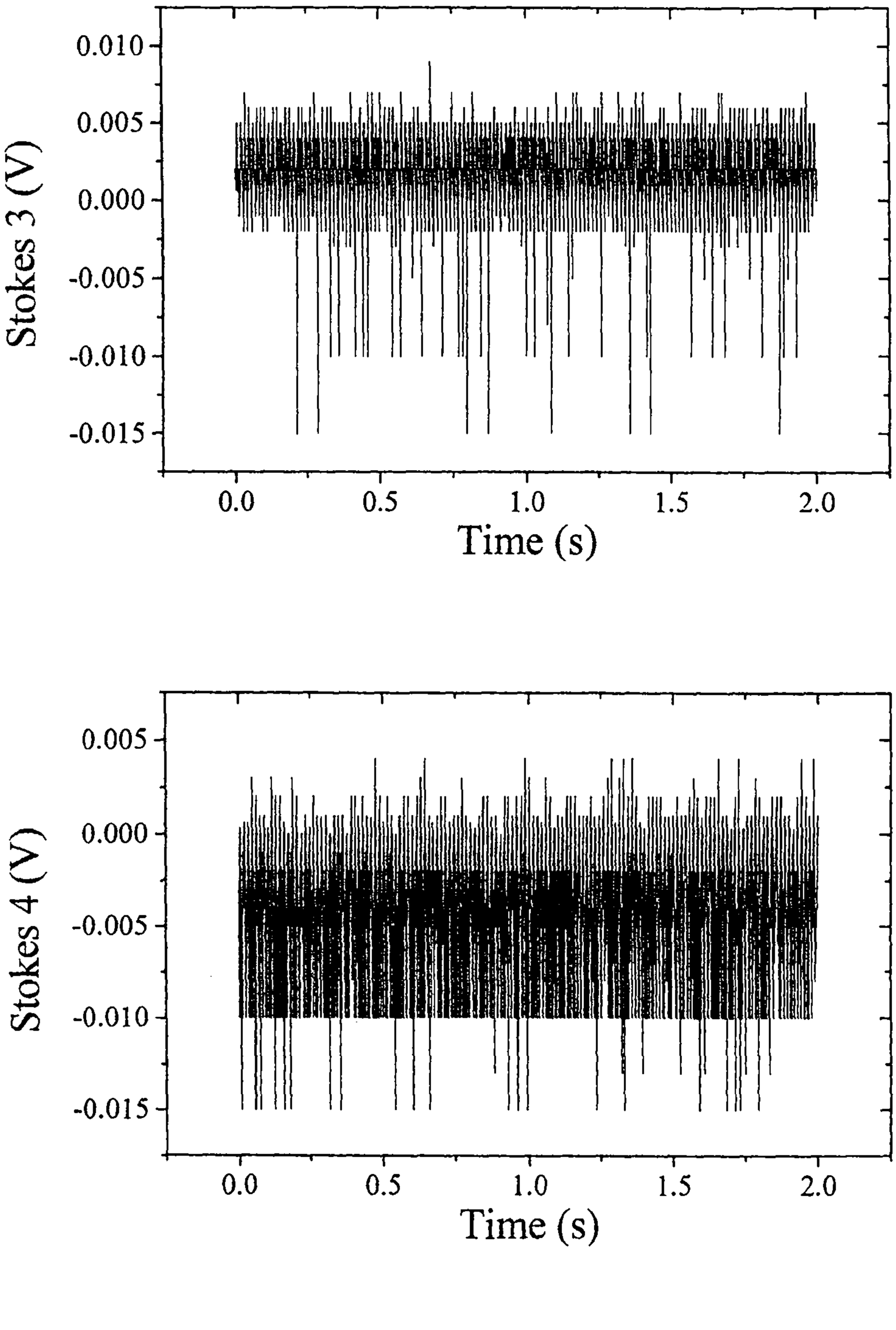

Fig. 3.23. The variation in the Stokes readings as each Stokes input is replaced with a shorted 0 V input, all three other leads connected as normal for each experiment. Data collected with the transient program, one reading taken every 325 μs, no data averaging

3.3. Conclusions

The air table clearly reduces the vibrational noise present, and the addition of a half inflated tyre underneath the ellipsometer appeared to yield further improvements. Though vibrational noise may remain, there are no simple measures to reduce it further.

The polarisation of the lasers had significant effects on the stability of the intensity. The randomly polarised lasers (594.1 and 543.5 nm) are unsuitable for use with the Stokesmeter, and the only solution is to replace them with polarised lasers. The fluctuating intensities also caused noise in Δ and Ψ, which is due to the four Stokes ouptuts being measured sequentially rather than simultaneously; intensity changes between the readings resulting in the ratio of the Stokes readings to one another, and hence the reported values of Δ and Ψ, fluctuating. It is planned to replace the Oxsys system and Atari with a dedicated PC, which ideally should have the capability of simultaneous measurement of the Stokes readings.

Given the levels of noise intrinsic to the computer system, resolution no better than 0.15^{0} on Δ, 0.04^{0} on Ψ and 0.5 % on intensity will be obtained. Using the transient program to collect data with a resolution of 325 μs resulted in a significant amount of shot noise not present when using the normal data collection procedure. This shot noise is unequivocally injected by the computer itself, and it is difficult to see how the transient measurements can be performed adequately with the current experimental setup. As it is already planned to build a dedicated PC to replace the Atari, a prolonged investigation of the exact source seems unnecessary.

Further improvements in the noise levels may result from replacing the mounting of the Stokesmeter. To allow the movement necessary to align the system, the Stokemeter is not rigidly fixed, and consequently can rock forward and backwards. Vibrational noise may contribute to this, but also placing the ellipsometer on the tyre will have destabilised it, allowing the whole system to move, and adding to any movement of the Stokesmeter relative to the beam. The ideal solution would be to replace the mounting with one that allows the same degree of adjustment for alignment as the present one, but which rigidly holds the Stokesmeter, though this is very difficult to design. Replacing the half inflated tyre under the ellipsometer with a series of rubber sheets of varying natural frequency, giving a more solid base for the ellipsometer to stand upon, may result in an improvement in the noise levels, and it may also be beneficial to move the mounting of the Stokesmeter nearer to the pivot of the ellipsometer, minimising the distance the beam has to travel, and consequently reducing the movement of the Stokesmeter relative to the beam.

3.4. References

1. P. Southworth, A. Hamnett, A. M. Riley, J. M. Sykes, *Corr. Sci*, 1988, **28**, 1139.

2. A. M. Riley, J. M. Sykes, A. Hamnett, *Corr. Sci.*, 1988, **28**, 799.

3. G. E. P. Box, W. G. Hunter, J. S. Hunter, *Statistics for Experimenters*, Wiley and Sons, 1978.

4. P. K. McBride, *Pascal made Simple*, 1997, Butterworth-Heinemann.

5. W. Savitch, *Pascal, An Introduction to the Art and Science of Programming*, 4th Ed., 1995, The Benjamin/Cummings Publishing Co., Inc.

4.1 Introduction.

In the twelve years since the polymerisation of Ni Salen complexes was first reported [1, 2], the electropolymerisation of metal Salens has been the subject of intensive investigation [see for example 3-9]. Long known for their properties as homogeneous catalysts [10-15], the discovery that they could be directly electro-polymerised raised the possibility of fabricating heterogenous catalysts from electrogenerated Salen films. The properties of monomers and polymers have been investigated for a number of Salen derivatives with a variety of central metals. [5-8, 17, 18]. While altering the central metal appears to have little effect on the conductivity of the resultant polymer films [5, 16], the substituents on the phenyl rings and carbon - carbon bridge between the two halves of the ligand can have profound effects on the structure and nature of the film [4-6, 8, 16]. The behaviour of these Salen films has never before been investigated with ellipsometry, despite the ability of the technique to produce significant insights into the nature and electrochemical behaviour of such conducting polymer films during growth and cycling. In collaboration with Dr. Cristina Freire and Dr. Miguel Vilas-Boas, who synthesised the Salen complexes described in the next two chapters, the SaltMe (studied in collaboration with Mr. D. Earley) and SaldMe complexes shown below in Fig. 4.1 were electropolymerised. The growth and potential cycling of the resultant films was monitored by ellipsometry to investigate the effect of altering the bridge substituents. The poly[Ni(SaltMe)] [4] modified electrode was studied using FTIR (in collaboration with Dr. Miguel Vilas-Boas), and these results are also discussed in light of the conclusions drawn from ellipsometry. A methoxy substituted tetramethyl Salen was also studied, and is discussed in chapter six. This has lead to the repetition

of some of the data for the tetramethyl Salen from this chapter, but was felt necessary for reasons of clarity in the comparison of the two complexes.

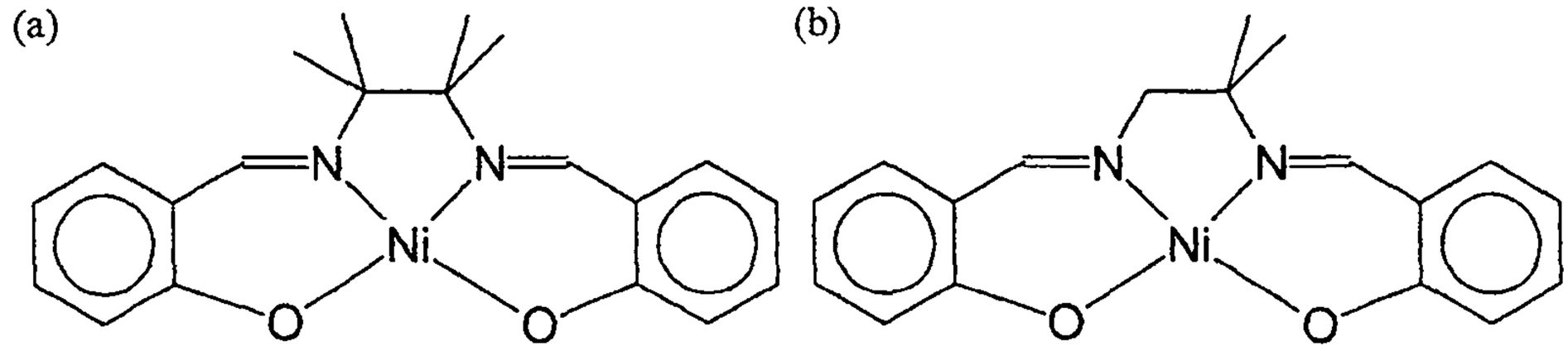

Fig 4.1. The structure of (a) N,N'-2,3-dimethylpropane-2,3-diyl-bis(salicylideneiminate)nickel(II) or Ni(SaltMe), and (b) N,N'-2-methylpropane-2,3-diyl-bis(salicylideneiminate)nickel(II) or Ni(SaldMe).

4.2 Results and Discussion

4.2.1 Experimental Data

4.2.1.1 Experimental data for the growth of the polymer films

The optical data gathered at 632.8 nm and the current passed during the five cycles of growth of poly[Ni(SaltMe)] are shown in Fig. 4.2 (a)-(d). The qualitative behavior of each parameter remains the same over all five cycles, Δ and the intensity (see Figs. 4.2(b) and (d)) show a steady decrease in value with each successive cycle while Ψ steadily increases (Fig. 4.2(b)). During the first anodic sweep none of the optical parameters alters before *ca.* 1.0 V. Clearly surface film formation is initiated only after this point as Δ and Ψ are surface sensitive. There appears to be some charge passed before 1.0 V as a small wave is seen between *ca.* 0.6 and 0.9 V, this does not result in the formation of any deposit as it occurs prior to any changes in the

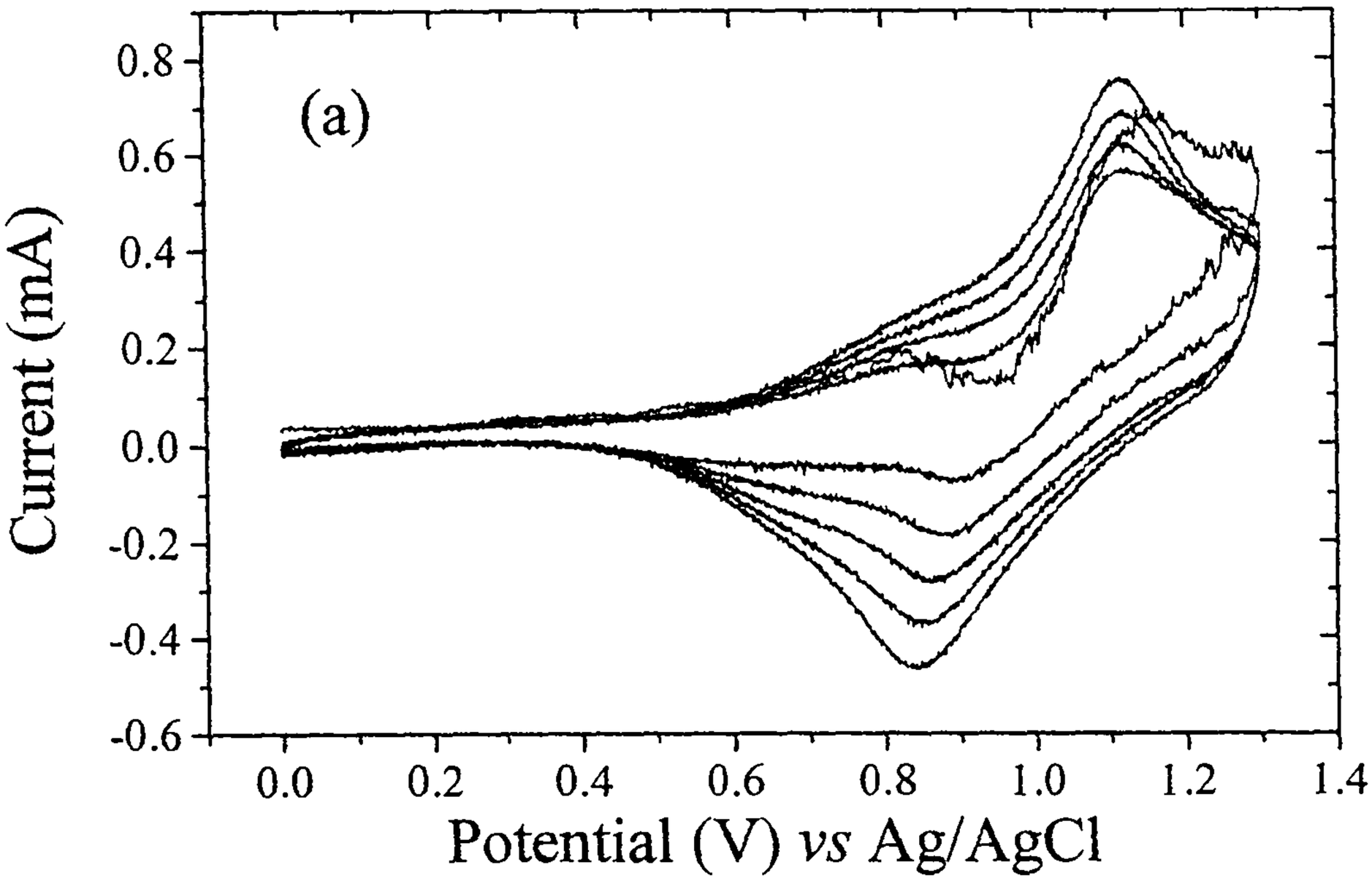

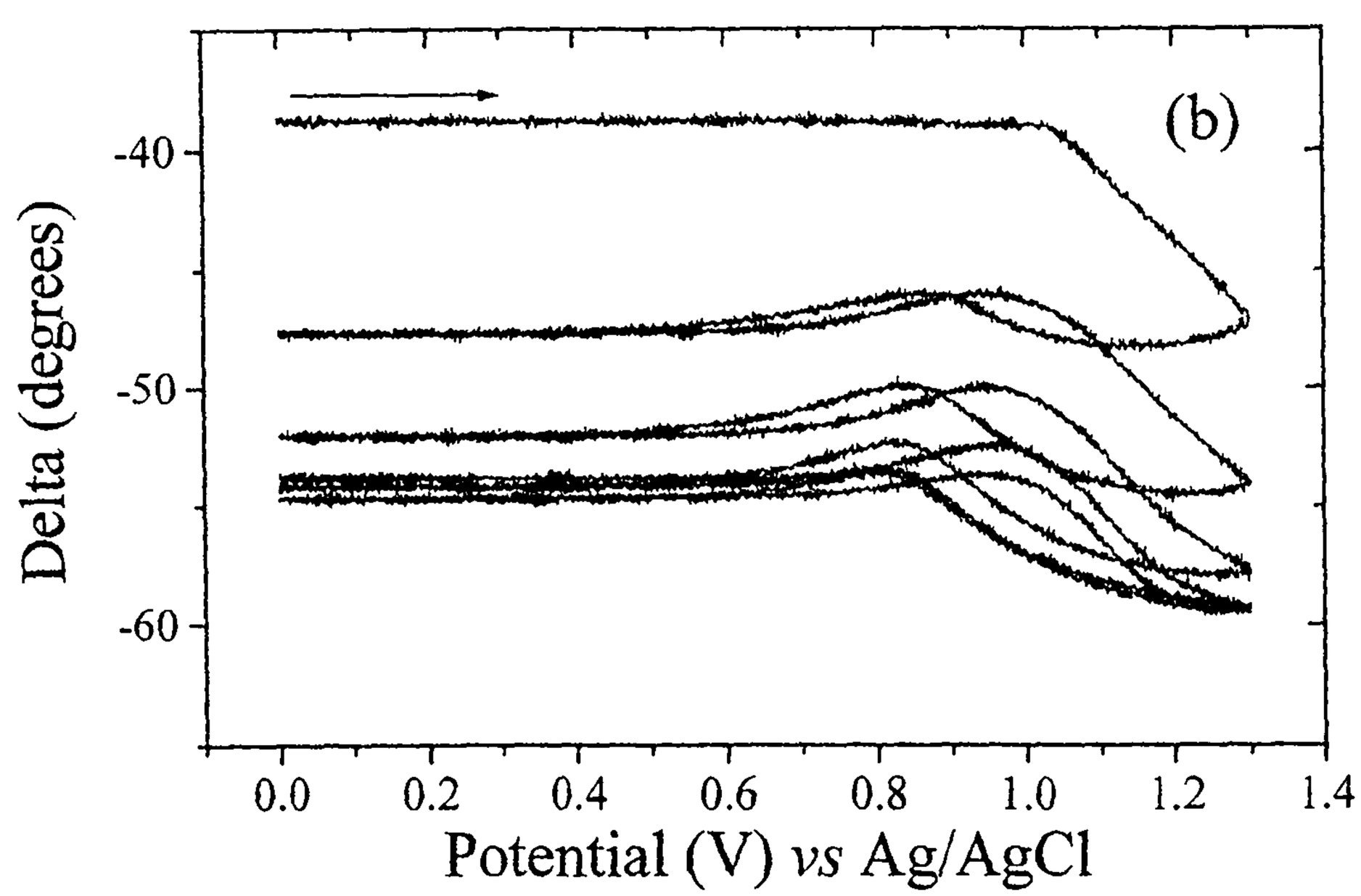

Fig. 4.2 The current passed (a) and the variation in Δ (b) during the growth of poly[Ni(SaltMe)] as a function of potential. The film was grown for 5 cycles between 0 and 1.3 V *vs* Ag/Ag^{+} at 100 mV s^{-1} on a Pt disk (0.64 cm^2)working electrode immersed in 1 mmol dm^{-3} of the Salen monomer in 0.1 mol dm^{-3} TEAP/MeCN

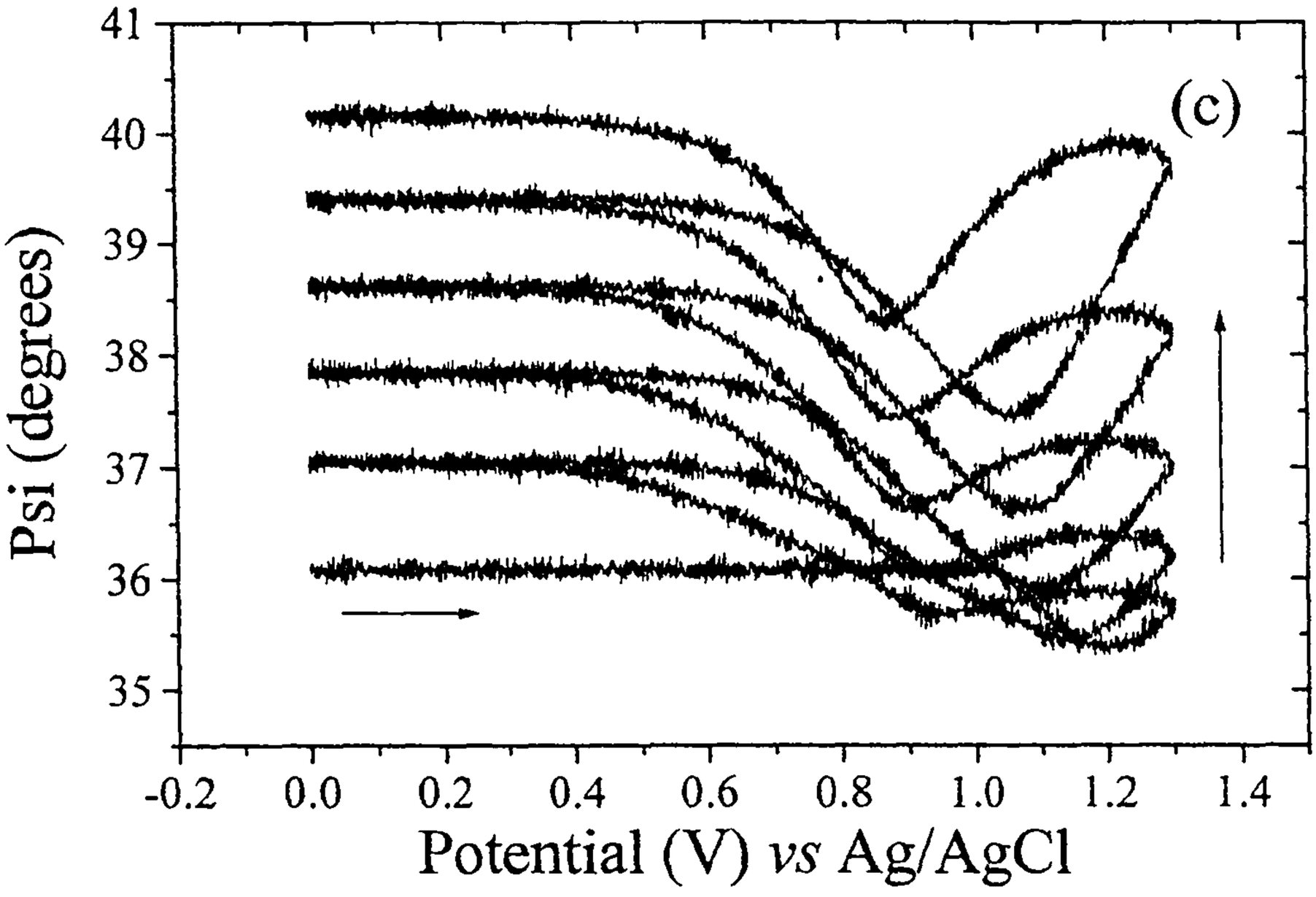

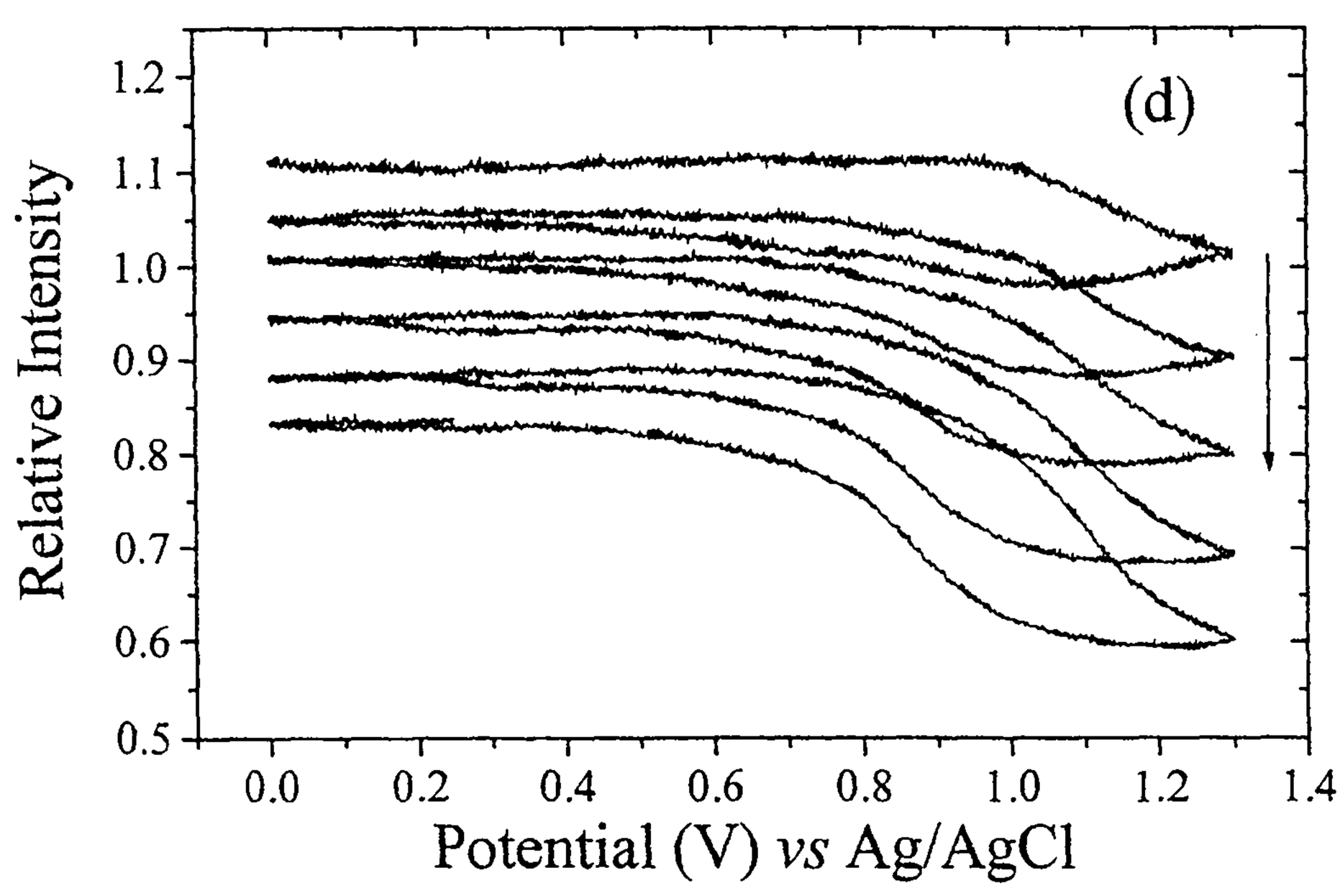

Fig. 4.2. The behaviour of Ψ (c) and the intensity (d) during the growth of poly[Ni(SaltMe)].

Conditions as for Fig. 4.2(a)

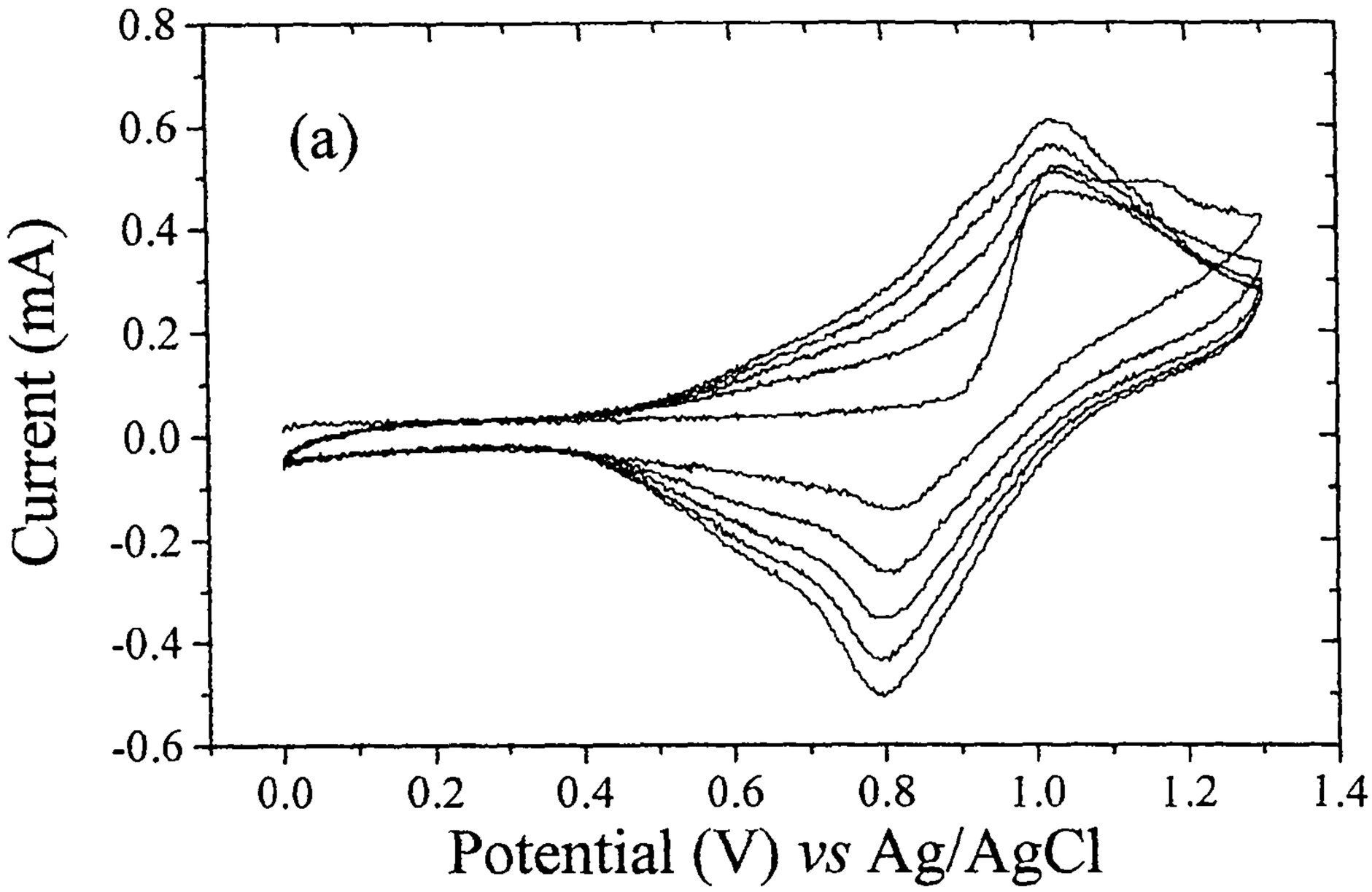

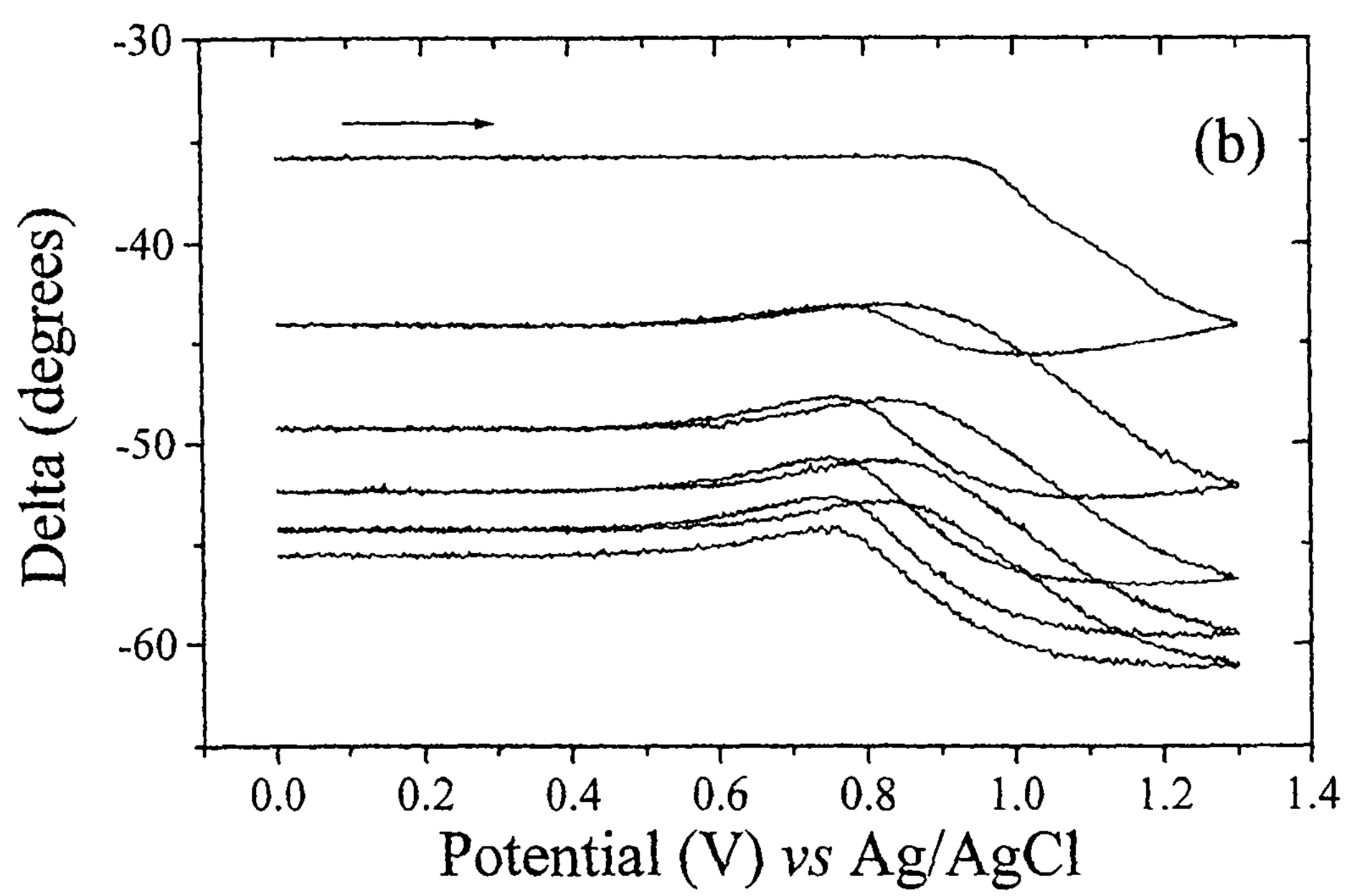

Fig. 4.3 The current passed (a) and the behaviour of Δ (b) during the growth of poly[Ni(SaldMe)]. The conditions were the same as for Fig 4.2(a).

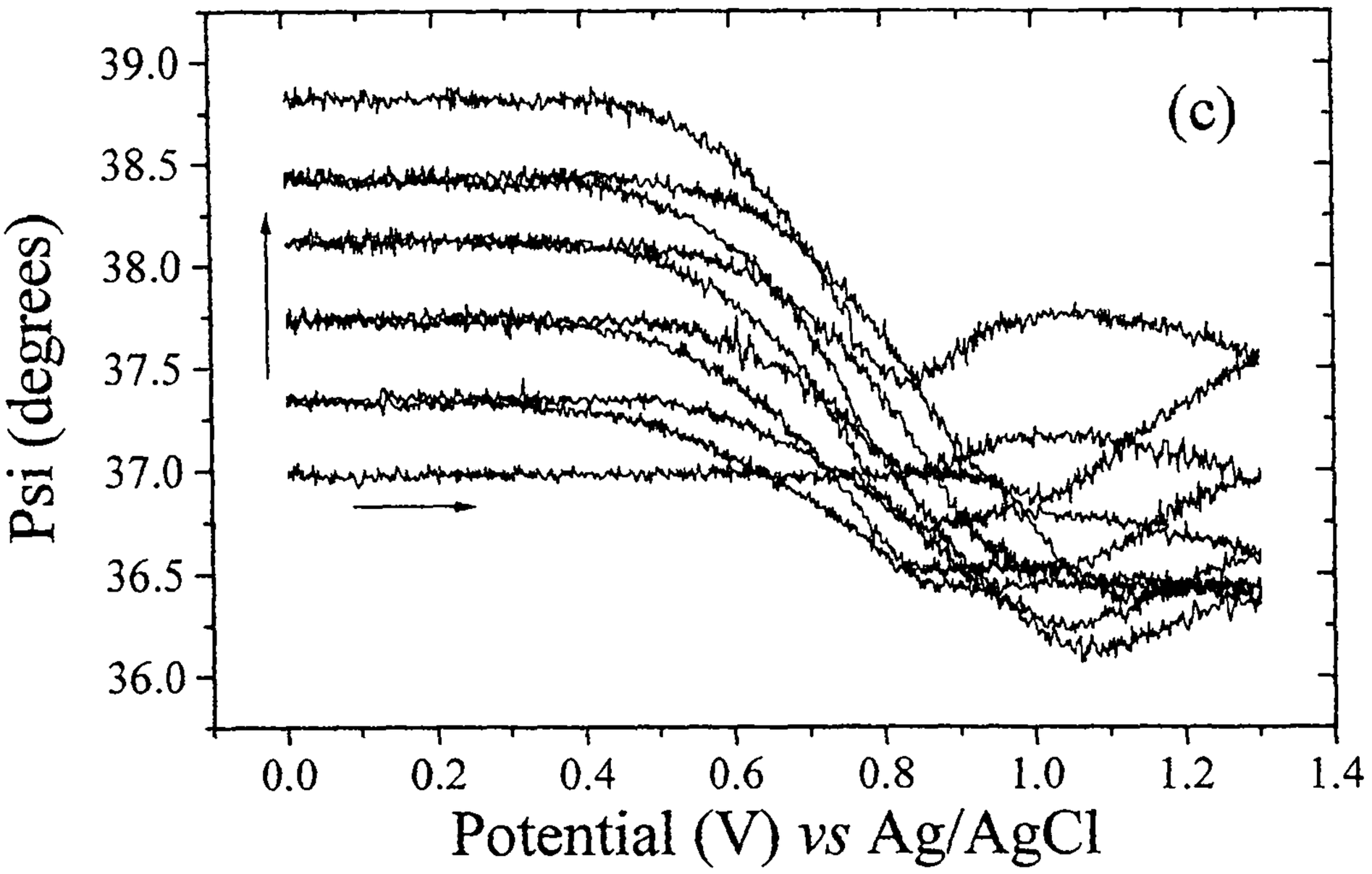

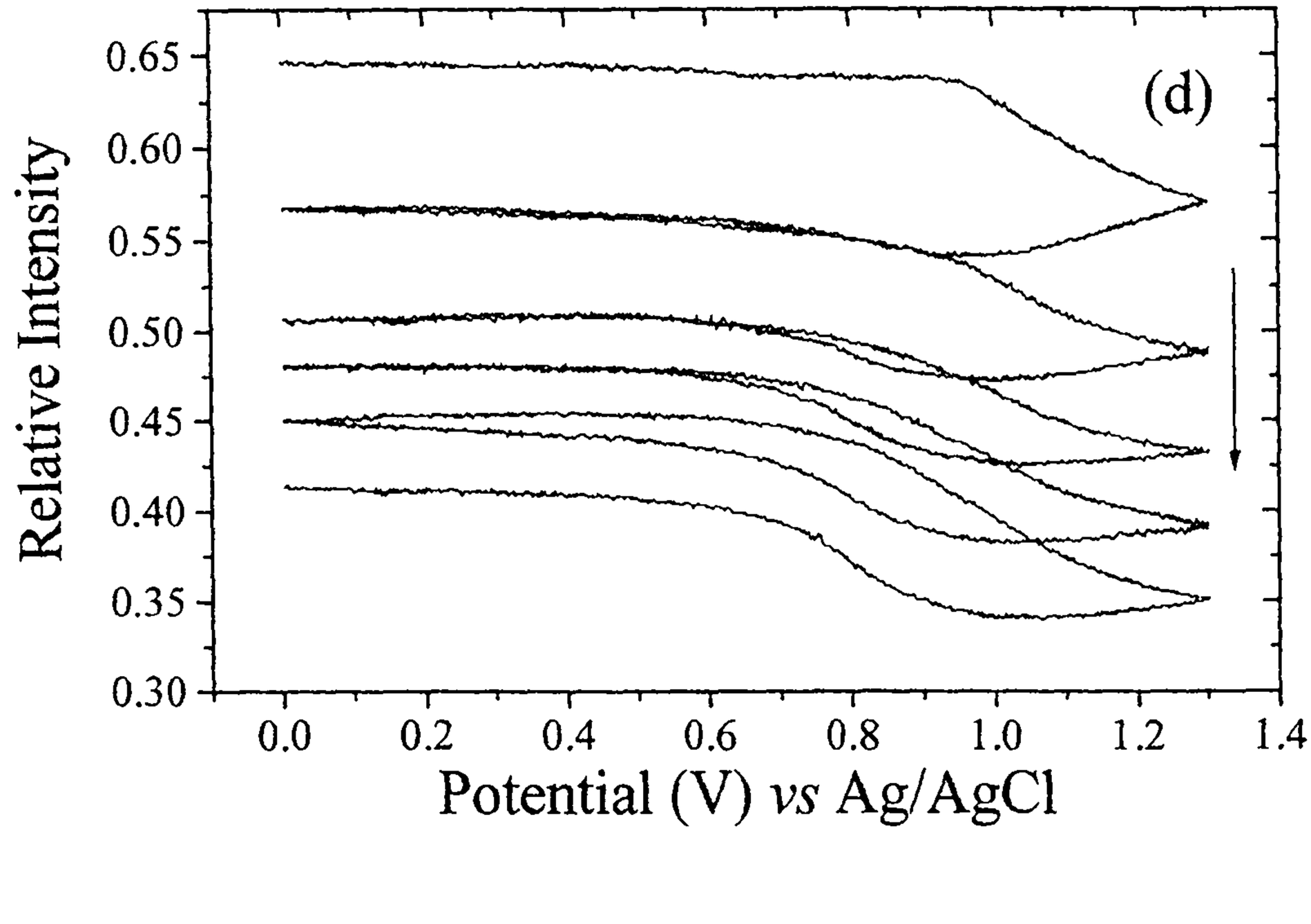

Fig. 4.3 The behaviour of Ψ (c) and the intensity (d) during the growth of poly[Ni(SaldMe)].

Conditions were as for Fig. 4.2(a).

parameters, and can be assigned to a solution oxidation. A second oxidation process occurs between *ca.* 1.0 and 1.3 V which clearly does result in the formation of a polymer deposit as the ellipsometric parameters are seen to alter markedly, Δ showing a sharp decrease and Ψ a slight increase in value. During the second anodic sweep the optical data start to alter at a much lower potential, from *ca.* 0.4 V to 0.95 V Δ increases slightly while Ψ and the intensity show a slight decrease. The changes, not being present during the first sweep, can be assigned to changes within the polymer film formed during the previous cycle, and as a shoulder on the main anodic peak is seen over this potential range it is clear the polymer film is being oxidised. There appear to be at least two separate processes occurring, only the second of which leads to polymerisation. The corresponding data for the five cycles of growth of the poly[Ni(SaldMe)] film are shown in Fig. 4.3 (a)-(d). There is clearly a great deal of similarity between the two sets of data, though the onset of polymerisation of the SaldMe film occurs at slightly lower potentials, *ca.* 0.95 V compared to 1.0 V for poly[Ni(SaltMe)] and in this case there is no significant charge passed on the first anodic sweep before film formation commences. On subsequent cycles, as with the poly[Ni(SaltMe)], a shoulder appears on the main oxidative peak at *ca.* 0.4-0.9 V, over which range changes in the ellipsometric parameters also occur which, as before, are due to oxidation of the polymer film.

4.2.1.2 Experimental data for potential cycling of the modified electrodes

The data for the potential cycling of the poly[Ni(SaldMe)] and poly[Ni(SaltMe)] films after growth in monomer free electrolyte are shown in

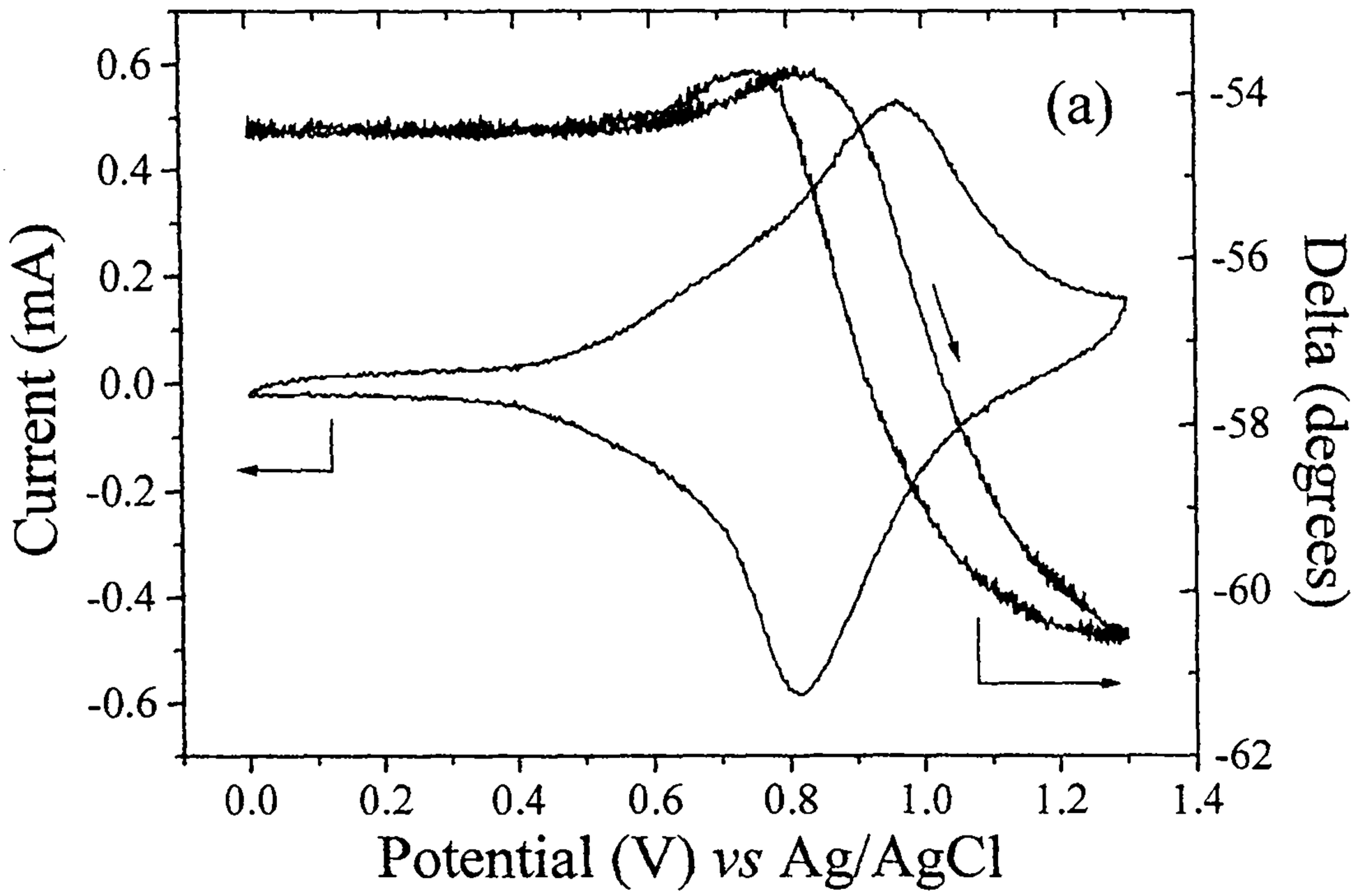

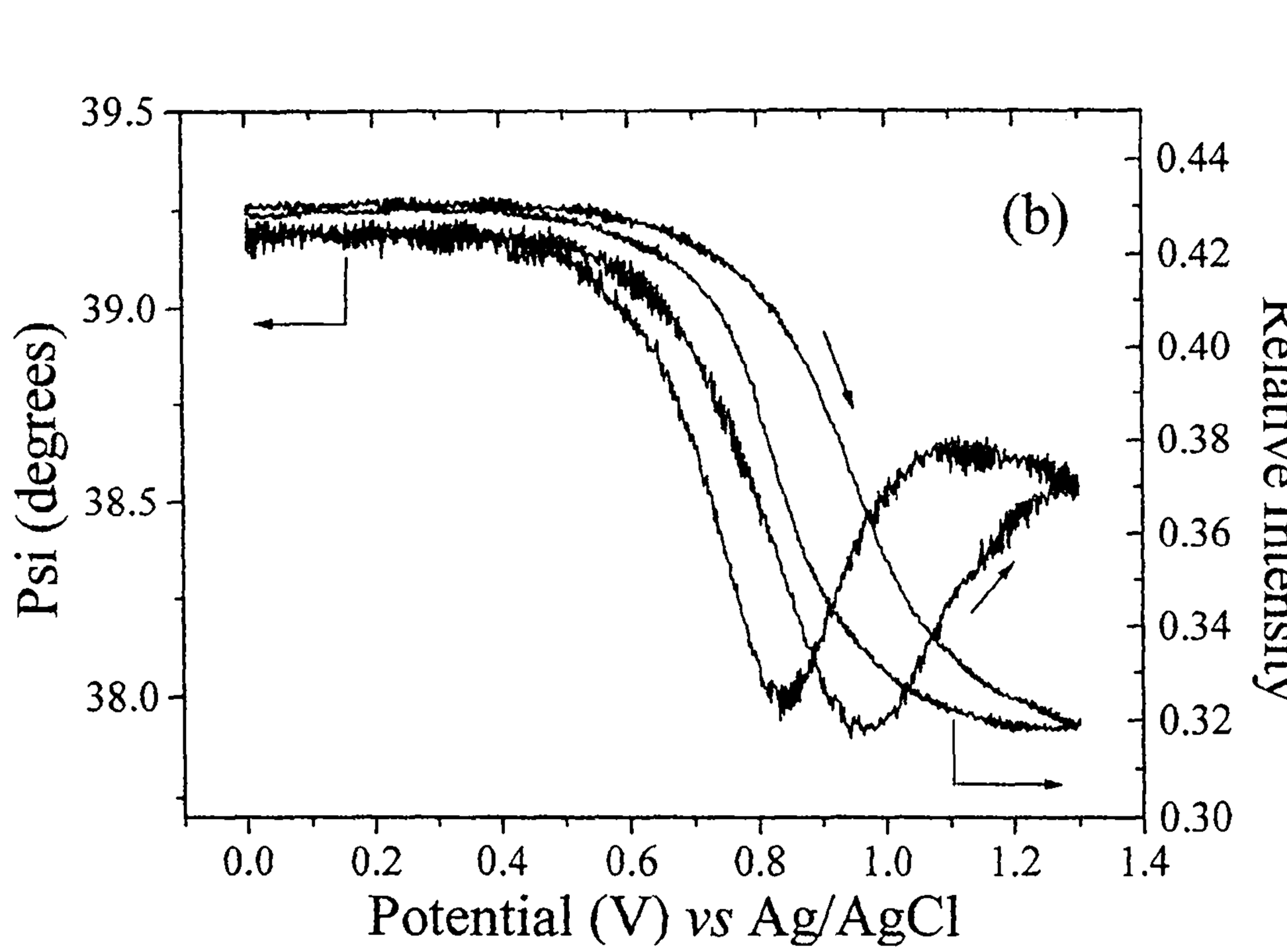

Fig. 4.4 The variation in the current and Δ (a), Ψ, and intensity (b) during potential cycling of the modified poly[Ni(SaldMe)] Pt disk electrode (0.64 cm^2) scan rate at 100 mV s^{-1}, 0.1 mol dm^{-3} TEAP in MeCN.

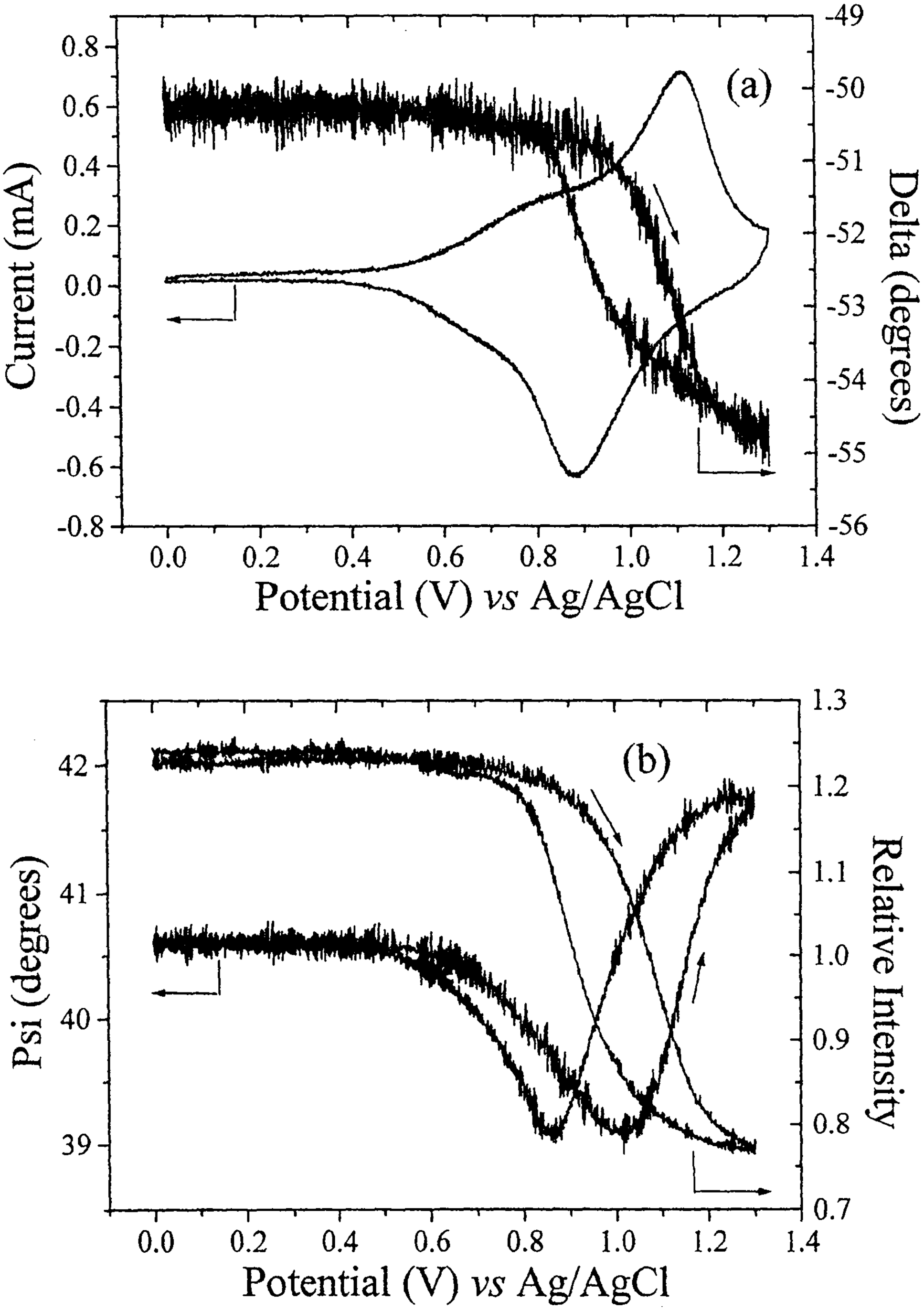

Fig. 4.5 The variation in the current and Δ (a), Ψ, and intensity (b) during potential cycling of the modified poly[Ni(SaltMe)] Pt disk electrode (0.64 cm^2) scan rate at 100 mV s^{-1}, 0.1 mol dm^{-3} TEAP in MeCN.

Figs. 4.4 and 4.5 respectively. The CVs and the qualitative behaviour of the ellipsometric parameters are very similar for the two films. In addition the cyclic voltammograms for growth and cycling are similar, still indicating the presence of two separate oxidative processes, one from *ca.* 0.4-0.9 V, causing in both films a slight increase in Δ, a large decrease in Ψ and a decrease in intensity; and a second between *ca.* 0.9 to 1.3 V, corresponding to a steeper decrease in the intensity, an increase in the value of Ψ and a sharp decrease in Δ. There do, however, appear to be some differences in behaviour; the peak between 0.4 and 0.9 V is much more pronounced for poly[Ni(SaltMe)], and there appears to be a 100 mV discrepancy between the oxidation process of the films, the main anodic peaks occurring at 0.95 V and 1.05 V, and the ellipsometric parameters beginning to alter at 0.6 V and 0.7 V for poly[Ni(SaltdMe)] and poly[Ni(SaldMe)] respectively

4.2.1.3 Potential Stepping of poly[Ni(SaldMe)]

Potential stepping experiments were performed on the poly[Ni(SaldMe)] modified electrode to see how the film responded on an extended time scale. 100 mV potential steps were used, stepping from 0.4 V to 1.3 V and back to 0.3 V, with the film held at each potential for 35 s. The ellipsometric data shown in Fig. 4.6 bear many similarities to the data for potential cycling in Fig. 4.4, Δ showing a slight increase between 0.4 and 0.8 V before decreasing strongly between 0.8 and 1.3 V, Ψ decreases between 0.4 and 0.8 V then increases between 0.8 and 1.3 V, and the intensity decreases throughout out the oxidation of the film. It is interesting that the data is qualitatively so similar for the cycling and stepping experiments, especially

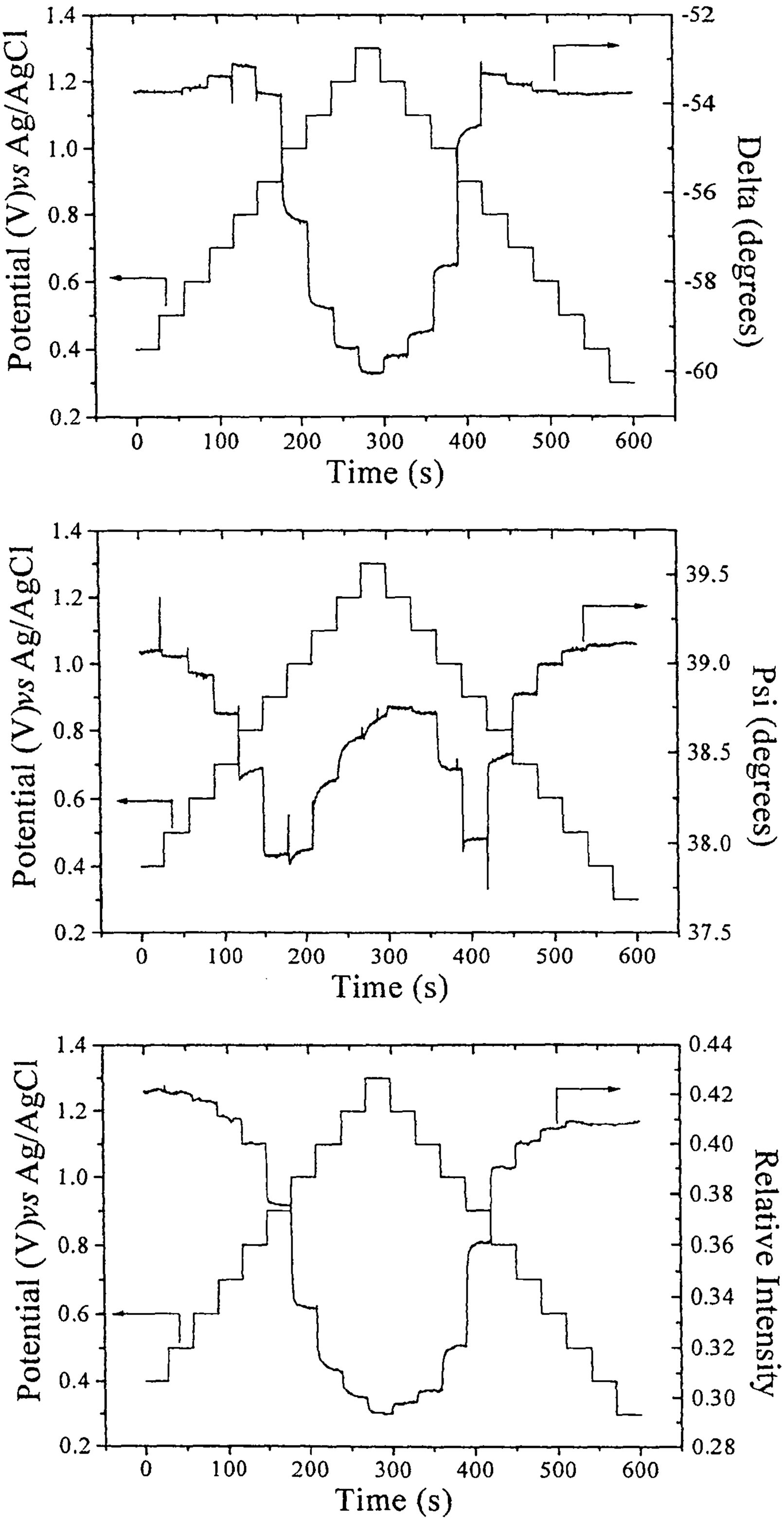

Fig. 4.6. Potential stepping of poly[Ni(SaldMe)] in 0.1 mol dm-1 TEAP/MeCN. Each step was 100 mV, with 35 s at each potential.

considering the film is clearly still evolving after 35 s at higher potentials, which would lead us to expect differences in the values of the parameters at the anodic limit of the experiments, which is not the case. The cumulative charge passed during the cycling of the poly[Ni(SaldMe)] (Fig. 4.4) and during stepping has been plotted in Fig. 4.7(a), and a comparison of the cumulative charge passed during the cycling of poly[Ni(SaltMe)] (Fig. 4.5) is shown in Fig. 4.7(b). Stepping experiments were performed on a poly[Ni(SaltMe)] modified electrode during the FTIR experiments, and again good agreement was found between the stepping and cycling of the film, however the film grown for investigation by FTIR was significantly thicker than the one grown for investigation by ellipsometry, and is discussed in section 4.2.3.

It is clear in all three experiments that the charge passed during the anodic sweep is not completely regained over the course of the cathodic sweep, this is known as charge trapping, and has been widely reported for various conducting polymers [19-23], and has been reported for poly[Ni(SaltMe)] [4]. Charge trapping is generally attributed to structural or conformational changes which limit polymer chain movement and/or the ingress or egress of charge compensating ions, causing regions of the polymer to remain oxidised even at the cathodic limit [4,20,23,24]. This can be due to a permanent chemical modification [20,23]; however, in this case it is clearly not a permanent over-oxidation of the polymer, as holding the film at the cathodic limit results in the recovery of the remaining charge [4,24]. There is clearly little difference in the extent of charge trapping during cycling of the two electrodes, the poly[Ni(SaltMe)] passing and retaining slightly more charge. During stepping of poly[Ni(SaldMe)] more charge is trapped than during cycling, though given the time scale of the stepping experiments it is perhaps surprising the difference is not larger.

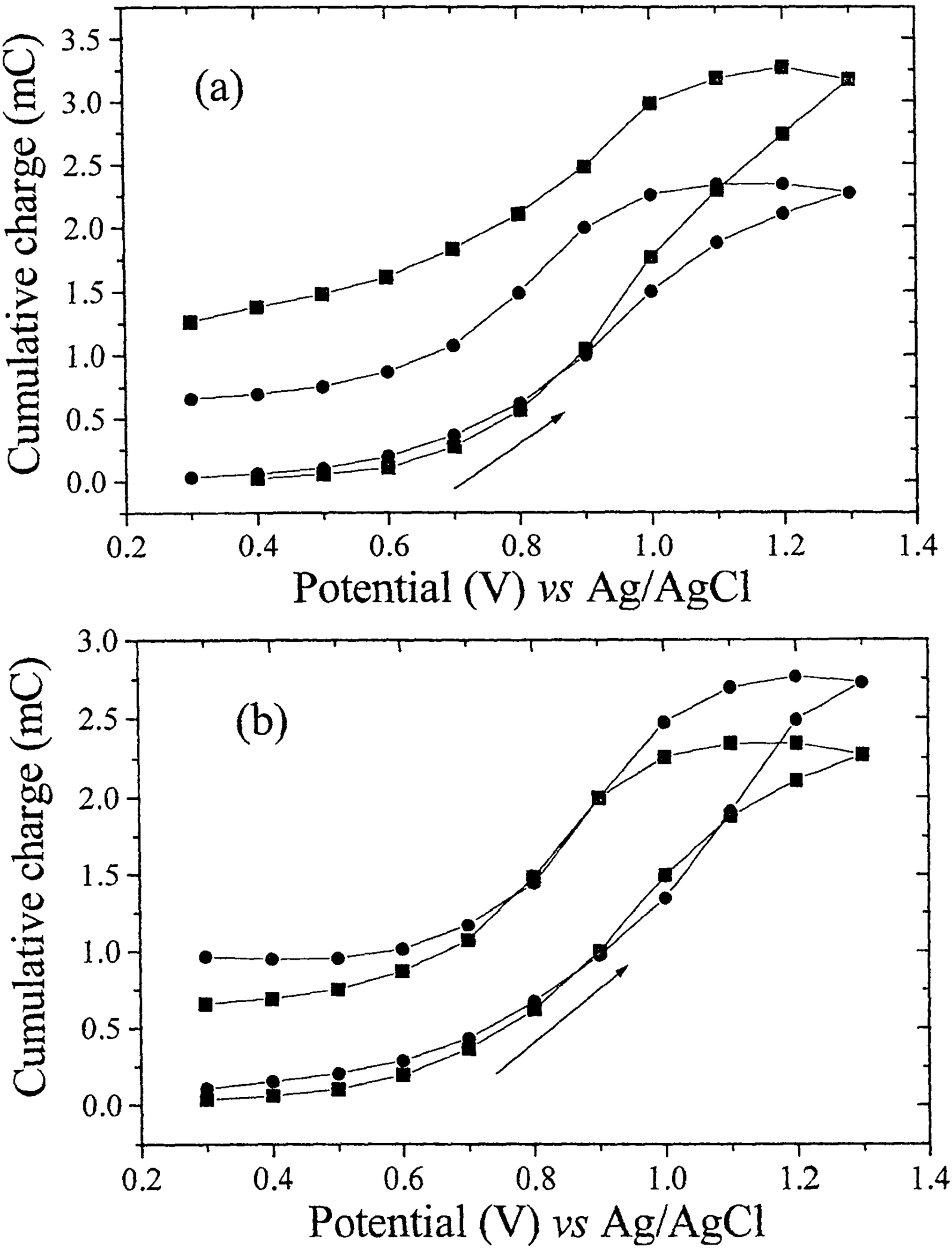

Fig. 4.7 (a)The cumulative charge passed during stepping (squares) and cycling (circles) of poly[Ni(SaldMe)]. (shown in Figs 4.6 and 4.4 respectively). (b) The cumulative charge passed during the cycling of poly[Ni(saldMe)] (squares) and poly[Ni(SaltMe)] (circles) (Figs. 4.4 and 4.5 respectively).

Though a greater amount of charge is trapped during potential stepping of the poly[Ni(SaldMe)] film, the difference in behaviour due to the longer timescale of oxidation during stepping is clearly insufficient to cause the ellipsometric parameters to alter noticeably from the behaviour observed during cycling..

4.2.2 Fitted Data

4.2.2.1 Fitted data for the growth of the polymer films

The process of fitting the data to a model proved relatively easy; in both cases, all five cycles of growth and the subsequent cycling fitted to a simple homogeneous model. The fitted data for the cycling of both films is shown in Figs. 4.8 and 4.9. The qualitative behaviour of both films is the same: n, k and the thickness are stationary between *ca.* 0 and 0.4 V; between *ca.* 0.4 and 0.9 V k is stationary, n decreases and the thickness increases; above 0.9 V n and k show a marked increase, while the thickness decreases by *ca.* 10 - 20 nm. During the growth of poly[Ni(SaldMe)], the thickness hardly alters between cycles while n and k show marked increases with each scan, suggesting that the growth process occurs by consolidation. The first scan clearly results in the deposition of a very diffuse layer of film which is mainly solvent as n and k differ very little from those of acetonitrile (1.344, 0) [25], on subsequent scans, n and k increase as polymerisation results in the film becoming denser and containing less solvent though the overall thickness changes very little. As polymerisation progresses it can be seen that k does not return to zero when the film is reduced, but increases with each cycle; this residual absorbance indicates the film is

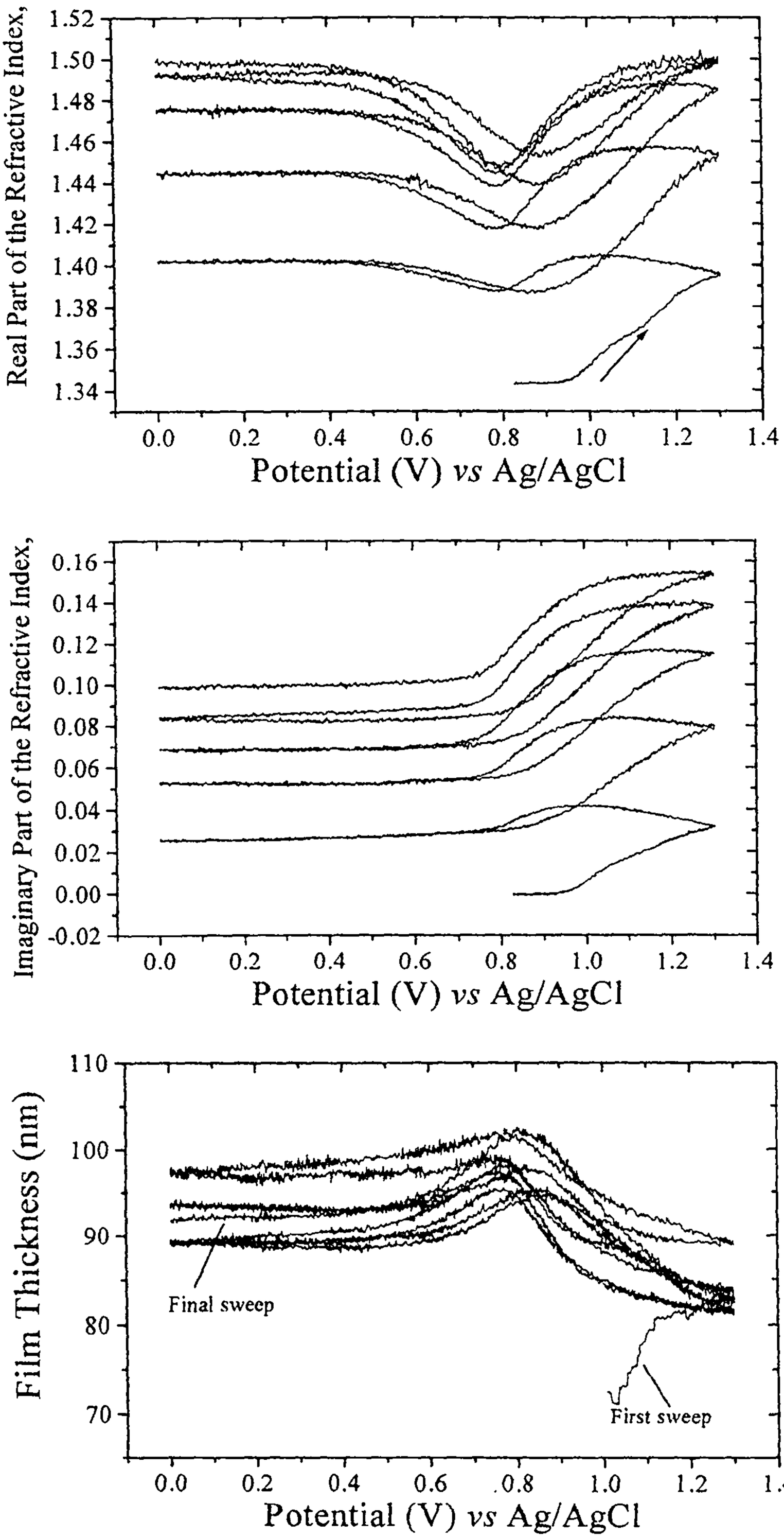

Fig. 4.8 Growth of poly[Ni(SaldMe)]. The data gathered at 632.8 nm was fitted to a homogeneous model to give the behaviour of *n*, *k*, and thickness shown. Conditions as in Fig. 4.2.

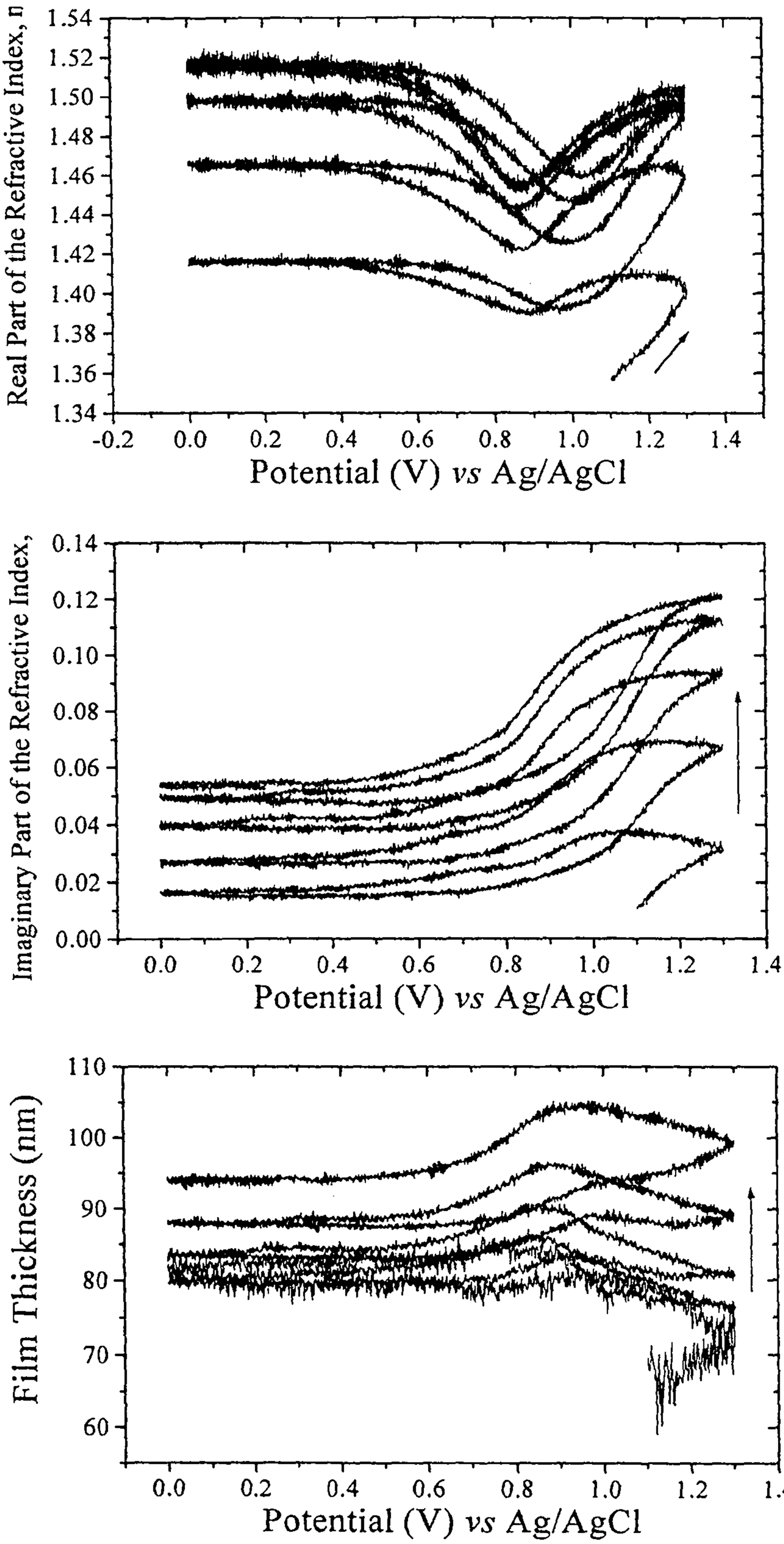

Fig. 4.9 Growth of poly[Ni(SaltMe)]. The data gathered at 632.8 nm was fitted to a homogeneous model to give the behaviour of *n*, *k*, and thickness shown. Conditions as in Fig. 4.2.

not fully reduced at the cathodic limit, in agreement with the charge trapping hypothesis discussed in the previous section.

Growth of the poly[Ni(SaltMe)] film would appear to progress by a similar mechanism as that of the poly[Ni(SaldMe)] film for at least the first three cycles, during which there are again marked increases in n and k but little change in the thickness. However in the case of this film steady increases in film thickness were observed during the fourth and fifth cycles while n and k are almost stationary, suggesting growth has reached a stage where the deposited layer is of the same composition as the underlying film .

The growth and cycling of poly[Ni(SaltMe)] has also been investigated using EQCM and probe beam deflection (PBD) by Freire and co-workers [24]. Although film growth was limited to the potential range 0 to 1.1 V *vs* Ag/Ag^+ for finer control over polymerisation, which would be expected to yield a significantly thinner film, the changes observed in the mass correspond well to the changes in thickness proposed by the homogeneous model used in this work. During the first polymerisation scan, the mass started to increase at 0.95 V, and continued to increase until 0.9 V on the return sweep. On subsequent scans the mass starts to increase at 0.4 V, a steep increase was observed between 0.9 and 1.1 V, and continued to display a slight increase until 0.9 V on the return sweep. These results lend a great deal of credibility to the homogeneous model proposed from the ellipsometric data. A slight contraction in thickness is predicted by the ellipsometric model between 1.0 and 1.3 V, which is not shown by the EQCM data. However as in the EQCM study, polymerisation was performed with an anodic limit of 1.1 V, so any contraction would have occurred to a much lesser extent than in the ellipsometric study with an anodic limit of 1.3 V. As yet

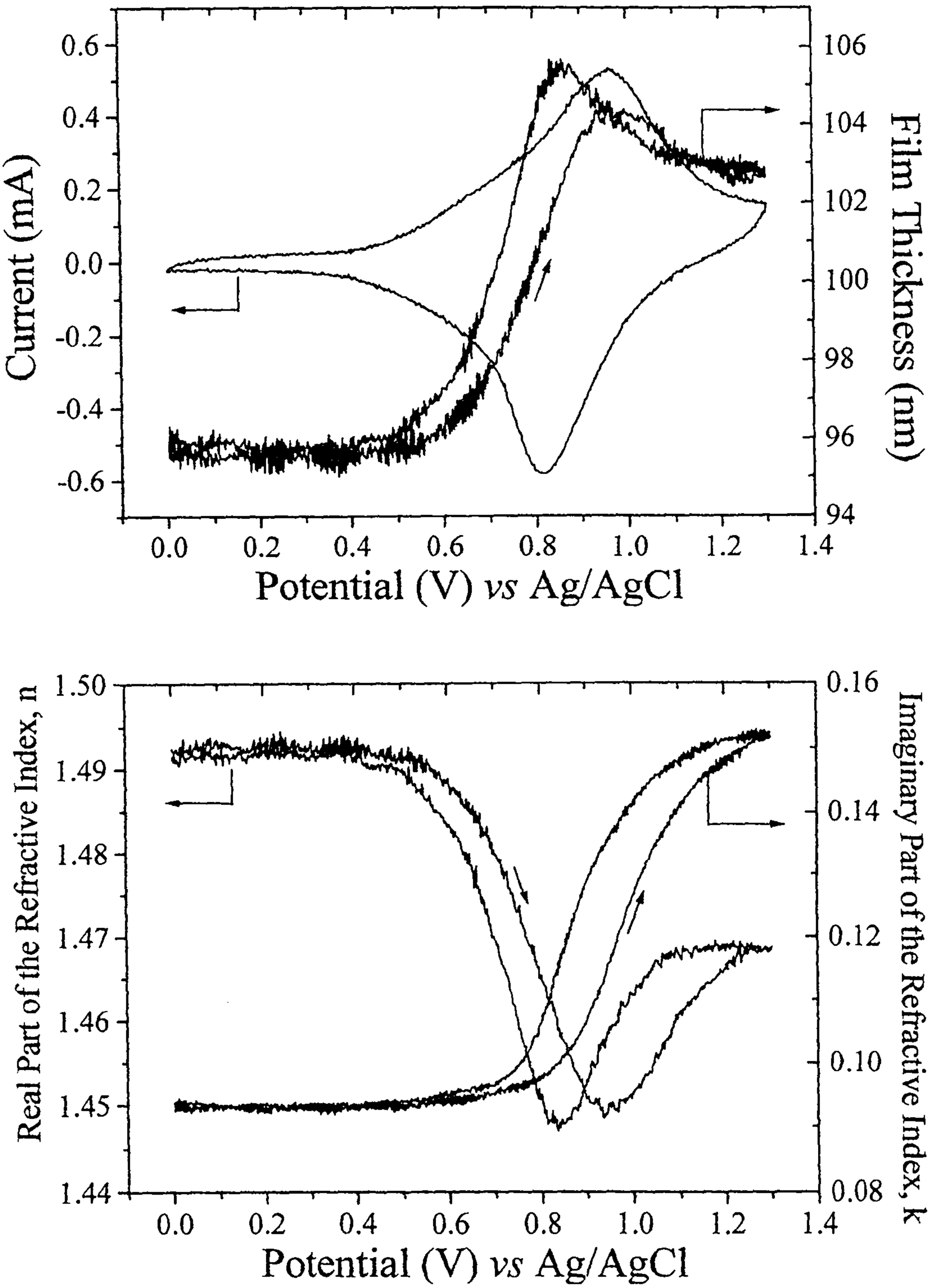

Fig. 4.10. Potential cycling of the poly[Ni(SaldMe)] electrode in 0.1 mol dm^{-3} TEAP in MeCN at 100 mV s^{-1}. The data gathered at 632.8 nm in Fig. 4.3 were fitted to a homogeneous model.

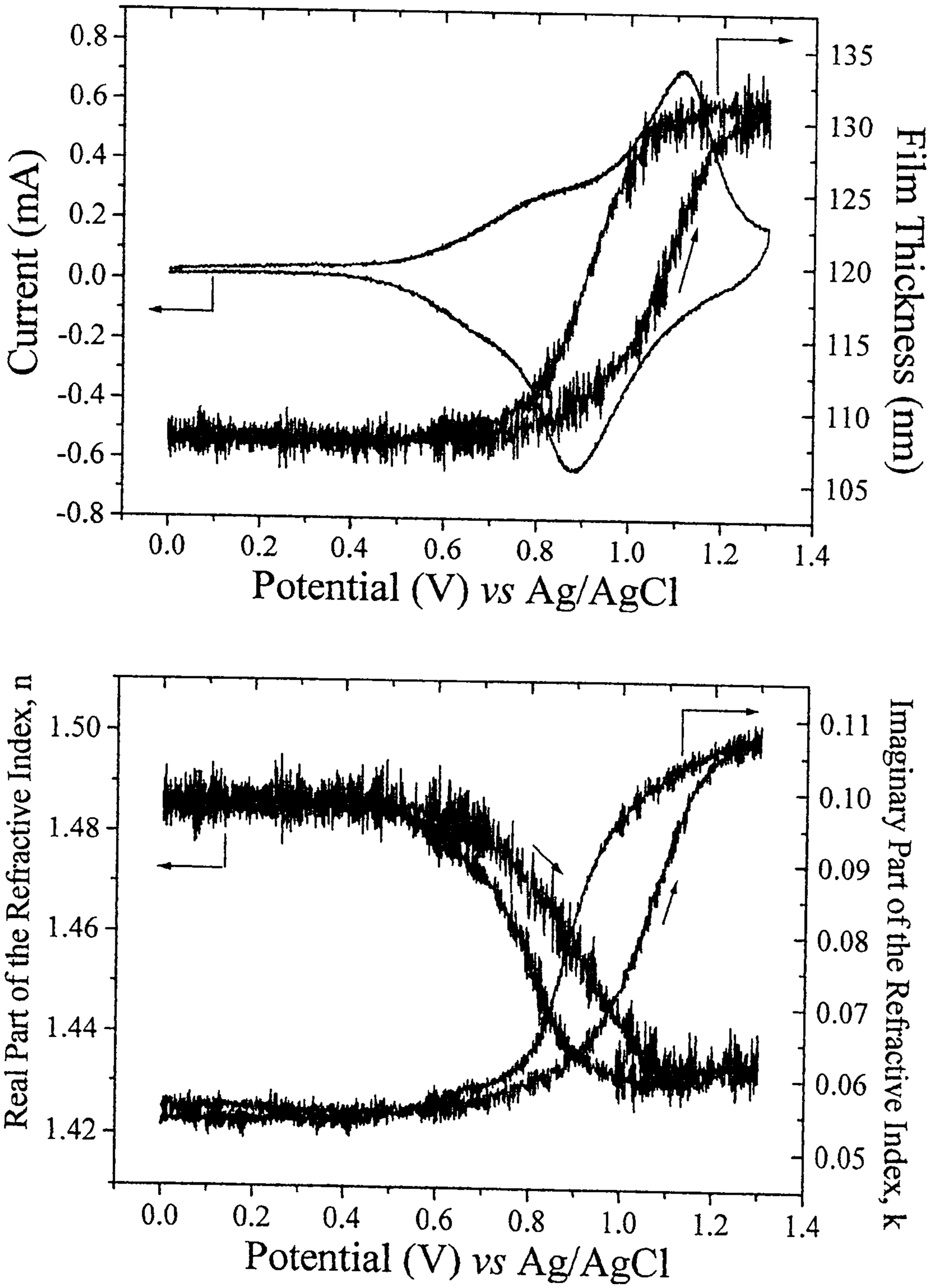

Fig. 4.11. Potential cycling of the poly[Ni(SaltMe)] electrode in 0.1 mol dm^{-3} TEAP in MeCN at 100 mV s^{-1}. The data gathered at 632.8 nm in Fig. 4.2 were fitted to a homogeneous model.

the growth and cycling of poly[Ni(SaldMe)] has not been investigated with EQCM, though is planned for the near future.

4.2.2.2 Fitted data for potential cycling and stepping of the modified electrodes

Figs. 4.10 and 4.11 show the fitted data for the potential cycling of the two as-grown films in monomer free electrolyte, and although growth of the two films appeared very similar, during the cycling marked differences were observed. One clear difference was the swelling of poly[Ni(SaltMe)] by about 13 nm, a *ca.* 14 % increase in thickness, between the last point recorded for film growth and the first point of cycling. The uptake of solvent by polymers at this point is not uncommon, often due to incomplete reduction at the end of the final cycle of growth resulting in electrolyte entering the film to compensate the charge. The electrolyte drags solvent with it causing the film to swell, which can easily occur in the time between the final growth data being gathered and the electrode being removed from the cell for the electrolyte to be replaced, and also between it being immersed in the monomer free electrolyte and the start of potential cycling; however, it is interesting to note that poly[Ni(SaldMe)] shows no similar increase, the film thickness being almost identical at the last point of growth and first of potential cycling.

During potential cycling, Poly[Ni(SaldMe)] shows very similar behaviour to that displayed during growth with three potential regions of behaviour being clearly visible: in the range 0-0.4 V the film is in the neutral form and all the parameters remain stationary; between *ca.* 0.4 - 0.95 V k shows a very slight increase, n decreases strongly and the thickness increases strongly; finally, over the range *ca.* 0.95-1.3 V, k shows a rapid increase, n a clear increase and the thickness

decreases slightly, which is exactly what was observed during growth. Poly[Ni(SaltMe)] displays similar behaviour at potentials lower than *ca.* 0.95 V but at higher potentials, though *k* rises in a similar manner, the thickness and *n* are almost stationary. In the case of the poly[Ni(SaldMe)] film two processes are occurring, the first between *ca.* 0.4 and 0.95 V and the second between *ca.* 0.95 - 1.3 V, though with the poly[Ni(SaltMe)] the behaviour between 0.4 and 0.95 V is the same as the dimethyl counterpart, the second process at higher potentials is absent.

For an optically absorbing film, the values of *n* and *k* are related to each other by the Kramers-Kronig dispersion relations [26]:

$$\alpha(\omega) - 1 = \frac{2}{\pi} P \int_0^\infty \frac{z\sigma(z)}{\left[z^2 - \omega^2\right]} dz \qquad \text{(Eqn. 4.1(a))}$$

$$\sigma(\omega) = \frac{2\omega}{\pi} P \int_0^\infty \frac{\left[\alpha(z) - 1\right]}{\left[\omega^2 - z^2\right]} dz \qquad \text{(Eqn. 4.1(b)}$$

where $\alpha = n^2 - k^2$, $\sigma = 2nk$, ω is the frequency of the probing beam, z a dummy variable, and P indicates the principle value of the integral is required. Equations 4.1(a) and (b) show that strong absorptions to lower energies (longer wavelengths) of the probe wavelength ($z<\omega$) lead to an decrease in the value of *n*, whereas the reverse is true for absorptions at higher energies. Hence the decrease in *n* between 0.4 and 0.95 V is well understood [27,28,29] and can be assigned to a strong absorption occurring in the near-IR due to the generation of charge carriers.

As the film is oxidised, solvent and electrolyte penetrate the chains to compensate the charge, leading to the swelling of the film observed. As with the growth, EQCM studies of the cycling of poly[Ni(SaltMe)] [24] show an excellent

correlation between the increase in mass observed upon oxidation and the variation in thickness predicted by ellipsometry. PBD experiments indicate electroneutrality of the polymer during oxidation is maintained primarily by the ingress of ClO_4^-, which coincides with a significant uptake of solvent. The ingress of solvent in itself will lower *n*, but refraction calculations showed that this cannot account for the whole extent of the change in value, and FTIR experiments clearly show absorption bands forming in the near-IR over this potential region.

With regard to the increase in *n* observed near the anodic limit for poly[Ni(SaldMe)], the Kramers-Kronig relations above describe how absorptions at lower wavelengths will cause an increase in the value of *n* at the probe wavelength, suggesting the increase seen at potentials greater than 0.95 V in poly[Ni(SaldMe)] may be assigned to an absorption in the UV region, the most likely cause of which would be charge transfer between the oxidised Ni centres of the monomer units and either the phenyl rings or Ni ions of other monomers, resulting in a charge transfer stack. The role of charge transfer in these polymers has been debated [7, 30], and it has been suggested that polymerisation occurs solely by the charge transfer stacking of monomer units to form a deposit [30], as shown in Fig. 4.12; however, the extensive and *reversible* swelling that occurs upon oxidation would seem to be conclusive evidence of the presence of carbon - carbon linkages between monomer units. It has also been postulated that a charge transfer stacked deposit is formed as a precursor to polymerisation [7]; however, the ellipsometric data clearly show the polymer films to consist primarily of solvent, as polymerisation is initiated which precludes the presence of a dense stacked deposit, though in the case of Ni(SaltMe) there is some charge passed before polymerisation which may be due to the formation of stacked oligomers in solution which then nucleate on the surface at the onset of

film formation. Although there is no evidence of a significant amount of charge transfer stacking prior to polymerisation, if it were to occur near the anodic limit in the poly[Ni(SaldMe)] film it would account for the absorption in the UV region, which was suggested to explain the increase in *n* observed between 0.95 and 1.3 V (Fig. 4.10), and the ordering of monomer units into stacks could also account for the for the contraction of the film observed over the same potential range. The UV-vis spectrum of poly[Ni(SaldMe)] has been recorded [31], and is very similar to that of poly[Ni(SaltMe)], it is difficult to determine any difference between the spectra in the UV region, though as a substantial part of the increase in *n* will have arisen from the egress of solvent, it is to be expected that any differences in the spectra would be small.

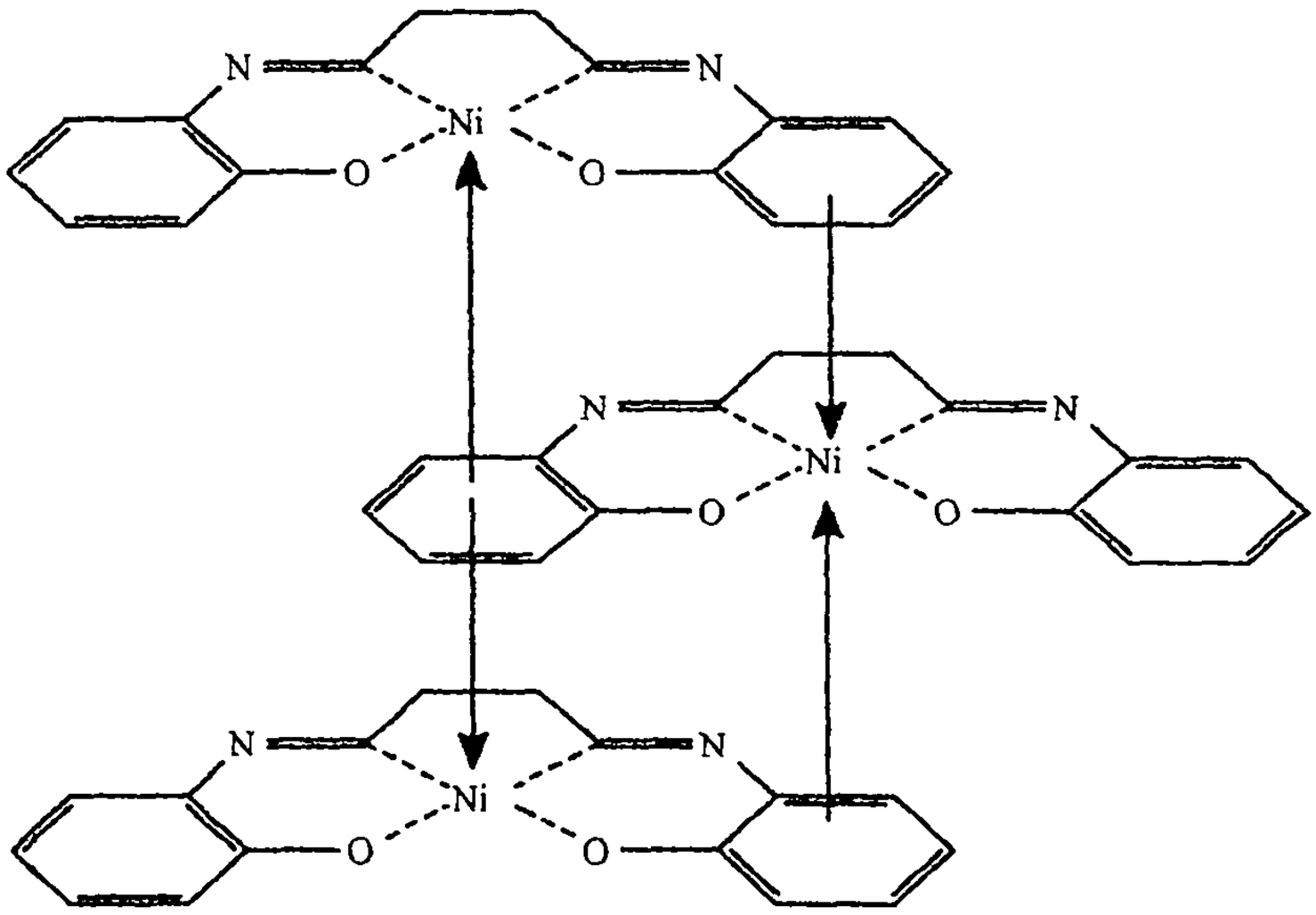

Fig. 4.12. Charge transfer stacking of Salen monomer units. Electron density from the phenyl rings is donated to oxidised metal centres to compensate the charge. This may also be possible between oxidised and neutral Ni centres.

Having provided a theory for the behaviour of the poly[Ni(SaldMe)] film it remains to be understood why contraction does not occur in poly[Ni(SaltMe)] also. It is possible to estimate the amount of charge per monomer unit in the oxidised polymer using the method first described for poly[Ni(Salen)] [3]. During polymerisation, each monomer unit will lose two electrons and two protons, one of each from each phenyl ring, and during oxidation the extent of doping per monomer is described as y electrons per phenyl ring and z electrons per metal site. This results in the ratio of the charge passed during growth to that passed during cycling being $(2+2y+z)/(2y+z)$. Experimentally this ratio was found to be 3.05 for poly[Ni(SaltMe)] [32], which, if oxidation is solely metal or solely ligand based, equates to either z = 0.96 or y = 0.48 respectively. In either case, or if both metal and ligand are partially oxidised, there is *ca.* 1 charge per monomer unit. Despite the doping level being 0.96 per monomer unit, FTIR, UV-vis and EPR provided substantial evidence that the oxidation was ligand based [32]. Using the same analysis for poly[Ni(SaldMe)] lead to very different results. The ratio of charge passed was found to be 4.23, which corresponds to a doping level of y = 0.31, or 2 positive charges delocalised over 3 monomer units. This may in part explain why the polymer contracts, as 3 monomers must become planar to delocalise the charge, resulting in a much greater degree of order than is imposed on poly[Ni(SaltMe)]. The value of y = 0.31 is exactly the value obtained for poly[Ni(Salen)] [3], however this has never been studied by ellipsometry due to problems with the stability of this polymer. If it were possible to gather any data on poly[Ni(Salen)], it would be interesting to see if the same contraction was present as with poly[Ni(SaldMe)].

The ease with which electrolyte can enter the films may also be a reason for the difference in behaviour of the two as poly[Ni(SaltMe)] swells by *ca.* 25 % of its

reduced thickness compared to only a *ca.* 8 % increase in thickness of poly[Ni(SaldMe)] before it starts to contract. Although previous studies have failed to identify the redox couple unambiguously, [2,5,7,11,16,33,34,35], given the prediction the two positive charges are delocalised over three monomer units, it is likely that both the ligand and the metal centre are partially oxidised: Salens are not completely conjugated, in order to achieve such extensive delocalisation either the saturated carbon-carbon bridge or the central metal ion will have to bear part of the charge, the metal seeming the more likely. Assuming partial oxidation of the Ni centres, coordination of solvent molecules to the axial positions of the metal may act as a stabilisation mechanism for the partial charge. In the case of poly[Ni(SaltMe)], solvent molecules are clearly very easily able to enter the film, however with poly[Ni(SaldMe)] significantly less solvent penetrates the film which may leave charge transfer as the only route for the Ni centres to become six coordinate. Certainly Ni(SaldMe) would be expected to stack better than Ni(SaltMe) being a slightly less bulky molecule; in the dry state Ni(SaldMe) has a unit cell volume 90 % of that of Ni(SaltMe) [36], which not only makes it more able to stack, but upon oxidation may lead to a denser film being formed initially which would account for the lower amount of solvent taken up. The crystallography [36] also showed that one methyl group in [Ni(SaldMe)] is orientated perpendicular to the plane of the ligand, while two methyl groups in [Ni(SaltMe)] are orientated perpendicular to the plane and in opposite directions. With the methyl groups orientated at this angle, the SaltMe has a clear disadvantage when attempting to stack. The swelling of poly[Ni(SaltMe)] between the end of growth and the start of the potential cycling may play a part in the difference in behaviour of the two films. Though not uncommon, 14 % is a surprisingly large increase and may be the result of a structural

alteration as yet not understood, which could cause the film to be so easily penetrated by electrolyte. Further support for the uptake of solvent being a pivotal factor comes from potential stepping experiments performed with the poly[Ni(SaldMe)] in which no contraction of the film was observed. The fitted data for the stepping is shown in Fig. 4.13. Although *n* still increases between 1.0 and 1.3 V, this is only about half of the increase in value observed during cycling, indicating charge transfer stacking is present, but the extent to which it occurs is lessened considerably. Instead of contracting, as observed during cycling, the thickness is held almost stationary between 1.0 and 1.3 V by the charge transfer stacking and the ingress of solvent roughly balancing one another. The film swells by *ca.* 12 % of the neutral thickness during stepping, compared to an 8 % increase during cycling, suggesting the scan rate of the CV is too fast for sufficient solvent to ingress into the film leading to a significant amount of charge transfer stacking as the (partially) oxidised Ni centres seek to become 6 coordinate, given a slower rate of potential increase the solvent can ingress sufficiently to prevent extensive charge transfer from occurring.

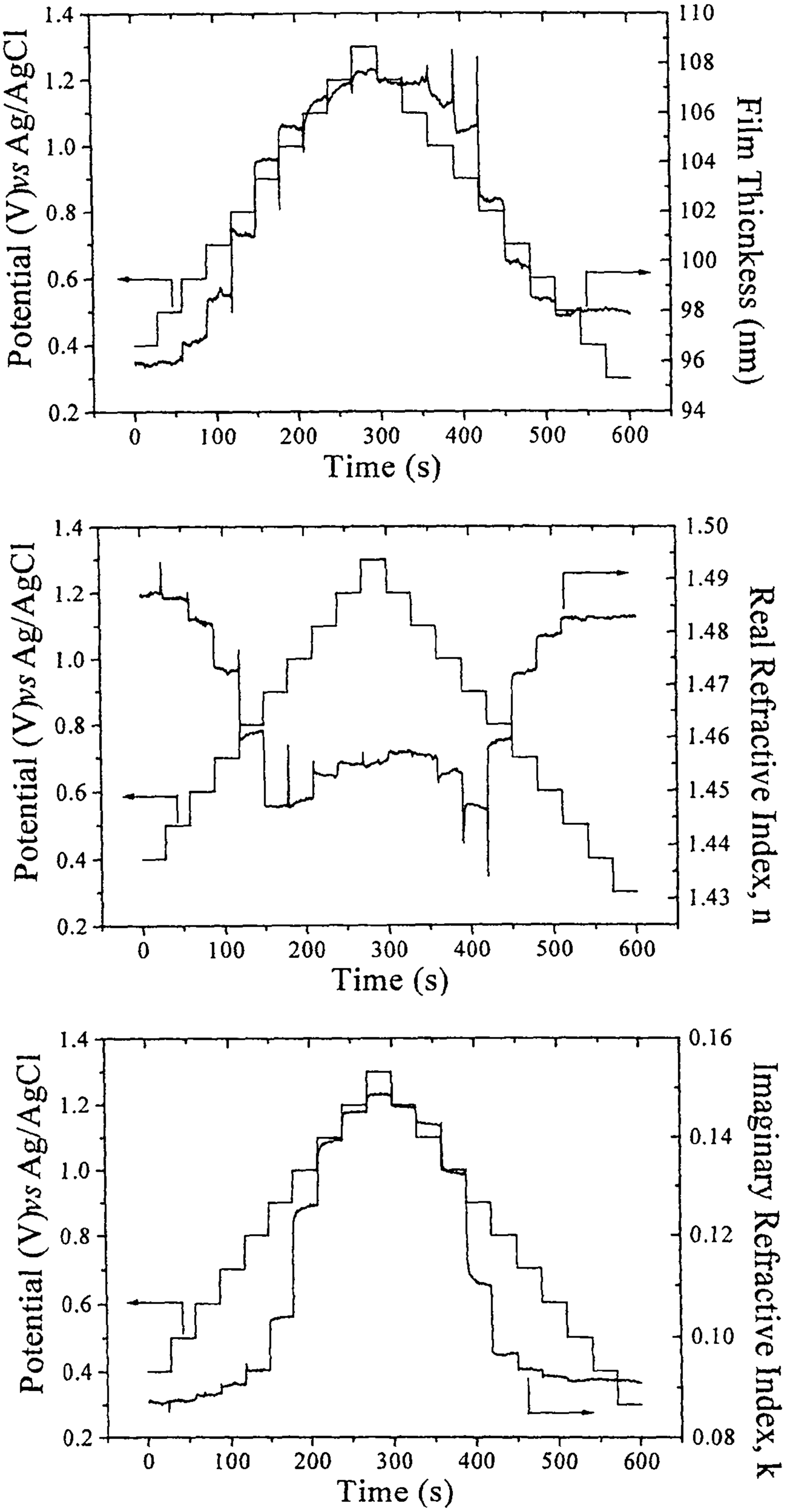

Fig. 4.13. Potential stepping of poly[Ni(SaldMe)]. 100 mV steps were performed with 35 s at each potential. Data gathered at 632.8 nm were fitted to a homogeneous model to generate the behaviour of *n*, *k* and thickness shown above.

4.2.3 Supporting FTIR data for poly[Ni(SaltMe)]

The investigation of the charge transport processes in poly[Ni(SaldMe)] using *in-situ* FTIR is planned; however data for poly[Ni(SaltMe)] has already been gathered and analysed. As described in the experimental chapter, the FTIR experiments were performed by stepping the potential of the working electrode rather than cycling, and spectra collected at each potential. Fig. 4.14 shows the cumulative charge passed during potential cycling (squares) of the film, and stepping (circles) during an FTIR experiment using the same film. There is clearly good agreement between the two sets of data, and both clearly show charge trapping by the polymer, as mentioned earlier in the chapter. It is interesting such good agreement between the sets of data is observed, particularly with regard to the extent of charge trapping, given the

Potential (V) *vs* Ag/Ag^{+}

Fig. 4.14. The cumulative charge passed during cyclic voltammetry at 100 mV s^{-1} (squares) and stepping with 35 s at each potential during an FTIR experiment (circles). Both experiments performed in 0.1 mol dm^{-3} TEAP in MeCN.

considerably longer time scale of the FTIR experiment, i.e. 35 s per data point, compared to the 100 mV s^{-1} scan rate employed in the voltammetric experiments. This charge trapping is once again a reversible process, as demonstrated by holding the polymer *ca.* 100 s at 0.0 V which returns it to a completely neutral state. Fig. 4.15 shows the absolute (i.e. normalised to the bare Pt electrode in MeCN/0.1 mol dm^{-3} TEAP) *in-situ* FTIR spectra of (i) the monomer and (ii) the polymer at 0.0 V. Between 1300 and 1550 cm^{-1} the monomer spectrum shows a broad loss feature, attributable to acetonitrile and to incomplete nulling of the solvent features, although some gain features in this region are still visible. The bands at 1606, 1534 and 1328 cm^{-1} may be assigned to the C=N stretching vibration, and vibrations of the chelate ring [3,37], and clearly occur at the same frequencies in the monomer and

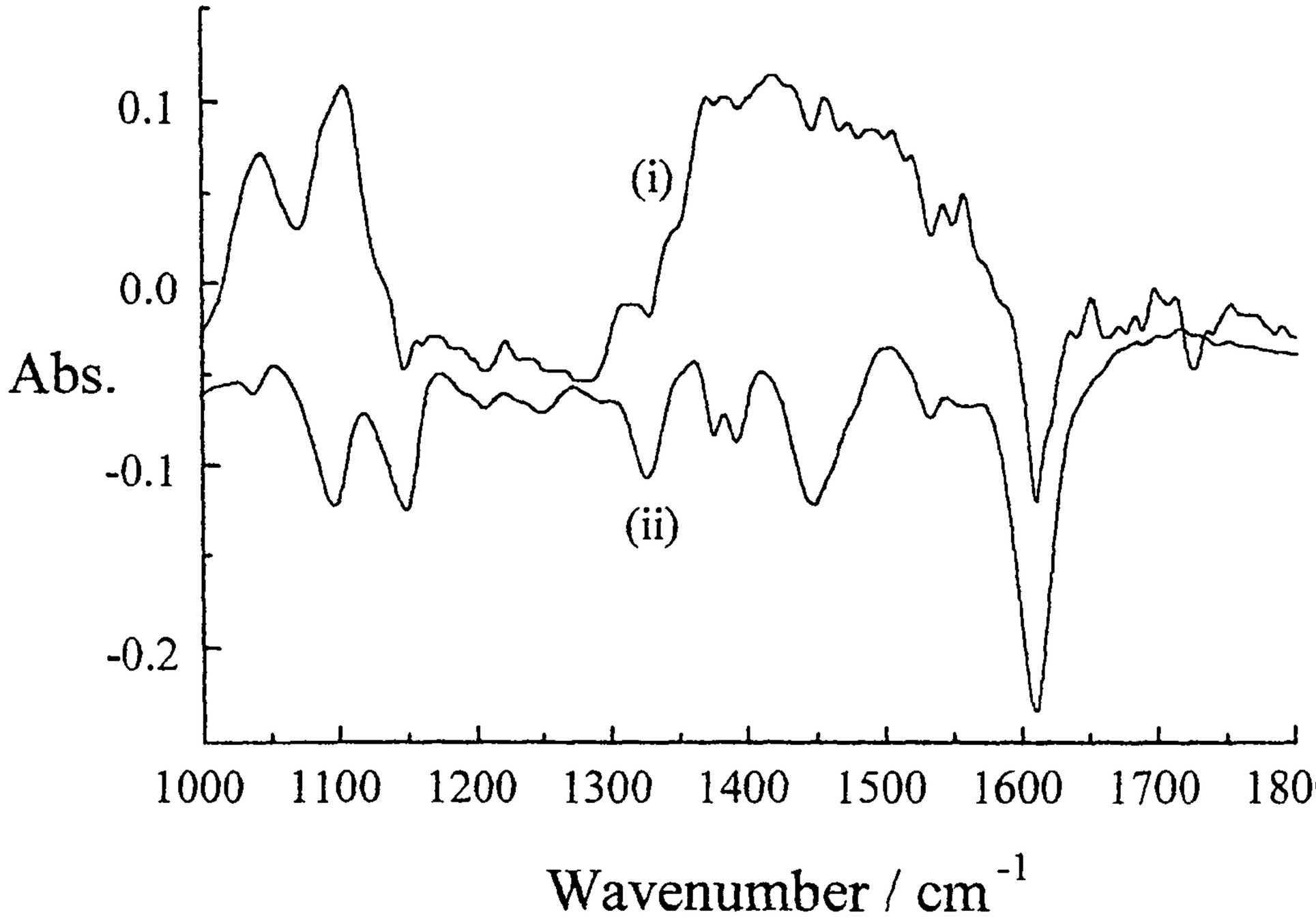

Fig. 4.15.Absolute in situ FTIR reflectance spectra 8 cm^{-1} resolution, 100 co-added and averaged scans, 40 kHz detector speed, in 0.1 mol dm^{-3} TEAP/MeCN of (i) 1 mmol dm^{-3} [Ni(SaltMe)] and (ii) the poly[Ni(SaltMe)] modified electrode at 0.0 V.

polymer, suggesting the coordination sphere of the nickel centre is unaffected by the polymerisation process. A number of other weak gain features can still be seen between 1300 and 1500 cm^{-1} in the spectrum of the monomer, which is the region in which phenyl ring vibrations would be expected to absorb. The differences in this region between the spectra for polymer and monomer suggest polymerisation occurs

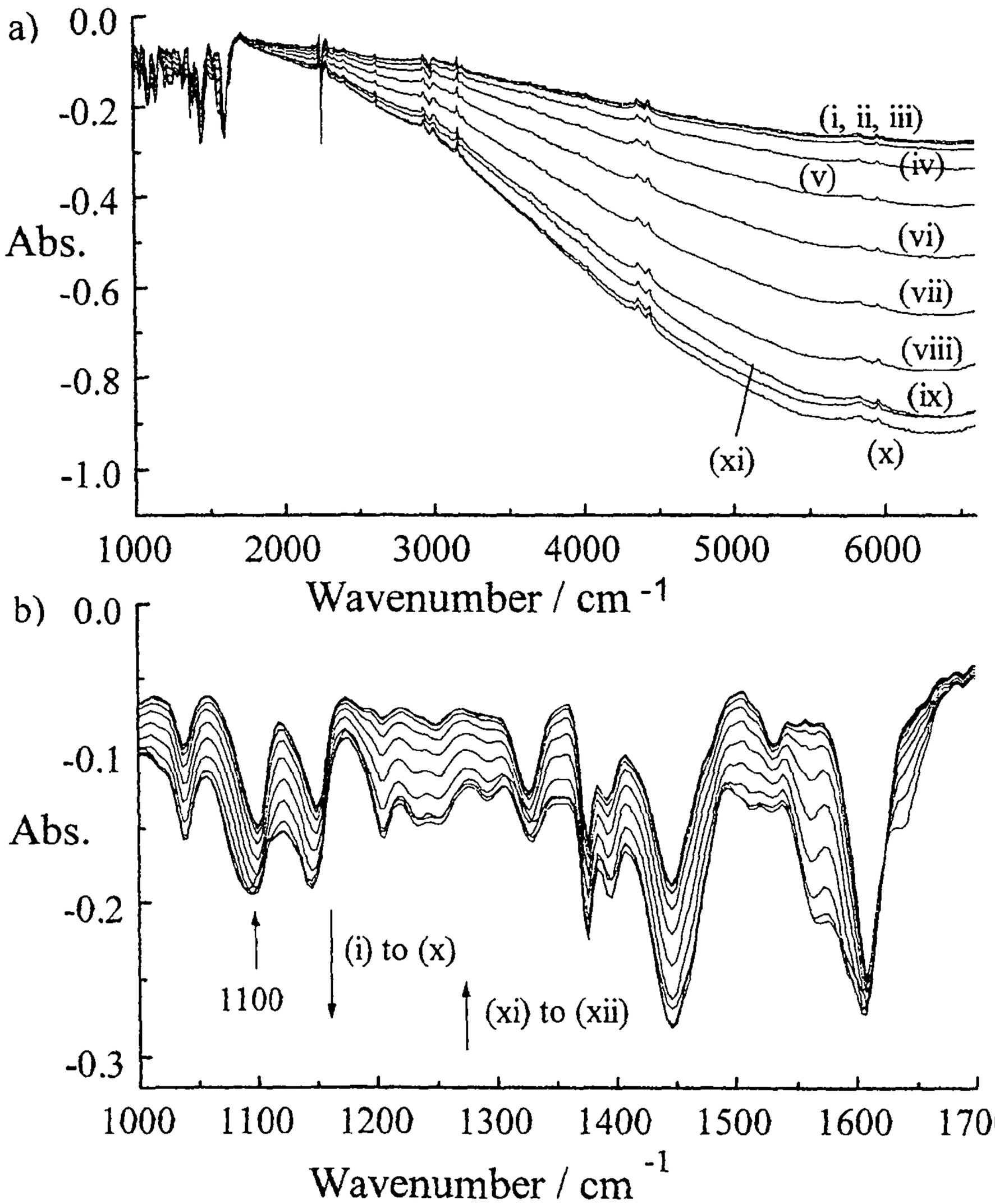

Fig. 4.16. Absolute reflectance spectra, conditions as in Fig. 4.15, spectra gathered at 0.1 V intervals: a) full range spectrum from 0.3 V i) to 1.3 V xi) normalised to 0 V, b) 1000-1700 cm^{-1} spectral region of a).

at the phenyl rings, as has been observed even more clearly for poly[Ni(Salen)] [3]. Figs. 4.16(a) and (b) show absolute spectra taken during the oxidation of the polymer in 0.10 V steps from 0.3 to 1.3 V. Above *ca.* 1700 cm^{-1} a broad electronic absorption grows, resulting from the generation of charge carriers in the polymer on oxidation. The growth of a strong optical absorption in the near-IR region as oxidation occurs was predicted from the ellipsometry (see Fig. 4.11) to explain the sharp decrease seen in n at 632.8 nm. Fig. 4.16(b) shows the IRAV region, which includes frequencies at which characteristic phenyl vibrations are expected to absorb, again indicating significant ligand involvement.

4.3 Conclusions

Polymerisation of both Ni(SaltMe) and Ni(SaldMe) does not occur until *ca.* 0.95 V, and proceeds by a consolidation process in both cases to yield homogenous films *ca.* 100 nm in thickness. The only significant difference in the growth of theses two films appears to be the clear increase in thickness poly[Ni(SaltMe)] displays during the last two cycles of growth as the film next to the electrode becomes sufficiently dense for new layers of polymer to be deposited on top of it, whereas growth occurs by consolidation throughout all five cycles for poly[Ni(SaldMe)].

During potential cycling after growth the behaviour of poly[Ni(SaldMe)] is the same as that observed during growth, though poly[Ni(SaltMe)], while showing the first oxidation process, no longer exhibits an increase in *n* or a contraction of the film above 0.95 V. This contraction appears to be due to the occurrence of charge transfer stacking, which would generate a UV absorption, accounting for the increase in *n* observed over the same potential range.

During stepping experiments the contraction of the poly[Ni(SaldMe)] film at higher potentials is absent, strongly suggesting the presence of charge transfer is due to the ability of solvent to penetrate the film and coordinate axially with the oxidised metal centres of the monomer units.

4.4 References

1. K. A. Goldsby, J. K. Blaho, L. A. Hofferkamp, *Polyhedron*, 1989, **8**,113.
2. K. A. Goldsby, *J. Coord. Chem*. 1988, **19**, 83.
3. M. Vilas-Boas, C. Freire, B. de Castro, P. A Christensen, A. R. Hillman, *Inorg. Chem.*, 1997, **36**, 4919.
4. M. Vilas-Boas, C. Freire, B. de Castro, P. A. Christensen, A. R. Hillman, *Chem. Eur. J.*, 2001, 7, 139.
5. P. Audbert, P. Capdevielle, M. Maumy, *New J., Chem*., 1992, **16**, 697.
6. P. Audbert, P. Capdevielle, M. Maumy, *New J., Chem*., 1991, **15**, 235.
7. C. E. Dahm, D. G. Peters, J. Simonet, *J. Electroanal. Chem*.,1996, **410**, 163.
8. P. Audbert, P. Capdevielle, M. Maumy, *Synth. Met*., 1991, **41**, 3049.
9. C. Freire, B. de Castro, *J. Chem. Soc., Dalton Trans*., 1998, 1491.
10. K. A. Goldsby, J. K. Blaho, L. A. Hofferkamp, *Polyhedron*, 1989, **8**,113.
11. C. E. Dahm, D. G. Peters, *J. Electroanal. Chem*. 1996, **406**, 119.
12. K. S. Alleman, D. G. Peters, *J. Electroanal. Chem*., 1998, **451**, 121.
13. A. D. Butler, D. G. Peters, *J. Electrochem. Soc*., 1997, **144**, 4212.
14. C. Gosden, J. B. Kerr, D. Pletcher, R. Roas, *J. Electroanal. Chem*., 1981, **117**, 101.
15. C. Gosden, K. P. Healy, D. Pletcher, *J. Chem. Soc, Dalton Trans*. 1978, 972.
16. P. Audbert, P Hapiot, P. Capdevielle, M. Maumy, *J. Electroanal. Chem*., 1992, **338**, 269.
17. M. de C. T Corrondo, B. de Castro, A. M. Coelho, D. Domingues, C. Freire, J. Morais, *Inorg. Chim. Acta*, 1993, **205**, 157.

18. F. Azevedo, M. de C. T. Carrondo, B. de Castro, M. Convery, D. Domingues, C. Freire, M. Teresa-Duarte, K. Nielsen, I. C. Santos, *Inorg. Chim. Acta*, 1994, **219**, 43.

19. H. D. Abruña, P. Denisevich, M. Umaña, T. J. Meyer, R. W. Murray, *J. Am. Chem. Soc.*, 1981, **103**, 1.

20. G. Zotti, G. Schiavon, S. Zecchin, *Synth. Met.*, 1995, **72**, 275.

21. I. Jureviciute, S. Bruckenstein, A. R. Hillman, *J. Electroanal. Chem.*, 2000, **488**, 73.

22. P. A. Christensen, A. Hamnett, *Electrochim. Acta*, 1991, **36**, 1263.

23. O. A. Semenikhin, E. V. Ovsyannikova, M. R. Eherenburg, N. M. Alpatova, V. E. Kazarinov, *J. Electroanal. Chem.*, 2000, **494**, 1.

24. M. Vilas-Boas, M. J. Henderson, C. Freire, A. R. Hillman, E. Vieil, *Chem. Eur. J.*, 2000, **6**, 1160.

25. Handbook of Chemistry and Physics, 66th Ed., 1985-1986, CRC Press, Inc.

26. A.S. Davydov, *Quantum Mechanics*, 2nd Ed., 1976, Pergamon Press Ltd.

27. S. Gottesfeld in *Electroanalytical Chemistry*, ed. A. J. Bard, Marcel Dekker, New York, 1989, vol. 15.

28. Abd El-Rahman, A. Kudelka, J. W. Shultze, *Ber. Bunsen-Ges. Phys. Chem.*, 1996, **100**, 1798.

29. A. Hamnett, A. R, Hillman, *Ber. Bunsen-Ges. Phys. Chem.*, 1987, **91**, 329.

30. V. V. Vasilieva, K. P. Balashev, A. M. Timonov, *Russ. J. Electrochem.*, 1998, **34**, 978.

31. M. J. R. Vilas-Boas, PhD Thesis, Eléctrodos Modificados por *Polimerização In-Situ* de Complexos de Níquel(II) com Bases de Schiff., Departmento de Química, Universidade do Porto, 2000.

32. M. Vilas-Boas, C. Freire, B. de Castro, A. R. Hillman, *J. Phys. Chem. B*, 1998, **102**, 8533.

33. M. Mauny, P. Capdevielle, P. H. Aubert, P. Audebert. M. Roche, *New J. Chem.*, 1997, **21**, 621.

34. K. A. Goldsby, L. A. Hoferkamp, *Chem. Mater.*, 1989, **1**, 348-352.

35. F. Bedioui, E. L. Abbe, S. Gutierrez-Granados, J. Devynck, *J. Electroanal. Chem.*, 1991, **301**, 267.

36. I. C. Santos, M. Vilas-Boas, M. F. M. Piedade, C. Frerie, M. T. Duarte, B. de Castro, *Polyhedron*, 2000, **19**, 655.

37. M. Dutta, D. H. Brown, W. E. Smith, *Spectrochim. Acta A*, 1983, **39**, 37.

5.1 Introduction

Further to experiments looking at the effect of altering substituents on the bridging carbons, altering the groups on the phenyl rings has also been shown to have a profound effect upon the nature of the monomer and the polymer film formed by its electro-oxidation, as has been demonstrated for methoxy substituted Salens of Cu [1], Co [3], and Ni [2,3,4]. Salens with methoxy substituents on the phenyl rings have been found to be more conductive in electrolyte solution than non-substituted Salens, and in all cases described in the literature display a redox potential *ca.* 200 mV lower than their homologues [1-4]. Unlike non-substituted Salens, those with a methoxy substituent also display conductivity in the dry state of *ca.* 10^{-3} S cm^{-1} [1,3], a figure which appears to be independent of the identity of the central metal ion [3].

In this chapter, the growth and cycling of a Nickel methoxy tetramethyl Salen, Ni(MeOSaltMe), (see Fig. 5.1) is described and compared with the behaviour of Ni(SaltMe) discussed in the previous chapter, (also see Fig. 5.1).

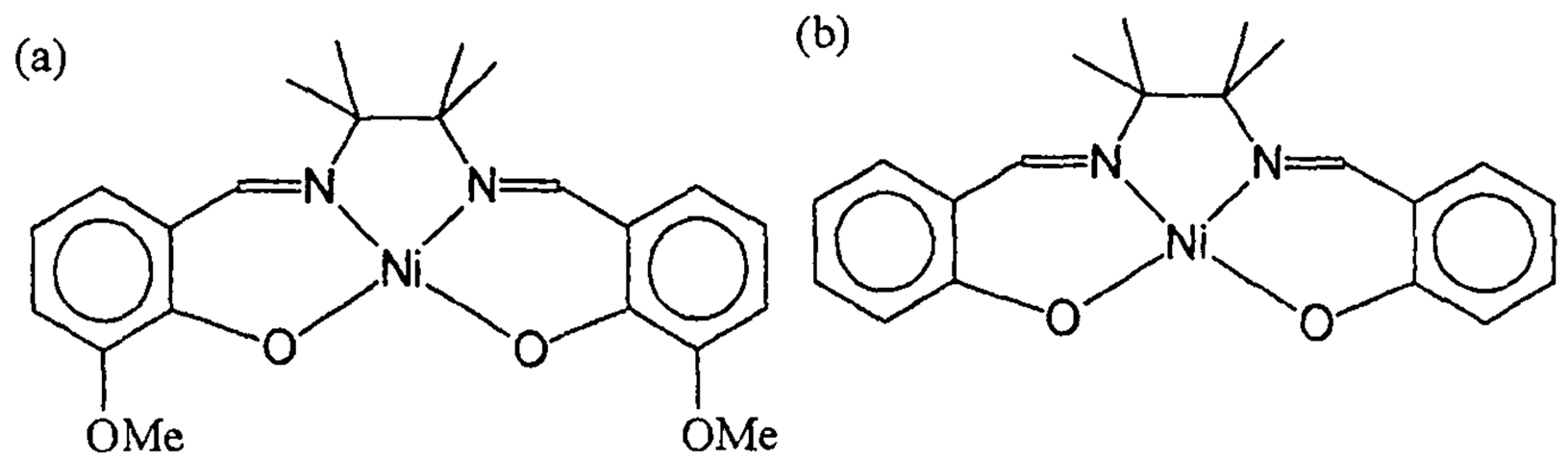

Fig. 5.1. The structure of (a) N,N'-2,3-dimethylpropane-2,3-diyl-bis(3-methoxysalicylideneiminate)nickel(II), or [Ni(OMeSaltMe)], and (b) [Ni(SaltMe)]

5.2 Results and Discussion

5.2.1 Experimental data

5.2.1.1 Growth of Poly[Ni(OMeSaltMe)]

Polymerisation was performed in same manner as for poly[Ni(SaltMe)], a Pt working electrode was cycled five times between 0 and 1.3 V *vs* Ag/Ag^+ in a 1 mmol dm^{-3} solution of the monomer and 0.1 mol dm^{-3} TEAP in acetonitrile. The ellipsometric data for poly[Ni(OMeSaltMe)] are shown in Fig. 5.2 with the data for poly[Ni(SaltMe)] reproduced in Fig 5.3 for comparison. The data for the two films clearly differ in many aspects over the course of growth. Delta shows similar behaviour for the first three cycles of growth, showing a slight increase in value between *ca.* 0.4 and 0.8 V and then a marked decrease in value at higher potential during the anodic sweep and decreasing in value with each subsequent cycle, but cycle four (and particularly cycle five) of growth for poly[Ni(OMeSaltMe)] show delta for the oxidised film increasing with each cycle, and during the cathodic sweep between 1.3 and 1.0 V on cycle five delta continues to increase. Psi displays similar qualitative behaviour during the growth of the two films, remaining stationary up to *ca.* 0.6 V, decreasing slightly between *ca.* 0.6 and 0.8 V, and increasing strongly during remainder of the anodic excursion, however the extent of this increase is markedly different, *ca.* 4 degrees for poly[Ni(SaltMe)] but up to 35 degrees for poly[Ni(OMeSaltMe)]. The behaviour of the relative intensity is very similar for the two films, displaying a slight decrease between 0.4 - 0.8 V then decreasing strongly at higher potentials, and steadily decreasing with each cycle indicating that both films

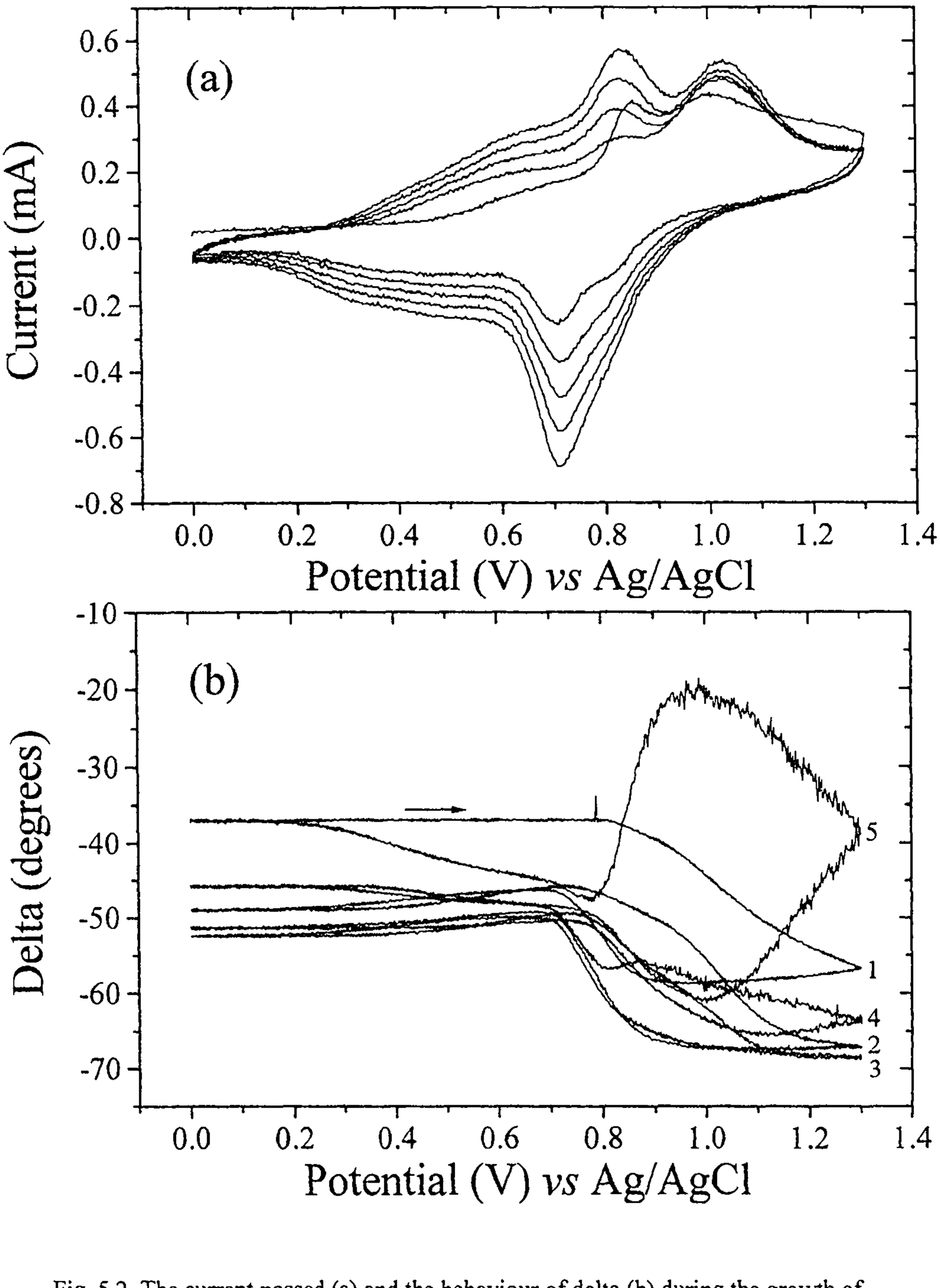

Fig. 5.2. The current passed (a) and the behaviour of delta (b) during the growth of poly[Ni(OMeSaltMe)]. The film was grown for five cycles (cycle number shown at anodic limit) between 0 and 1.3 V at 100 mV s^{-1} in 0.1 mol dm^{-3} TEAP and 1 mmol dm^{-3} of the monomer in MeCN.

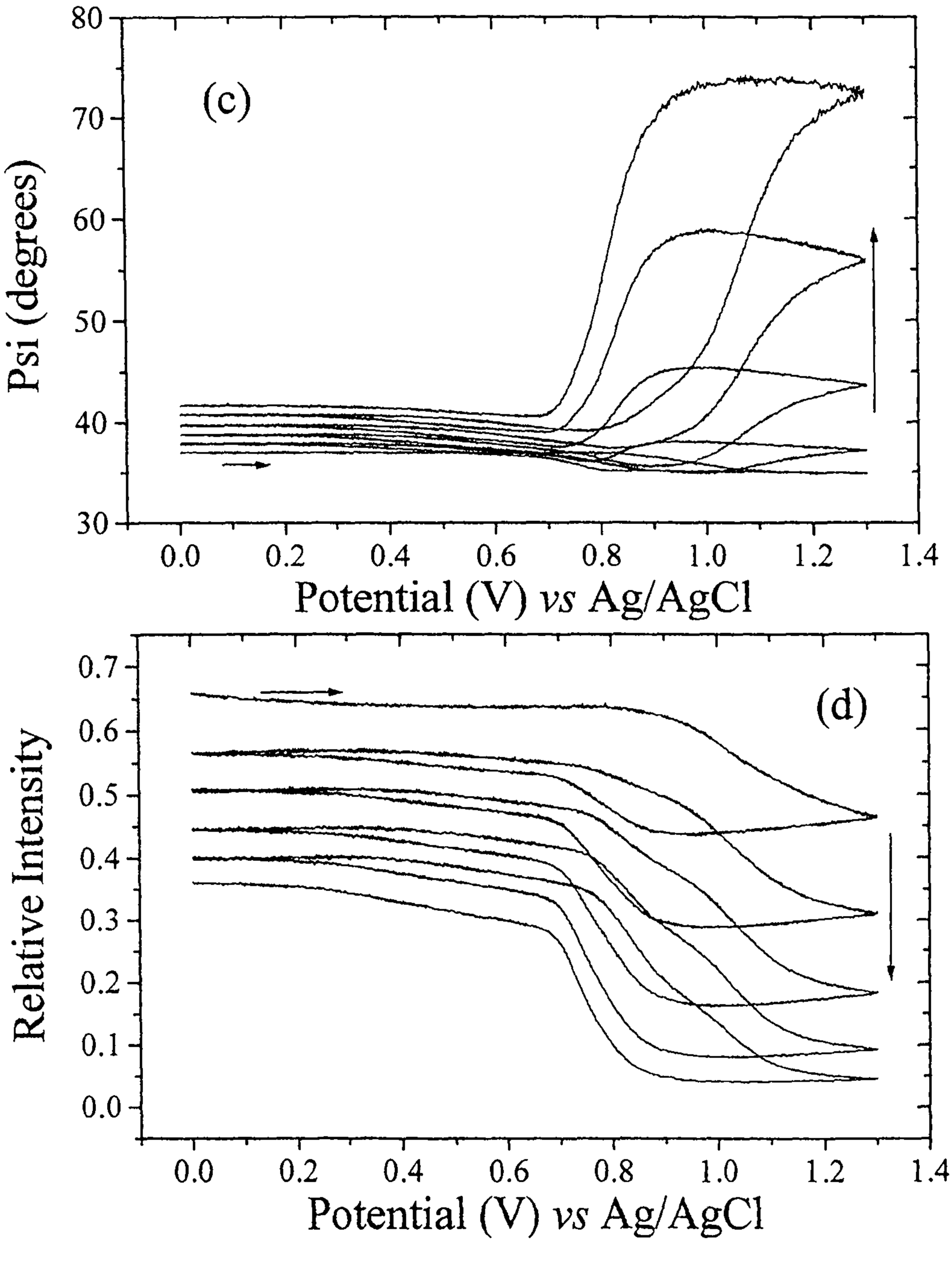

Fig. 5.2. The behaviour of psi (c) and intensity (d) during the growth of poly[Ni(OMeSaltMe)]. The film was grown for five cycles between 0 and 1.3 V at 100 mV s^{-1} in 0.1 mol dm^{-3} TEAP and 1 mmol dm^{-3} of the monomer in MeCN.

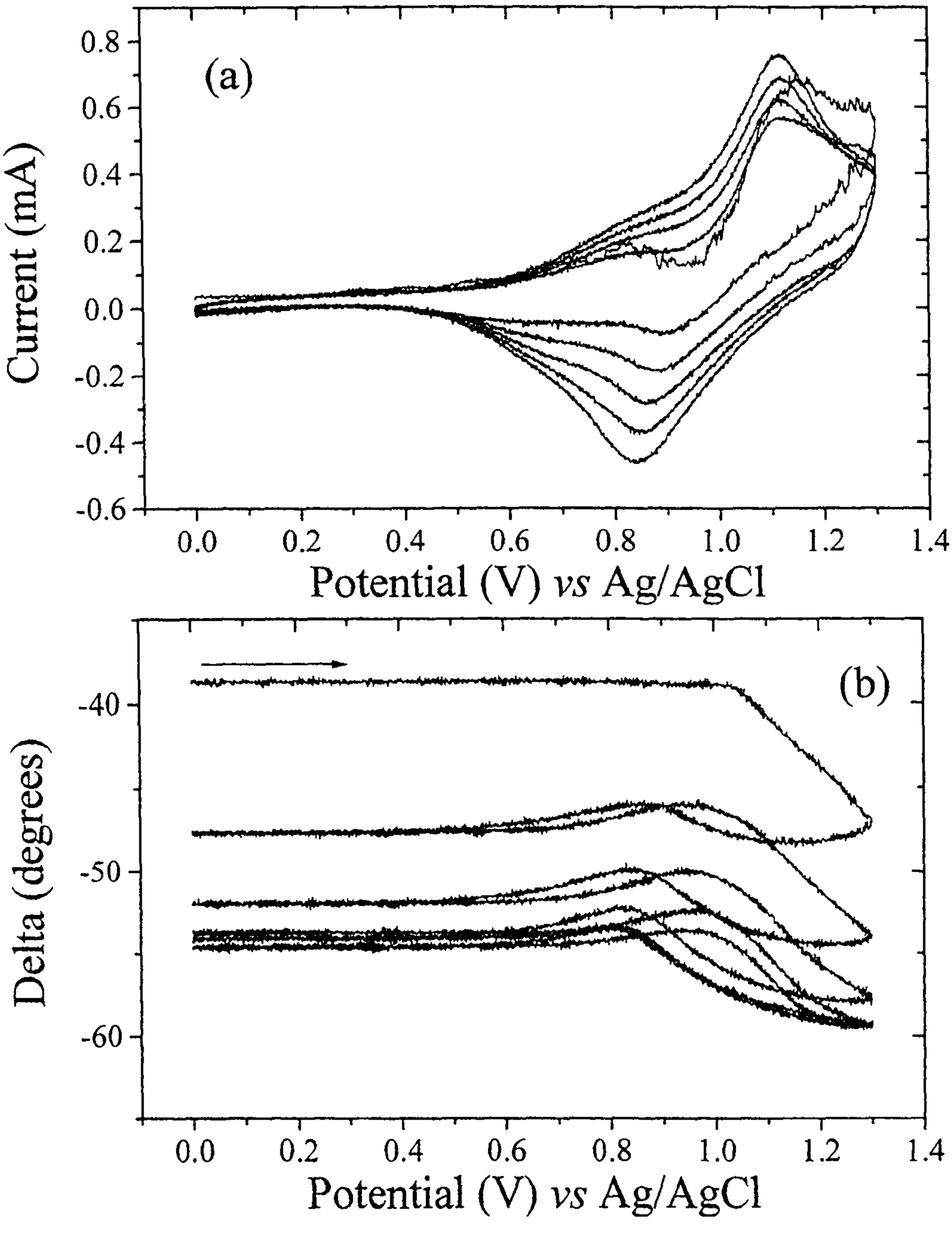

Fig. 5.3. The current passed (a) and the behaviour of delta (b) during the growth of poly[Ni(SaltMe)]. The film was grown for five cycles between 0 and 1.3 V at 100 mV s^{-1} in 0.1 mol dm^{-3} TEAP and 1 mmol dm^{-3} of the monomer in MeCN.

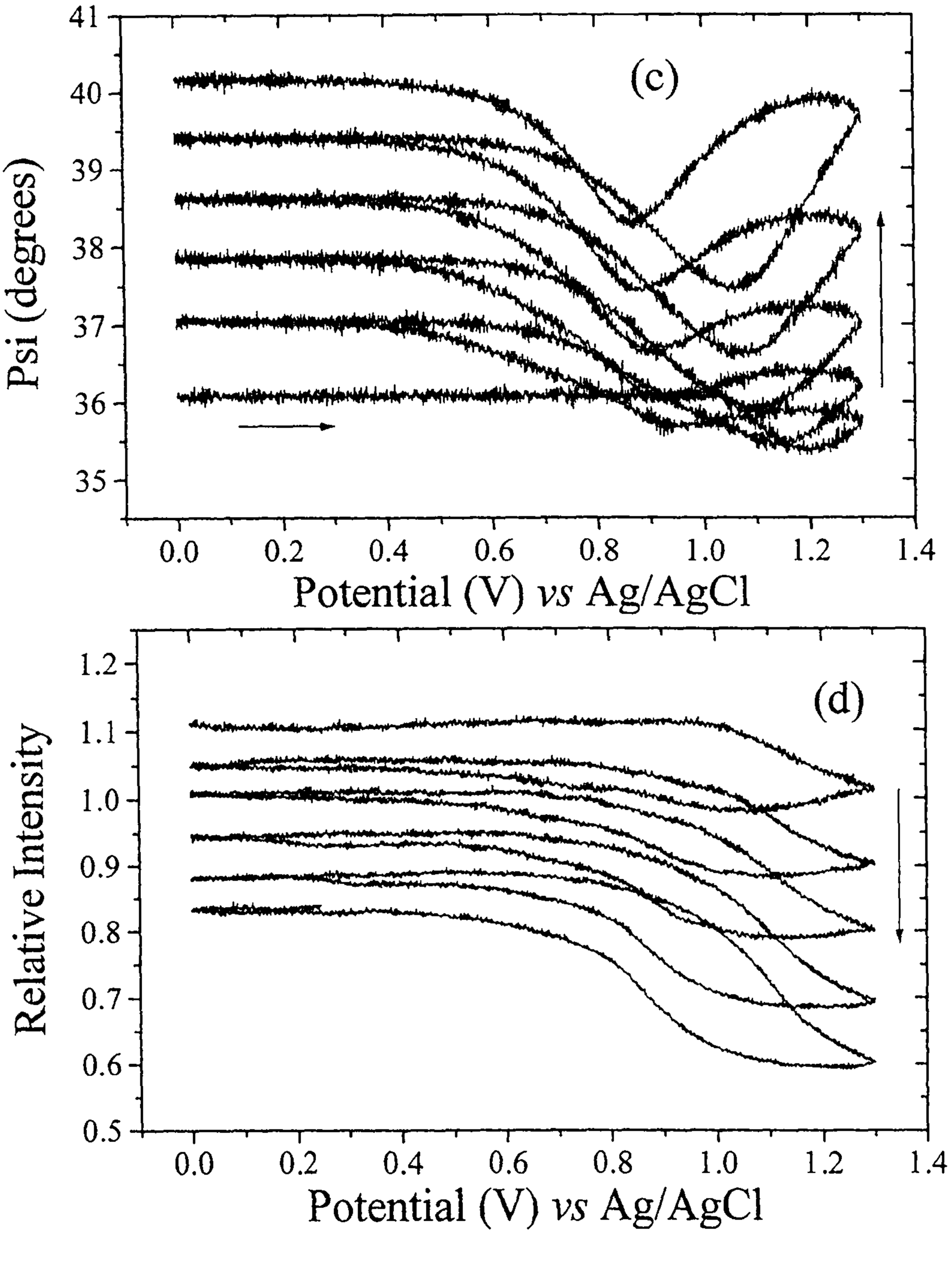

Fig. 5.3. The behaviour of psi (c) and the intensity (d) during the growth of poly[Ni(OMeSaltMe)]. The film was grown for five cycles between 0 and 1.3 V at 100 mV s^{-1} in 0.1 mol dm^{-3} TEAP and 1 mmol dm^{-3} of the monomer in MeCN.

absorb at 632.6 nm, even to some extent in the reduced state. The CVs are also markedly different, with a new peak present at *ca.* 0.8 V during the polymerisation of Ni(OMeSaltMe) as described in the literature [1-4], compared to the single peak displayed during the formation of poly[Ni(SaltMe)]. An obvious suggestion would be the presence of the methoxy groups on the ligand alters the metal and ligand band energies and separates the two oxidation processes. Studies of methoxy Salens have found the redox potential to be 200 mV lower than that of the relevant homologues [2,3,4], a figure which appears not to depend on the identity of the central metal. In Fig. 5.2 polymerisation of Ni(OMeSaltMe) can be seen to occur *ca.* 200 mV earlier than Ni(SaltMe) as delta and psi start to alter at *ca.* 0.8 V on the first oxidative scan, corresponding to first oxidative wave, instead of at 1.0 V for Ni(SaltMe). This would again suggest the presence of the methoxy groups has an effect on the band energies, raising the HOMO and making oxidation easier.

5.2.1.2 Ellipsometric data for potential cycling of the modified electrodes.

The data for cycling after growth are shown in Figs. 5.4 and 5.5 for poly[Ni(OMeSaltMe)] and poly[Ni(SaltMe)]. The two anodic peaks displayed in the CV of polymerisation of poly[Ni(OMeSaltMe)] no longer appear, and a single anodic wave at *ca.* 0.9 V is now the main peak, preceded by a broad wave between *ca.* 0.2 and 0.7 V, which would appear to correspond to the shoulder for poly[Ni(SaltMe)] between *ca.* 0.4 and 0.9 V, given the 200 mV difference in the onset of polymerisation observed above. While the ellipsometric data for the potential cycling

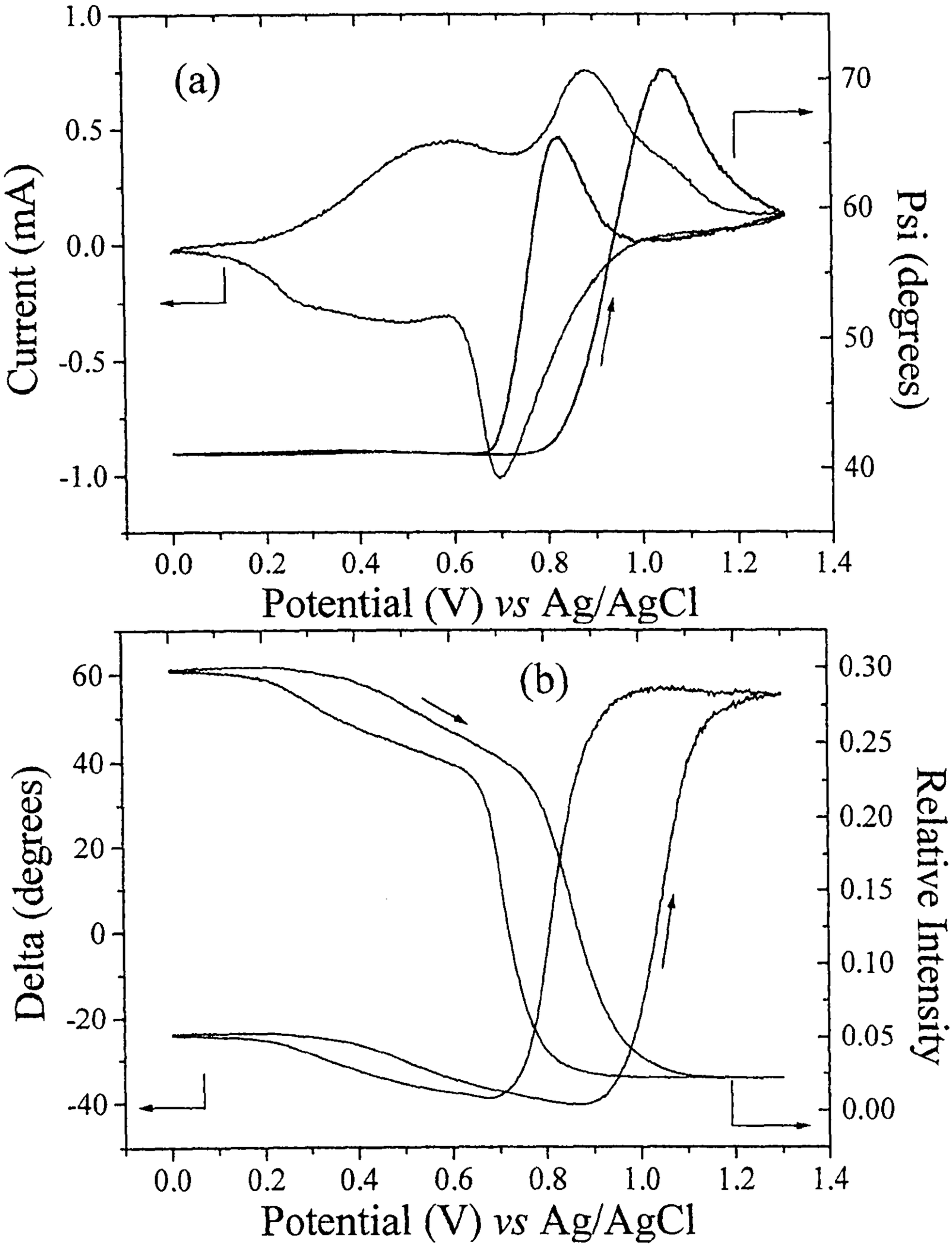

Fig. 5.4 The current passed and behaviour of psi (a), delta and intensity (b) during potential cycling of poly[Ni(OMeSaltMe)]. The film was cycled at 100 mV s^{-1} in 0.1 mol dm^{-3} TEAP in MeCN.

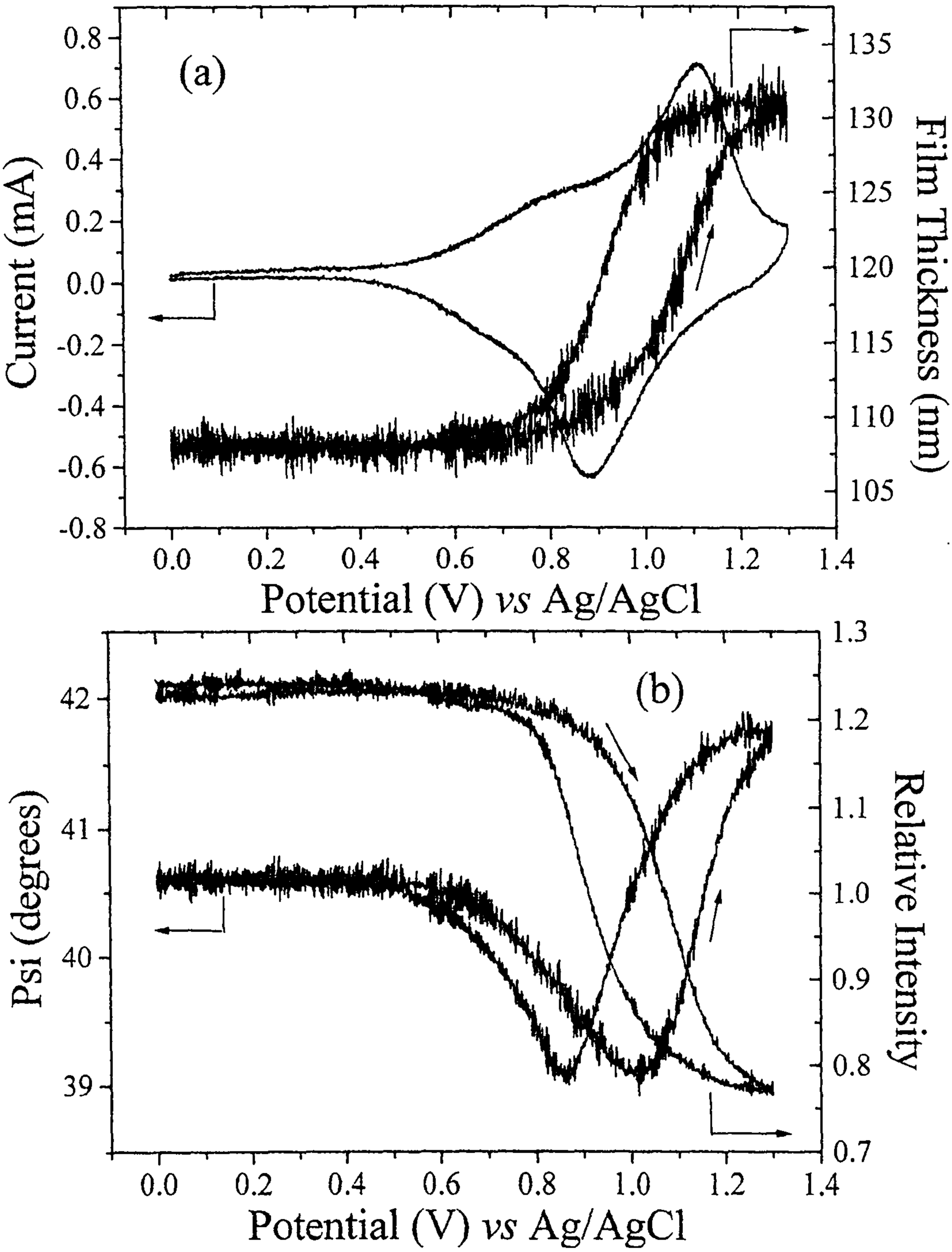

Fig. 5.5 The current passed and behaviour of delta (a), psi and intensity (b) during potential cycling of poly[Ni(SaltMe)]. The film was cycled at 100 mV s^{-1} in 0.1 mol dm^{-3} TEAP in MeCN.

of poly[Ni(SaltMe)] display little difference from that recorded during the growth, the intensity and delta decreasing strongly with oxidation, and psi decreasing between *ca.* 0.5 and 1.0 V then strongly increasing at higher potentials, however the data for poly[Ni(OMeSaltMe)] are markedly different from that recorded during growth. Between 0 and *ca.* 0.8 V psi is stationary, and delta and the intensity show a slight decrease, between 0.8-1.0 V psi and delta strongly increase, the intensity strongly decreases, and between 1.0-1.3 V psi shows a strong decrease not seen during growth, whilst delta and intensity were almost stationary.

5.2.1.3 Potential stepping of Poly[Ni(OMeSaltMe)]

To assess the effect of a slower potential sweep rate the poly[Ni(OMeSaltMe)] modified electrode was also investigated under potential stepping conditions. The potential was ramped from 0 to 1.3 V and down again in 100 mV steps taking 35 s at each potential, and the ellipsometric data are shown in Fig. 5.6. The behaviour of delta and the relative intensity is very similar both qualitatively and quantitatively to that observed during potential cycling in Fig. 5.4; between 0.4 and 0.8 V delta decreases by *ca.* 15^{0} and the intensity decreases slightly, between 0.9 and 1.1 V delta displays a sharp increase to a maximum value of *ca.* 60^{0}, and the intensity decreases from *ca.* 0.2 to 0.025, and both parameters remain almost stationary at higher potentials. Psi starts to show a slight increase from 0.5 V, about 300 mV earlier than during cycling, increases sharply in value between 0.9 and 1.0 V to reach a maximum value of *ca.* 70^{0} as observed during cycling, then a sharp

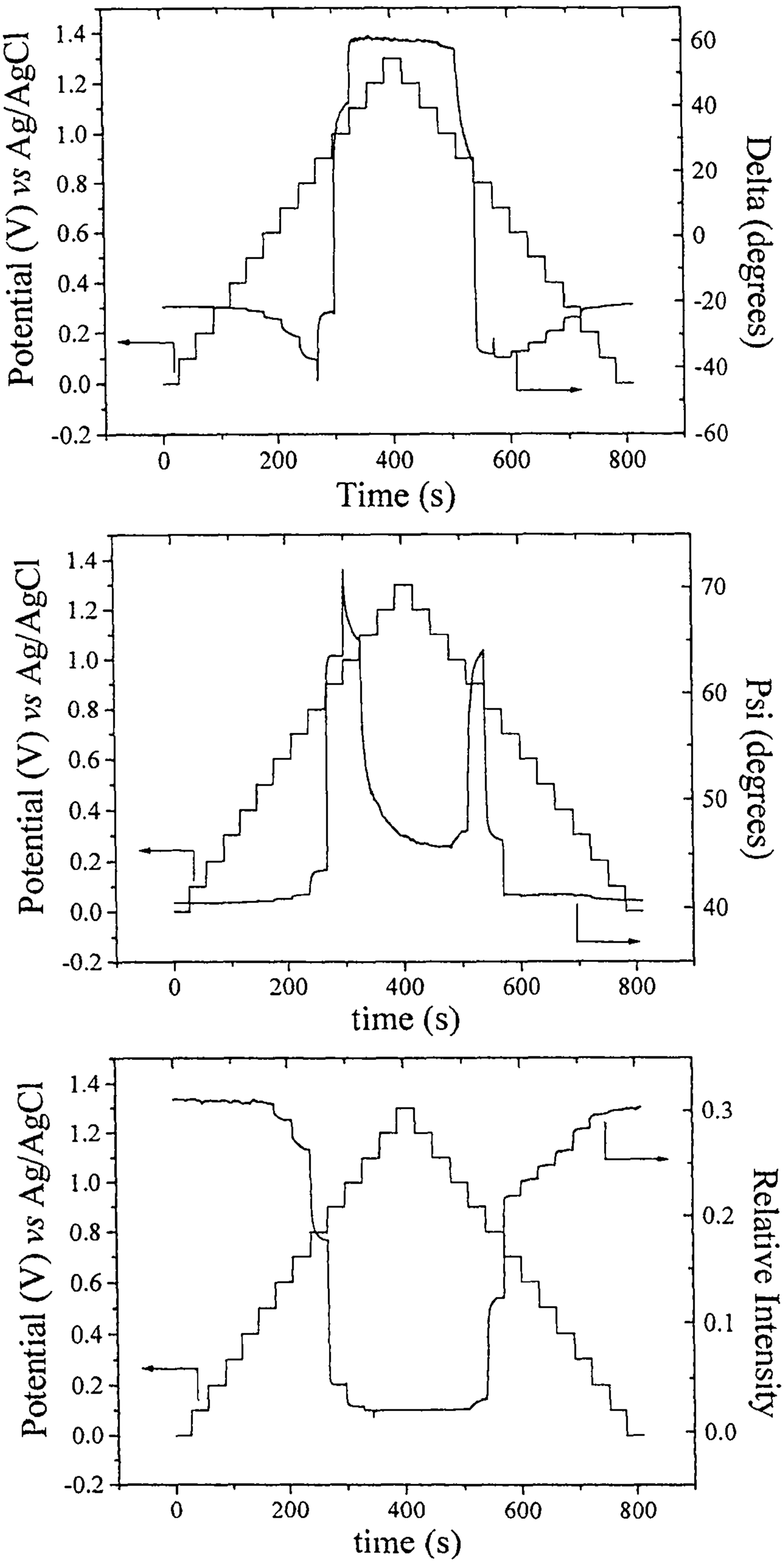

Fig. 5.6. Potential stepping of poly[Ni(OMeSaltMe)]. The potential was altered in 100 mV steps, 35 s at each potential, in 0.1 mol dm^{-3} TEAP/MeCN.

decrease, the minimum value being *ca.* 46 ^{0} compared to *ca.* 57 degrees during cycling. All three parameters had almost returned to their original values by the end of the experiment, and the slower rate of potential change has little effect on their behavior, which is surprising given that, during stepping, the film is still quite clearly still evolving after 35 s at higher potentials. Fig. 5.7 shows the cumulative charge passed during the cycling and stepping experiments shown in Figs. 5.4 and 5.6, and it can be seen that the two track one another almost exactly. During stepping, the amount of charge passed and extent of charge trapping [5,6] are slightly greater than during cycling, but given the difference in timescale, the traces are surprisingly alike and support the ellipsometric data in showing no significant difference in the behaviour of the film during the two experiments.

5.2.2 Fitted Data

5.2.2.1 Fitted data for the growth of the polymer films.

As discussed in the previous chapter, the poly[Ni(SaltMe)] data fitted easily to a simple homogeneous model during both growth and potential cycling. The modeling of poly[Ni(OMeSaltMe)] proved much more difficult, the first three cycles of growth fitting to a homogeneous model, but the remainder of the growth and subsequent experiments could only be fitted to an inhomogeneous model, with the film being much more compact next to the electrode than at the electrolyte/film interface. In order to achieve this, the film was considered to consist of ten layers of equal thickness, (as shown in Fig. 2.8, section 2.3), within themselves homogeneous. The complex refractive index of the outermost layer is fixed at a suitable value, in

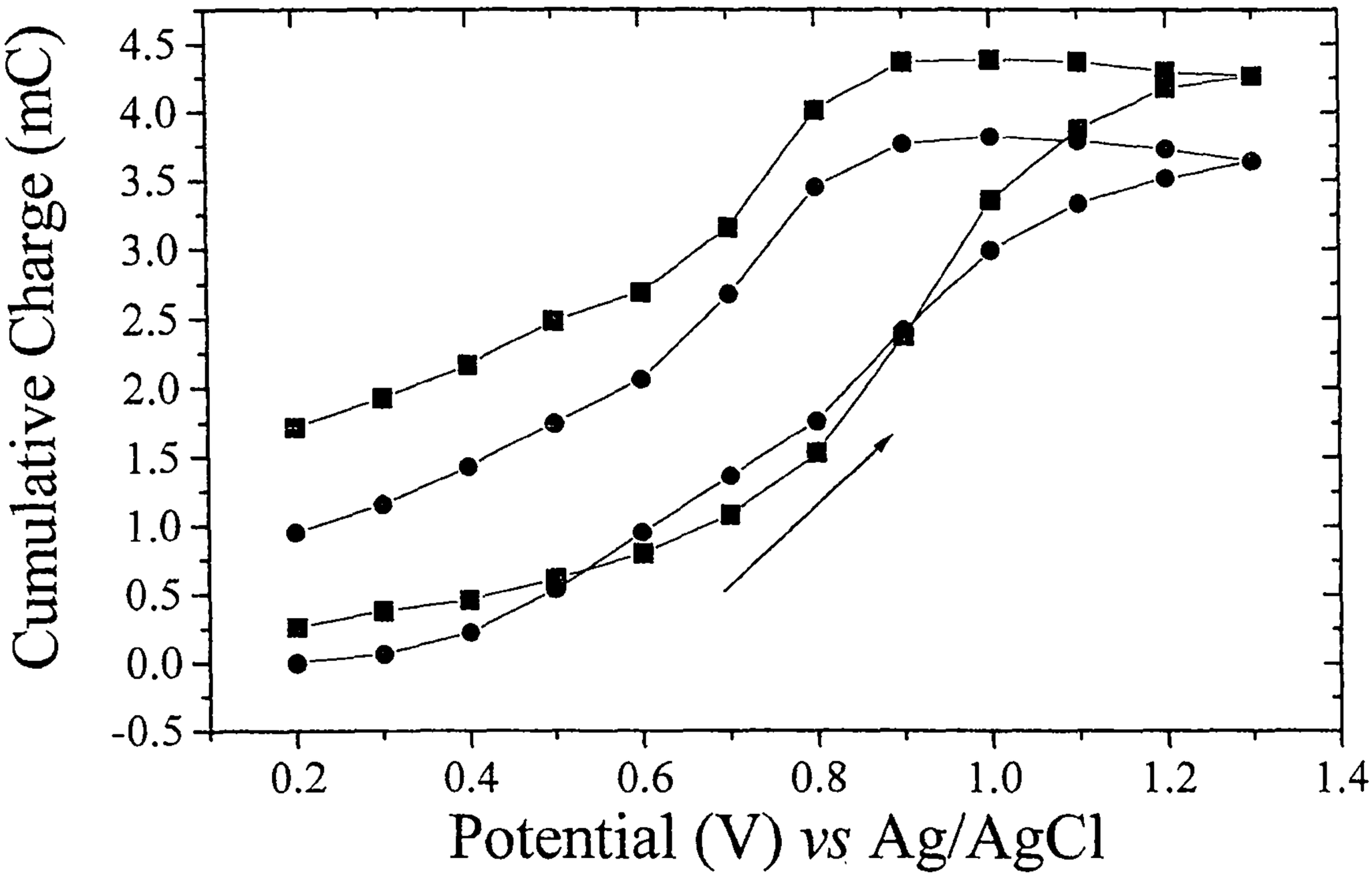

Fig. 5.7. The cumulative charge passed during potential cycling (circles) and stepping (squares) of poly[Ni(OMeSaltMe)]. Conditions as in Figs. 5.4 and 5.6 respectively.

this case approximately that of the solvent, while the refractive index of the innermost layer and the overall thickness are allowed to float during the fitting process. The values of n and k for the inner layers of the film vary linearly between the values of the inner and outer film. The data for n, k and film thickness for the first 3 cycles fitted to a homogeneous model are shown in Fig. 5.8, and the behaviour of n and k for the innermost film and the overall film thickness for the third to fifth cycles fitted to an inhomogeneous model are shown in Fig. 5.9. The data for the homogenous poly[Ni(SaltMe)] film is shown again in Fig. 5.10 for comparison. The qualitative behaviour of the poly[Ni(OMeSaltMe)] film once it had become inhomogeneous was the same regardless of the choice of n and k for the outermost

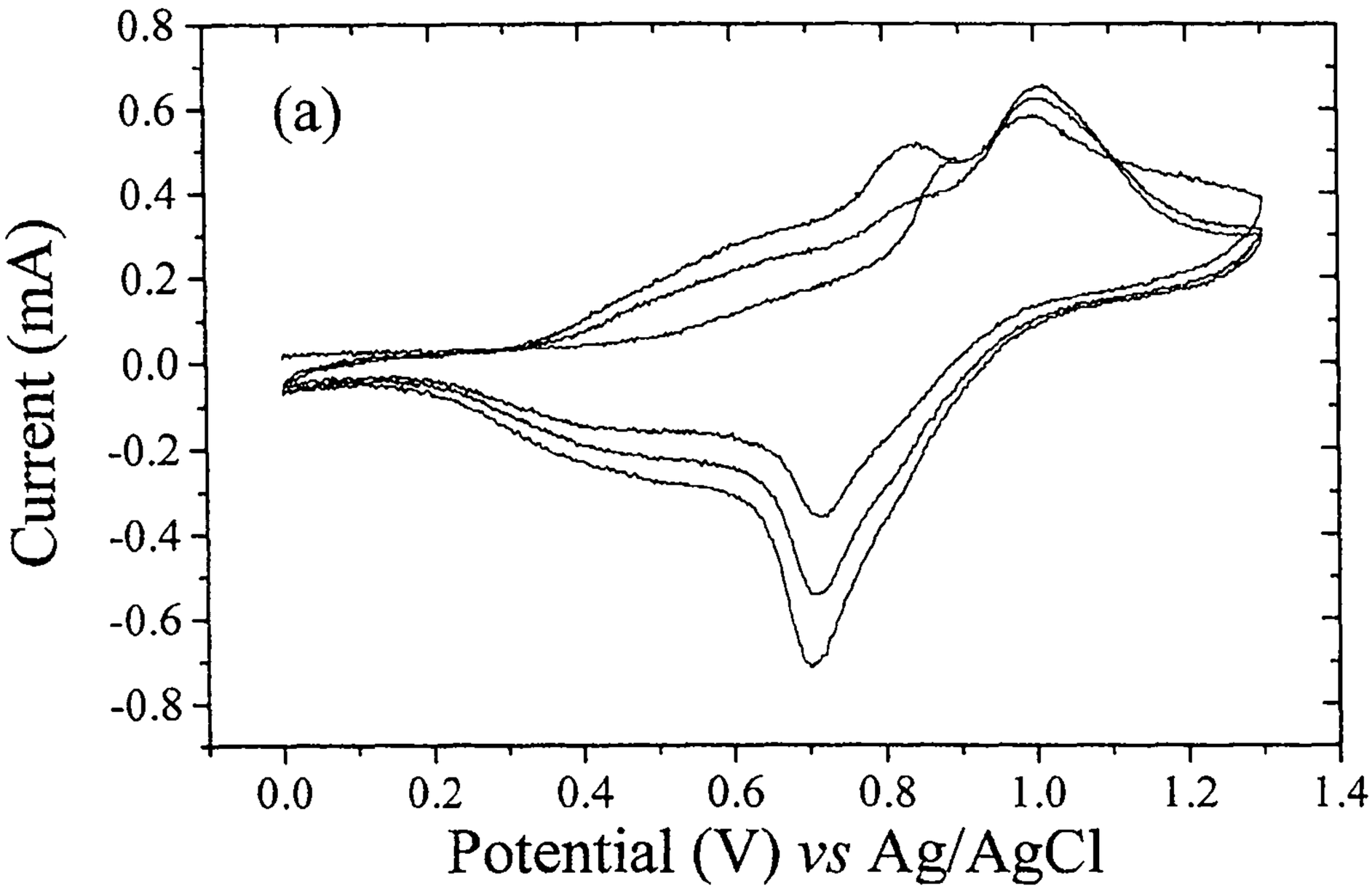

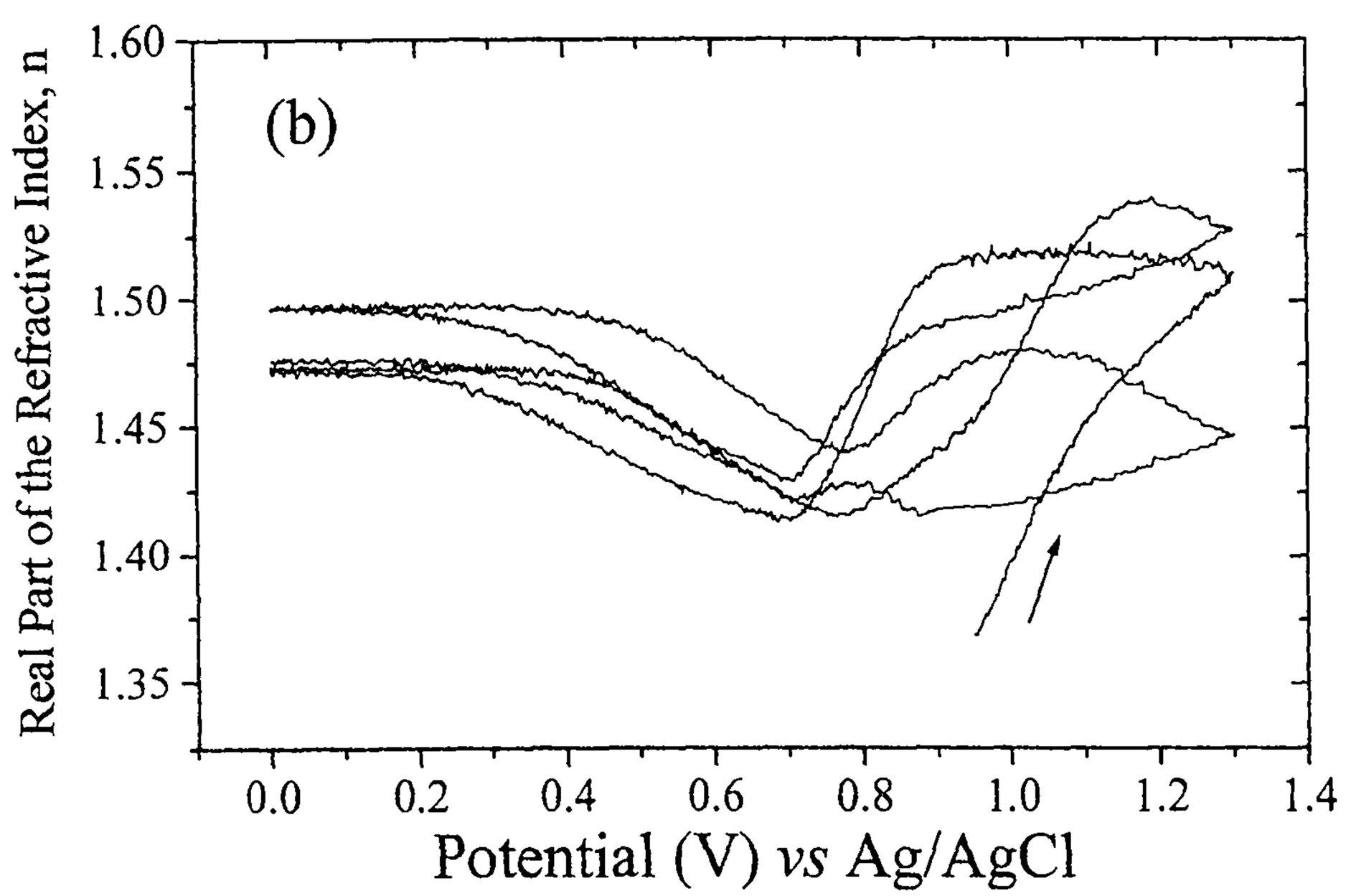

Fig. 5.8. The current passed (a) and behaviour of the real part of the refractive index, *n*, (b) during the first three cycles of growth of poly[Ni(OMeSaltMe)]. Data gathered at 632.8 nm in Fig. 5.2 has been fitted to a homogeneous model.

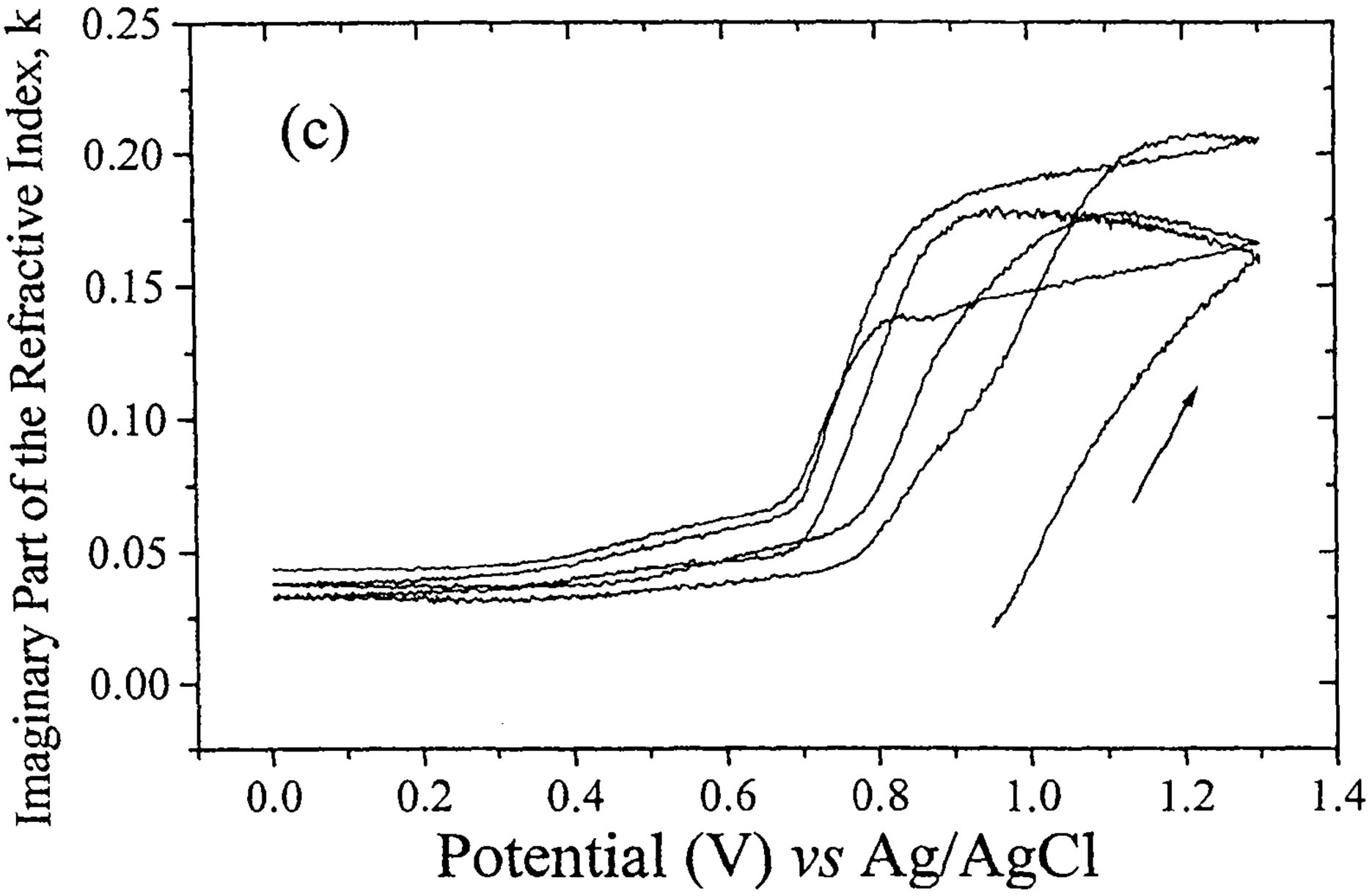

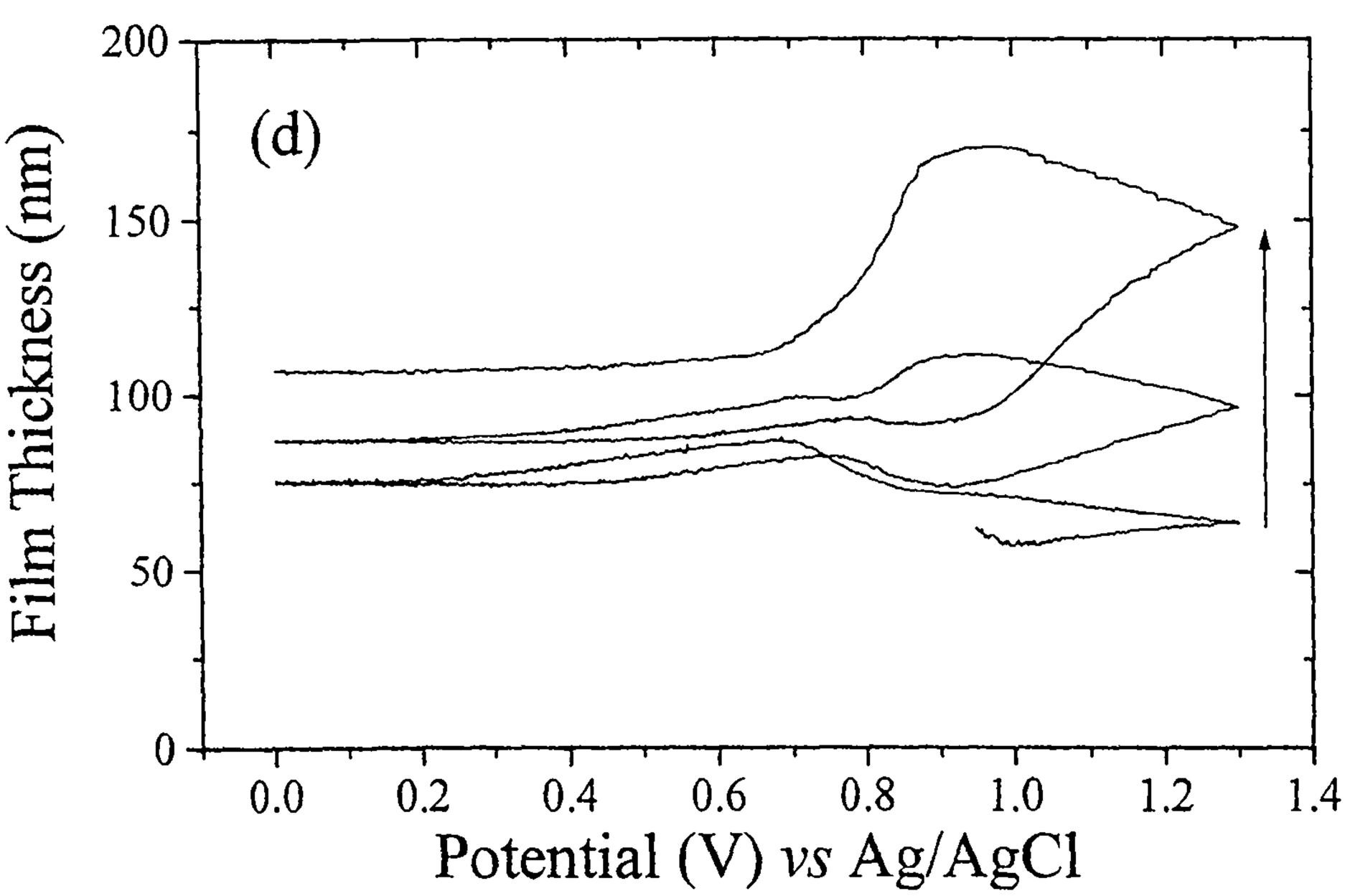

Fig. 5.8. The behaviour of the imaginary part of the refractive index, *k* (c) and film thickness (d) during the first three cycles of growth of poly[Ni(OMeSaltMe)]. Data gathered at 632.8 nm in Fig. 5.2 has been fitted to a homogeneous model.

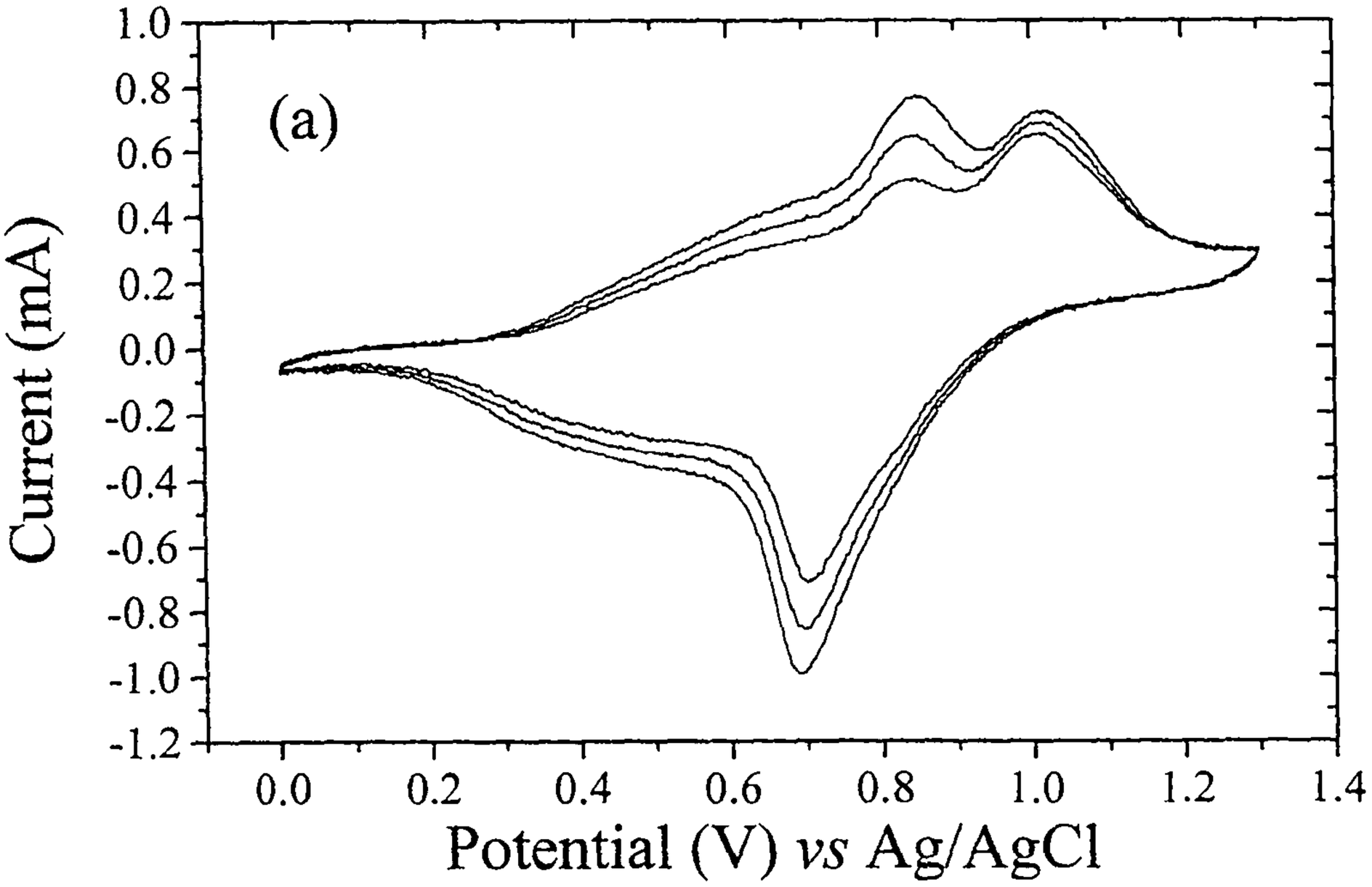

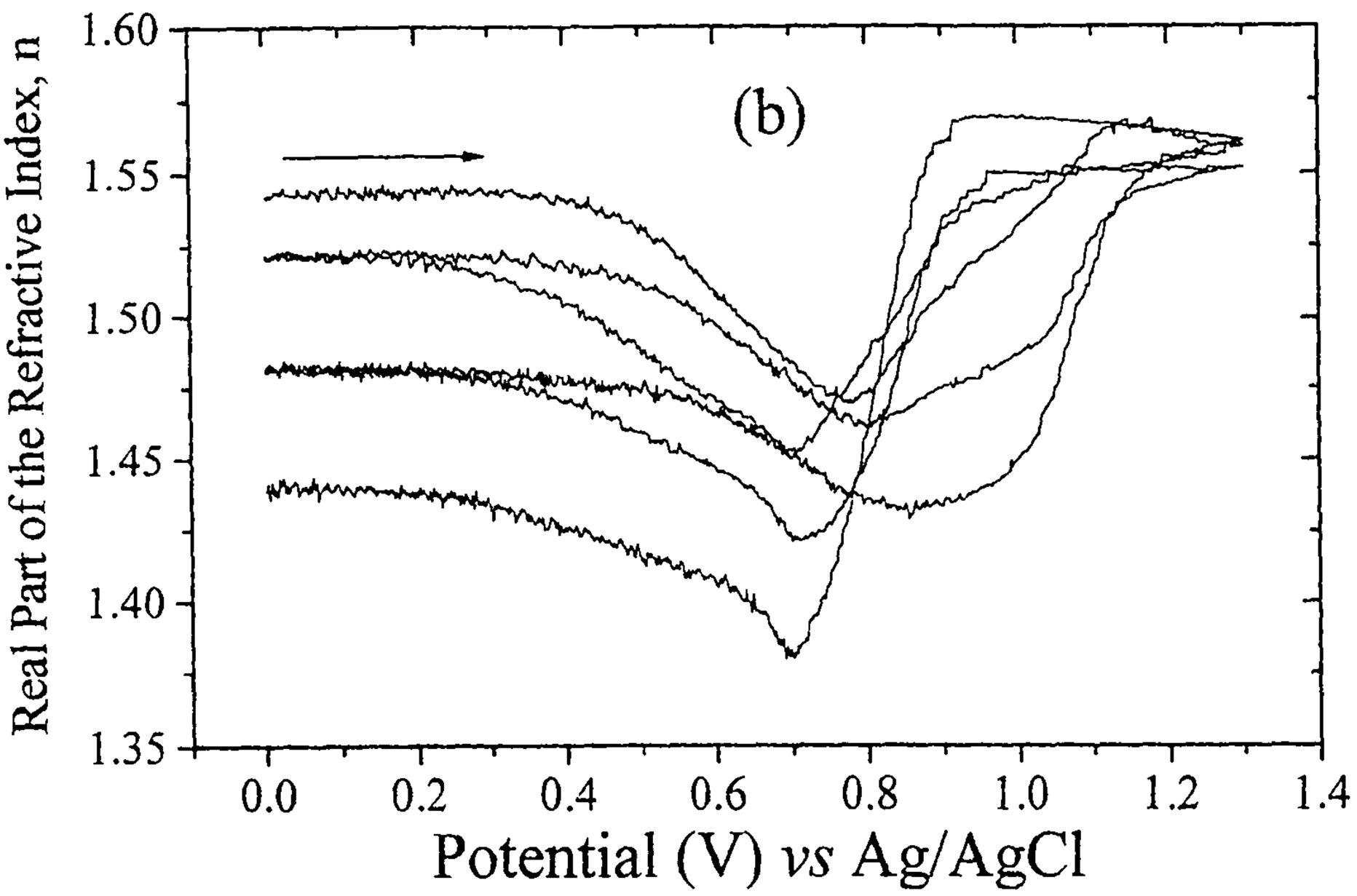

Fig. 5.9. The current passed (a) and behaviour of the real part of the refractive index, *n*, (b) during the last three cycles of growth of poly[Ni(OMeSaltMe)]. Data gathered at 632.8 nm in Fig. 5.2 has been fitted to an inhomogeneous model.

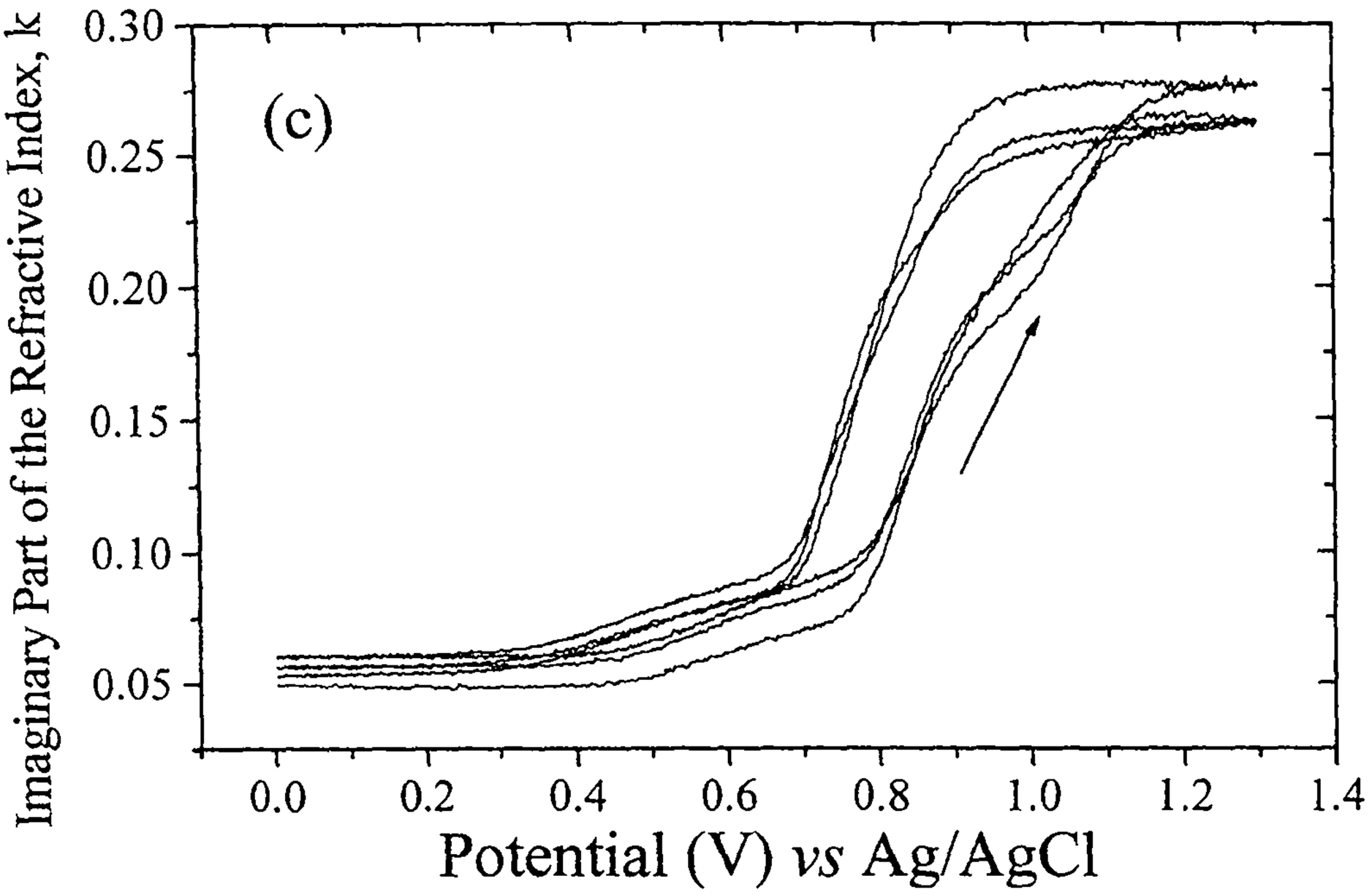

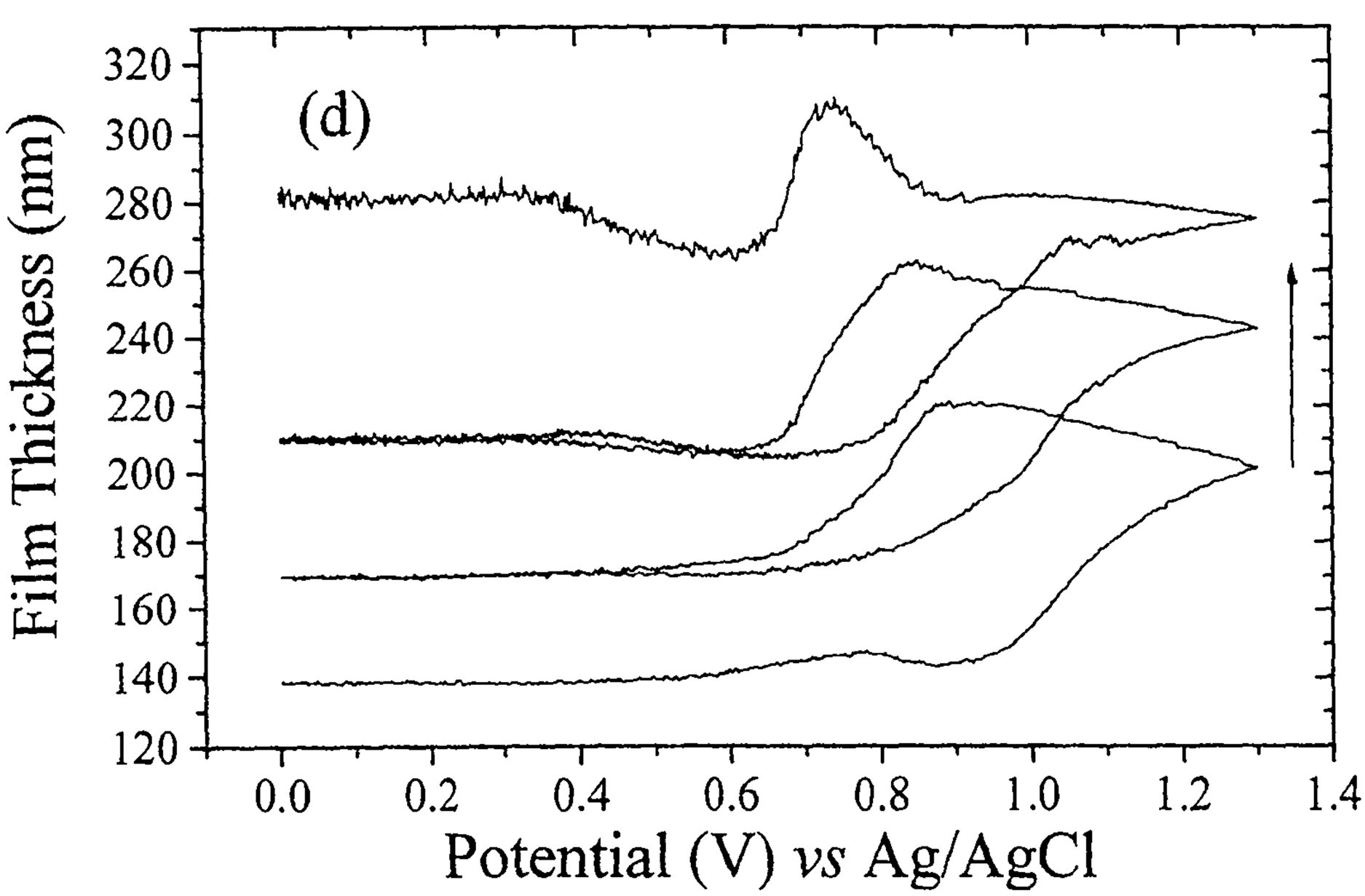

Fig. 5.9. The behaviour of the imaginary part of the refractive index, *k* (c) and film thickness (d) during the last three cycles of growth of poly[Ni(OMeSaltMe)]. Data gathered at 632.8 nm in Fig. 5.2 has been fitted to an inhomogeneous model.

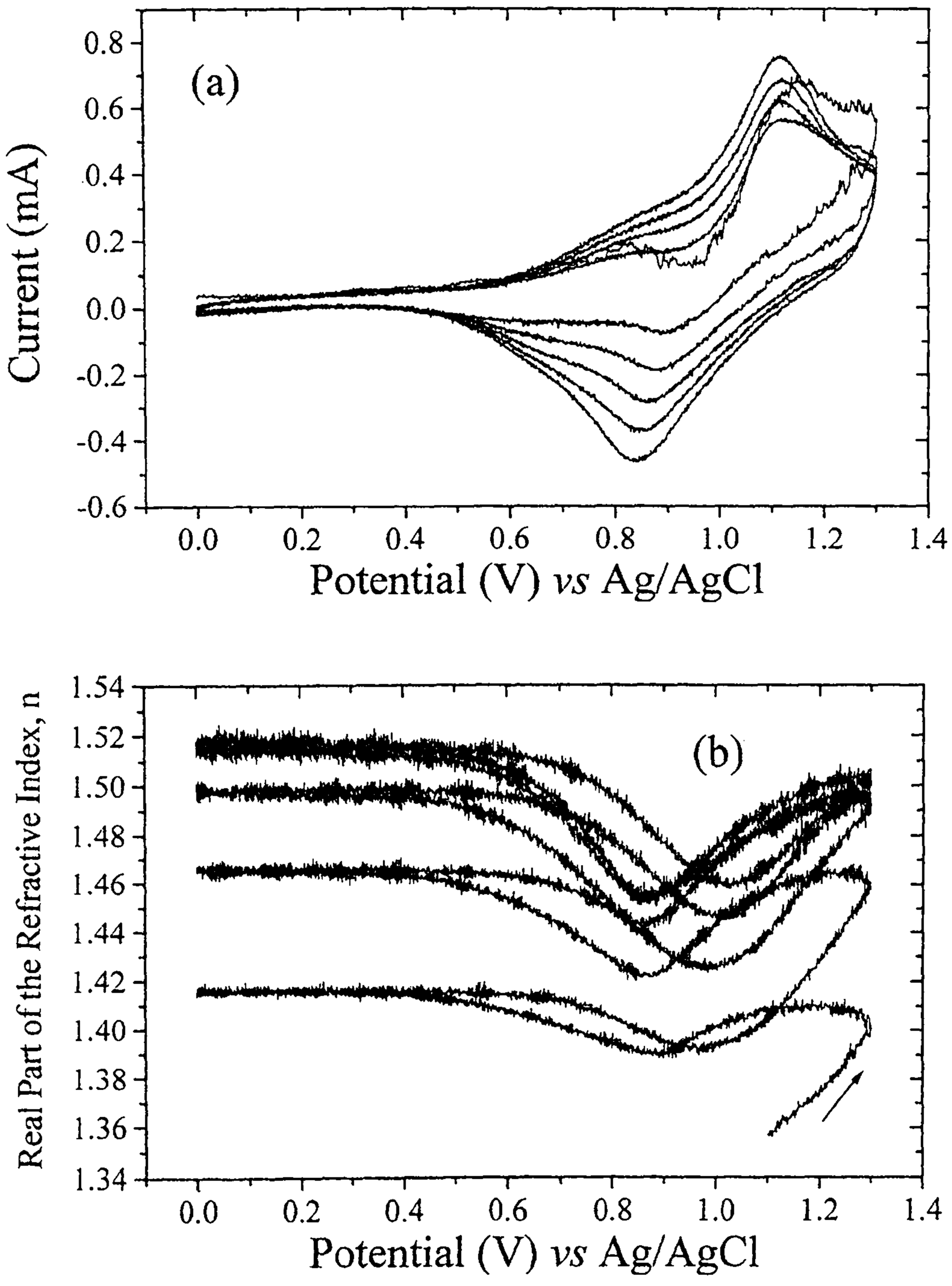

Fig. 5.10. The current passed (a) and behaviour of the real part of the refractive index, *n*, (b) during the growth of poly[Ni(SaltMe)]. Data gathered at 632.8 nm in Fig. 5.3 has been fitted to a homogeneous model.

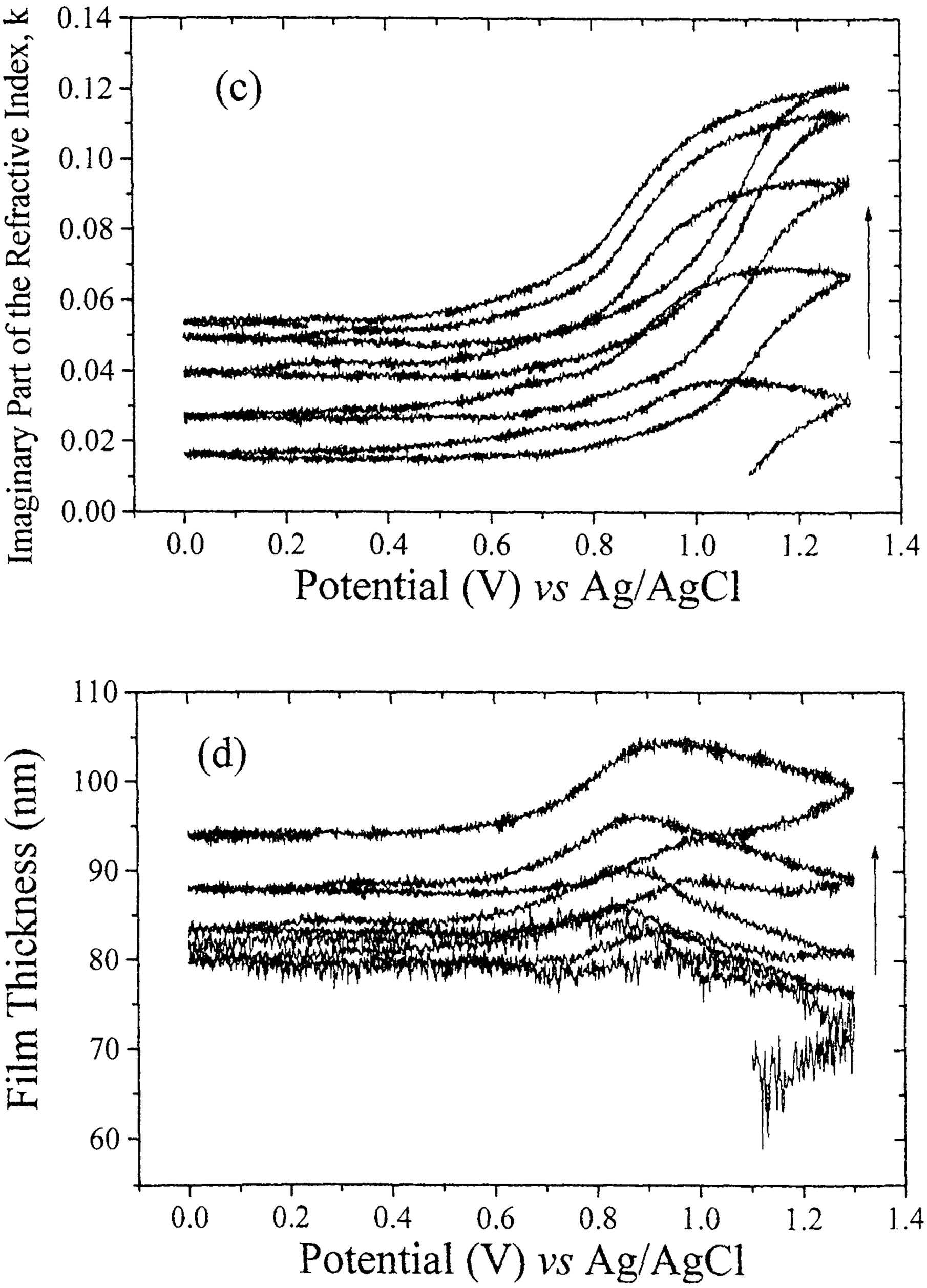

Fig. 5.10. The behaviour of the imaginary part of the refractive index, *k*, (c) and film thickness (d) during the growth of poly[Ni(SaltMe)]. Data gathered at 632.8 nm in Fig. 5.3 has been fitted to a homogeneous model.

layer within reasonable limits, indicating the model accurately describes the film, though data at many more wavelengths would be needed for a precise model.

It can be clearly seen from Figs 5.8, 5.9 and 5.10 that the transition of the poly[Ni(OMeSaltMe)] film from homogeneous to inhomogeneous has little effect on the behavior of *n*, *k*, and the thickness and that the qualitative behaviour of the parameters during growth is similar to that of the poly[Ni(SaltMe)]; during all five cycles of growth and with both models used, the three parameters for poly[Ni(OMeSaltMe)] show four potential regions of behaviour: between 0 and 0.4 V the film is in the neutral state and the parameters are stationary; 0.4-0.8 V *n* shows a marked decrease, *k* and the thickness a slight increase; 0.8-1.1 V all three parameters show a strong increase, and between 1.1-1.3 V *n*, *k* and the thickness are stationary.

The behaviour of the parameters for the two films from cycle to cycle differs, the poly[Ni(SaltMe)] shows clear increases in the values of *n* and *k* with each cycle while the thickness varies very little over the entire growth process, particularly during the early cycles, suggesting a process of consolidation as discussed in the previous chapter. In contrast, the poly[Ni(OMeSaltMe)] film shows little change in the values of *n* and *k* over the five cycles but the thickness shows a marked increase with each subsequent cycle, even during the first three cycles when the film is still homogeneous, indicating from the outset the mechanism of growth for this film differs from that of poly[Ni(SaltMe)]. The changes in thickness with each cycle indicate that, rather than a process of consolidation, the film grows by the deposition of a new layer with each potential cycle. As *n* and *k* alter very little while the film is homogeneous it is not unreasonable to conclude that each deposited layer is of a similar composition to the last. As the film becomes inhomogeneous the outer layers

must become more diffuse and contain a higher percentage of solvent, so the layers deposited are likely to differ from the film already present underneath, confirmed by the success of the model which holds the values of n and k of the outermost layer to those of the solvent, while n and k of the innermost layer shown in Fig. 5.9 alter very little from the homogenous film, as would be expected.

As discussed in the previous chapter, the data for poly[Ni(SaldMe)] and poly[Ni(SaltMe)] show no indication of a charge transfer stacked precursor to polymerisation, as was proposed by Dahm *et al* [7]. The data for poly[Ni(OMeSaltMe)] also show n and k at the onset of growth to be very close to the values of the solvent (1.344, 0), indicating the initial deposition process results in a polymer film which at this stage consists almost entirely of solvent rather than a dense deposit.

During the final cycle of growth, the behaviour of the two films is quantitatively very different. n exhibits similar values for the two films, *ca.* 1.5-1.55 at 1.3 V during the final cycle and *ca.* 1.45-1.5 at the end of the final sweep. In contrast, k at 1.3 V during the final cycle is over twice as large for poly[|Ni(OMeSaltMe)] as for poly[Ni(SaltMe)], *ca.* 0.28 and 0.12 respectively, though by the end of the last sweep both have attained values of approximately 0.05. The most obvious difference is in the variation in thickness, poly[Ni(OMeSaltMe)] is over 3 times the thickness of the poly[Ni(SaltMe)] film in the neutral state at the end of growth, *ca.* 300 nm compared to less than 100 nm. The inhomogeneous model indicates poly[Ni(OMeSaltMe)] contains a large amount of solvent, especially in the outer layers, which may explain at least to some extent the difference in thickness observed, also the charge passed during growth is 13 % greater than for poly[Ni(OMeSaltMe)], so assuming the oxidation processes are sufficiently alike this

would also substantiate a thicker film. As mentioned above, the choice of refractive index for the outermost layer of the inhomogeneous film during the modeling process had no effect on the qualitative behaviour of the film, and had little effect on the value of the thickness, consistently producing a film approximately three times as thick as poly[Ni(SaltMe)]. Data would be needed at a great many more wavelengths for a precise assessment of the thickness which is not possible at the moment with the current experimental set up, however data was collected for the growth and cycling during repeat experiments at two other wavelengths, 594.1 nm and 670 nm. Modeling returned values of 317 nm and 325 nm for the thickness, which are in close agreement with the value of 280 nm obtained with the data presented. This indicated a substantially thicker film than the poly[Ni(SaltMe)] counterpart, and lent a great deal of confidence to this model.

5.2.2.2 Potential Cycling of the Modified Electrodes

The behaviour of the poly[Ni(SaltMe)] and poly[Ni(OMeSaltMe)] films during potential cycling, shown in Figs. 5.11 and 5.12, can be seen to be markedly different in the oxidised region, though similar in the reduced region given the 200 mV difference in the onset of polymerisation observed above. Between 0 V and *ca.* 0.4 V in the case of poly[Ni(SaltMe)] and 0.2 V for poly[Ni(OMeSaltMe)] the films are neutral and all three parameters are stationary; between 0.4-1.0 V and 0.2-0.8 V for the SaltMe and OMeSaltMe films respectively *n* displays a strong decrease,

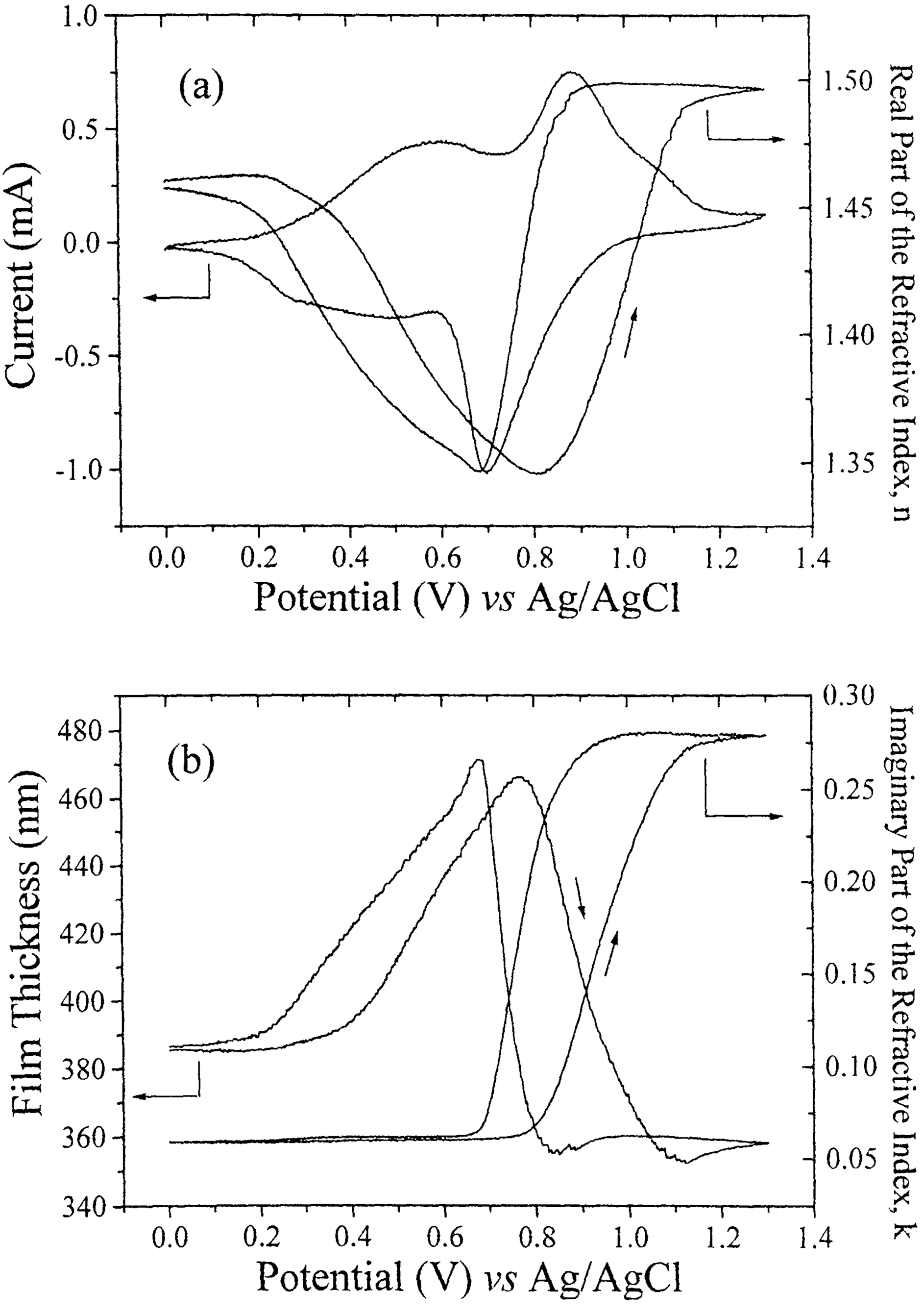

Fig. 5.11. Potential cycling of poly[Ni(OMeSaltMe)], performed in 0.1 mol dm^{-3} TEAP in MeCN at 100 mV s^{-1}. Data collected at 632.8 nm has been fitted to an inhomogeneous model.

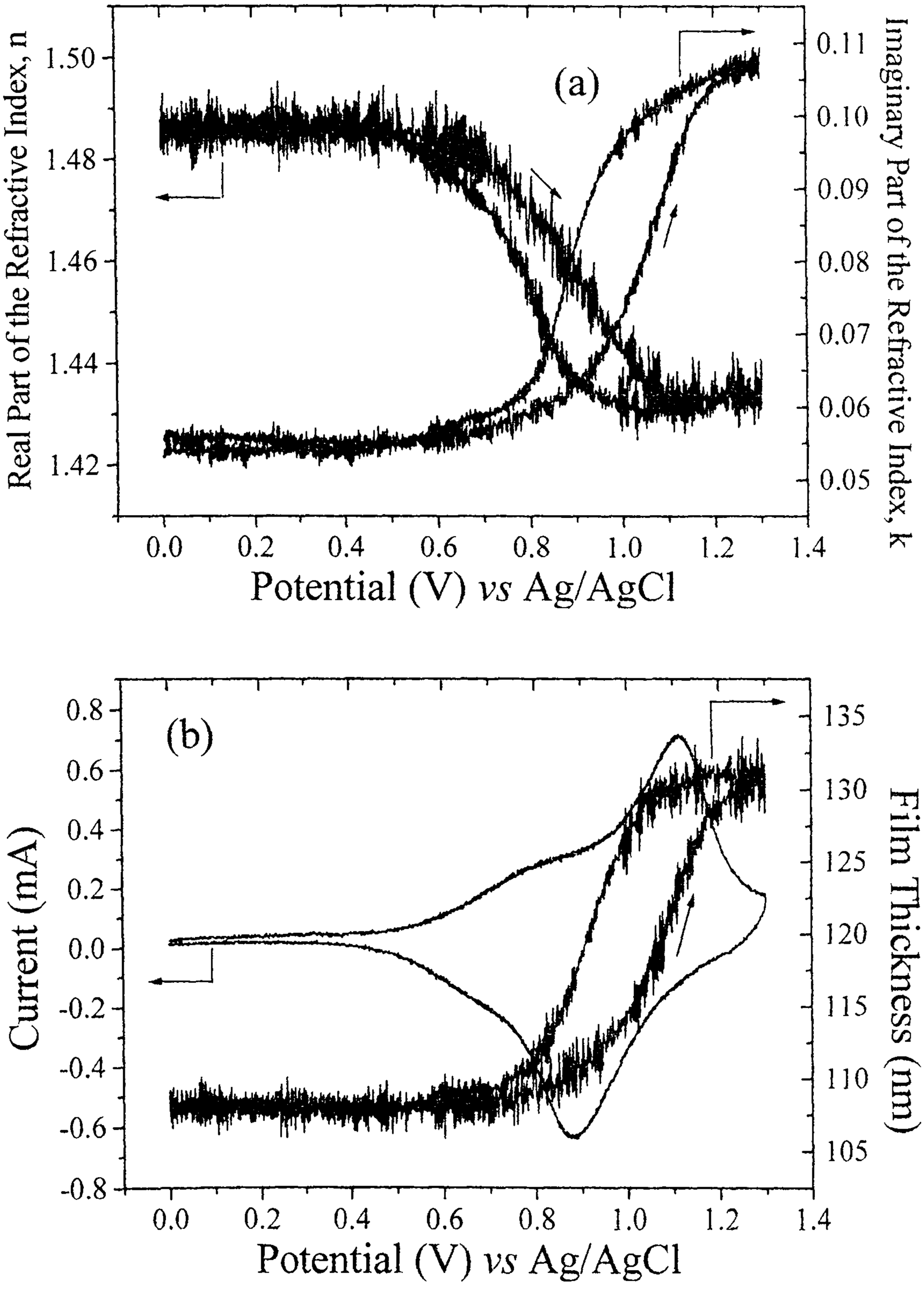

Fig. 5.12. Potential cycling of poly[Ni(SaltMe)], performed in 0.1 mol dm^{-3} TEAP in MeCN at 100 mV s^{-1}. Data collected at 632.8 nm has been fitted to a homogeneous model.

the thickness increases strongly, and *k* is stationary for poly[Ni(OMeSaltMe)] but shows a slight increase for poly[Ni(SaltMe)], indicating the first oxidation process is of the same origin for both films, however between 0.8 and 1.1 V a secondary process occurs in the poly[Ni(OMeSaltMe)] which is absent in poly[Ni(SaltMe)] and is characterised by a steep decrease in the thickness, the film becoming thinner in the oxidised state than the neutral form. Such marked decreases in thickness during oxidation are known to occur with other conducting polymers, for example polypyrrole films contract by *ca.* 30 % of their neutral thickness upon oxidation, which is assigned to the expulsion of solvent (and cations) and some form of electrostriction process [5]. The contraction of poly[Ni(OMeSaltMe)] is accompanied by a sharp increase in *n* not seen in poly[Ni(saltMe)], and an increase in *k* qualitatively similar in both films, but the value for poly[Ni(OMeSaltMe)] at 1.3 V being *ca.* three times the value of *k* for poly[Ni(SaltMe)]. Between 1.1 and 1.3 V the parameters are stationary for both films.

In the previous chapter similar behaviour was observed for poly[Ni(SaldMe)] in the oxidised region, though not to the same extent as for poly[Ni(OMeSaltMe)], which was explained by the presence of charge transfer stacking in the oxidised film generating an absorbance in the UV which would cause the value of *n* at longer wavelengths such as those used to probe the system to rise, and may also offer an explanation of the contraction observed for poly[Ni(OMeSaltMe)]. In the case of poly[Ni(SaldMe)], the occurrence of charge transfer stacking was attributed to the inability of the solvent to penetrate the film in sufficient quantity to coordinate axially with partially oxidised Ni centres, causing them to resort to charge transfer with other monomer units to achieve octahedral coordination. In the case of

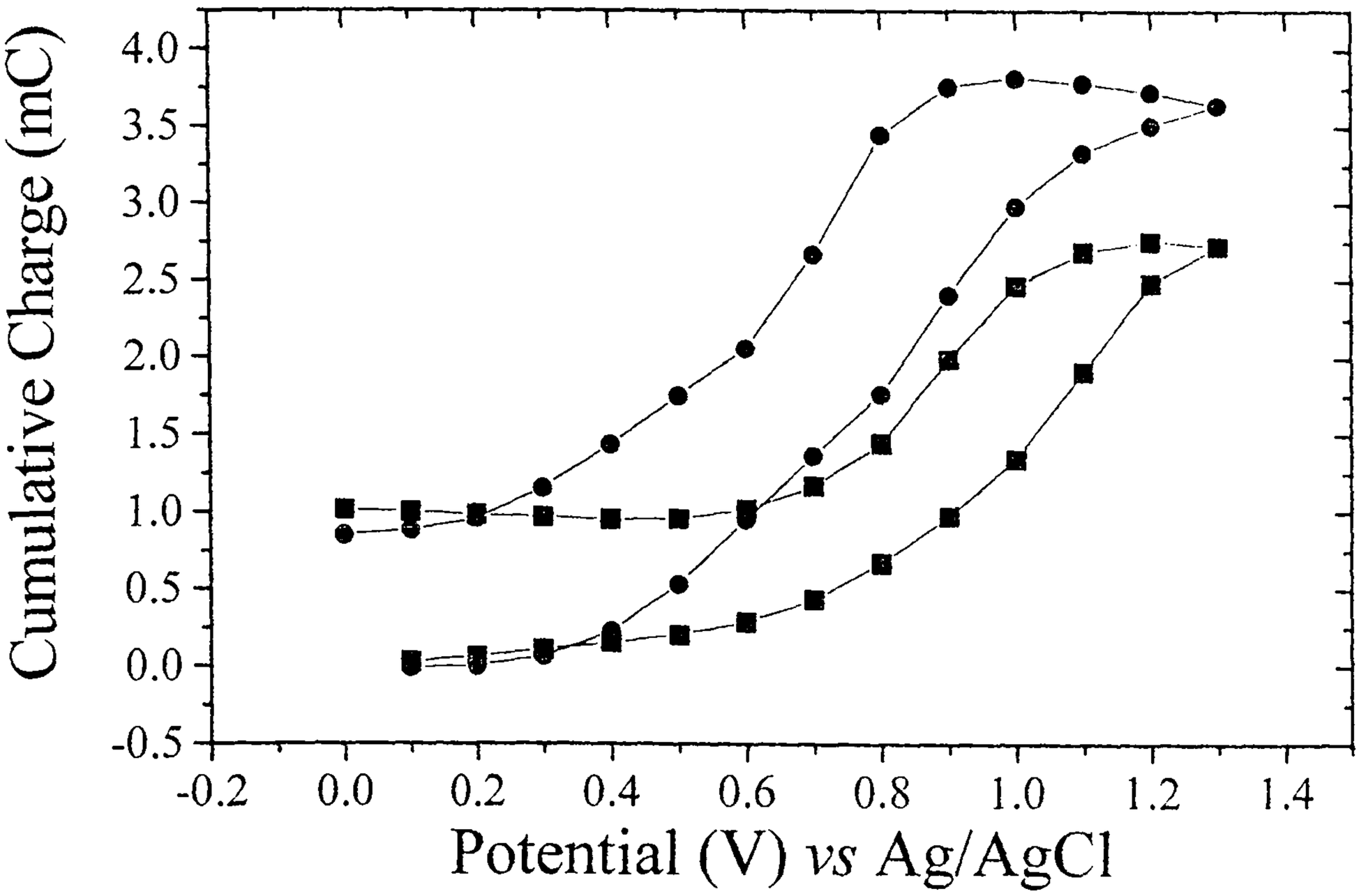

Fig. 5.13. The cumulative charge passed during potential cycling of poly[Ni(OMeSaltMe)] (circles) and poly[Ni(SaltMe)] (squares). Conditions as in Figs. 5.4 and 5.5 respectively.

poly[Ni(OMeSaltMe)], a lack of solvent is unlikely as the outer layers in particular mainly consist of acetonitrile, also the extent to which it swells prior to contracting is *ca.* 24 % of its neutral thickness, almost the same as poly[Ni(SaltMe)], instead the same stacking process may be occurring but due to electronic rather than steric effects. From comparison of the cyclic voltammograms for the growth of poly[Ni(OMeSaltMe)] and poly[Ni(SaltMe)], it is clear the addition of the methoxy group has an effect on the relative band energies of the metal and ligand, apparently separating the oxidation processes of the two, and possibly altering the site and extent of oxidation. The extent of oxidation of the Ni centres can be approximated from the value of k, the absorption occurring at 632.8 nm arising from ligand to metal charge transfer within the monomer units. The much larger value of k for oxidised

poly[Ni(OMeSaltMe)] than for poly[Ni(SaltMe)] suggests the extent of oxidation on the metal centres is significantly greater, leading to the possibility of extensive charge transfer stacking which may explain the massive decrease in thickness and strong UV absorptions. It is unlikely *k* is larger simply because a greater number of Ni centres are accessible for oxidation, as the cumulative charge passed for the two films during potential cycling is very similar, as shown in Fig. 5.13. The maximum charge stored by poly[Ni(OMeSaltMe)] is *ca.* 15 % higher than that of poly[Ni(SaltMe)], corresponding very closely to the 13 % more charge passed during polymerisation, suggesting that it is the extent of oxidation of the Ni centres which is higher in poly[Ni(OMeSaltMe)] rather than the density of Ni sites. In either case, it would appear charge transfer stacking is the preferred route to obtaining octahedral coordination for the oxidised metal centres, as opposed to solvent coordination in the case of poly[Ni(SaltMe)]. Using the same analysis [8] as described in the previous chapter, the doping level of poly[Ni(OMeSaltMe)] was estimated. The ratio of charge passed during polymerisation and redox switching is assumed to be equal to $(2+2y+z)/(2y+z)$, where y and z are the doping levels of each phenyl ring and the metal respectively. This yielded a dopant level of 0.62 per monomer unit, very similar to the value of poly[Ni(SaldMe)], which, given the difference in behaviour, may indicate that though the dopant level is similar the distribution of the charge is different and the Ni centre bears more of the positive charge in poly[Ni(OMeSaltMe)] than in poly[Ni(SaltMe)] or poly[Ni(SaldMe)], hence the much greater tendency of the former to form charge transfer stacks.

5.2.2.3 Stepping of Poly[Ni(OMeSaltMe)]

The fitted data for the potential stepping experiments on poly[Ni(OMeSaltMe)] are shown in Fig. 5.14. When compared with the data from cycling, *k* shows very similar behaviour, reaching a slightly higher value at the anodic limit during the stepping. The decrease in the value of *n* during the early stages of oxidation is much smaller during potential stepping then cycling, and at 1.3 V the maximum value of *ca.* 1.6 is clearly higher than the corresponding value during cycling of *ca.* 1.5. The thickness does not increase during the early stages of oxidation as seen in the cycling, though contraction occurs to a similar extent over the same potential range of *ca.* 0.7-1.0 V, however at higher potentials the thickness is almost stationary during cycling, but during stepping an increase of *ca.* 15 nm occurs before decreasing over the same range during the return steps. During the early stages of oxidation during stepping it appears some charge transfer is occurring, limiting the amount by which *n* decreases and balancing the influx of solvent to keep the film thickness almost constant. At higher potentials the extent of oxidation becomes greater and extensive charge transfer is required to stabilise the oxidised centres, resulting in the decrease in *n* and thickness, and between *ca.* 1.1 and 1.3 V, while the thickness is almost stationary during cycling some solvent appears to seep into the outer layers, having little effect on *n* and *k* of the inner layers.

That contraction still occurs even over this longer time scale indicates that charge transfer is the preferred route for Ni centres to become six coordinate,

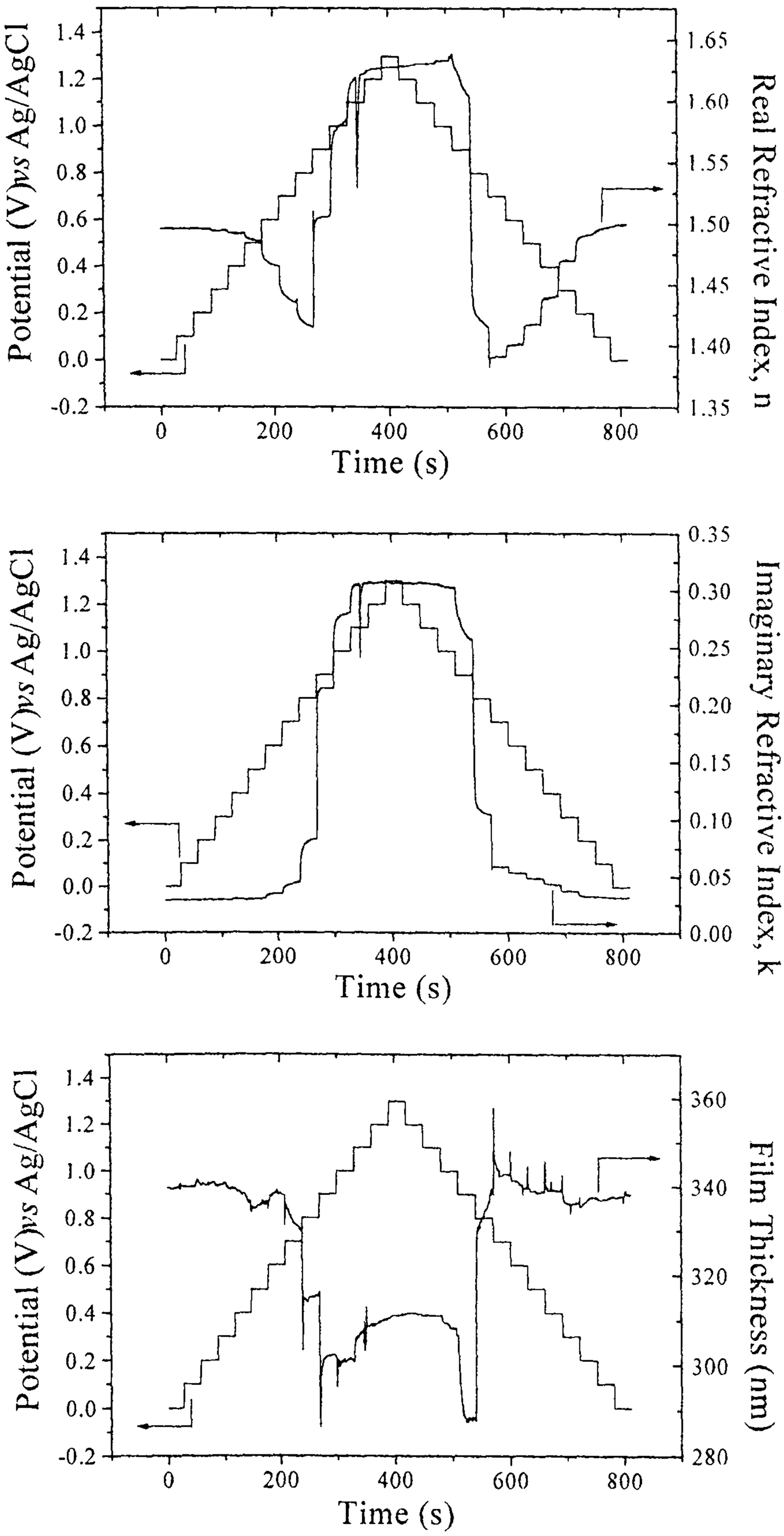

Fig. 5.14 Potential stepping of poly[Ni(OMeSaltMe)]. 100 mV steps, 35 s at each potential, in 0.1 mol dm^{-3} TEAP MeCN.

presumably offering greater stabilisation than the coordination of solvent. Under the same circumstances poly[Ni(SaldMe)] showed no contraction, suggesting at longer time scales when enough solvent could enter the film this was sufficient to stabilise the partially oxidised Ni centres, and the contraction at higher scan rates was due to steric effects limiting the ingress of solvent. This is clearly not the case with poly[Ni(OMeSaltMe)], in which a greater amount of charge appears to reside on the Ni, causing charge transfer stacking to occur even at low potential scan rates.

5.3 Conclusions

The addition of a methoxy group to phenyl rings of the ligands has a profound effect on the electrochemical and structural properties of poly[Ni(Salen)] films. From the electrochemical data it is clear that the onset of polymerisation and the potential of the redox couple during cycling are 200 mV lower than in the corresponding Ni[SaltMe] film, and the addition of the methoxy groups has altered the level of the ligand and/or metal HOMOs and resulted in the splitting of the two oxidation processes so two clear anodic peaks are visible during polymerisation.

The ellipsometric data fit only to an inhomogeneous film from the third cycle of growth onwards, including during subsequent experiments, which indicates the outer layers are very diffuse, consisting almost entirely of solvent, with the film more compact next to the electrode. The film is much thicker than the poly[Ni(SaltMe)] grown under the same conditions, though during oxidation undergoes a marked contraction, resulting in a thinner film at the anodic limit than in the reduced state. It is suggested this is the result of charge transfer stacking to stabilise the Ni centres, oxidised to a greater degree than in poly[Ni(SaltMe)], for which there is considerable evidence for ligand based oxidation processes.

5.4. References

1. P. Audebert, P. Capdevielle, M. Maumy, *Synth. Met.*, 1991, **41**, 3049.

2. P. Audebert, P. Hapiot, P. Capdevielle, M. Maumy, *J. Electroanal. Chem.*, 1992, **338**, 269.

3. P. Audebert, P. Capdevielle, M. Maumy, *New. J. Chem.*, 1992, **16**, 697.

4. S. V. Vasil'eva, K. P. Balashev, A. M. Timonov, *Russ. J. Electrochem.*, 1998, **34**, 978.

5. P. A. Christensen, A Hamnett, *Electrochim. Acta*, 1991, **36**, 1263.

6. I. Jurevivute, S. Bruckenstein, A. R. Hillman, *J. Electroanal. Chem.*, 2000, **488**, 73.

7. C. E. Dahm, D. G. Peters, J. Simonet, *J. Electroanal. Chem.*, 1996, **410**, 163.

8. M. Vilas-Boas, C. Freire, B. de Castro, A. R. Hillman, *J. Phys. Chem. B*, 1998, **102**, 8533.

6.1 Introduction

The electropolymerisation of complexes derived from salicylaldehydes and their derivatives has been of much interest since it was first observed in 1988 [1-3], and the electroactive polymer films of a variety of salens have been intensively investigated.[4-15]. Much work has focused on salen complexes containing first row transition metals; however, instability of these films led to the investigation of other metal salens and functionalised ligands. Timonov began investigating salens of second row transition metals (Rh & Pd) in 1987 [13,15] and found them to be much more stable than their first row metal counterparts. This chapter describes work done to characterise [Pd(OMeSalen)], shown in Fig. 6.1, and its Ni counterpart (both synthesised by Timonov's group) using ellipsometry to investigate the growth of poly[M(OMeSalen)], and ellipsometry and *in-situ* FTIR (performed by Jintana Eameaim), to study the behaviour of the modified electrodes during potential cycling.

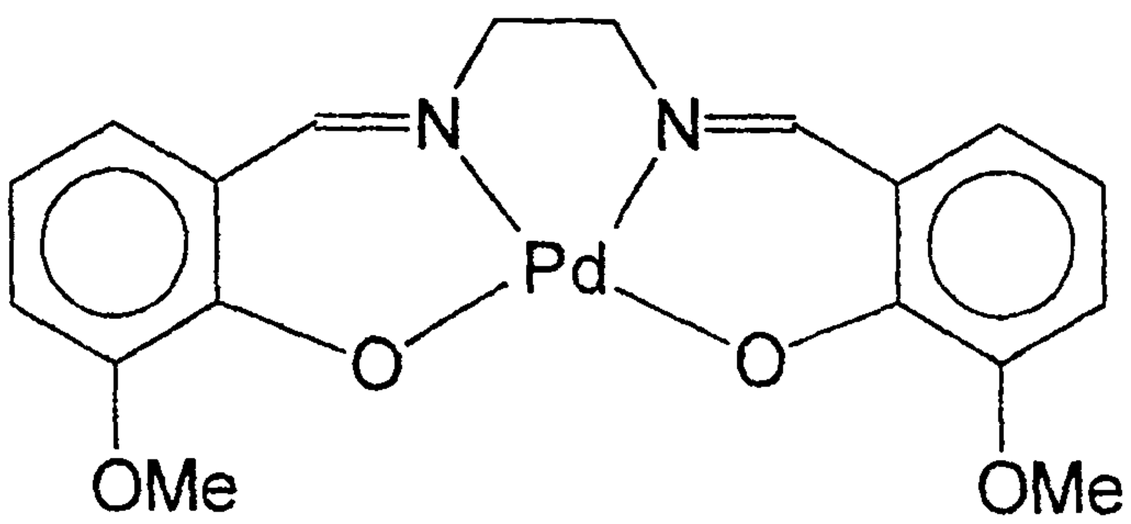

Fig. 6.1. The structure of N.N'-ethylene-bis(3-methoxysalicylideiminato)Palladium(II) or Pd(OMeSalen).

6.2. Results and Discussion

6.2.1 Experimental Data

6.2.1.1 Growth of the Growth of poly[Pd(OMeSalen)]

The current passed during the fifteen cycles of growth is shown in Fig. 6.2. The CVs clearly show an increase in the charge passed on each cycle, indicative of the growth of a polymer film. Two oxidative waves are observed, the first at *ca.* 0.4 - 0.8 V and the second *ca.* 0.9 - 1.2 V. Figs. 6.3(a)-(d) show the current passed and the ellipsometric parameters at 632.8 nm for the first three cycles of growth. The ellipsometric parameters are all constant until approximately 0.9 V during the first sweep, however it is clear that significant charge is passed before this

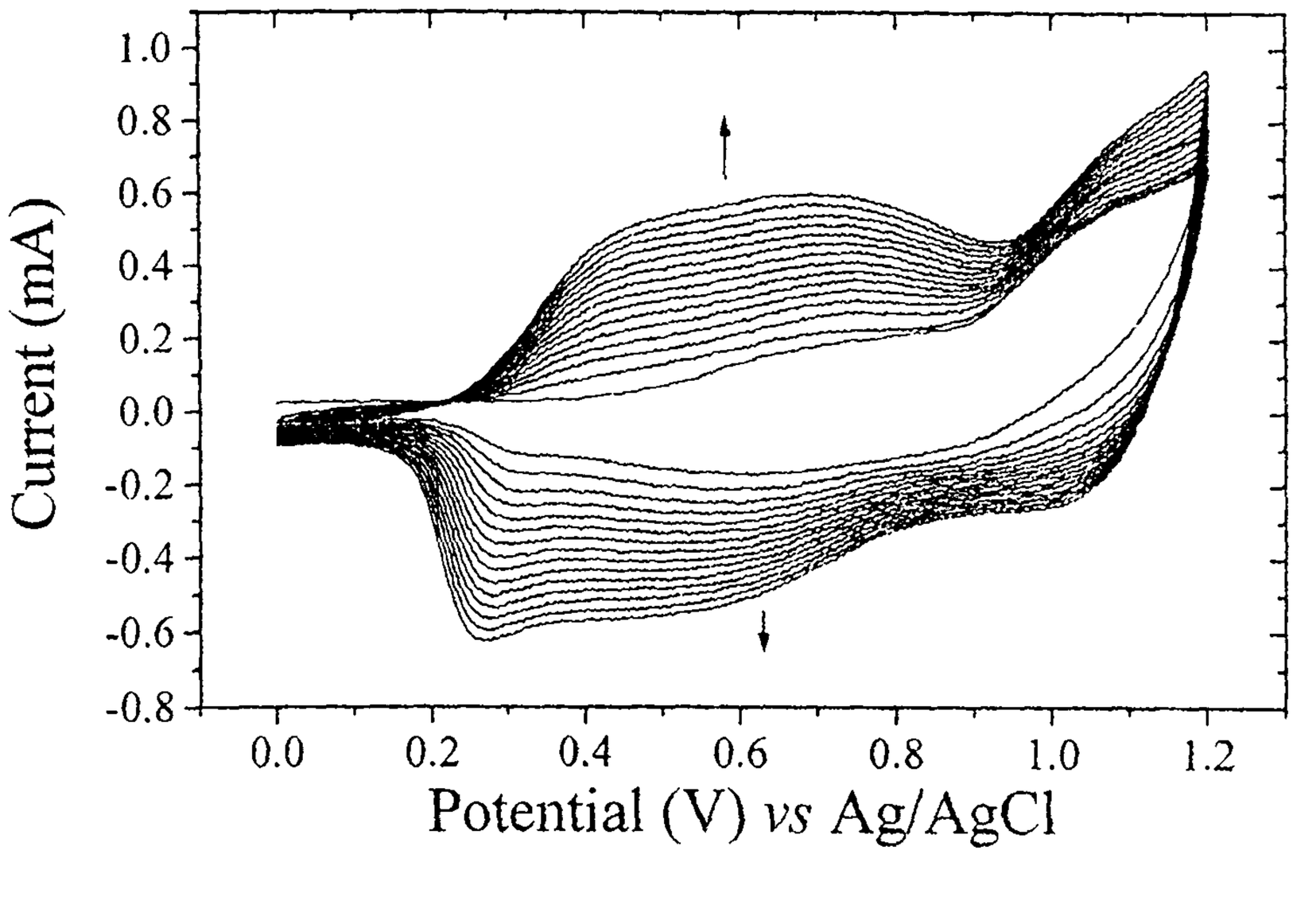

Fig. 6.2. Cyclic Voltammograms showing the anodic polymerisation of 1 mmol dm^{-3} [Pd(OMeSalen)] in 0.1 mol dm^{-3} TBAT-MeCN at a 0.64 cm^2 Pt disk electrode during potential cycling between 0 and 1.2 V vs Ag/Ag^+ at 100 mV s^{-1}.

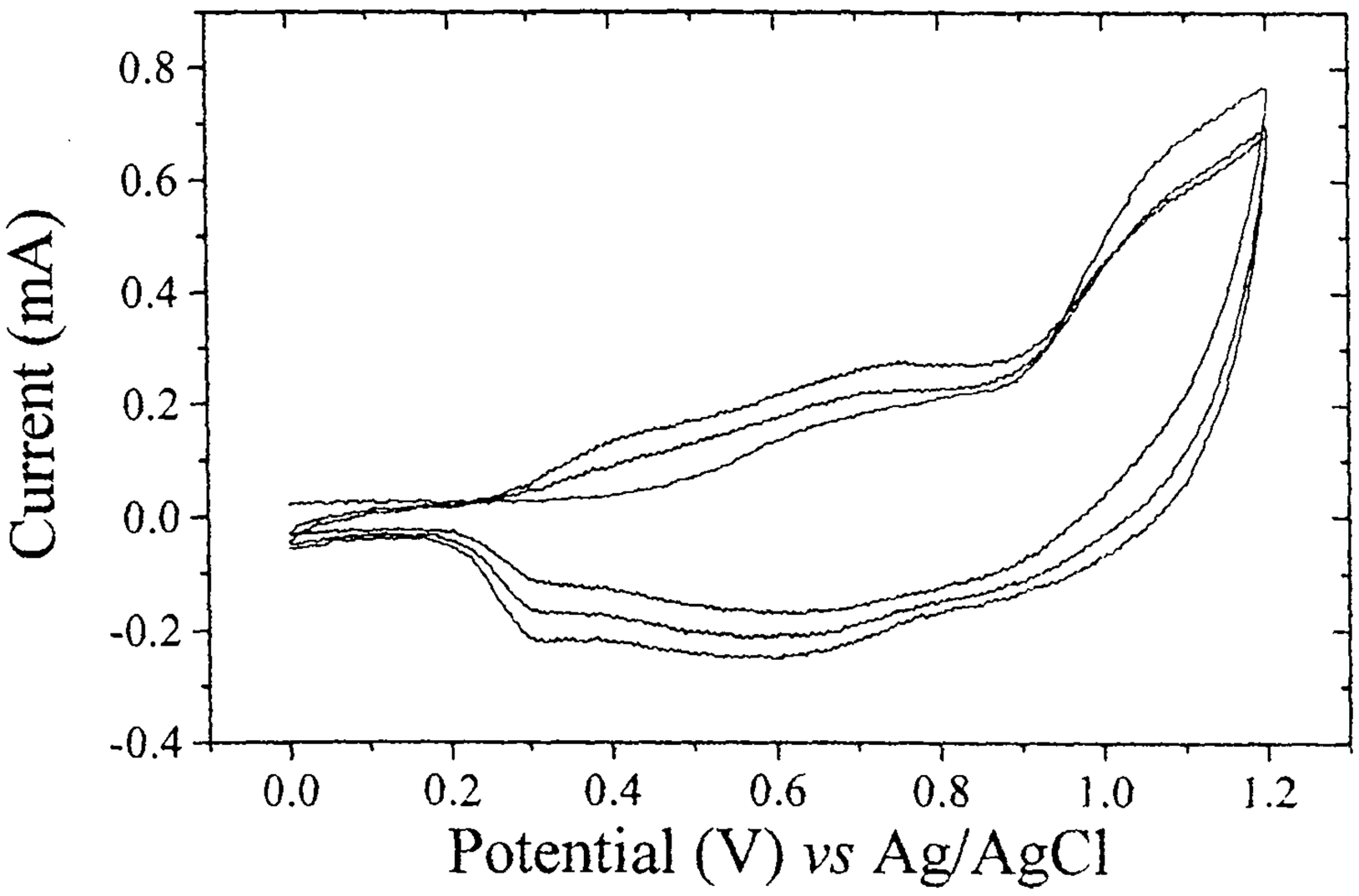

(a)

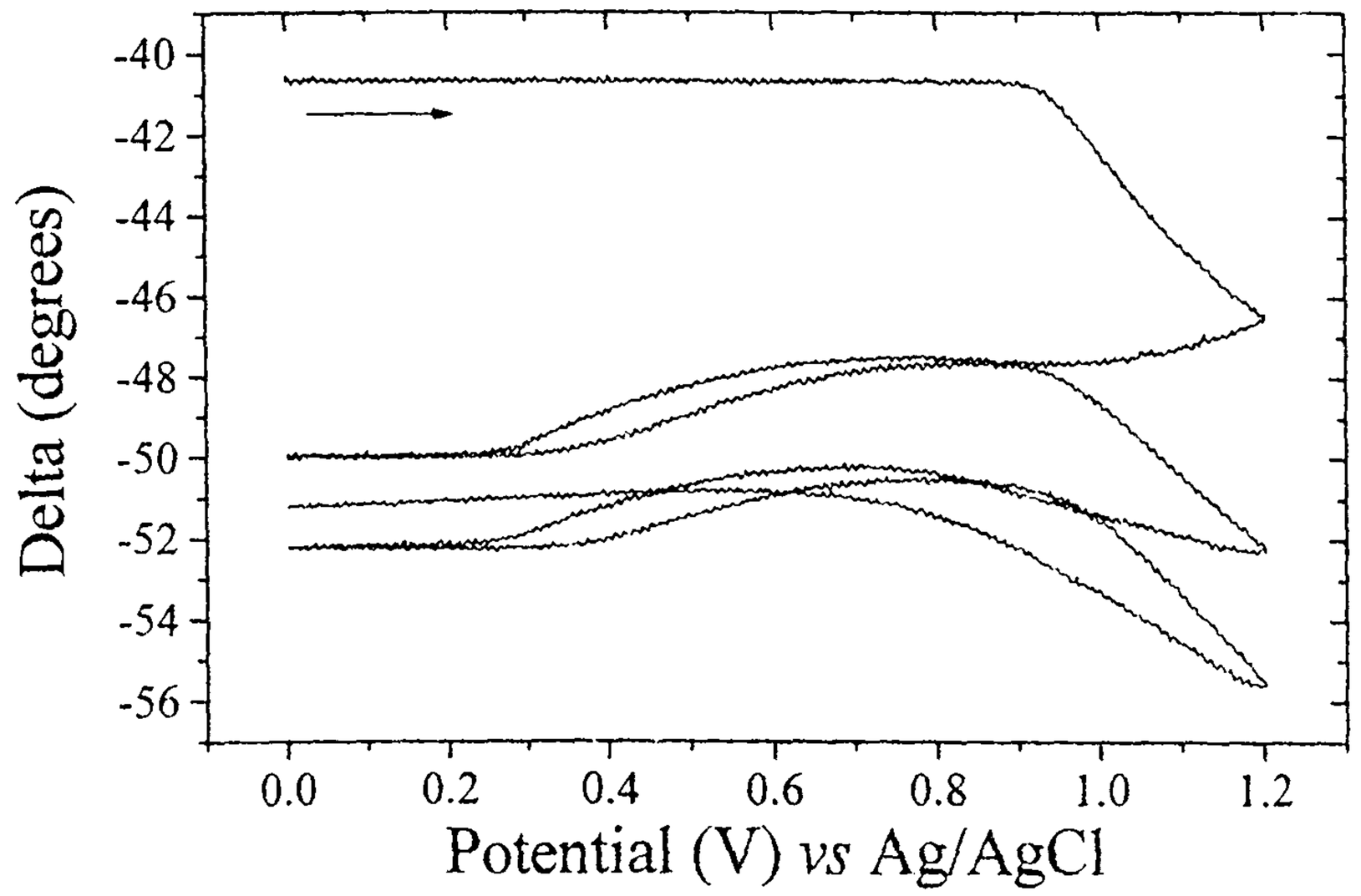

(b)

Fig. 6.3. (a) The first three cyclic voltammograms collected during the growth of poly[Pd(OMeSalen)], and (b), the corresponding variation of Δ recorded at 632.8 nm. Conditions as in Fig. 6.2.

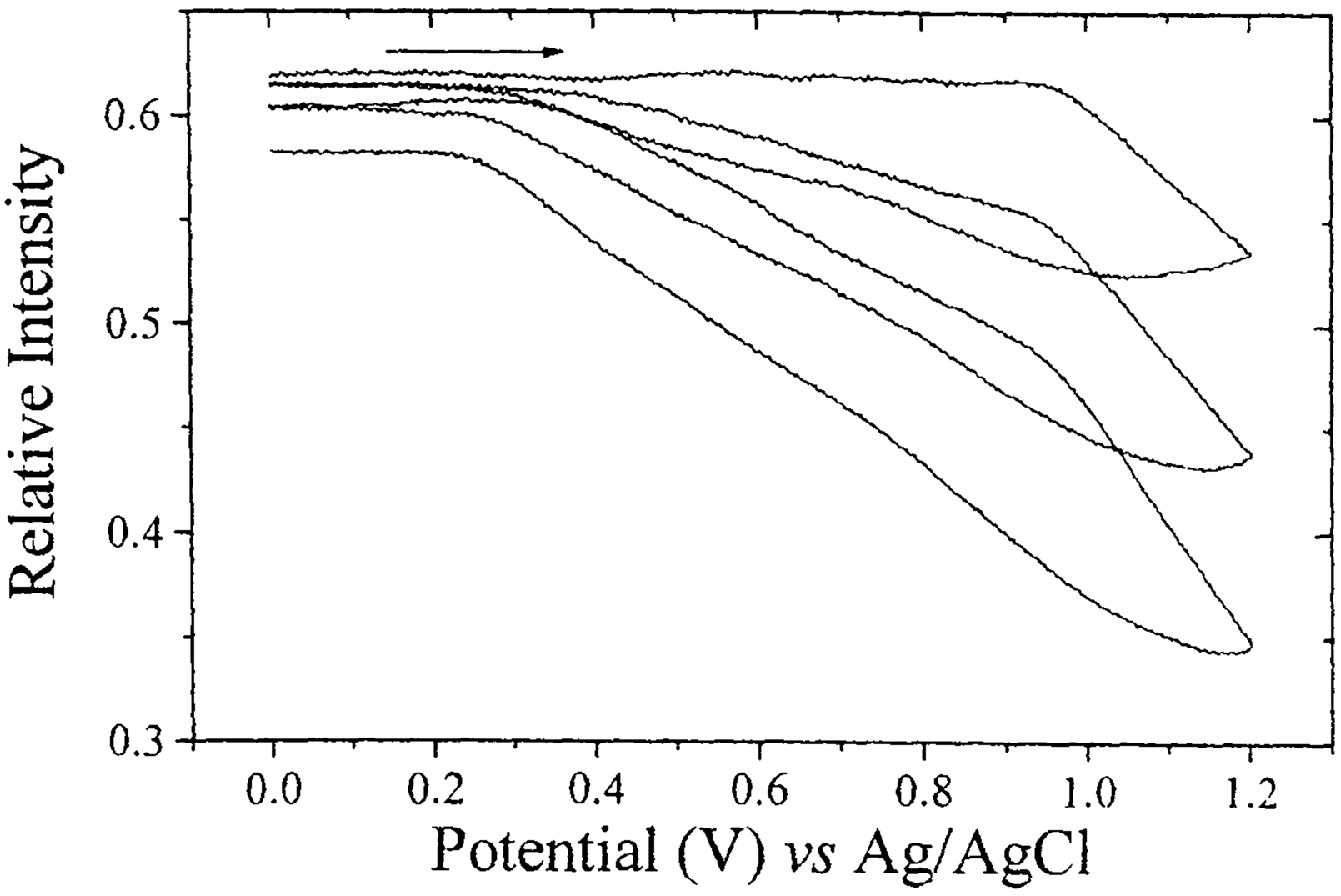

(c)

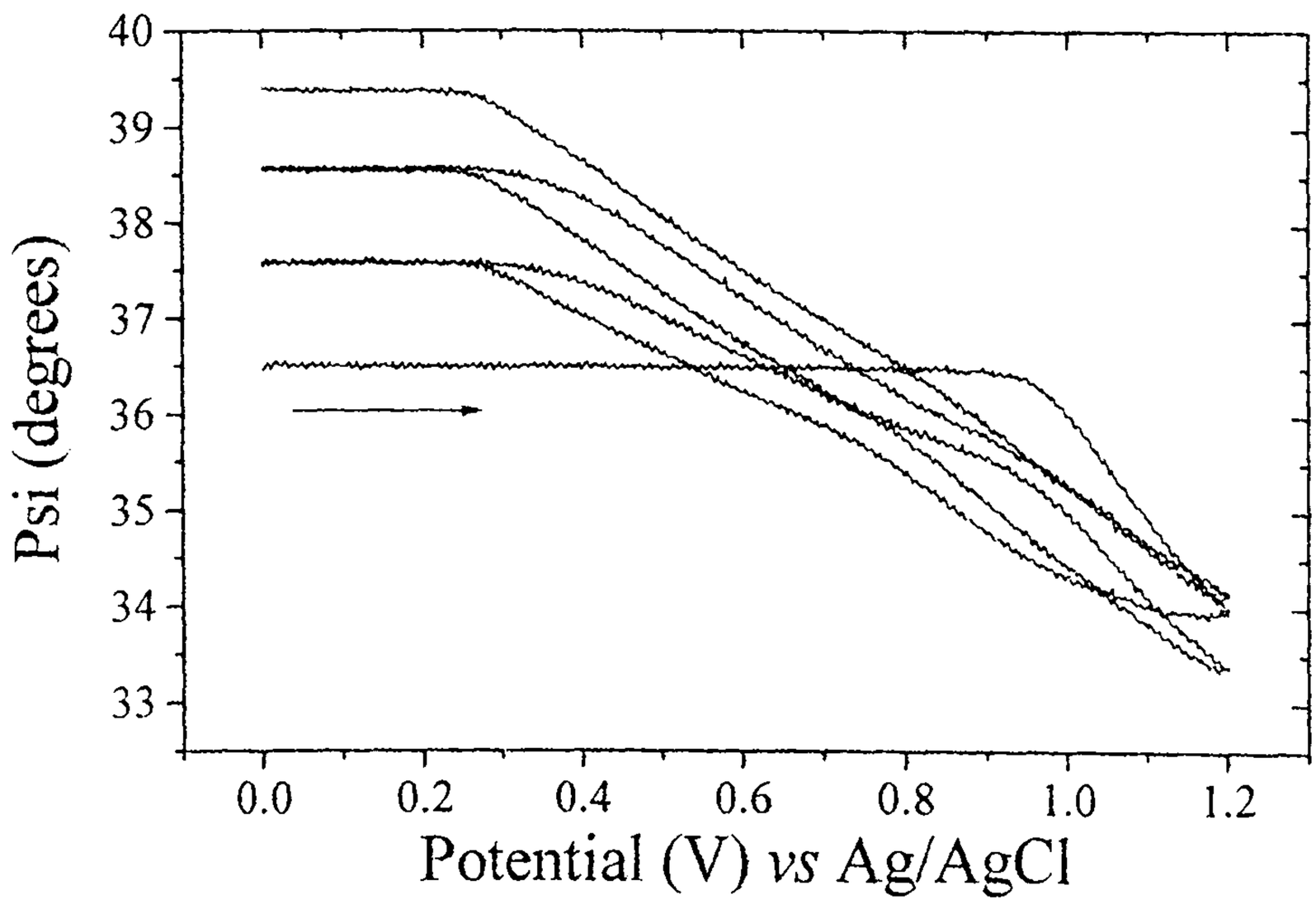

(d)

Fig. 6.3. (c) The relative intensity and (d) the variation of Ψ recorded at 632.8 nm during the first three cyclic voltammograms collected during the growth of poly[Pd(OMeSalen)]. Conditions as in Fig. 6.2.

point. Evidently this process, whatever its origin, has no effect on delta and psi and is therefore occurring in solution only, though the intensity data show any species forming in the solution have very little or no absorption at 632.8 nm. Beyond 0.9 V on the first sweep, significant changes are seen in all three ellipsometric parameters corresponding to the onset of the second oxidative wave, which can clearly be assigned to the onset of polymerisation.

During subsequent cycles the first oxidative wave becomes more pronounced and the ellipsometric parameters begin to alter at *ca.* 0.3 V, corresponding to the onset of the first peak. The behaviour of the ellipsometric parameters differs during the two oxidative waves, Δ showing a slight increase in value during the first peak before a decrease during the second, while Ψ and the intensity show a much less pronounced decrease in value between 0.3 and 0.9 V than during the second wave. There appear to be two distinct oxidation processes occurring, only the second of which leads to polymerisation. The current passed between *ca.* 0.3 and 0.9 V during the first anodic sweep is due to a solution oxidation, as mentioned above, however subsequent scans show a more pronounced wave and changes in the ellipsometric parameters in this region, indicating that though further solution oxidation may be occurring, the current passed is at least in part due to a surface process, likely to be oxidation of the polymer film already deposited in previous cycles

Fig. 6.4 shows the ellipsometric parameters for all fifteen cycles of growth. Both Δ and Ψ decrease in value over the first three cycles, before showing an increase in value with each of the subsequent scans suggesting a possible change in the properties of the film and/or the mechanism of deposition. The intensity steadily decreases with each of the fifteen cycles indicating the film absorbs at 632.8 nm .

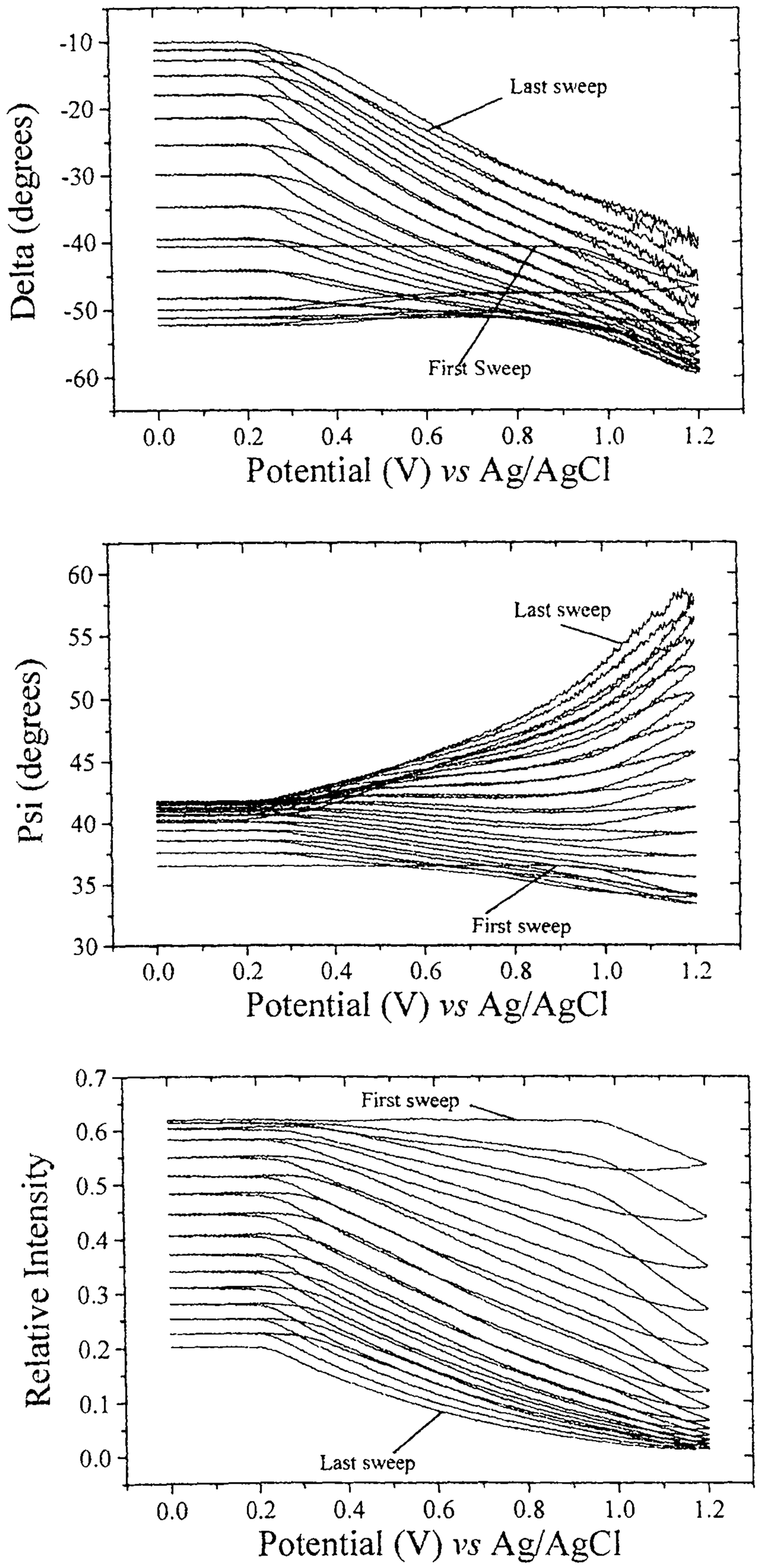

Fig. 6.4. The variation in Δ, Ψ and relative intensity during all 15 cycles of the growth of poly[Pd(OMeSalen)]. Conditions as in Fig. 6.2.

6.2.1.2 Potential Cycling of the Modified Electrode

The current and optical data for the potential cycling of the film in monomer-free electrolyte are shown in Fig. 6.5 (a) and (b). The behaviour of the ellipsometric parameters is very similar to that observed during the last cycle of growth, however the CV is markedly different, the second oxidative peak is much smaller than during the growth, the peak current being *ca.* 0.5 mA compared to *ca.* 0.8 mA at the same potential during growth. In contrast the first oxidative wave has a slightly higher peak current, *ca.* 7.5 mA, *ca.* 1 mA larger than during growth, this would support our initial assignment of the two peaks as the first being due to oxidation of the polymer film while the second is primarily due to oxidative polymerisation, though clearly there is a second oxidation process occurring in the film as the peak is still present during the potential cycling.

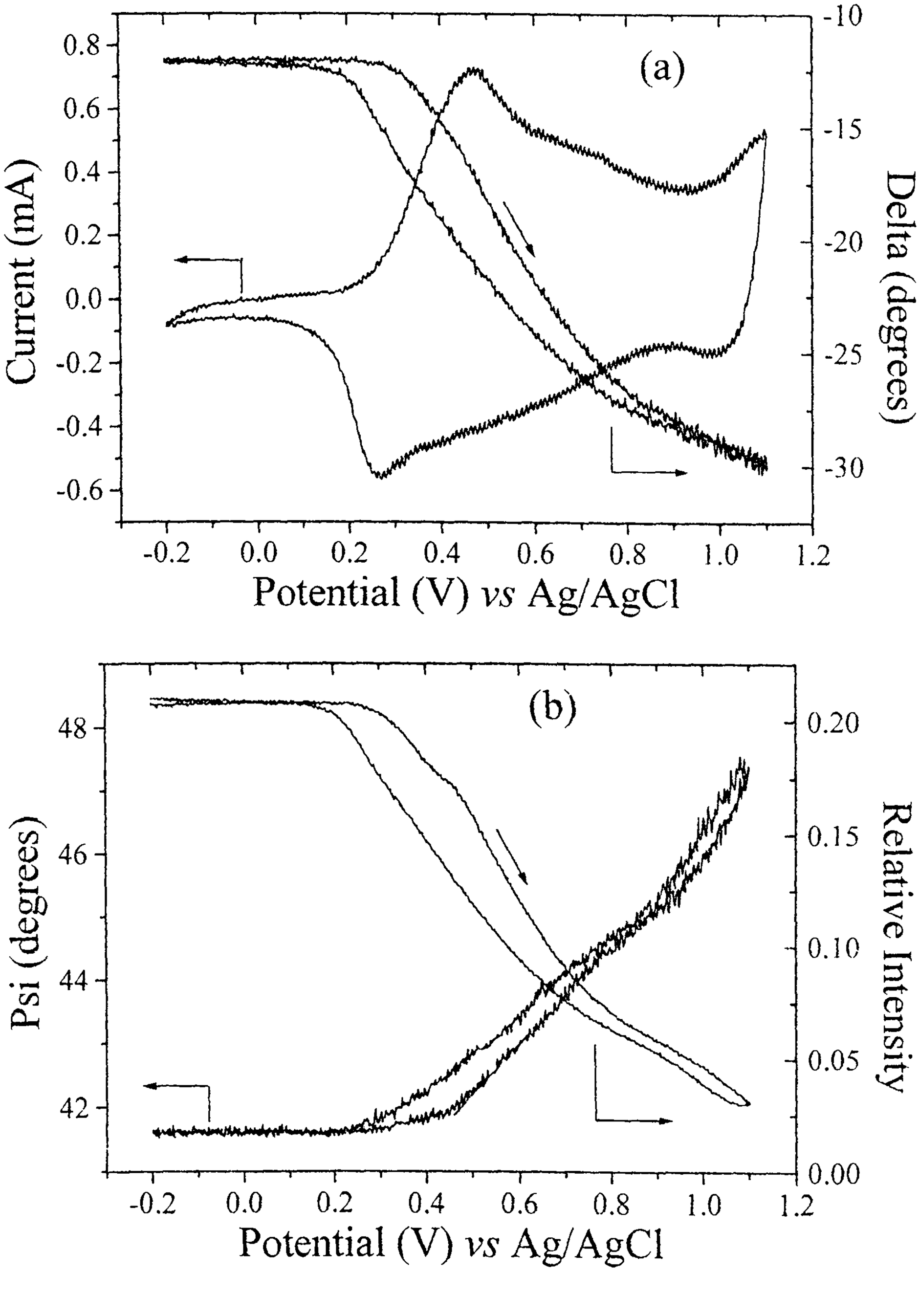

Fig. 6.5. The variation of Δ (a), Ψ and relative intensity (b) during the first cyclic voltammogram of the polymer coated electrode after the completion of growth. The film was cycled at 100 mV s^{-1} in 0.1 mol dm^{-3} TBAT/MeCN

6.2.1.3 Potential Stepping of Modified Electrode

Potential stepping experiments were performed for comparison with the cyclic voltammograms and FTIR data, the optical data is presented in Figs. 6.6 (a) and (b). While it is clear that in the potential range *ca.* 0.4 - 1.1 - 0.8 V the film is still evolving 35 s after the potential step, the values reached at the anodic limit, 1.1 V, are similar to those obtained during the much faster potential changes while cycling: the maximum value of Psi is *ca.* 1 degree higher than during cycling, Delta is *ca.* 2 degrees lower and the intensity drops to *ca.* 0.06 during stepping compared to *ca.* 0.03 when cycling. Despite the small changes in value at the anodic limit, the optical parameters clearly do not return to their original values at the end of the potential stepping, in contrast to what was observed during cycling. Delta and Psi are close to their original values but the intensity is significantly lower, possibly indicating charge trapping within the film, which is supported by the coulombic data from the cycling experiments, which show up to 30 % of the charge passed during the anodic sweep is uncompensated at -0.2 V on the cathodic sweep.

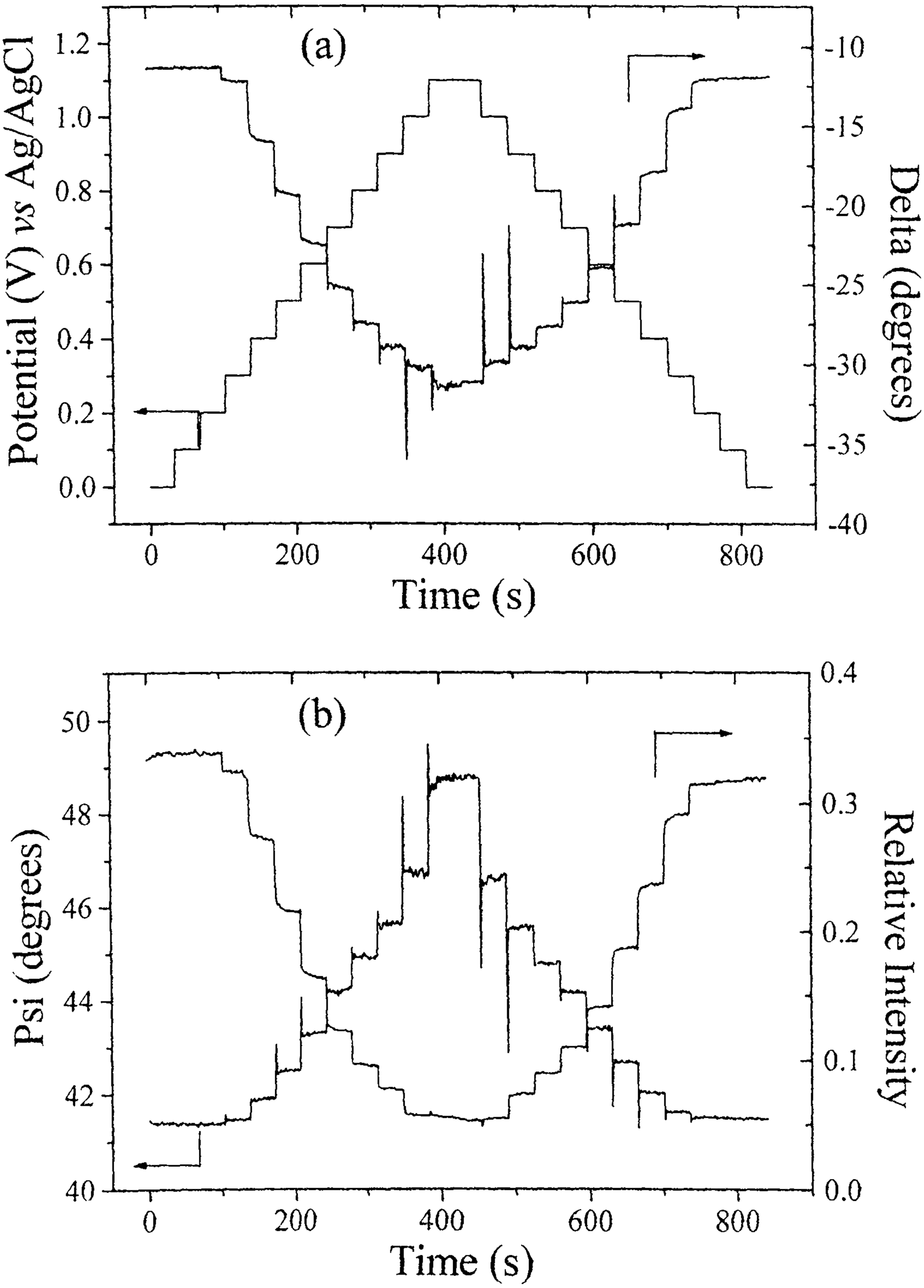

Fig. 6.6. Variation of Δ (a), Ψ and the relative intensity (b)during potential stepping of the film. The steps were 100 mV and the film was held at each potential for 35 s.

6.2.2 Fitted data

6.2.2.1 Growth of poly[Pd(OMeSalen)]

The fitting of the ellipsometric data proved quite arduous, the first three cycles of growth fitting relatively easily to a simple homogeneous model, but the subsequent cycles fitting only to an inhomogenous model.

The variation of *n*, *k*, and the thickness for the first three cycles fitted to a homogeneous model are shown in Fig. 6.7 (a)-(d). Growth is initiated by nucleation onto the surface by strands of up to 40 nm in length, or shorter strands which rapidly grow to this length, to form a film which clearly consists mainly of solvent at this point, the values of *n* and *k* being very close to those of the acetonitrile (1.344, 0). Dahm and co-workers have postulated that polymerisation of poly[Ni(Salen)] is initiated by the formation of a charge transfer stacked deposit [5], as discussed in the introduction, however this is not consistent with the ellipsometric data presented here which clearly indicate the film is very diffuse during the early stages of formation.

As the potential is swept up during the first scan, *k* rapidly increases to 0.06, *n* to 1.37 and the thickness to 60 nm. On the reverse scan, *k* rapidly returns to a low value but *n* continues to rise to 1.51, and by the end of the third cycle it reaches 1.56. These are quite high values and suggest a significant exaltation due to electron delocalisation [16]. Fig. 6.8 shows the variation of *n*, *k* and the thickness during the last five cycles of growth with the data having been fitted to an inhomogeneous model, identical to that described in the experimental chapter (section 2.3) and was also used to fit the poly[Ni(OMeSaltMe)] in the previous chapter (section 5.2.2.1) . The film was considered to consist of ten layers of equal thickness, each layer within

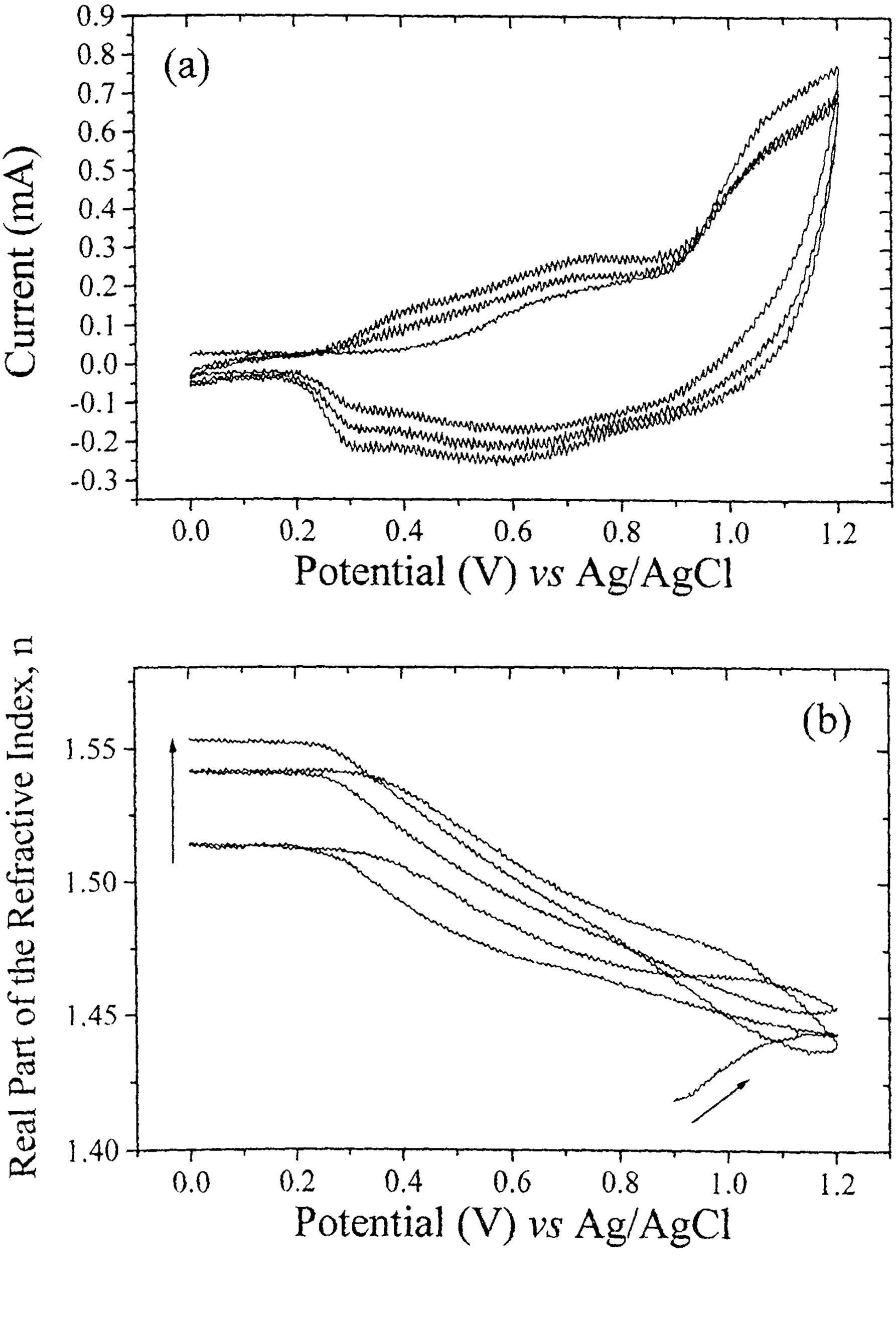

Fig. 6.7 (a) The current passed during the first three cycles of polymerisation on a Pt disk electrode at 100 mV s^{-1}. (b) The variation of the real part of the refractive index, n, from data gathered at 632.8 nm fitted to a homogeneous model.

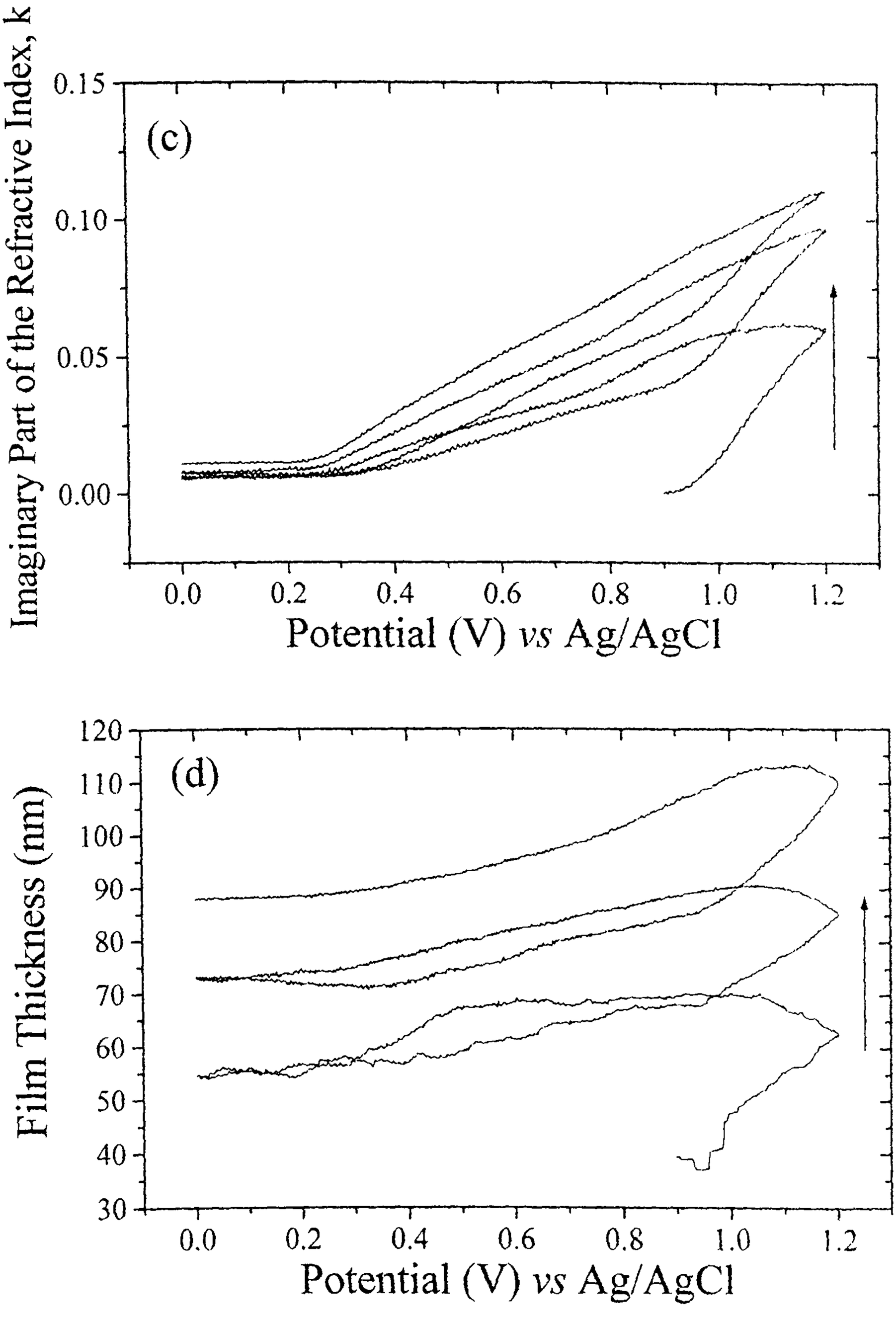

Fig. 6.7 The variation of the imaginary part of the refractive index, k ,(c) and film thickness (d) during the first three cycles of polymerisation from data gathered at 632.8 nm fitted to a homogeneous model.

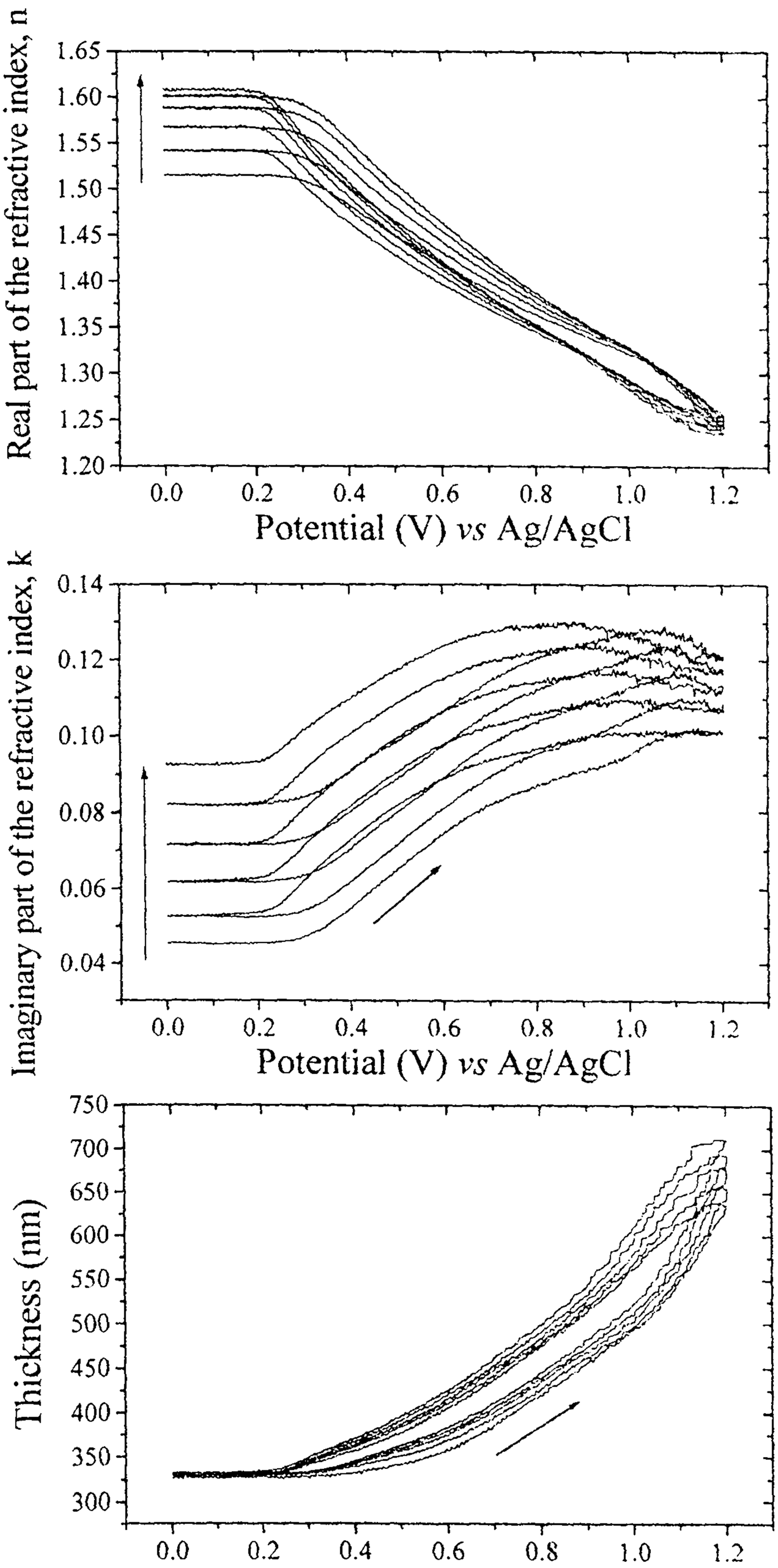

Fig. 6.8. The last five cycles of growth fitted to an inhomogeneous model as described in the text. The film was grown for a total of fifteen cycles between 0 and 1.2 V vs Ag/Ag^{+} at 100 mV s^{-1}, in 0.1 mol dm^{-1} TBAT in MeCN with 1 mmol dm^{-3} Pd(OmeSalen)

itself being homogeneous. The innermost layer next to the electrode contains the smallest amount of solvent and is the most compact, the film becoming more diffuse and containing more solvent with each layer away from the electrode. The complex refractive index, i.e. *n* and *k*, was fixed for the outermost layer to be equal to that of the solvent (acetonitrile, 1.344, 0) while *n* and *k* of the innermost layer and the overall thickness of the film were allowed to float during the fitting procedure. The values of *n* and *k* for the inner layers vary linearly between the values of the inner and outermost layers. A more detailed model is not possible without data from a number more wavelengths, however the behaviour of the film was qualitatively the same regardless of the exact choice of values for *n* and *k* of the outermost layer, so the model would appear, at least qualitatively, to be very reliable.

Over the course of the film growth, both homogeneous and inhomogenous, *k* steadily increases with each subsequent cycle even when the film is in its neutral form, most likely due to incomplete reduction of the film in later cycles. In later cycles the value of *n* continues to increase with each cycle for the film in the neutral state, however the decrease that occurs upon oxidation is a great deal more marked in later cycles than for the early scans, this is due to the appearance of a strong absorption in the near IR region, confirmed by our IR studies (see section 2.5) and frequently observed in previous studies [17-19]. The thickness shows very little change during the last five cycles of polymerisation, in contrast to marked changes over the course of the first three, suggesting that the first stages of polymerisation result in both increasing thickness of the polymer network and consolidation within it (indicated by *n* and *k* changing with each cycle), while in the later stages of polymerisation only consolidation is occurring, as *n* and *k* continue to increase but the

thickness remains stationary. It is interesting to note that, as the *n* and *k* values shown in Fig 6.8 relate to the innermost part of the film, i.e. that next to the electrode, after fifteen cycles of growth consolidation is still able to occur in the most compact part of the film.

6.2.2.2 Potential Cycling of the Modified Electrode

The film clearly remains inhomogenous after growth and the data was fitted in the same manner as that for the growth. The values of *n* and *k* for the innermost layer of the film and the overall thickness during potential cycling are shown in Fig. 6.9 (a)&(b). There appear to be four distinct potential regions, a reduced region below 0.3 V, a region from 0.3 to *ca.* 0.7 V in which *n* falls rapidly and *k* rises rapidly and the thickness increases steadily, from 0.7 to *ca.* 0.95 V the rate of change of all three parameters is less, and a region between 0.95 and 1.1 V in which *n* falls rapidly again, the thickness increases markedly but *k* changes very little. The increase in thickness is in contrast to the massive contraction observed of the inhomogeneous poly[Ni(OMeSaltMe)], discussed in the previous chapter, and is much higher than might have been expected, swelling to almost a factor of two at the highest potential reached. The quantitative behaviour of the film was unaltered by the exact choice of value for the outer refractive index, as reasonable values for the optical parameters showed *n* decreasing strongly while *k* and the thickness show a large increase with increasing potential. The increase in the thickness can be explained by the influx of solvent as electrolyte floods into the oxidised film to compensate the charge, dragging solvent with it. As with the Ni Salens described in earlier chapters, the

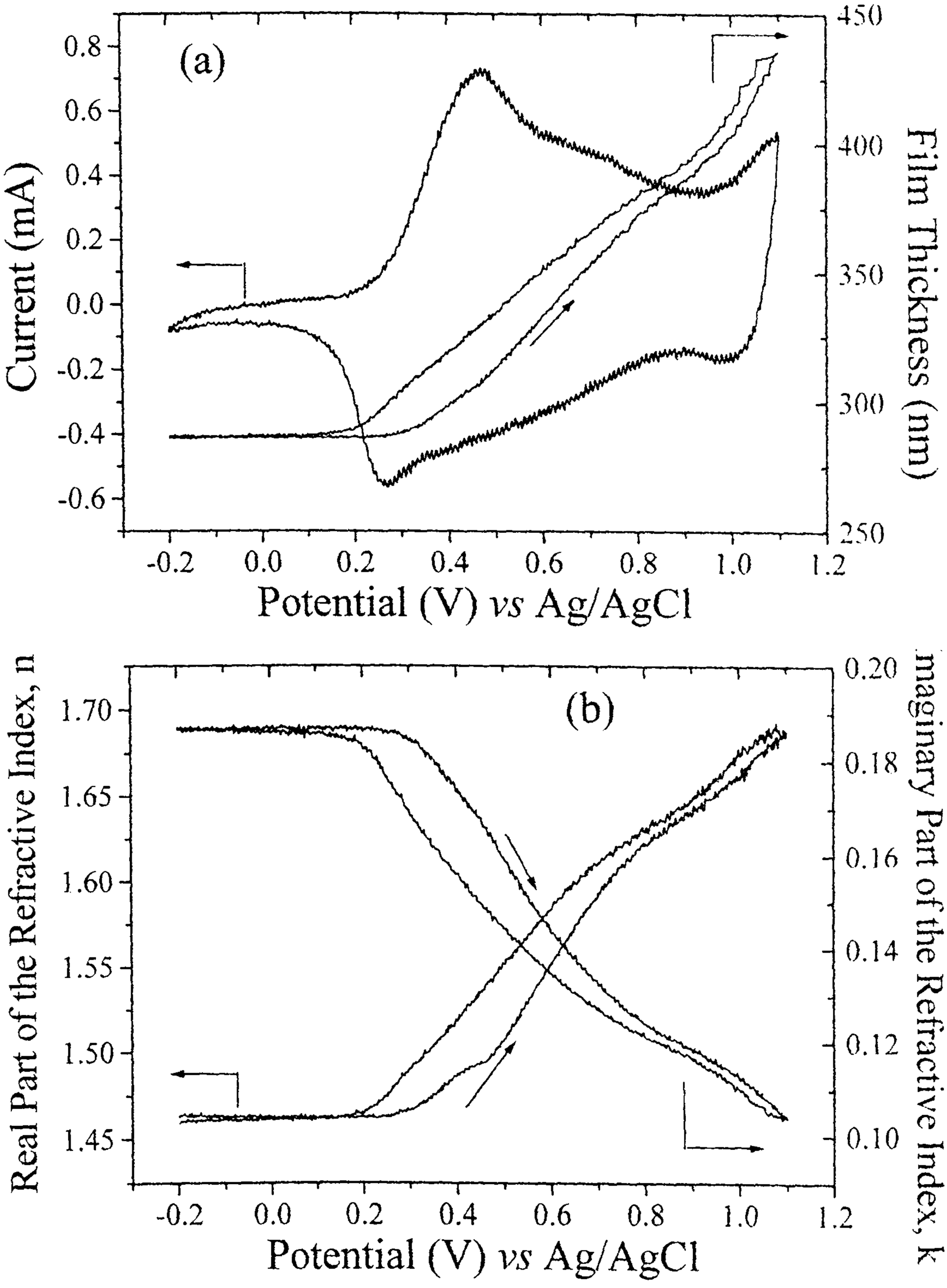

Fig. 6.9. The variation in (a) thickness and (b) n and k during the first cyclic voltammogram of the polymer coated electrode. The experimental data was fitted to an inhomogeneous model, the film being considered to consist of 10 layers, the innermost being compact film varying to the outermost consisting of 100 % solvent. See Fig. 2.8 in chapter 2.

extent of the increase, in this case the film almost doubles in thickness at the anodic limit, indicates carbon linkages between monomer units must be formed during polymerisation, or the film would simply dissipate into solution, whereas the cycling shows any oxidation processes are clearly reversible, the original values of *n*, *k* and the thickness being obtained at the end of the cycle. The large increase shown by *k* can be explained by the film becoming more absorbing at the probe wavelength, and to some extent this can be seen by eye, the golden yellow film becoming increasingly green and darker with potential. The decrease in *n* is due to the film becoming strongly absorbing in the near-IR as it is oxidised (see section 2.5), this absorbance having the effect of reducing the value of the refractive index at the probe wavelength.

6.2.2.3 Potential Stepping of the Modified Electrode

The fitted data for the potential stepping experiments is presented in Fig. 6.10. There is a sudden increase in thickness at 1.1 V which is much more pronounced than the increase seen during cyclic voltammetry, though the maximum thickness reached is approximately the same. At intermediate potentials the relaxation time of the film is of the order of a few seconds, however upon stepping to 1.0 and 1.1 V the film is still evolving after 35 s. Upon returning to 0 V the original values are not regained, the thickness being *ca.* 15 nm greater and *k* being 0.004 higher, though *n* is almost unchanged, this is in agreement with the coulombic data for the cycling which suggest the film is not fully reduced. The four regions of behaviour described for the cyclic voltammograms are also in evidence during the stepping, a reduced region below 0.3 V, a region between 0.4 and 0.7 V in which *n* decreases

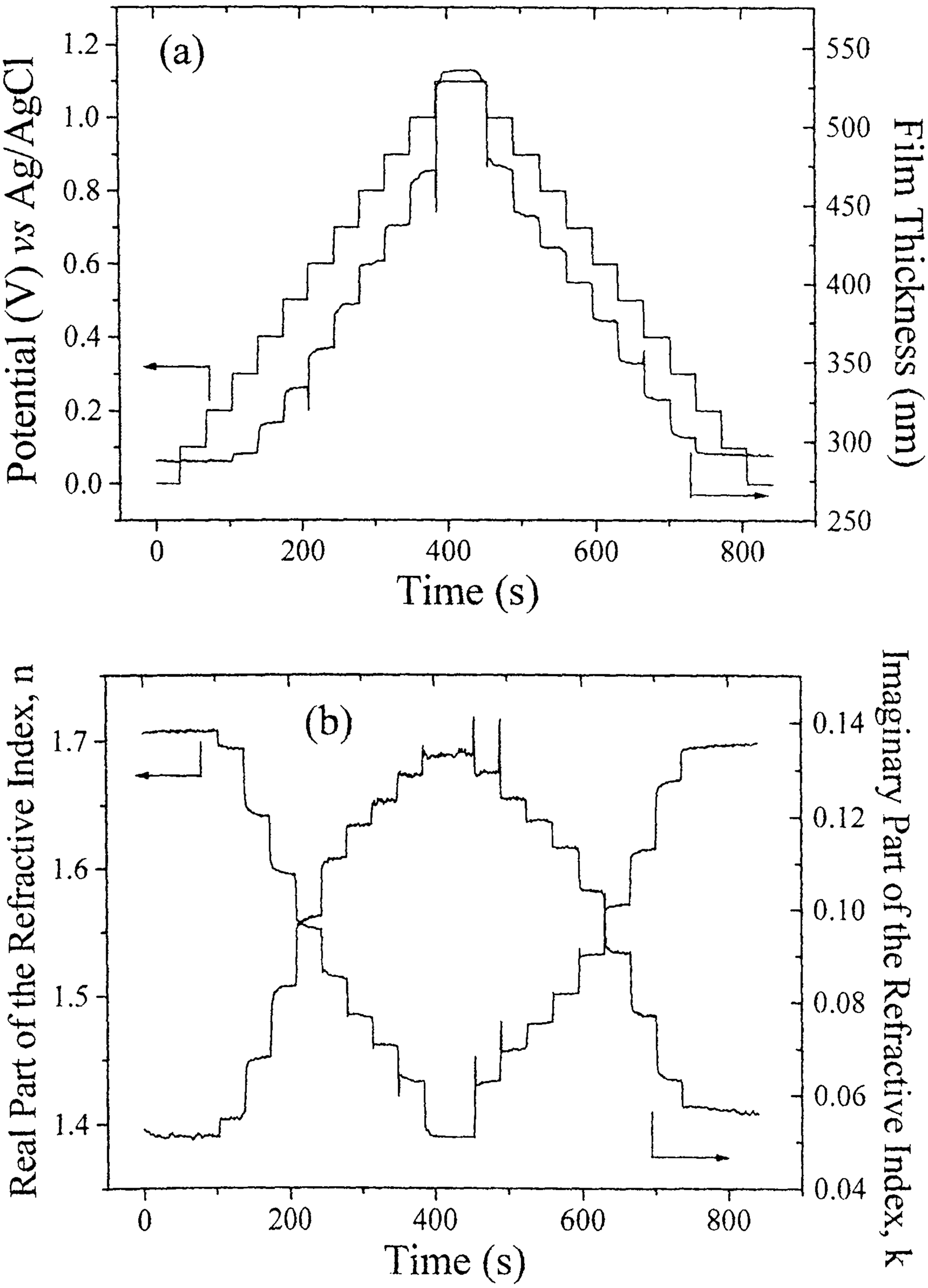

Fig. 6.10. The variation of film thickness (a) and n and k (b) during potential stepping. The potential was altered from 0-1.1-0 V in 100 mV steps, 35 s at each potential.

strongly and *k* increases strongly, a region 0.7 - 0.9 V in which the rate of change of *n* and *k* is less rapid and the thickness increases, and a final region 1.0 - 1.1 V in which the thickness increases rapidly, *n* decreases strongly and *k* is almost stationary.

6.2.3 Data collected at 594.1 nm - poly[Pd(OMeSalen)] Film 2

As an important check of the validity of the model, data were also gathered using a laser of 594.1 nm wavelength. A second film was grown and the data collected at 594.1 nm was compared to the data gathered at 632.8 nm for film 1. The cyclic voltammograms during the growth of film 2, shown in Fig. 6.11, and behaviour of the ellipsometric parameters mirrored the data gathered at 632.8 nm for

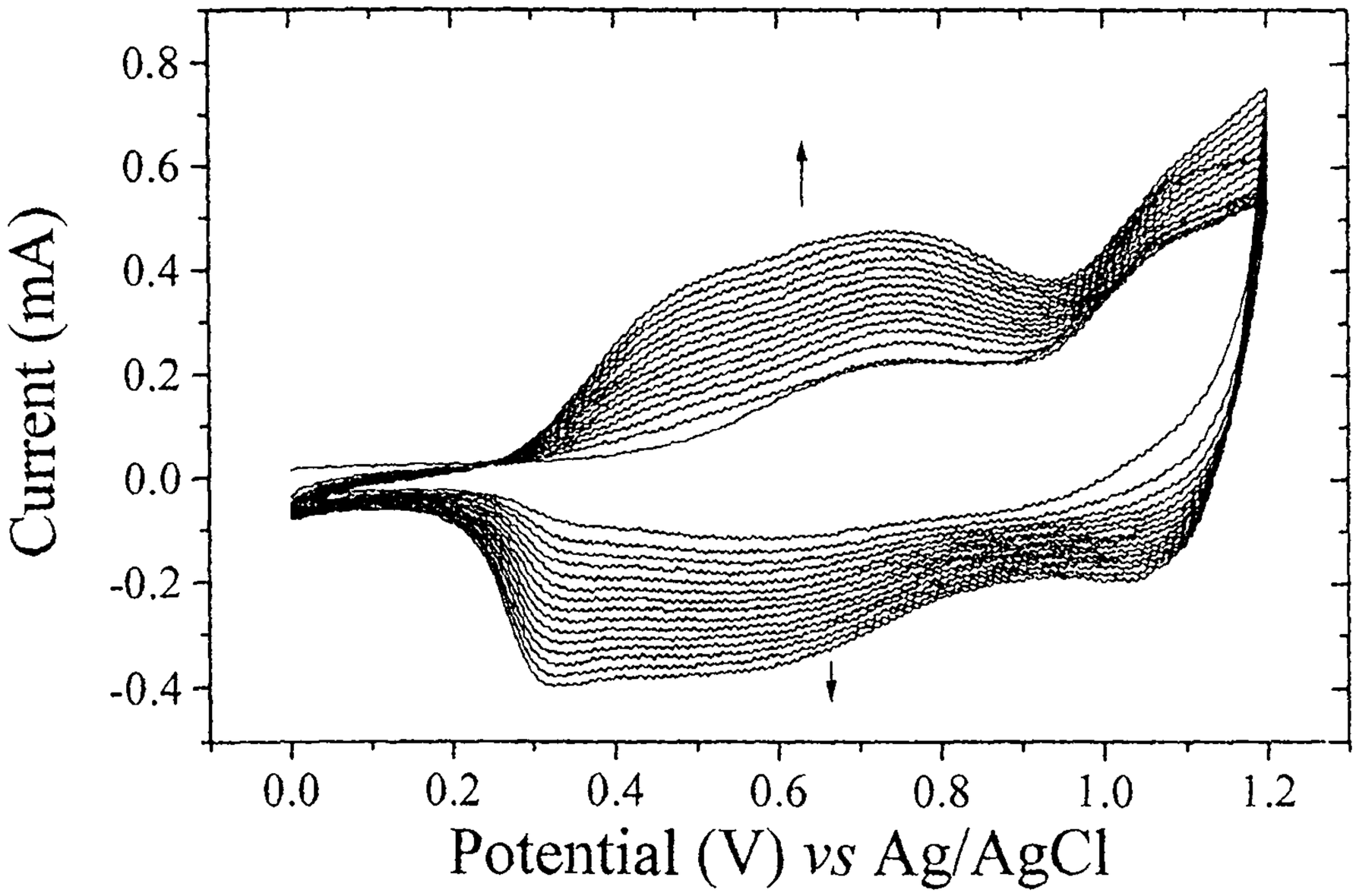

Fig. 6.11. The growth of poly[Pd(OMeSalen)] film 2. The electrochemical conditions as in Fig. 6.2, the ellipsomtric parameters were measured at 594.1 nm during growth and cycling.

film 1. Again the film could only be fitted to an inhomogeneous model for all except the very first steps of growth, however the thickness generated from the data was substantially lower than that for film 1. The ratio of the charge passed during the growth of the two films corresponds closely to the ratio of the thicknesses, the total charge passed during growth being 10.12 mC and 7.33 mC, and the thicknesses of the films after growth is completed *ca.* 270 nm and 185 nm for films 1 and 2 respectively. The charge passed during the growth of film 2 is 73 % of that passed for film 1, and the final thickness is 68 % of film 1, so the validity of the model seems to be confirmed, and uncontrollable variability in experimental conditions the most likely source of the difference. Due to the large volume of the ellipsometric cell there was only enough Pd(OMeSalen) to make up one monomer solution, and given there were over two weeks between the growths of the two films, changes in the monomer solution as it aged seem the most likely cause. The CV after cycling shown in Figs. 6.12 (a) and (b) can be seen to differ from the corresponding one for film 1 above (Fig. 6.9), the peak at 0.4 V being not so pronounced and the slight hump at *ca.* 0.7 V has now become the main anodic peak. None of the films grown between the studies of films 1 and 2 are directly comparable with either of the two discussed, though a thinner film was grown (10 cycles, 0 - 1.2 V) and the CV of this film appears to be a hybrid of the two presented, the peaks at *ca.* 0.4 and 0.9 V being roughly the same height, suggesting there was indeed some continuing degradation of the monomer solution, possibly due to the uptake of water.

Despite the differing CVs, the qualitative behaviour of the film remains unaltered. The thickness, n, and k start to alter at *ca.* 0.3 V for both films even though the first peak is much less pronounced in the case of film 2, though at higher

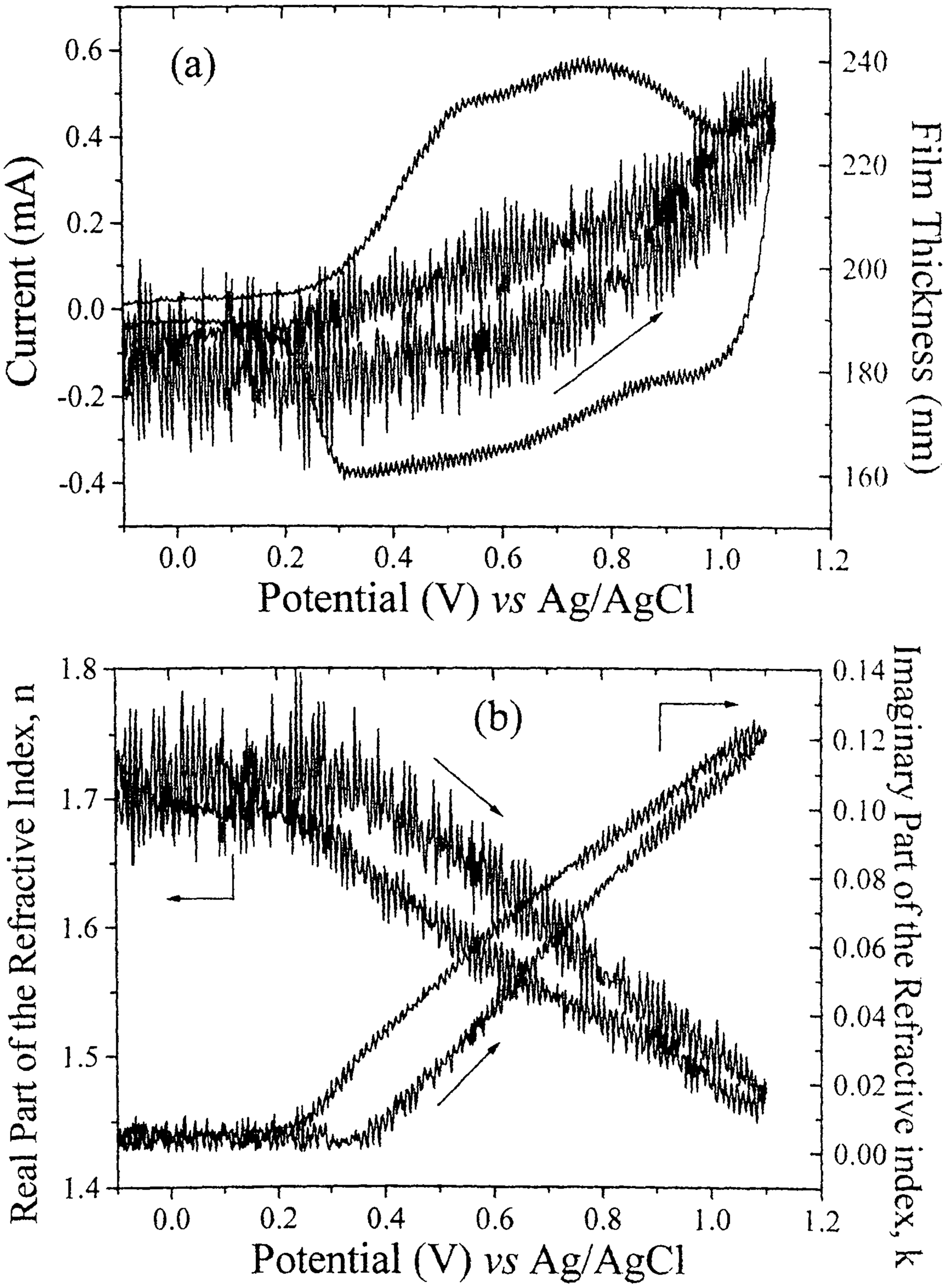

Fig. 6.12. Film 2.The variation of film thickness (a) and *n* and *k* (b) during the first cycle after growth of poly[Pd(OMeSalen)] fitted from data collected at 594.1 nm.

potentials differences between the films become clear. The changes in *n* are very similar both quantitatively and qualitatively, though *k* shows an increase in value similar to that observed for the first film, but to a lesser extent, rising to a maximum value of *ca.* 0.12 compared to 0.18 at 1.1 V. The thickness increases in a similar manner to the first film, though again to a lesser extent, the increase being of the order of 30 % of the reduced film thickness in comparison with over 60 % for the film probed at 632.8 nm. The first film had increased by *ca.* 30 % of its reduced thickness at just over 0.8 V, this is just before the fourth region of oxidation described above, suggesting the final oxidation process of the sweep is not happening in the second film, or at least not to the same extent, as it is clear that the peak at 1.1 V is not as pronounced in the CV of the film 2. It is interesting to note that the CV after growth of the film 2 resembles the CVs recorded during growth far more closely than that of film 1. Fig. 6.13 shows the last cycle of growth overlaid on the first cycle after growth was completed for the two films. As discussed above, the first broad wave during growth was assigned to oxidation of polymer already deposited, and the second sharper peak to further oxidative polymerisation, therefore the first wave would be expected to be almost unchanged between growth and cycling. While this is the case for film 2, film 1 shows a pronounced peak at 0.4 V at the beginning of the broad wave. The presence of the peak at 0.4 V was observed for other films grown as checks on reproducibility, and the peak appears to diminish as the monomer solution ages, indicating some of the differences observed between films 1 and 2 may be due to changes in the monomer solution with time.

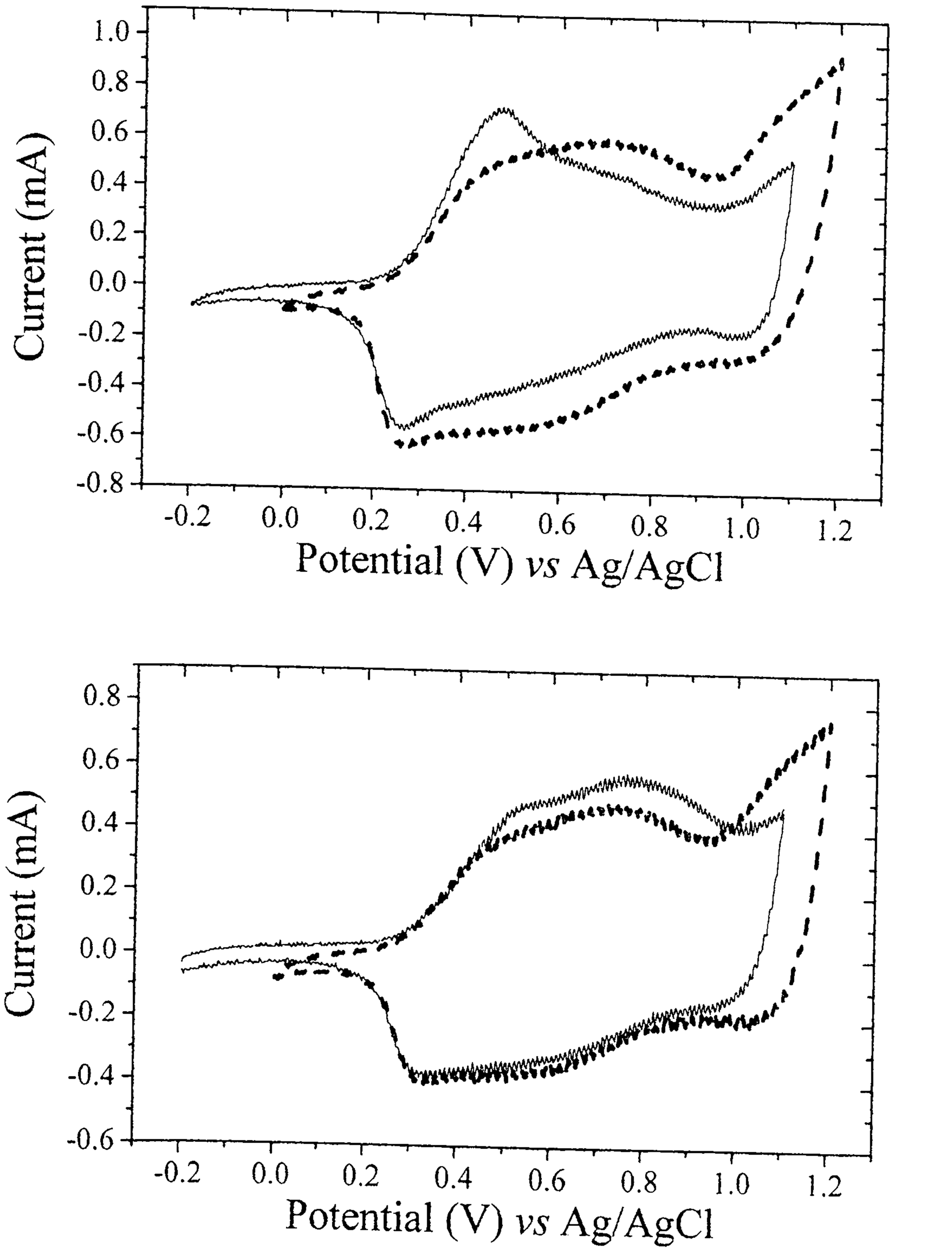

Fig. 6.13. A comparison of the last CV of growth (dashed) and the first cycle of the modified electrode for film 1 (top) and 2 (below)

6.2.4 Characterisation of poly[Ni(OMeSalen)]

The corresponding Ni complex was also synthesised and investigated. The ellipsometric cell is relatively large, and there was insufficient Ni(OMeSalen) to make the necessary 250 ml 1 mmol dm^{-3} monomer solution to study polymerisation. It was however still possible to study the cycling of the modified electrode in monomer free electrolyte: polymerisation was performed in a smaller cell and the electrode then transferred to the ellipsometric cell and immersed in 0.1 mol dm^{-3} TBAT in MeCN.

Fig. 6.14 shows the CVs recorded during growth of the poly[Ni(OMeSalen)] film, which can be seen to differ from the cyclic voltammograms for poly[Pd(OMeSalen)] in a number of ways (see Fig 6.2). During the growth of

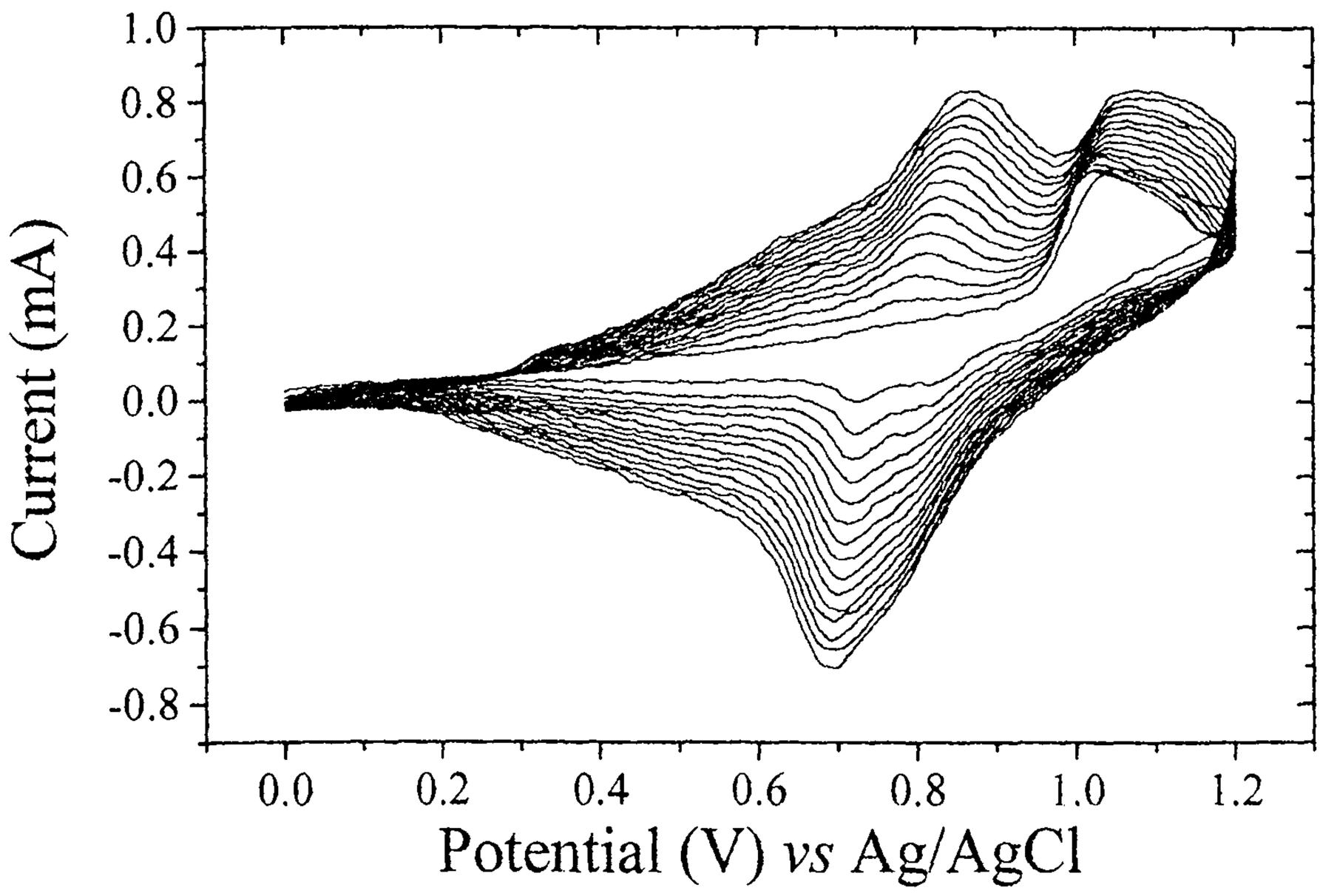

Fig. 6.14. Growth of poly[Ni(OMeSalen)]. A Pt disk electrode was cycled at 100 mV s^{-1} in 1 mmol dm^{-3} [Ni(OMeSalen)] with 0.1 mol dm^{-3} TBAT/MeCN

poly[Pd(OMeSalen)] a broad wave was observed between 0.4 and 0.9 V, the peak current being reached at *ca.* 0.7 V, before a second oxidative wave between 1.0 and 1.2 V, with the current still increasing at the anodic limit. In contrast during the growth of poly[Ni(OMeSalen)] a broad shoulder is observed from 0.3 - 0.7 V, a peak at 0.8 - 0.9 V before a second wave from 1.0 - 1.2 V, but with the peak current reached before the anodic limit. As mentioned, there is no ellipsometric data for the growth, but the sharp increase in the current at *ca.* 0.9 V on the first anodic sweep would suggest the second peak between 1.0 and 1.2 V is due to oxidative polymerisation, as seen with poly[Pd(OMeSalen)]. The shape of the peak between 0.3 and 0.9 V is markedly different from the same region for poly[Pd(OMeSalen)], but is likely to be again due to oxidation of the polymer already deposited as the broad shoulder and sharp peak are features also of the cyclic voltammograms recorded after growth, shown in Fig. 6.15. The CVs of the poly[Ni(OMeSalen)] modified electrode in Fig. 6.15 and the Pd counterpart (Fig. 6.5) both have an oxidative wave between 0.3 and 0.9 V, but the form it takes is markedly different, a sharp peak at 0.4 V for poly[Pd(OMeSalen)] compared to a broad shoulder up to *ca* 0.75 V and a clear peak at *ca.* 0.85 V displayed by poly[Ni(OMeSalen)]. The behaviour of the ellipsometric parameters is very similar for the two films, but Ψ and the intensity show a much less marked change between 0.4 and 0.8 V than for poly[Pd(OMeSalen)], and increase more steeply between 0.8 - 0.9 V, corresponding to the oxidative wave, suggesting the same processes occurring in the two films with the peak at 0.4 V in the Pd film masking the smaller changes seen around this potential in the Ni film.

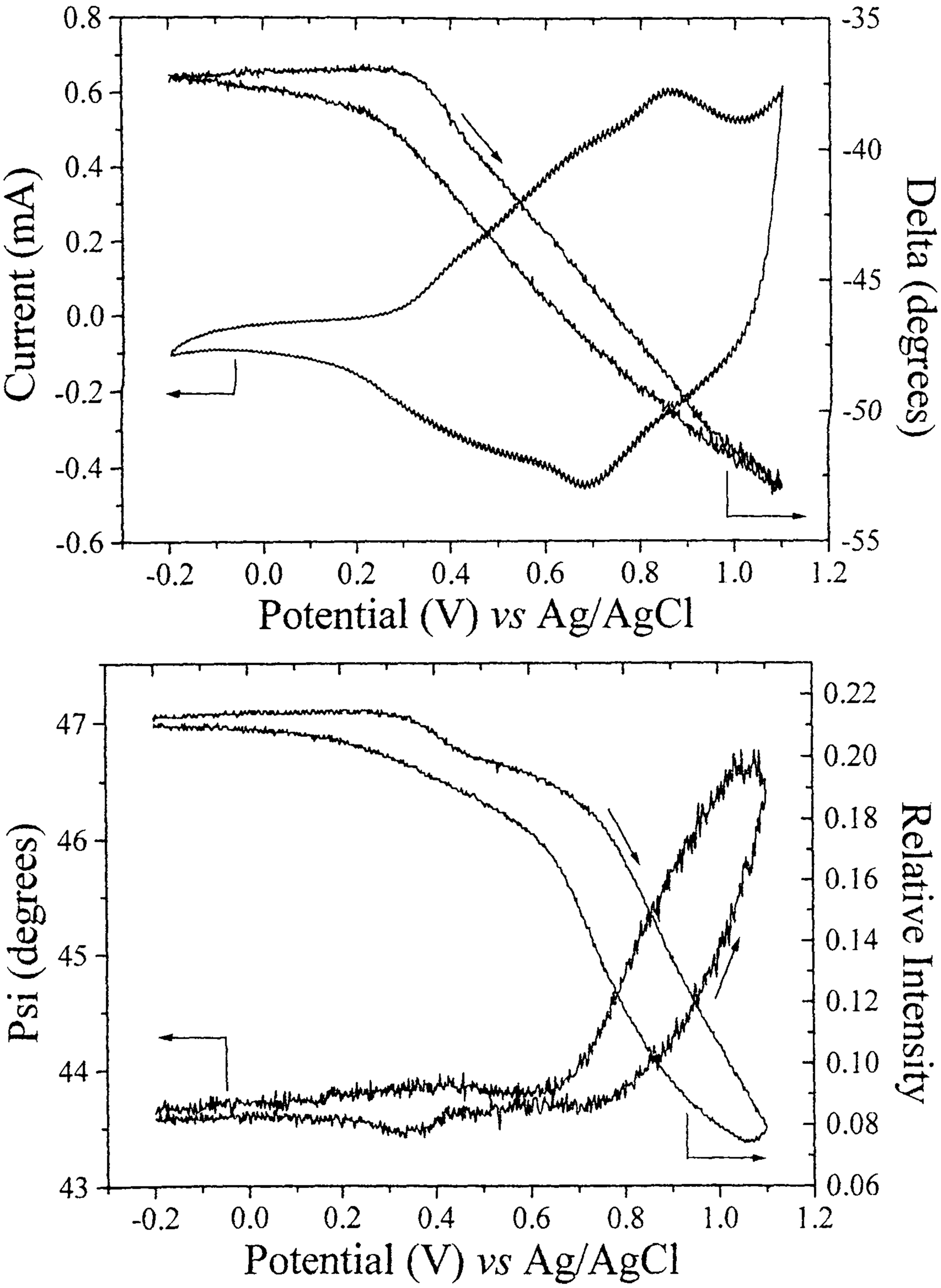

Fig. 6.15. The behaviour of Δ, Ψ and intensity during potential cycling of the poly[Ni(OMeSalen)] electrode in 0.1 mol dm^{-3} TBAT in MeCN

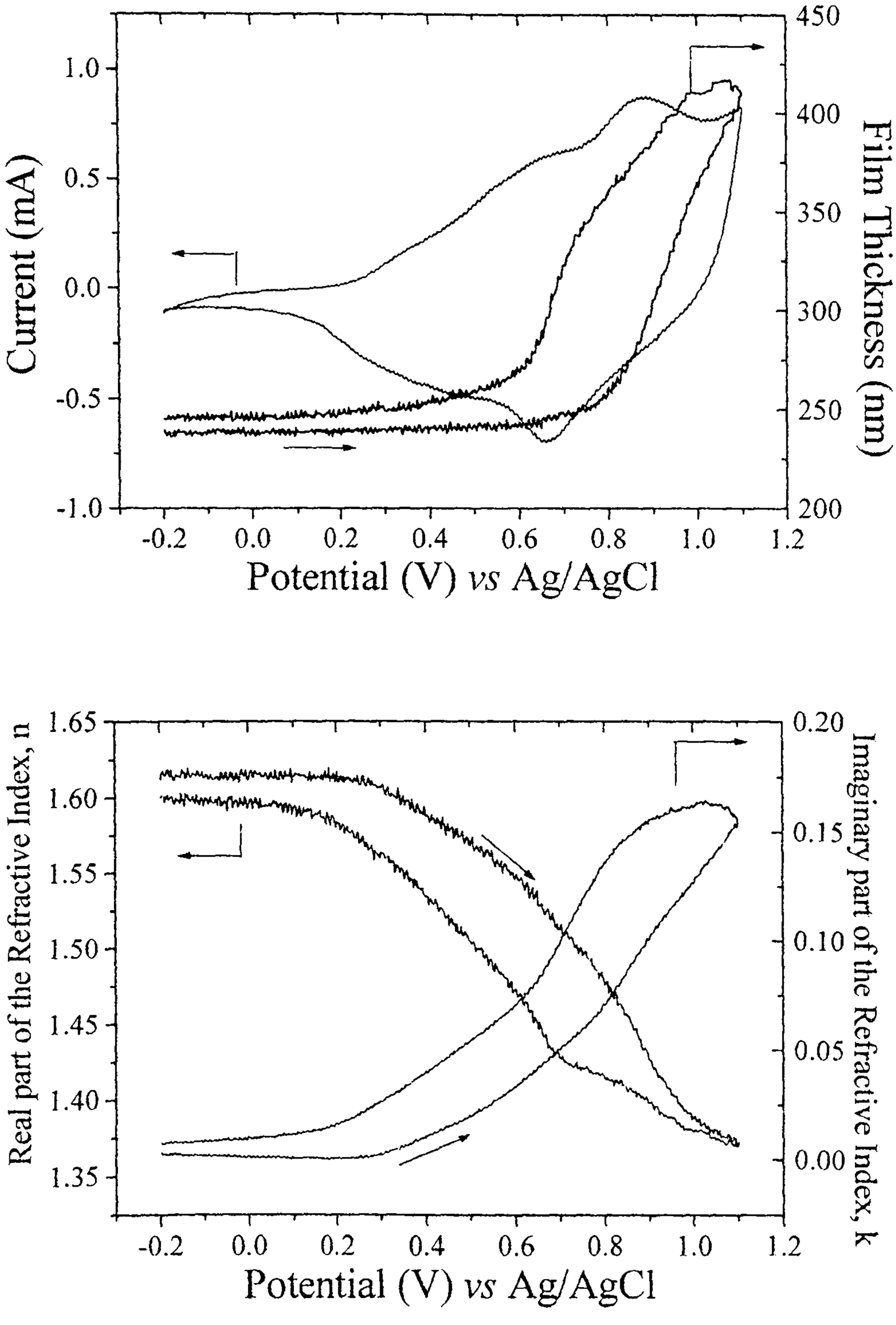

Fig. 6.16. Fitted data for the potential cycling of poly[Ni(OMeSalen)]. The data were fitted to an inhomogeneous model as described in the text. The film was scanned at 100 mV s^{-1} in 0.1 mol dm^{-3} TBAT in MeCN.

In order to fit the data for the cycling of poly[Ni(OMeSalen)] without the aid of ellipsometric data for the growth or the bare electrode, the final point of the cycle was considered; values for *n*, *k*, and the thickness were entered manually and the program returned values of Δ, Ψ and intensity. These returned values were compared with those obtained experimentally, and adjusted until the values of Δ and Ψ returned matched those observed, and the returned value of intensity was used with the observed value to scale all the intensities (a process normally done using the data for the bare electrode, see section 2.3). The film was fitted to an inhomogeneous model identical to that used for poly[Pd(OMeSalen)], and in fact the film could not be fitted to a homogeneous model. The entire file for the cycling of poly[Ni(OMeSalen)] was then fitted in the usual manner, and the fitted data is shown in Fig. 6.16. The data for the Pd and Ni films are strikingly similar (see also Fig. 6.9), though a slightly greater amount of hysteresis is observed in all three parameters for poly[Ni(OMeSalen)]. The quantitative behaviour of the thickness is very similar for the two films, while the values of *n* and *k* for poly[Pd(OMeSalen)] are slightly higher than for poly[Ni(OMeSalen)] over the entire cycle.

Although it would be a little perilous to try and draw any conclusions from the fitted poly[Ni(OMeSalen)] figures given the lack of any data from the bare electrode, it is certainly interesting that with no assumptions from the fitting of the Pd polymer affecting the fitting procedure used for poly[Ni(OMeSalen)], the behaviour of poly[Pd(OMeSalen)] and poly[Ni(OMeSalen)] is so similar. This certainly lends a great deal of credence to the model of a highly inhomogeneous film which swells by up to 50 % of its thickness upon oxidation.

6.2.5 Supporting FTIR data.

Figs. 6.17 (a) and (b) below show the in-situ FTIR spectra collected during the oxidation of poly[Pd(OMeSalen)], with an upper limit of 1.2 V. Fig 6.15(a) shows the complete spectral range, and Fig. 6.17(b) the range from 1000 to 1800 cm^{-1}, all spectra are normalised to the reference taken at 0.2 V.

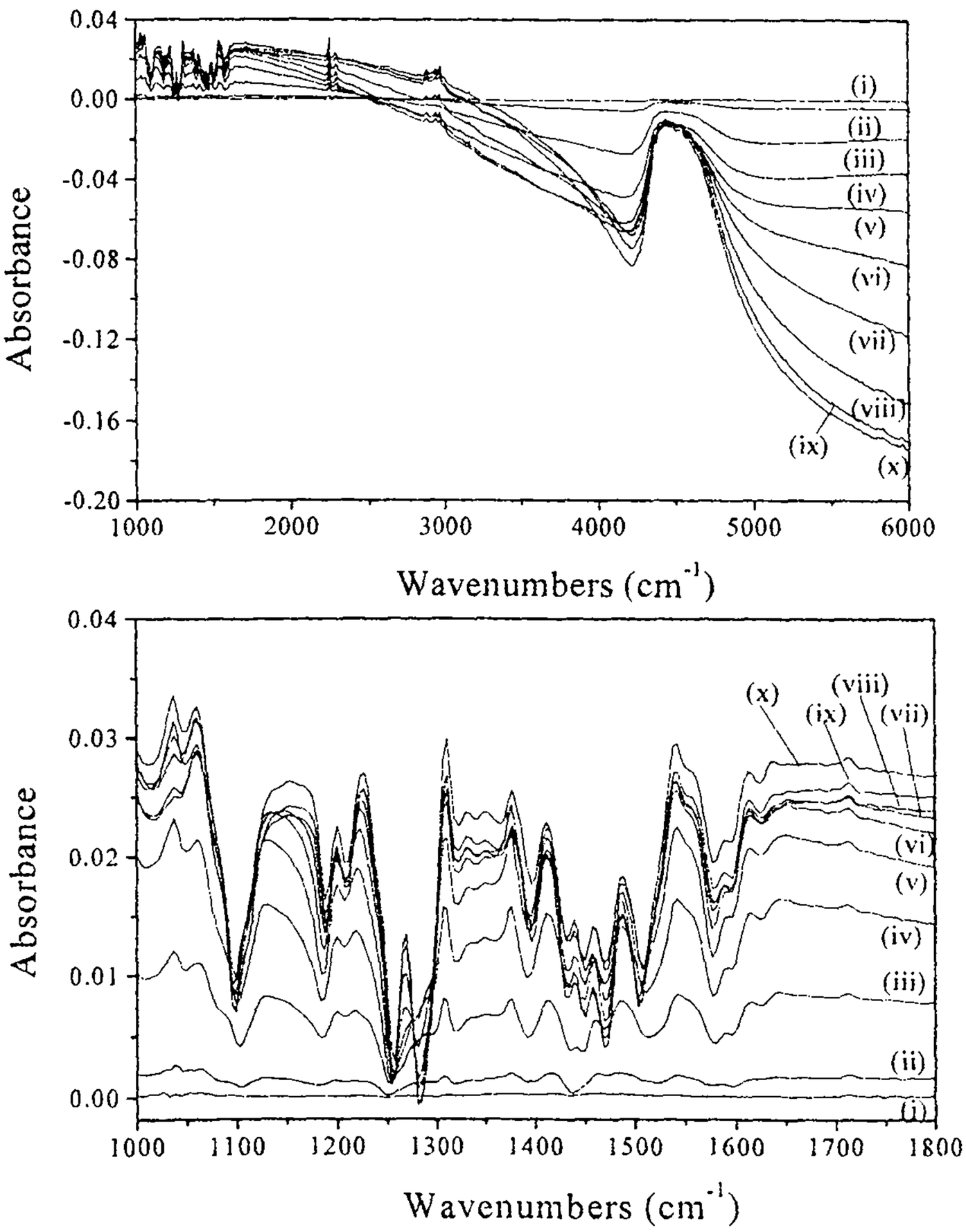

Fig. 6.17. In situ FTIR spectra of a poly[Pd(OMeSalen)] film on a 0.64 cm^2 Pt electrode in 0.1 mol dm^{-3} TBAT/MeCN taken during an experiment in which the potential of the electrode was stepped from 0.2 V to 1.2 V in 100 mV steps with spectra (1)-(x) being collected at each step: (a) the full spectral range, (b) the IRAV region from 1000 cm^{-1} to 1800 cm^{-1}.

Fig. 6.18 shows a plot of the area under the spectral region between 1050 and 1700 cm^{-1} as a function of potential. Figs. 6.17(a) and (b) show that the FTIR response is very complex, and Fig. 6.18 confirms the conclusions of the ellipsometric data that there are four potential regions, corresponding roughly to the potentials identified from the ellipsometry: a reduced region below 0.3 V, a rapid change in the parameters of the film between 0.3 and 0.7 V, between 0.7 and 0.9 V smaller changes were seen in the ellipsometric parameters, and the % area can be seen to be almost stationary, then between 0.9 V and 1.2 V the ellipsometric parameters displayed large changes again, and this corresponds to a decrease in the % area of the IRAV bands, again suggesting the presence of four different charge carriers as the film is oxidised, though, even with the FTIR data, it is still not possibly to identify them.

Figs. 6.19 (a) - (d) show the spectra in more detail. In the region 0.3 to 0.6 V (still referenced to the spectrum at 0.2 V) there is a clear gain of an electronic absorption in the near IR region between *ca.* 4000 and 5400 cm^{-1}, superimposed on which are losses due to C-H and C≡N stretches of acetonitrile. There are two bands

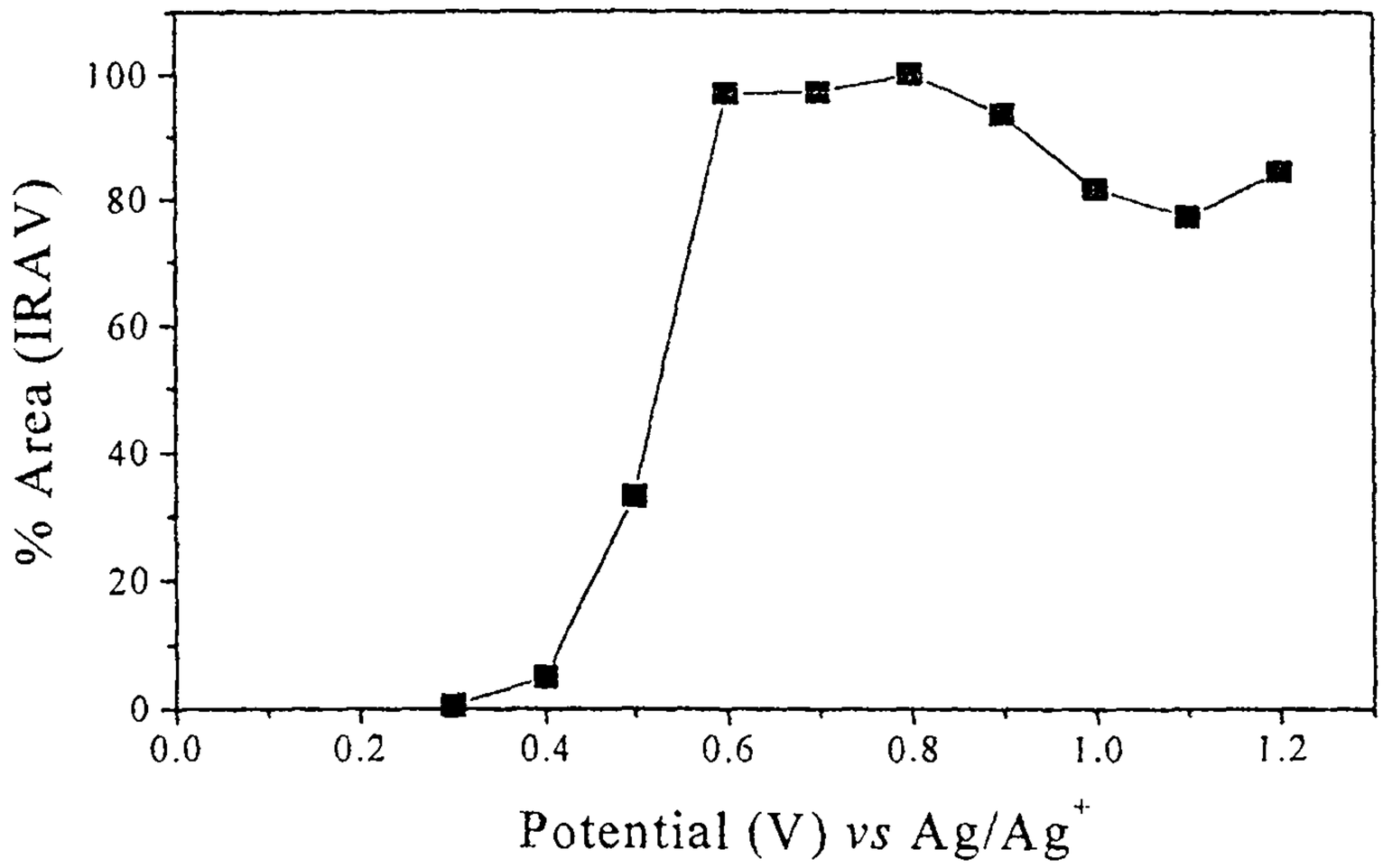

Fig. 6.18. Plot of the area under the IRAV region in Fig. 6.15(b) as a function of potential

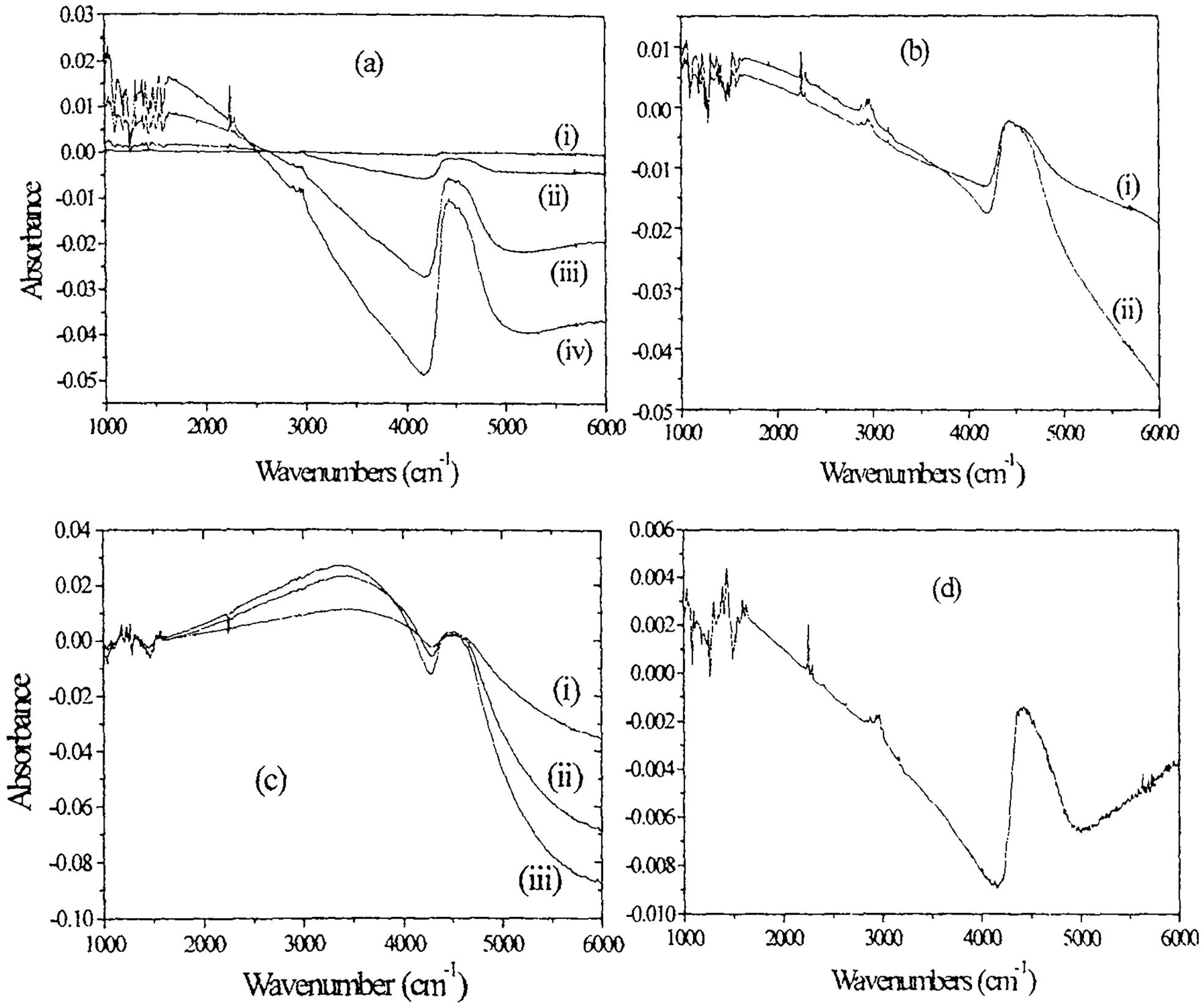

Fig. 6.19 (a) Spectra collected at 0.3 - 0.6 V ((i)-(iv)), normalised to 0.2 V, (b) spectra collected at 0.7(i) and 0.8 V(ii) normalised to that taken at 0.6 V, (c) spectra collected at 0.9 (i), 1.0 (ii) and 1.1 V (iii) normalised to that taken at 0.8 V, (d) spectrum collected at 1.2 V normalised to that taken at 1.1 V.

at 2250 and 2290 cm^{-1}, due to the $\nu(C\equiv N)$ fundamental and a combination band involving CH_3 torsion respectively, the ratio of which is known from previous work [20, 21] to be very sensitive to the environment of the acetonitrile: in pure liquid the ratio is 3.2, but increases for acetonitrile coordinated inside polymer films. The ratio for the two peaks in Fig. 6.19(a) is 3.4, suggesting that the acetonitrile loss corresponds to uncoordinated solvent, which is easily understood in terms of the expansion of the film displacing solvent from the thin layer. This corresponds well with the ellipsometry, which indicated that the film began swelling at *ca.* 0.3 V and

expanded by almost 40 nm between 0.2 and 0.6 V (see Fig. 6.9(a)) Losses are also seen near 1040 and 1060 cm^{-1} that can be attributed to BF_4^-. In the spectral range from 1000 to 1600cm^{-1} there is a series of gains which are similar in nature to those frequently observed in conducting polymer films: they arise from an electronic enhancement due to the excitation of certain skeletal modes which can facilitate carrier hopping along the polymer backbone, and hence lead to large values of the transition dipole moment. This enhancement is termed the IRAV effect [20 and 22 and references therein]. The fact that the enhancement is seen below 1600 cm^{-1} is strong evidence that the carriers are delocalised over the phenyl rings of the polymer. Strong support for this is that the two most intense features in this region are found at 1254 and 1100 cm^{-1}, which can be assigned to the C-O-C symmetric and asymmetric stretches of the Me-O-Aryl unit [23].

In the potential region between 0.6 and 0.8 V (Fig. 6.19 (b), now referenced to the spectrum at 0.6 V) there is continuing loss of acetonitrile, and the near IR electronic absorption continues to increase, as expected from the ellipsometric data. In the potential region from 0.9 to 1.1 V (Fig. 6.19(c)) now referenced to the spectrum at 0.8 V), the loss of the mid-IR electronic band is now clear, superimposed upon the continuing gain of the near-IR electronic band, the latter having a substantial effect on *n*. There is now a gain in the acetonitrile C≡N region, with the ratio of the two bands close to 5.6, which is typical of coordinated acetonitrile, though the ratio decreases to 3.1 : 1 at 1.2 V (see Fig. 6.19(d)), where a loss of free acetonitrile is apparent as the previous gain in coordinated solvent is offset by expansion of the film.

A study of Ni(Salen) by *in-situ* FTIR/UV-vis and *ex-situ* EPR [8] also concluded polymerisation proceeded *via* a ligand based mechanism, having found, as

with this study, that the clearest changes between the monomer and polymer spectra are due to the phenyl rings rather than the coordination sphere around the metal. Audebert *et al.* [10-12] have previously found the identity of the metal had little effect on the conductivity of Salen films, and hence suggested the redox processes were ligand based. Fig. 6.20 shows the overlapping spectra of poly[Pd(OMeSalen)] and poly[Ni(OMeSalen)], both taken at 0.6 V. They are clearly remarkably similar, again suggesting that the metal plays very little role in the charge conduction mechanism. For further discussion of the FTIR data of poly[Pd(OMeSalen)] and poly[Ni(OMeSalen)] see [24].

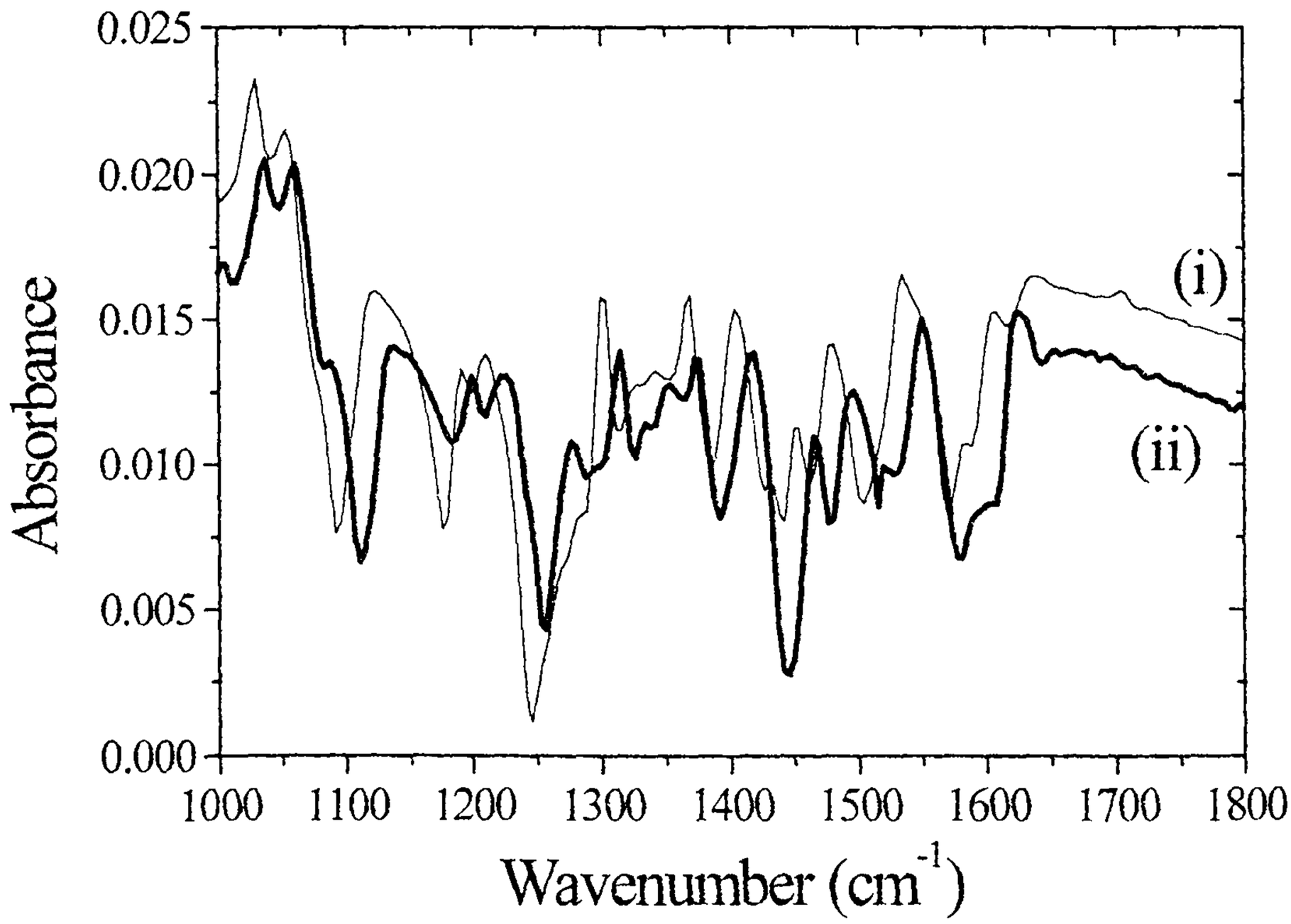

Fig. 6.20. The spectra of (i) [Pd(OMeSalen)] and (ii) [Ni(OMeSalen)] both taken at 0.6 V and normalised to the reference taken at 0.2 V for each film.

6.3. Conclusions

The ellipsometric data unequivocally indicate that surface film formation does not occur until the potential reaches 0.9 V, though clearly charge is passed before this point. One possibility, consistent with the evidence gathered by Timonov and co-workers is that oligomers containing stacked metal complexes form in solution prior to the main polymerisation process above 0.9 V for which they are the key intermediates, there is however no evidence of a stacked deposit being formed on the electrode as suggested by Dahm and Audebert. There is strong evidence that only the second oxidation process during anodic sweeps leads to growth of the polymer film, the steady increase in thickness between 0.3 and 0.7 V being due to the influx of solvent and electrolyte as a charge compensation mechanism for the oxidised polymer chains which continues at higher potentials as further polymerisation occurs.

The IR spectra seem to indicate the presence of at least two different types of charge carrier, one of which disappears at higher potentials. One hypothesis is that in the reduced form the film is compact and relatively free of solvent. In this situation charge stacking between monomer units may occur and in the early stages of oxidation charge carriers could hop between chains from one planar group to another. Conduction in the oxidised form of the polymer would appear to be limited to along the polymer chains, charge carriers would find it almost impossible to hop between monomer units by virtue of the shear volume of solvent present in the oxidised form of the polymer as the positively charged chains repel one another and solvent floods in with the electrolyte to compensate the charge. Given that the swelling of the film upon oxidation appears to be a completely reversible process, the formation of

carbon-carbon linkages between adjacent monomers appears to be a certainty as without some form of linkage other than metal - metal charge transfer the outer layer of the film would dissipate into solution upon such drastic swelling. As to the site of oxidation for the two processes, this remains a matter of controversy. Certainly FTIR evidence suggests the first process is mainly ligand based, however the second process is more difficult to assign and while it appears to be mainly ligand based, there may be considerable overlapping of the metal and ligand orbitals and both may be partially oxidised.

6.4. References

1. K. A. Goldsby, *J. Coord. Chem.*, 1988, **19**, 83.

2. K. A. Goldsby, J. K. Blaho, L. A. Hoferkamp, *Polyhedron*, 1989, **8**, 113

3. K. A. Goldsby, L. A. Hoferkamp, *Chem. Mater.*, 1989, **1**, 348.

4. F. Bedioui, E. Labbe, S. Gutierrez-Granados, S. Devynek. *J. Electroanal. Chem.*, 1991, **301**, 267.

5. C. E. Dahm, D. G. Peters, J. Simonet, *J. Electroanal. Chem.*, 1996, **410**, 163.

6. C. E. Dahm, D. G. Peters, *Anal. Chem.*, 1994, **66**, 3117.

7. C. E. Dahm, D. G Peters, *J. Electroanal. Chem.*, 1996, **406**, 119.

8. M. Vilas-Boas, C. Freire, B. de Castro, P. A. Christensen, A. R. Hillman, *Inorg. Chem.*,1997, **36** ,4919.

9. P. Audebert, P. Hapiot, P. Capdevielle, M. Maumy, *J. Electroanal. Chem.*, 1992, **338**, 269.

10. P. Audebert, P. Hapiot, P. Capdevielle, M. Maumy, *Synth. Met.*, 1991, **41**, 3049.

11. P. Audebert, P. Capdevielle, M. Maumy, *New J. Chem.*, 1991, **15**, 235.

12. P. Audebert, P. Capdevielle, M. Maumy, *New J. Chem.*, 1992, **16**, 697.

13. V. N. Aleynikova, V. V. Vasiliev, A. M. Timonov, G. A. Shagisultanova, *Russ. J. Phys. Chem.*, 1987, **61**, 1117.

14. V. V. Vasilieva, K. P. Balashev, A. M. Timonov, *Russ. J. Electrochem.*, 1998, **34**, 978.

15. I. E. Popeko, A. M. Timonov, G. A. Shagisultanova, *J. Appl. Chem. USSR*, 1990, **63**, 2033.

16. S. Glasstone, *Textbook of Physical Chemistry*, MacMillan, London, 1966.

17. S. Gottesfeld in *Electroanalytical Chemistry*, ed. A. J. Bard, Marcel Dekker, New York, 1989, vol. 15.

18. Abd El-Rahman, A. Kudelka, J. W. Shultze, *Ber. Bunsen-Ges. Phys. Chem.*, 1996, **100**, 1798.

19. A. Hamnett, A. R, Hillman, *Ber. Bunsen-Ges. Phys. Chem.*, 1987, **91**, 329.

20. P. A. Christensen, A. Hamnett, A. R. Hillman, M. J. Swann, and S. J. Higgins, *J. Chem. Soc., Faraday Trans.*,1992, **88**, 595.

21. P. A. Christensen, A. Hamnett, and D. C. Read, *Synth. Met.*, 1994, **62**, 141.

22. P. A. Christensen, A. Hamnett, *Electrochim. Acta*, 1991, **36**, 1263.

23. G. Socrates, *Infrared Characteristic Group Frequencies*, John Wiley and Sons, Chichester, 1980.

24. Jintana Eameaim, Ph.D. Thesis, The Application of Fourier Transform Infra-Red to the Study of the Electrode/Electrolyte Interface, University of Newcastle upon Tyne, 2001.

7.1 Introduction

In this chapter the main conclusions of this thesis are summarised and, where appropriate, future work suggested.

7.2 Conclusions on the Sources and Reduction of Noise

7.2.1 Conclusions on the Sources of Noise within the Ellipsometric System

Two of the four lasers used in the ellipsometric system are randomly polarised, i.e. emit linearly polarised photons at random angles. When passed through the polarising components of the ellipsometer this yields a beam of fluctuating intensity. The relative intensity recorded with the ellipsometric angles displayed significantly more noise than that recorded for the linearly or circularly polarised lasers and, as would be expected, was clearly reduced by the addition of a quarter wave plate between the laser and polarising components.

Δ and Ψ should be independent of any changes in intensity, however this was clearly not the case. This was due to the experimental set-up, in which the outputs of the four photodiodes within the Stokesmeter are recorded sequentially rather than simultaneously.

The computer recording the electrochemical and ellipsometric data is also introducing noise. Using the transient program to collect data resulted in a significant amount of shot noise that is not present when using the normal data collection procedure. This shot noise is unequivocally injected by the computer itself.

7.2.2 Improvements to the Ellipsometric System.

It is planned to build a dedicated PC to replace the Atari. As this will be built specifically for the ellipsometer, at each stage of construction it should be possible to test for any potential problems, and exclude the shot noise present during transient measurements. It should also be possible to sample the four Stokesmeter outputs simultaneously.

With regard to the noise arising from the randomly polarised lasers, the only viable option is to replace them with ones of a constant polarisation, though sampling the Stokesmeter outputs simultaneously would reduce the noise on Δ and Ψ considerably.

Further improvements in the noise levels may result from replacing the mounting of the Stokesmeter, as the current mount is very flexible, though designing a rigid mount which also allows the necessary movement for aligning the system is no small task. It may also be beneficial to move the mounting of the Stokesmeter nearer to the pivot of the ellipsometer, minimising the distance the beam has to travel, and consequently reducing the movement of the Stokesmeter relative to the beam.

7.3 Conclusions from the Investigation of Poly[Salens]

From the polymerisation of Ni(SaldMe) and Ni(SaltMe) it is clear even relatively minor structural alterations created well away from the site of polymerisation can have marked effects on the characteristics of the polymer film produced. Both materials displayed similar behaviour during polymerisation, producing homogeneous films of a similar thickness by a mechanism of consolidation. During potential cycling, differences in behaviour were observed above 0.95 V with *n*, *k* and the thickness remaining almost stationary for poly[Ni(SaltMe)], while a marked contraction was observed for poly[Ni(SaldMe)] and *n* displayed an increase in value. During the much slower process of potential stepping, no decrease in thickness was observed at higher potentials, and only a very small increase in *n*, indicating that these processes are connected with the mechanism of charge compensation when the film is oxidised. It was suggested that, during the rapid change in potential during cycling, insufficient solvent can enter the film, and charge transfer stacking occurs to compensate the charge on the partially oxidised Ni centres, while during the stepping experiments, the much slower rate of potential change allows sufficient solvent to enter the film and hence no contraction is observed.

The investigation of [Ni(OMeSaltMe)] demonstrated that the addition of electron-donating substituents on the phenyl rings had an even greater effect on the characteristics of the polymer film produced than structural changes on the carbon-carbon bridge. From the start of the growth process differences were clear between [Ni(OMeSaltMe)] and [Ni(SaltMe)]: while the first three cycles of growth of

poly[Ni(OMeSaltMe)] produced a homogeneous film, each cycle produced a clear increase in thickness, rather than progressing by consolidation, as observed for poly[Ni(SaltMe)]. Beyond the third cycle of growth, poly[Ni(OMeSaltMe)] became inhomogeneous, being very dense next to the electrode and becoming more diffuse and containing a higher percentage of solvent as the film/solvent interface is approached. During oxidation of the polymer, a massive contraction was observed above 0.85 V and *n* was seen to increase markedly. This again is consistent with charge transfer stacking; however, this behaviour is repeated in the stepping experiments suggesting it does not occur only because of dynamic considerations, but is the preferred mechanism of charge stabilisation. The values of *k* observed for poly[Ni(OMeSaltMe)] were significantly higher than for poly[Ni(SaltMe)], suggesting the degree of oxidation on the Ni centre is greater and a greater degree of charge compensation is necessary. The same process was occurring in both poly[Ni(SaldMe)] and poly[Ni(OMeSaltMe)], however, in the former case, the solvent can provide adequate charge compensation if given enough time for sufficient solvent to enter, in the latter case, the greater extent of oxidation on the Ni centre results in charge transfer stacking being necessary for sufficient charge compensation.

The investigation of poly[Pd(OMeSalen)] also yielded an inhomogeneous film, a characteristic clearly the result of the electron donating -OMe substituent. Upon oxidation the film swelled reversibly to almost twice its thickness in the neutral state, due to the influx of solvent to compensate the charge on the polymer chains. Poly[Ni(OMeSalen)] was also investigated, and though less stable than its Pd counterpart, still mirrored the inhomogeneous behaviour observed. The increase in thickness (and *k*) upon oxidation, and the decrease in *n* were not linear with potential,

and appeared to display four potential dependent regions of behaviour, which may be due to conformational changes or changes in the structure of the charge carrier. The IR spectra seem to indicate the presence of at least two different types of charge carrier, one of which disappears at higher potentials.

Given that the swelling (and subsequent contraction in some cases) of all the films upon oxidation appear to be completely reversible processes, the formation of carbon-carbon linkages between adjacent monomers appears to be extremely likely as, without some form of linkage other than metal - metal charge transfer, the outer layer of the film would dissipate into solution upon such drastic swelling. The site of oxidation remains a matter of controversy, though much evidence suggests partial oxidation of both the ligand and metal.

7.4 Possible Further Systems to Investigate

The main aim of this project was to exploit the ultra-fast electrochemical ellipsometer, and in order to do this more fully a variety of systems could be studied. Ellipsometry is not just useful for the study of conducting polymers, but is an unparalleled technique for the characterisation of *any* thin film, i.e. any system which results in deposition at the working electrode can be studied. In order to exploit the ellipsometer to the full, systems which would benefit from the higher time resolution possible with the use of the Stokesmeter would be ideal.

One such system would be the passivation of iron, which has been studied with ellipsometry in the past [1], but never with the time resolution now possible. Past studies [1,2] have indicated that passivation in carbonate buffer is a two step

process, a layer of ferrous hydroxide or ferrous carbonate forming first, then at higher potentials further oxidation occurs, yielding an inner mixed valence film, and an outer film containing only ferric species. Dissolution of the film during reduction appears to commence with the outer layer, although there is evidence that the inner layer dissolves throughout the reduction process, not only once the outer layer has been stripped. Both passivation and depassivation occur over a millisecond timescale, and the sampling time of 200 ms used in [1] was inadequate to observe detailed changes. With the current experimental setup resolution of 5 ms is possible using the ordinary data collection programs, and 325 μs using the transient collection method. However, preliminary experiments were unsuccessful due to the noise present, typical data is shown in Fig. 7.1. It would be beneficial to the understanding of this system to study film formation and dissolution at the higher time resolution of which the Stokesmeter is capable. This is not possible with the current experimental set-up, however with the reduction in noise anticipated by replacing the Atari with a dedicated PC, it may well be possible to return to this system and investigate it further.

Another system which may benefit from fast-ellipsometric investigation is the electrodeposition of semiconductor thin films, such as CdSe, CdTe, ZnSe and ZnTe. The growing use of these semiconductors in photovoltaic devices has lead to the search for efficient low cost production methods, and electrodeposition appears a suitable candidate. Little is known about the mechanistic aspects of such depositions [3], or the effects that varying the experimental conditions has on the nature of the films deposited, and ellipsometry would be an ideal tool with which to probe these effects.

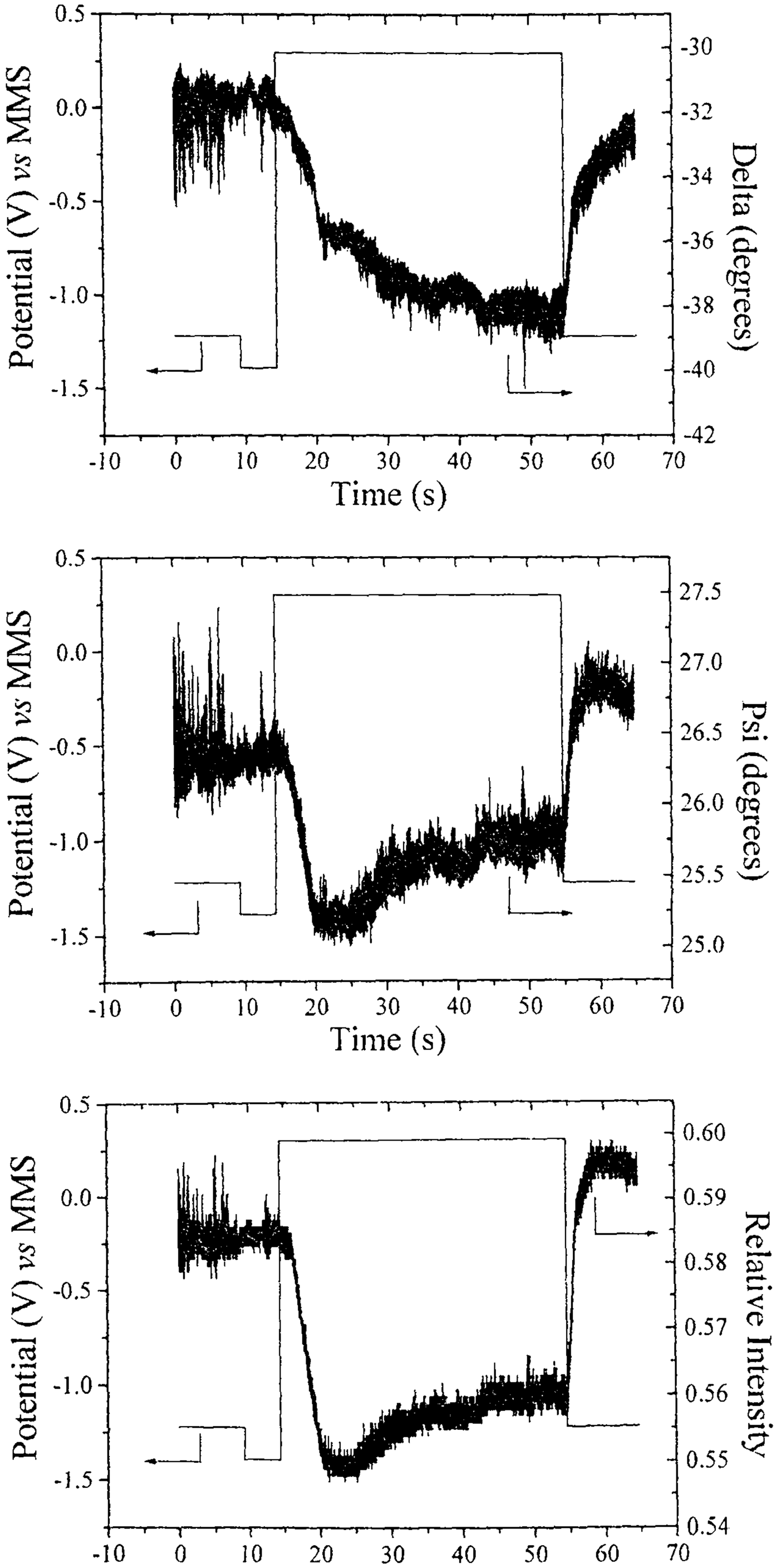

Fig. 7.1. Typical data for the passivation of iron. An iron disk electrode was stepped from the rest potential (-1.22 V) to -1.39 V to clean the surface of any residual oxide, then to a passivation potential (0.3 V), before returning to the rest potential.

These are just two possible systems which have already been considered for investigation with the Stokesmeter based ellipsometer. As stated above, *any* system involving the formation of a thin film of any kind can be investigated with ellipsometry, and with the time resolution already available, and especially with that potentially available, the Newcastle instrument is an exceptionally powerful tool.

7.5 References

1. P. Southworth, A. Hamnettt, A. M. Riley, J. M. Sykes, *Corr. Sci.*, 1988, **28**, 1139.

2. A. M. Riley, J. M. Sykes, A. Hamnettt, *Corr. Sci.*, 1988, **28**, 799.

3. K. K. Mishra, K. Rajeshwar, *J. Electroanal. Chem.*, 1989, **273**, 169, and references therein.